# Development and Optimisation of Regenerative Adsorbent Structures for Carbon Dioxide and Contaminants Removal

Hong, Wan Yun

*Award date:*
2017

*Awarding institution:*
University of Bath

# Development and Optimisation of Regenerative Adsorbent Structures for Carbon Dioxide and Contaminants Removal

Wan Yun Hong

A thesis submitted for the degree of Doctor of Philosophy

University of Bath

Department of Chemical Engineering

July 2016

# Abstract

This thesis presents the research on the development and optimisation of energy efficient adsorbent monoliths and foam-monoliths for the removal of carbon dioxide ($CO_2$) and other contaminants such as hydrogen sulfide ($H_2S$) and water ($H_2O$) vapour from the biogas stream. Zeolite and MIL-101(Cr) monoliths and carbonate-based zeolite foam-monoliths of novel chemical formulations have been manufactured, characterised and tested for adsorption. Using the prepared adsorbent monoliths as models, their kinetic adsorption and gas flow dynamic performances have also been evaluated and compared with packed beds of commercially available adsorbent beads.

The research mainly comprised of three parts. The first part was concerned with the manufacturing, characterising and optimising the adsorbent monoliths and foam-monoliths. The adsorbent monoliths and foam-monoliths have been fabricated successfully using the unique paste extrusion technique described in this thesis. This includes monoliths of 13X zeolite, LiLSX zeolite, 5A zeolite, clinoptilolite and MIL-101(Cr) and foam-monoliths of $K_2CO_3$/13X zeolite and $Na_2CO_3$/13X zeolite. The incorporation of a decomposable pore former such as Licowax C micropowder PM into their paste formulations were found to improve their structural porosity, adsorption performance and mass transfer. It has been found that the best type of adsorbent structure for $CO_2$ adsorption were 13X zeolite and purified MIL-101(Cr) monoliths and $K_2CO_3$/13X zeolite foam-monoliths. The $CO_2$ adsorption performances of purified MIL-101(Cr) monoliths and $K_2CO_3$/13X zeolite foam-monoliths have been shown to be comparable to a packed bed of 13X zeolite beads (in terms of effectiveness of the adsorbent bed utilisation and equilibrium adsorption capacity on mass basis, respectively). This confirmed that the prepared adsorbent monoliths and foam-monoliths were potential adsorbent structures for $CO_2$ adsorption.

The second part involved testing the prepared adsorbent monoliths and foam-monoliths with single (such as $CO_2$, $CH_4$ and $H_2S$) and mixed (such as $CO_2$/$CH_4$ and $CO_2$/$CH_4$/$H_2O$ vapour) gases under different operating conditions to assess their dynamic adsorption performances for biogas upgrading. 13X zeolite and MIL-101(Cr) monoliths and $K_2CO_3$/13X zeolite foam-monoliths were used as model adsorbent structures in single and mixed gas adsorption experiments. The study has shown that 13X zeolite monoliths and $K_2CO_3$/13X zeolite foam-monoliths have excellent adsorption performances for $CO_2$, $H_2S$ and $H_2O$ vapour and they could upgrade the biogas to a high quality (i.e., up to about 98% vol. $CH_4$). For purified MIL-101(Cr) monoliths, it was discovered that they have

relatively good adsorption performance for $CO_2$, $H_2S$, $CH_4$ and $H_2O$ vapour and they could upgrade the biogas to a moderate quality (i.e., up to about 67% vol. $CH_4$). In both humid and dry conditions, $K_2CO_3$/13X zeolite foam-monoliths were found to have the highest selectivity of $CO_2$ over $CH_4$ compared to 13X zeolite and purified MIL-101(Cr) monoliths.

The third part was related to the evaluation and comparison of kinetic adsorption and gas flow dynamic performances of the prepared adsorbent monoliths with those of packed beds of adsorbent beads. In these studies, LiLSX zeolite monoliths and beads were used as model adsorbent structures. The kinetic adsorption study has discovered that LiLSX zeolite monoliths have slightly higher overall mass transfer resistance than packed beds of LiLSX zeolite beads. It has been shown that the overall mass transfer resistance in monoliths could be reduced by decreasing the channel diameter and increasing the wall thickness. The gas flow dynamic study found that the mass transfer in monoliths was not contributed by the axial dispersion of gases and this was in contrast to the mass transfer in packed beds. LiLSX zeolite monoliths were found to have lower pressure drop compared to packed beds of LiLSX zeolite beads. This showed that the biogas upgrading process would be more energy efficient using adsorbent monolith/foam-monolith systems compared to packed bed systems.

# Acknowledgements

The author would like to express her gratitude to the Brunei Government for awarding a scholarship to her for pursuing a doctoral research programme (PhD in Chemical Engineering) at University of Bath, UK. Financial supports provided by the Brunei Government to the author for carrying out this research were gratefully acknowledged.

This research was under the supervisions of Professor Semali Perera from the Department of Chemical Engineering, University of Bath and Professor Andrew Burrows from the Department of Chemistry, University of Bath. Their kind supports and guidance given to the author were sincerely appreciated.

Technical supports and advices provided by the member of staffs in the Department of Chemical Engineering, Department of Chemistry, Department of Mechanical Engineering and Microscopy and Analysis Suite (MAS) at University of Bath to the author were also appreciated; with special thanks to Dr Olivier Camus, Mrs Ursula Potter, Dr Gabriele Kociok-Köhn, Mr Alan Carver, Mrs Clare Ball, Dr Daniel Lou-Hing, Mr Alexander Ciupa, Mr John Bishop, Mr Robert Brain, Mr Fernando Acosta, Mrs Suzanne Barkley and Mr Thomas Richard. Further thanks were also expressed to Mr Andrew Physick for helping with the isotherm measurements.

# Contents

# List of Tables

# List of Figures

# Nomenclature

| | |
|---|---|
| $A$ | Cross-sectional area ($m^2$) |
| $A_s$ | External specific surface area of adsorbent bed ($m^2\ m^{-3}$) |
| $C$ | Effluent adsorbate gas concentration (ppmv or % vol. or g $m^{-3}$) |
| $C_b$ | Adsorbate gas concentration in the bulk gas phase (mol $m^{-3}$) |
| $C_e$ | Effluent adsorbate gas concentration at equilibrium (ppmv or % vol. or g $m^{-3}$) |
| $C_s$ | Adsorbate gas concentration at the external surface of the adsorbent particle (mol $m^{-3}$) |
| $C_0$ | Influent adsorbate gas concentration (ppmv or % or g $m^{-3}$) |
| $d_c$ | Monolith channel diameter (mm) |
| $d_m$ | Diameter of extruded monolith (mm) |
| $d_p$ | Particle diameter (m or mm) |
| $d_{pore}$ | Pore diameter (mm) |
| $d_{mean}$ | Mean pore diameter (mm) |
| $D$ | Adsorbent bed diameter (m) |
| $D_{ax}$ | Axial dispersion coefficient ($m^2\ s^{-1}$) |
| $D_e$ | Effective diffusion diffusivity ($m^2\ s^{-1}$) |
| $D_M$ | Maxwellian diffusion coefficient/molecular diffusivity ($m^2\ s^{-1}$) |
| $D_o$ | Overall diffusion coefficient ($m^2\ s^{-1}$) |
| $D_s$ | Extruder screw diameter (mm) |
| $E$ | Elastic modulus (MPa) |
| $F_c$ | Compressive load (N) |
| $k$ | Overall mass transfer coefficient ($m\ s^{-1}$) |
| $k_B$ | Boltzmann constant ($\approx 1.3807 \times 10^{-23}\ J\ K^{-1}$) |
| $k_f$ | External gas film mass transfer coefficient ($m\ s^{-1}$) |
| $k_p$ | Pore mass transfer coefficient ($m\ s^{-1}$) |
| $l$ | Extension of the sample (mm) |
| $L$ | Bed length (m) |
| $L_c$ | Original length of the sample for compression test (mm) |
| $L_{MTZ}$ | Length of the mass transfer zone (m) |
| $\bar{L}_{MTZ}$ | Percentage length of mass transfer zone in adsorbent bed (%) |

| | |
|---|---|
| $L_{pore}$ | Length of pore (mm) |
| $LUB$ | Length of unused bed (m) |
| $LES$ | Length of equilibrium section of the bed (m) |
| $m$ | Bed mass, i.e. mass of adsorbent + mass of binder (g) |
| $m_{ad}$ | Mass of adsorbent (g) |
| $M_w$ | Molecular mass (g mol$^{-1}$ or kg mol$^{-1}$) |
| $P$ | Pressure (Pa or bar) |
| $P_T$ | Total pressure (bar) |
| $P_i$ | Partial pressure (bar), where $i$ is the gas component |
| $\Delta P$ | Pressure drop (Pa) |
| $\bar{q}_b$ | Breakthrough adsorption capacity (mmol g$^{-1}$) |
| $\bar{q}_e$ | Equilibrium adsorption capacity (mmol g$^{-1}$) |
| $\hat{Q}$ | Molar flow rate (mmol s$^{-1}$) |
| $R_g$ | Universal gas constant (≈ 8.314 × 10$^{-5}$ m$^3$ bar mol$^{-1}$ K$^{-1}$) |
| $R_m$ | Mass transfer rate (mol m$^{-3}$ s$^{-1}$) |
| $Re$ | Reynolds number; $Re = \frac{\rho u_s d}{\mu}$ where $d = d_p$ for packed bed or $d = d_c$ for monolithic bed (dimensionless) |
| $RH$ | Relative humidity of the effluent adsorbate gas (%) |
| $RH_0$ | Initial relative humidity of the feed/influent adsorbate gas (%) |
| $S_{pore}$ | Pore surface area (mm$^2$) |
| $S_{pore,t}$ | Total pore surface area (mm$^2$) |
| $Sc$ | Schmidt number; $Sc = \frac{\mu}{\rho D_M}$ (dimensionless) |
| $Sh$ | Sherwood number; $Sh = \frac{kd}{D_M}$ where $d = d_p$ for packed bed or $d = d_c$ for monolithic bed (dimensionless) |
| $t$ | Time (s) |
| $t_b$ | Breakthrough time (s) |
| $t_{eq}$ | Equilibrium time (s) |
| $t_w$ | Monolith wall thickness (mm) |
| $\bar{t}$ | Normalised time (s g$^{-1}$) |
| $\bar{t}_b$ | Normalised breakthrough time (s g$^{-1}$) |
| $\bar{t}_{eq}$ | Normalised equilibrium time (s g$^{-1}$) |
| $T$ | Temperature (K) |

| | |
|---|---|
| $u_{MTZ}$ | Adsorbate gas velocity in the mass transfer zone (m $s^{-1}$) |
| $u_s$ | Superficial velocity of flowing gas (m $s^{-1}$) |
| $V_{pore}$ | Pore volume ($mm^3$) |
| $V_{pore,t}$ | Total pore volume ($mm^3$) |
| $x$ | Mole/volume fraction of a component in the adsorbed phase (dimensionless) |
| $y$ | Mole/volume fraction of a component in the bulk gas phase (dimensionless) |

## Greek letters

| | |
|---|---|
| $\alpha_{CO_2/CH_4}$ | Selectivity for absorbing $CO_2$ relative to $CH_4$ (dimensionless) |
| $\gamma$ | Surface tension of mercury (480 mN $m^{-1}$) |
| $\varepsilon$ | Bed voidage/porosity (dimensionless) |
| $\epsilon$ | Compressive strain (m $m^{-1}$) |
| $\vartheta$ | Constant in the Lennard-Jonas potential function/average collision diameter (nm) |
| $\mu$ | Dynamic viscosity of flowing gas (N s $m^{-2}$) |
| $\xi$ | Characteristic energy of flowing gas |
| $\varpi_{bed}$ | Effectiveness of adsorbent bed utilisation (%) |
| $\rho$ | Density of flowing gas (kg $m^{-3}$) |
| $\rho_b$ | Bulk density of packed bed (kg $m^{-3}$) |
| $\rho_B$ | Bulk density of adsorbent (kg $m^{-3}$) |
| $\rho_{cell}$ | Cell density (cell $cm^{-2}$) |
| $\rho_p$ | Particle density (kg $m^{-3}$) |
| $\sigma$ | Compressive strength or stress (MPa) |
| $\tau$ | Tortuosity factor (dimensionless) |
| $\varphi$ | Contact angle between the solid and mercury (140°) |
| $\Omega$ | Collision integral of flowing gas (dimensionless) |

## Subscripts

| | |
|---|---|
| $A$ | Component $A$ |
| $B$ | Component $B$ |

# Chapter 1 Introduction

The development and optimisation of regenerative adsorbent structures for removing carbon dioxide ($CO_2$) and other contaminants such as hydrogen sulfide ($H_2S$) and water ($H_2O$) vapour from the biogas stream will be presented in this thesis. The thesis consists of the following chapters:

- Chapter 1 will describe the importance of the research. The aim, objectives and scope of the research will also be included.
- Chapter 2 will cover the background of the research. This includes: (a) an overview of biogas, their utilisation and current upgrading technologies, (b) the fundamental theories of adsorption that are related to the research as well as the choice of regeneration methods, (c) the choice of suitable adsorbents (such as zeolites, metal-organic frameworks (MOFs) and alkali metal carbonates) for biogas upgrading, (d) the choice of suitable binders (such as clays) that will provide mechanical stability to the adsorbent structures and (e) a range of possible structured adsorbents (such as beads, pellets, granules, monoliths and foams).
- Chapter 3 will present the unique fabrication procedures of zeolite monoliths using 13X zeolite, LiLSX zeolite, 5A zeolite and clinoptilolite as model zeolite adsorbents. Their thermal stability, crystal and pore structures, surface morphology and mechanical strength will be characterised using established methods.
- Chapter 4 will disclose the special fabrication methods used in the fabrication of MOF monoliths using MIL-101(Cr) as the model MOF adsorbent. Their physical characteristics such as thermal stability, crystal and pore structures, surface morphology, mechanical strength and $CO_2$ adsorption capacity will be determined using established methods.
- Chapter 5 will reveal the novel fabrication techniques used in producing the carbonate-based zeolite foam-monoliths of enhanced adsorption capacity. Carbonates such as potassium and sodium carbonates will be formed chemically within the monoliths. Their thermal stability, crystal and pore structures, surface morphology and mechanical strength will be characterised using similar methods as those described in Chapter 3.
- Chapter 6 will describe the optimisation of adsorbent monoliths and foam-monoliths with $CO_2$ adsorption. Zeolite and MIL-101(Cr) monoliths and carbonate-based zeolite foam-monoliths will be used as model adsorbent structures. Their composition (i.e., types of adsorbents and bentonites, adsorbent to bentonite ratio and inclusion of a

pore forming agent), firing temperature, physical structure (i.e., wall thickness and bed length) and regeneration temperature will be considered. Comparison of their $CO_2$ adsorption performance will also be made with adsorbent beads.

- Chapter 7 will determine the dynamic adsorption performance of adsorbent monoliths and foam-monoliths for biogas upgrading. The prepared 13X zeolite and purified MIL-101(Cr) monoliths and $K_2CO_3$/13X zeolite foam-monoliths will be used as model adsorbent structures and tested for single ($CO_2$, $CH_4$ and $H_2S$) and mixed ($CO_2$/$CH_4$ and $CO_2$/$CH_4$/$H_2O$ vapour) gas adsorption with a range of operating conditions.

- Chapter 8 will evaluate the kinetic adsorption and gas flow dynamic performances of adsorbent monoliths and packed beds of adsorbent beads. LiLSX zeolite monoliths and beads will be used as model adsorbent structures. Their mass transfer and gas diffusional resistances, axial dispersion and pressure drop will be evaluated for a biogas upgrading system.

- Chapter 9 will conclude the entire research works presented in this thesis. Possible future developments of the research will also be included.

## 1.1 Importance of the Research

Contaminants such as $CO_2$, $H_2O$ vapour and $H_2S$ can be hazardous to some processes as they may cause corrosion effects on equipment. When they are present too much in the atmosphere, they affect the environment as well as the ecosystems and species within them, which includes humans. For example, the increasing emissions of $CO_2$ gas into the atmosphere causes global warming and climate change (Hofmann *et al.*, 2009). If the air has a high moisture content, i.e. above 50% relative humidity (RH), the environment becomes uncomfortable to humans. On the other hand, the emissions of $H_2S$ gas above the exposure limit of 10 parts per million in volume (ppmv) is lethal to humans. To reduce their emissions, it is crucial to capture these contaminants in a cost effective and safe way.

Due to these reasons, numerous technologies have been proposed and used in industrial processes for capturing these contaminants. For examples, adsorption, absorption and membrane separation, to name a few. Although these existing technologies have been established since a few decades ago, there are often problems associated with the suggested technologies that are affecting the overall performance of the system. This can be in terms of energy demand and efficiency of product recovery and generation. For instance, some of the drawbacks for using gas absorption technique in

separating $CO_2$ from biogas with alkanolamine solutions (such as monoethanolamine, MEA) are high energy requirement for the regeneration of amine solutions, continuous needs of replacing the saturated amine solutions with new/regenerated ones and occurrence of severe corrosion on equipment (Allegue and Hinge, 2012; Persson *et al.*, 2006).

It is also important to select and use suitable packing structure for the process since they will influence the system performance. For example, the performance and energy efficiency of current biogas upgrading technologies is often limited with the use of packed beds since they generally have pressure drop and mass transfer issues (Akhtar *et al.*, 2014). In addition, the materials used in current technologies can degrade after long-term usage, damage due to $H_2O$ vapour intolerance and poison by the toxic $H_2S$. Hence, improvements to existing biogas upgrading technologies are necessary to enhance their system performance and energy efficiency.

The need of an energy efficient technology for $CO_2$, $H_2O$ vapour and $H_2S$ capture using low pressure drop structures (such as monoliths) inspires this research to be carried out. The model gas chosen for this research is biogas. The reasons are because it is a clean renewable fuel and it has a broad range of applications such as generation of heat and electricity or use as transport fuels (Wellinger and Lindberg, 2001).

In brief, this research intends to develop a green technology that could provide improvements to existing technologies by exploring on new materials that are suitable for removing $CO_2$, $H_2O$ vapour and $H_2S$ from biogas. The manufacturing of low pressure drops monolithic and foam-monolithic structures will be described in this thesis using different procedures than those reported in the literature, for examples, Lee (1997) and Li (1998). The manufacturing of novel structured adsorbents such as zeolite and MIL-101(Cr) monoliths and carbonate-based zeolite foam-monoliths will be described for the first time in this thesis. These novel structured adsorbents will be characterised and compared with the current state-of-the-art adsorbent structures such as beads. Lastly, the adsorption (i.e., dynamic and kinetic) and gas flow dynamic performances of the prepared adsorbent monoliths and foam-monoliths will be evaluated for a biogas upgrading system.

## 1.2 Aim and Objectives

The overall aim of this research is to develop porous, low pressure drop and regenerative monolithic and foam-monolithic adsorbent structures that are capable of capturing $CO_2$ and other contaminants such as $H_2O$ vapour and $H_2S$ for biogas upgrading application. The main objectives of the research are:

a) Selection of suitable adsorbents (such as zeolites, metal-organic frameworks (MOFs) and alkali metal carbonates) for removing $CO_2$, $H_2O$ vapour and $H_2S$.

b) Preparation of adsorbent monoliths and foam-monoliths from unique formulations and techniques.

c) Characterisation of the prepared adsorbent monoliths and foam-monoliths using various established techniques to determine their physical properties such as thermal stability, crystal and pore structures, surface morphology and mechanical strength.

d) Optimisation of the prepared adsorbent monoliths and foam-monoliths with $CO_2$ adsorption and comparison with a packed bed of adsorbent beads.

e) Evaluation on the dynamic adsorption performances of the prepared adsorbent monoliths and foam-monoliths for biogas upgrading by carrying out single (such as $CO_2$, $CH_4$ and $H_2S$) and mixed (such as $CO_2/CH_4$ and $CO_2/CH_4/H_2O$ vapour) gas adsorption experiments under different operating conditions.

f) Evaluation on the kinetic adsorption and gas flow dynamic performances of the prepared adsorbent monoliths and packed beds of adsorbent beads by determining their mass transfer, diffusion and axial dispersion coefficients and pressure drop theoretically and/or experimentally.

## 1.3 Scope of the Research

The scope of this research is restricted to:

- the removal of $CO_2$, $H_2O$ vapour and $H_2S$ from biogas stream;
- the manufacture of zeolite monoliths using selected zeolite adsorbent powders (such as 13X zeolite, LiLSX zeolite, 5A zeolite and clinoptilolite);
- the synthesis of a model MOF powder for the manufacture of novel MOF monoliths (for example, MIL-101(Cr) which has high adsorption capacity for $CO_2$ and $H_2S$ as well as good resistance to $H_2O$ vapour);

- the manufacture of alkali metal carbonates (such as $K_2CO_3$ and $Na_2CO_3$) based on 13X zeolite foam-monoliths with enhanced adsorption capacity;
- the physical characterisation of the prepared adsorbent monoliths and foam-monoliths to determine their thermal stability, crystal and pore structures, surface morphology and mechanical compressive strength;
- the optimisation of adsorbent monoliths and foam-monoliths with $CO_2$ adsorption and comparison with a packed bed of adsorbent beads;
- the study of dynamic adsorption performances of the prepared adsorbent monoliths and foam-monoliths for biogas upgrading using single (such as $CO_2$, $CH_4$ and $H_2S$) and mixed (such as $CO_2/CH_4$ and $CO_2/CH_4/H_2O$ vapour) gases; and
- the study of kinetic adsorption and gas flow dynamic performances of the prepared adsorbent monoliths and packed beds of adsorbent beads for biogas upgrading.

# Chapter 2 Background of the Research

This chapter covers the background information of the research. First, an overview of biogas (which is the chosen model gas for this research) and their utilisation will be provided. The technical, energy, environmental and economic performance of various current biogas upgrading technologies (such as pressure swing adsorption, water scrubbing, chemical absorption with amine solutions and membrane separation) will be reviewed and compared to choose a suitable upgrading technology. This research will focus on adsorption since it is a promising technology for biogas upgrading.

Then, the fundamental principles of adsorption that are applicable to this research will be covered. This includes the dynamics and kinetics of adsorption, the dynamics of gas flow through adsorbent monoliths or packed beds of adsorbent beads (axial dispersion and pressure drop), the equilibria of adsorption and common regeneration methods (such as temperature and pressure swing regenerations) for desorbing and regenerating saturated adsorbents. Equations used for evaluating the dynamic, kinetic and gas flow performance of the adsorption process are also provided.

Adsorbents that are suitable for removing gas contaminants such as $CO_2$, $H_2O$ vapour and $H_2S$ from the raw biogas stream will be reviewed since they have an influence on the adsorption performance of the biogas upgrading system. This includes zeolites, metal-organic frameworks and alkali metal carbonates. Binders such as clays will also be considered and discussed in this chapter as they play an important role in providing the necessary mechanical stability to the adsorbent structures.

Lastly, various types of adsorbent structures will be reviewed to assess their suitability for use in biogas upgrading process. This includes current state-of-the-art adsorbents (such as beads, pellets and granules) and novel structures (such as monoliths and foams). Mass transfer and pressure drop associated with these structures will be discussed as they are related to the rate of adsorption and energy efficiency of the system.

## 2.1 Biogas: Overview, Utilisation and Current Upgrading Technologies

This section covers the overview of biogas, their utilisation and current upgrading technologies. A brief overview of biogas and their utilisation in different applications are provided in Section 2.1.1. Then, the technical performance of significant biogas upgrading technologies such as pressure swing adsorption (PSA), water scrubbing, chemical absorption and membrane separation are discussed in Section 2.1.2. Their energy, environmental and economic performance are also compared.

### 2.1.1 Overview of biogas and their utilisation

Biogas is produced by digesting organic feedstock (such as sewage and animal/crop wastes) under anaerobic conditions using bacteria and enzymes (SEAI, 2012; Tobi, 2009). A raw biogas generally contains $CH_4$ and contaminants such as $CO_2$, $H_2O$ vapour, $H_2S$ and other trace gases (Wellinger and Lindberg, 2001). The typical composition of biogas and some physical properties of the gas components are given in Table 2.1.

**Table 2.1** Typical composition of biogas and physical properties of the gas components. [Data obtained from SEAI (2012) and Sircar and Myers (2003).]

| Gas component | Chemical formula | Concentration (% vol.) | Molecular mass (g $mol^{-1}$) | Kinetic diameter (nm) |
|---|---|---|---|---|
| **Methane** | $CH_4$ | 50 – 75 | 16.04 | 0.38 |
| **Carbon dioxide** | $CO_2$ | 25 – 45 | 44.01 | 0.33 – 0.39 |
| **Water vapour** | $H_2O$ | 2 – 7 | 18.02 | 0.26 |
| **Oxygen** | $O_2$ | < 2 | 32.00 | 0.35 |
| **Nitrogen** | $N_2$ | < 2 | 28.01 | 0.36 – 0.38 |
| **Ammonia** | $NH_3$ | < 1 | 17.03 | 0.29 |
| **Hydrogen** | $H_2$ | < 1 | 2.02 | 0.29 |
| **Hydrogen sulfide** | $H_2S$ | 0.002 – 2 | 34.08 | 0.36 |

As mentioned before, biogas is a clean renewable fuel that can be used in a range of applications such as to generate heat, electricity and transport fuels. Their production and demand are increasing significantly despite falling global prices for fossil fuels and continuing fossil fuels subsides (Sawin *et al.*, 2016). The reasons are because of their benefits in mitigating climate change (i.e., by reducing $CO_2$ and $CH_4$ emissions to the atmosphere) and enhancing energy security (for example, reducing the dependency on

liquid transport fuels) (Petersson and Wellinger, 2009). Navigant Research (2016) recently reported that the raw biogas production capacity is predicted to increase 2 141 billion cubic feet per year by 2024 with global cumulative revenue from investment in biogas production capacity expect to reach $25.8 billion.

Biogas can be utilised for a variety of energy applications depending on their gas quality (Wellinger and Lindberg, 2001). Generally, a low to moderate quality biogas (i.e., $CH_4$ content between 50% vol. and 95% vol.) is used in boilers for generating heat, kitchen stoves for cooking and stationary combined heat and power (CHP) engines for generating heat and electricity. On the hand, a high quality biogas (i.e., $CH_4$ content above 96% vol.) is normally used as vehicle fuel for transportation and injected into natural gas grid (Persson *et al.*, 2006; Wellinger and Lindberg, 2001).

Gas standards for different applications can vary from one application to another, thus resulting in different requirements for the removal of $H_2S$, $CO_2$ and $H_2O$ vapour from biogas (Wellinger and Lindberg, 2001), as shown in Table 2.2. Due to the toxic and corrosive effects of $H_2S$, the concentration of $H_2S$ should be reduced to lower than 0.1% vol. for boilers and CHP engines (Wellinger and Lindberg, 2001) and lower than 0.001% vol. for kitchen stoves (Sun *et al.*, 2015). For boilers and kitchen stoves, it is also recommended to condense the $H_2O$ vapour in the raw biogas to prevent corrosion in the gas nozzles (Wellinger and Lindberg, 2001; Petersson and Wellinger, 2009). According to Table 2.2, biogas can be used in boilers, kitchen stoves and CHP engines without removing $CO_2$.

**Table 2.2** Requirements to remove $H_2S$, $H_2O$ vapour and $CO_2$ from biogas for utilisation in different applications. [Data adapted from Wellinger and Lindberg (2001).]

| Application | $H_2S$ | $H_2O$ vapour | $CO_2$ |
|---|---|---|---|
| **Gas heater (boiler)** | < 0.1% vol. | No | No |
| **Kitchen stove** | Yes | No | No |
| **Stationary (CHP) engine** | < 0.1% vol. | No condensation | No |
| **Vehicle fuel** | Yes | Yes | Recommended |
| **Natural gas grid** | Yes | Yes | Yes |

For the utilisation of biogas as vehicle fuel and injection into the natural gas grid, the gas quality requirements are strict so the raw biogas has to be upgraded by removing $CO_2$, $H_2S$, $H_2O$ vapour and other trace gases to enrich its $CH_4$ concentration (Wellinger

and Lindberg, 2001). The gas quality requirements for utilising biogas as vehicle fuel and for natural gas grid injection also differ with the country at which the upgraded biogas is utilised (Wellinger and Lindberg, 2001; Petersson and Wellinger, 2009). Based on the four countries listed in Table 2.3, a high gas quality with an average $CH_4$ content above 96% vol. is generally required for use as vehicle fuel and natural gas grid injection.

**Table 2.3** National gas quality standards for utilisation of upgraded biogas as vehicle fuel and for grid injection in different countries. [Data obtained from Persson *et al.* (2006) and Wellinger and Lindberg (2001).]

| | Sweden | Switzerland | Germany | France |
|---|---|---|---|---|
| **Gas type (H-gas means high quality gas)** | – | Unlimited injection | Unlimited injection in H-gas grid | H-gas |
| **$CH_4$ content, % vol.** | 95 – 99 | > 96 | > 97.5 | – |
| **$CO_2$ content, % vol.** | < 3 | < 6 | < 6 | < 2 |
| **$O_2$ content, % vol.** | < 1 | < 0.5 | < 3 | < 0.01 |
| **$CO_2$+$O_2$+$N_2$ content, % vol.** | < 5 | – | – | – |
| **$H_2S$ content, % vol.** | < 23 | < 5 | – | – |
| **$H_2O$ vapour content, % vol.** | < 32 | – | – | < 100 |

### 2.1.2 Biogas upgrading technologies

It is important to upgrade the biogas to meet the requirements of gas quality for vehicle fuel/grid injection, to improve the calorific value of the gas, to make sure that the gas is consistent in its components, to reduce impacts on the environment and to prevent the corrosion effects on equipment and piping systems. In a biogas upgrading process, contaminants such as $CO_2$, $H_2O$ vapour, $H_2S$ and other trace gases are removed from the biogas stream (Deublein and Steinhauser, 2008; Ryckebosch *et al.*, 2011; Wellinger and Lindberg, 2001). This research will focus on the removal of the three main contaminants in biogas, which are: $CO_2$, $H_2O$ vapour and $H_2S$. The reasons are because their presence in the biogas will greatly degrade the gas quality and affect the equipment (Wellinger and Lindberg, 2001).

Some commercial technologies that are commonly used for removing $CO_2$, $H_2O$ vapour, $H_2S$ from biogas stream are summarized in Table 2.4. It seems that the most common technologies used to remove these contaminants from the raw biogas are adsorption using porous adsorbent solids (such as zeolites), absorption using absorbent liquids (such as water and amine solutions) and membrane separation using a permeable membrane contactor. According to IEA (2015), there are more than 400 biogas upgrading plants in Europe. About 17% of the plants employed pressure swing adsorption. The most

dominant technology employed are water scrubbing and chemical (amine) absorption, with about 34% and 21% share. Membrane separation technology also has about 21% share. Other technologies such as physical absorption and cryogenic have about 7% share.

**Table 2.4** Common commercial technologies used for removing $CO_2$, $H_2O$ vapour and $H_2S$ from biogas. [Data obtained from Deublein and Steinhauser (2008), Ryckebosch *et al.* (2011) and Wellinger and Lindberg (2001).]

| Components | Technologies |
|---|---|
| **$CO_2$** | ❖ Absorption by scrubbing with water, polyethylene glycol or amine solutions (for e.g. monoethanolamine, MEA)<br>❖ Adsorption using molecular sieves, zeolites or alumina silicates<br>❖ Membrane separation |
| **$H_2O$ vapour** | ❖ Cooling<br>❖ Compression<br>❖ Absorption in glycol solutions or using hygroscopic salts<br>❖ Adsorption using silica, activated carbon or molecular sieves |
| **$H_2S$** | ❖ Biological desulphurisation using air/oxygen dosing in digester biogas<br>❖ Biological filters with combined absorption (water scrubbing) & biological desulphurisation<br>❖ Addition of iron chloride in digester slurry<br>❖ Absorption by scrubbing with water, Selexol (solvent containing dimethylether of polyethylene glycol-DMPEG) or NaOH<br>❖ Adsorption using iron oxide wood chips or pellets and activated carbon |

#### 2.1.2.1 Pressure swing adsorption

Pressure swing adsorption (PSA) processes are based on the ability of adsorbent materials to selectively retain one or more compounds from a gas mixture at different pressure according to molecular size (Sun *et al.*, 2015). In the case of $CH_4$ (molecular size of 0.38 nm)/$CO_2$ (molecular size of 0.34 nm) separation, the PSA technology can be used to separate $CH_4$ from $CO_2$ by capturing $CO_2$ molecules using an adsorbent (for example, with a pore size of 0.37 nm) since $CO_2$ molecules are smaller than $CH_4$ molecules (Patterson *et al.*, 2011). This technology is flexible as various adsorbents can be used in the overall PSA process (Patterson *et al.*, 2011). Usually, adsorbents such as zeolites (Siriwardane *et al.*, 2003; Alonso-Vicario *et al.*, 2010; Mulgundmath *et al.*, 2012; Mofarahi and Gholipour, 2014) and activated carbons (Sircar *et al.*, 1996; Siriwardane *et al.*, 2001; Goetz *et al.*, 2006; Álvarez-Gutiérrez *et al.*, 2016) are used.

The adsorption of gas components onto the adsorbent material is carried out under elevated pressure (usually between 4 bar to 10 bar) and the adsorbed gas components can be desorbed from the material by reducing the pressure (Grande, 2011; Persson *et al.*, 2006; SEAI, 2012) or by heating the adsorbent (Biernat and Samson-Bręk, 2011). This thermal (or temperature swing) regeneration method can be combined with

depressurisation if the adsorbent material is likely to decompose after frequent heating (Biernat and Samson-Bręk, 2011). Alonso-Vicario *et al.* (2010) carried out comparative studies of two synthetic zeolites (13X and 5A) and a natural zeolite (clinoptilolite) as adsorbents based on PSA technique with thermal desorption for biogas upgrading. They found that the maximum removal of $CO_2$ was achieved using natural zeolite (clinoptilolite) with $CO_2$ adsorption capacity of 3.95 mmol $g^{-1}$. Their studies also showed that clinoptilolite is completely regenerable and stable through several adsorption-desorption cycles.

Industrially, PSA for biogas upgrading consists of several columns (usually four) packed with adsorbents (Patterson *et al.*, 2011; SEAI, 2012). These columns are linked together in parallel to create a continuous operation and to reduce the energy demand for gas compression (Persson *et al.*, 2006). Depending on the ease of regenerability of the adsorbent material for the adsorption of $H_2S$, a pretreatment to remove/reduce the concentration of $H_2S$ in the raw biogas stream may be required (Patterson *et al.*, 2011). The reason is because the adsorbent material used for biogas upgrading adsorbs $H_2S$ irreversibly and this makes the material hard to be regenerated (Grande, 2011; Sun *et al.*, 2015). $H_2O$ vapour in the raw biogas stream can also be removed together with $CO_2$ depending on the choice of the adsorbent (Grande, 2011).

The typical $CH_4$ concentration after upgrading is about 96% to 98% and the $CH_4$ losses is about 2% to 4% (Allegue and Hinge, 2012). This PSA technology has a power demand of about 0.25 kWh $N^{-1}$ $m^{-3}$ of raw biogas and it has no heat demand if the process only involves varying pressure (Allegue and Hinge, 2012). Data obtained from IEA (2015) indicates that PSA is used in biogas plants for a wide range of biogas flow rate (between 20 N $m^3$ $h^{-1}$ of raw biogas and 4 400 N $m^3$ $h^{-1}$ of raw biogas).

#### 2.1.2.2 Water scrubbing

Water scrubbing is a process based on physical absorption, which used water as a solvent for removing $CO_2$ and also $H_2S$ from the raw biogas (Sun *et al.*, 2015; Wellinger and Lindberg, 2001). The principle of this method is that $CO_2$ and $H_2S$ are more soluble in water than $CH_4$ (Persson *et al.*, 2006; Wellinger and Lindberg, 2001). Water scrubbing is usually carried out by feeding pressurised raw biogas (of about 9 bar to 12 bar) to the bottom of the packed scrubber column and flows upward whilst water is fed at the top of the column and flows downward (Allegue and Hinge, 2012; Persson *et al.*, 2006).

The scrubber column is usually packed with a high surface area media (such as plastic pall rings) to give a high contact area between gas and water (Patterson *et al.*, 2011; Petersson and Wellinger, 2009). The biogas leaving the top of the column is enriched in $CH_4$ and saturated with $H_2O$ (Persson *et al.*, 2006). The $H_2O$ vapour can be removed by drying the upgraded biogas stream and compressed (to around 200 bar) for storage (Patterson *et al.*, 2011; Persson *et al.*, 2006).

The water leaving the bottom of the column is saturated with $CO_2$ and $H_2S$. This scrubbed water is either regenerated in a desorption column by reducing the pressure and reused for absorption or used once in a single pass system (Patterson *et al.*, 2011). The desorbed $CO_2$ is released to the atmosphere (Persson *et al.*, 2006). Since $H_2S$ is highly soluble in water, not all $H_2S$ is desorbed and some of it is oxidised to sulphur in the desorption column (Håkansson, 2006). The chemical reaction for the oxidation of $H_2S$ to sulphur and water is given by the equation below (Ryckebosch *et al.*, 2011):

$$2H_2S + O_2 \rightarrow 2S + 2H_2O \qquad (2.1)$$

The sulphur accumulates in the water and it can cause fouling and plugging of pipework after operation for some time (Håkansson, 2006; Persson *et al.*, 2006; Wellinger and Lindberg, 2001). In addition, the release of desorbed $H_2S$ to the atmosphere causes an emission problem (Persson *et al.*, 2006). So, it is recommended to remove $H_2S$ before the raw biogas enters the scrubbing column (Håkansson, 2006; Persson *et al.*, 2006). Any $CH_4$ dissolved in the water is captured by depressurising the water (usually 2 bar to 4 bar) in a flash tank and returned to the bottom of the column to minimize $CH_4$ losses (Håkansson, 2006).

Depending on the raw biogas composition and column size, the typical $CH_4$ concentration after upgrading by water scrubbing is about 98% and the $CH_4$ losses is about 1% to 2% (Allegue and Hinge, 2012). Similar to PSA technology, the power demand of water scrubbing process is about 0.25 kWh $N^{-1}$ $m^{-3}$ raw biogas and it has no heat demand since the process only involves change in pressure (Allegue and Hinge, 2012). Data gained from IEA (2015) indicates that biogas plants employing water scrubbing technology have capacity ranging from 10 N $m^3$ $h^{-1}$ of raw biogas to 20 000 N $m^3$ $h^{-1}$ of raw biogas.

### 2.1.2.3 Chemical absorption

Chemical absorption technology uses amine solutions as the chemical solvent to dissolve and react selectively with $CO_2$ is a combination of physical and chemical absorption (Allegue and Hinge, 2012; Petersson and Wellinger, 2009). Usually, organic amines such as monoethanolamine (MEA), diethanolamine (DEA) and diglycolamine (DGA) are used as they are highly selective for absorbing $CO_2$ and can dissolve significantly more $CO_2$ per unit volume when compared to water scrubbing, resulting to smaller volumes and plant sizes (Patterson *et al.*, 2011).

The technological arrangement of this technology is the same as water scrubbing with regeneration, in which the raw biogas is fed to the bottom of the column and is in counter-flow to the amine solution (Persson *et al.*, 2006). Reactions taking place during chemical absorption and desorption are given below:

$CO_2$ absorption: $$\mathrm{RNH_2 + H_2O + CO_2 \rightarrow RNH_3^+ + HCO_3^-} \quad (2.2)$$

$CO_2$ desorption: $$\mathrm{HCO_3^- + RNH_3^+ \rightarrow RNH_2 + H_2O + CO_2} \quad (2.3)$$

where $\mathrm{R}$ is the remaining organic component and is not specific in above equations (Ryckebosch *et al.*, 2011).

The chemical absorption process can be operated at lower pressure (usually a few mbars) compared to water scrubbing and this leads to reduce compression energy requirements (Allegue and Hinge, 2012; Patterson *et al.*, 2011). However, the regeneration of amine solutions before recirculation to the absorption column requires a large amount of high-temperature heat as a result of strong chemical interaction between $CO_2$ and amine solution (Petersson and Wellinger, 2009; Sun *et al.*, 2015). A heat demand of about 0.5 kWh $N^{-1}$ $m^{-3}$ of upgraded biogas is needed at 120 °C to 160 °C in the desorption column to regenerate amines (Allegue and Hinge, 2012). Because of this, the technology has a drawback of having high energy consumption for regeneration (Allegue and Hinge, 2012; Persson *et al.*, 2006).

The chemical solvent may be contaminated if $H_2O$ is present in the raw biogas stream, which reduces its efficiency and therefore needs to be replaced (Allegue and Hinge, 2012). Pretreatment of $H_2S$ is recommended before the raw biogas enters the bottom of the column otherwise higher temperature is required for regenerating the amine solutions (Biernat and Samson-Bręk, 2011; Petersson and Wellinger, 2009). The $CH_4$ concentration in the upgraded biogas stream can be as high as 99.5% if there is no $N_2$

and/or $O_2$ in the effluent biogas stream (Allegue and Hinge, 2012). Since the amine solutions are highly selective for absorbing $CO_2$, the process has reduced $CH_4$ losses to less than 0.1% (Allegue and Hinge, 2012; Petersson and Wellinger, 2009). Based on the data obtained from IEA (2015), the capacity range for biogas upgrading plants with chemical absorption system is between 70 N $m^3$ $h^{-1}$ of raw biogas and 12 000 N $m^3$ $h^{-1}$ of raw biogas.

#### 2.1.2.4 Membrane separation

Membrane separation technology is based on the selective permeability nature of membranes that allows one or more components from a gas mixture to pass through a semi-permeable membrane to the permeate side and retained other components (Ryckebosch *et al.*, 2011). The driving force of this process is the difference in partial pressures (Allegue and Hinge, 2012). For biogas upgrading, $CO_2$ and $H_2S$ pass through the membrane while $CH_4$ is retained (Sun *et al.*, 2015). Commercially, there are two types of membrane separation available: (1) high pressure gas separation system with gas phase on both sides of the membrane and (2) low pressure gas-liquid absorption separation with a liquid absorbing the diffused molecules (Persson *et al.*, 2006).

High pressure membrane separation systems can either be operated at pressure above 20 bar or between 8 bar and 10 bar (Persson *et al.*, 2006). Membranes made of acetate-cellulose can separate $CO_2$, $H_2O$ vapour and $H_2S$ from $CH_4$ (Ryckebosch *et al.*, 2011; Sun *et al.*, 2015). Normally, biogas is upgraded in a multi-stage process to achieve a $CH_4$ concentration above 96%. Waste gases from the first two stages are recycled to recover the $CH_4$ while the waste gas from the final stage is either flared or used for heat production as it contains 10% vol. $CH_4$ to 20% vol. $CH_4$ (Wellinger and Lindberg, 2001).

Low pressure membrane separation systems work at approximately atmospheric pressure, allowing low cost construction. A microporous hydrophobic membrane is used to separate the raw biogas stream from a liquid phase absorbent. $H_2S$ can be removed using sodium hydroxide while $CO_2$ can be removed using an amine solution, which can be regenerated by heating. This process can upgrade raw biogas (containing 55% vol. $CH_4$ and 43% vol. $CO_2$) to above 96% vol. $CH_4$ (Wellinger and Lindberg, 2001).

To increase the lifetime of the membrane, $H_2S$ is usually removed before the raw biogas passes through the membrane (Allegue and Hinge, 2012). The electrical energy consumption for biogas upgrading with membrane separation technology is about 0.3

kWh $N^{-1}$ $m^{-3}$ of upgraded biogas (Makaruk *et al.*, 2010). Data obtained from IEA (2015) indicates that membrane separation technique is used in biogas upgrading plants of low and medium flow rates, ranging between 1.5 N $m^3$ $h^{-1}$ of raw biogas and 2 800 N $m^3$ $h^{-1}$ of raw biogas.

### 2.1.2.5 Comparison of biogas upgrading technologies

In the selection of technology, it is important to consider the energy (electricity and/or heat) requirements to upgrade the raw biogas, the level of $CH_4$ losses and the achievable purity of $CH_4$ in the upgraded biogas stream. More net energy is available for end use if the energy requirement for upgrading is low. Additionally, $CH_4$ lost in the process means lost revenue (as the $CH_4$ purity in the upgraded biogas stream is reduced) and cause emission problems (as $CH_4$ is a greenhouse gas, which is 21 times more harmful than $CO_2$) (Patterson *et al.*, 2011). The energy and environmental performance of some commercial technologies for biogas upgrading such as PSA, water scrubbing, chemical absorption with amine solutions and membrane separation are summarised in Table 2.5.

**Table 2.5** Energy consumption (electricity and heat), level of $CH_4$ losses and purity of different biogas upgrading technologies.

| Parameters | PSA | Water scrubbing | Chemical absorption (amines) | Membrane separation |
|---|---|---|---|---|
| **Electrical consumption (kWh $N^{-1}$ $m^{-3}$ of upgraded biogas)** | 0.24[a]<br>0.27[b] | 0.2[a]<br>0.3[b] | 0.12 (electricity);<br>0.44 (thermal)[a]<br>0.67[b] | 0.19[a]<br>0.3[c] |
| **Heat consumption (kWh $N^{-1}$ $m^{-3}$) and heat demand (°C)** | None[d] | None[d] | 0.3[d]<br>120 – 160[d] | None[d] |
| **$CH_4$ losses (% vol.)** | 2 – 4[d]<br>2[e] | 1 – 2[d]<br>< 2[e] | < 0.1[d,e,f] | ~ 2[d]<br>> 10[e] |
| **$CH_4$ purity (% vol.)** | 83 – 99[b]<br>96 – 98[d] | 98.5[b]<br>98[d] | 99[b]<br>99.5[d] | 90[b]<br>> 96[g] |

[a] Beil (2009); [b] Electrigaz Technologies Inc. (2008); [c] Makaruk *et al.* (2010); [d] Allegue and Hinge (2012); [e] Dirkse (2009); [f] Petersson and Wellinger (2009); [g] Wellinger and Lindberg (2001)

Energy consumption (electricity and heat) data for both PSA and water scrubbing technologies appear to be relatively consistent. Electrical energy consumption data for PSA has range from 0.24 kWh $N^{-1}$ $m^{-3}$ of upgraded biogas to 0.27 kWh $N^{-1}$ $m^{-3}$ of upgraded biogas while those for water scrubbing has range from 0.2 kWh $N^{-1}$ $m^{-3}$ of upgraded biogas to 0.3 kWh $N^{-1}$ $m^{-3}$ of upgraded biogas. For chemical absorption using amines, a wide variation in energy requirement is seen and this is caused by excluding or including thermal energy consumption for regeneration of the amine solutions. The energy (electrical) consumption data for membrane separation shows high variability and this can

be due to the differences in the types of membrane and operating pressures (Patterson *et al.*, 2011). Data in Table 2.5 indicates that chemical absorption using amines is the most energy demanding technology compared to PSA, water scrubbing and membrane separation.

In the case of environmental performance, the lowest $CH_4$ losses is demonstrated by chemical absorption with amine solutions and the highest $CH_4$ losses is demonstrated by membrane separation, as shown in Table 2.5. The high $CH_4$ losses indicated for membrane separation is most likely due to technological arrangement (i.e., number of stages in the overall process). A further key parameter to consider when comparing the upgrading technologies is the $CH_4$ purity in the upgraded biogas stream (Bauer *et al.*, 2013). To meet the gas quality requirements for utilising biogas as vehicle fuel, the concentration of $CH_4$ in the upgraded biogas stream must be above 96% (Persson *et al.*, 2006; Wellinger and Lindberg, 2001). Data in Table 2.5 indicates that both chemical absorption with amine solutions and PSA can yield high $CH_4$ purity (> 99%) compared to water scrubbing and membrane separation.

The cost of upgrading raw biogas also needs to be taken into consideration when choosing a technology for biogas upgrading. Usually, the cost of upgrading raw biogas is inversely related to the plant capacity (see Figure 2.1). A large plant has lower upgrading cost compared to a small plant (Sun *et al.*, 2015). The upgrading cost of PSA, water scrubbing and chemical absorption with amine solutions from various manufactures shown in Figure 2.1 indicate a large drop in upgrading cost when the plant size was scaled up from 250 N $m^3$ $h^{-1}$ of raw biogas to 2 000 N $m^3$ $h^{-1}$ of raw biogas. In the case of membrane separation, the upgrading cost is about 0.79 € cents per kWh to 1.19 € cents per kWh for plant capacity of 1 000 N $m^3$ $h^{-1}$ of raw biogas (Allegue and Hinge, 2012; Sun *et al.*, 2015).

The economic data of different biogas upgrading technologies with plant capacity of 1 000 N $m^3$ $h^{-1}$ of raw biogas indicates that the lowest upgrading cost is demonstrated by membrane separation, followed by water scrubbing (from Malmberg) and PSA (from Carbotech). With the same plant capacity of 1 000 N $m^3$ $h^{-1}$ of raw biogas, the highest upgrading cost is demonstrated by water scrubbing (from Flotech) and chemical absorption with amine solutions (from MT-Energie), see Figure 2.1. The upgrading cost is expected to be lower as more plants are being built. Nowadays, plants with capacity lower

than 250 N $m^3$ $h^{-1}$ of raw biogas and those with capacity higher than 2 000 N $m^3$ $h^{-1}$ of raw biogas are being built (Petersson and Wellinger, 2009).

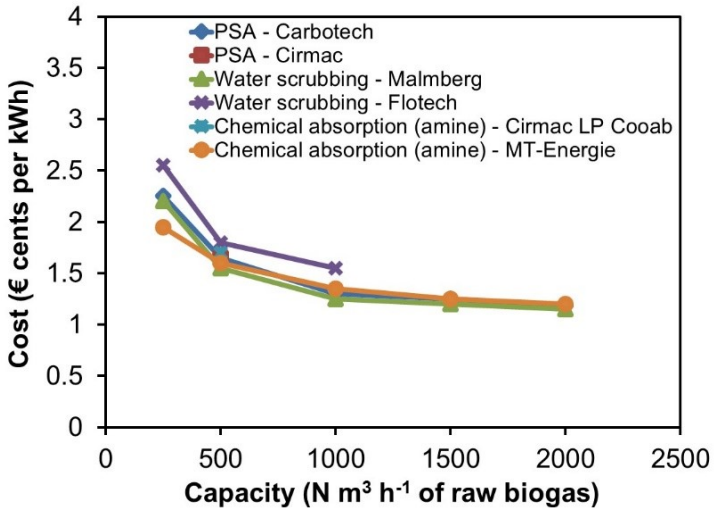


**Figure 2.1** Cost of some commercial biogas upgrading technologies. [Redrawn from Petersson and Wellinger (2009).]

Biogas upgrading plants generally made their choices based on the presence of suppliers for the technology in the particular country (Allegue and Hinge, 2012). The upgrading plants list gathered by IEA (2015) indicates that United Kingdom mostly used membrane separation. In Germany, they use PSA, water scrubbing and chemical absorption. In Sweden, they prefer water scrubbing.

For this research, the advantages and disadvantages of various current upgrading technologies such as PSA, water scrubbing, chemical absorption with amine solutions and membrane separation are compared to determine a suitable technology that can be operated in laboratory scale at low cost. Table 2.6 summarised the advantages and disadvantages of the selected upgrading technologies. After comparing their technical, energy, environmental and economic performance, PSA seems to be the most suitable technology for biogas upgrading compared to water scrubbing, chemical absorption with amine solutions and membrane separation. The reasons are PSA can yield high $CH_4$ content efficiency (95% to 98%) in a single stage, low energy requirement, relatively cheap and compact technology, ability to remove $H_2S$ and can be design for laboratory scale-size of low gas flow rate. Because of these, the research will concentrate on adsorption for biogas upgrading. The principles of adsorption for biogas upgrading are explained in the next section.

**Table 2.6** Advantages and disadvantages of various biogas upgrading technologies. [Data adapted from Allegue and Hinge (2012) and Ryckebosch *et al.* (2011).]

| Technologies | Advantages | Disadvantages |
|---|---|---|
| **PSA** | ❖ High $CH_4$ content efficiency (95% - 98%)<br>❖ Low energy use: high pressure, but regenerative<br>❖ No chemical or heat demand<br>❖ Relatively cheap technology<br>❖ Compact technique<br>❖ Also for small capacities plants<br>❖ $H_2S$ is removed<br>❖ Co-removal of $N_2$ and $O_2$ possible | ❖ Medium $CH_4$ content in upgraded biogas stream<br>❖ Medium $CH_4$ losses (2% - 4%)<br>❖ Components such as $H_2S$ and $H_2O$ have to be removed before the process<br>❖ Extensive process control needed<br>❖ $CH_4$ losses when malfunction of valves |
| **Water scrubbing** | ❖ High $CH_4$ content efficiency (> 97%)<br>❖ Cheap and simple technology<br>❖ Co-removal of $NH_3$ and $H_2S$ when $H_2S$ > 300/500 ppmv (tolerance for impurities)<br>❖ Easy in operation<br>❖ Capacity is adjustable by changing pressure or temperature<br>❖ Low $CH_4$ losses | ❖ Expensive investment and operation<br>❖ Requires a lot of water, even with the regeneration process<br>❖ $H_2S$ damages equipment (if $H_2S$ > 300/500 ppmv)<br>❖ Medium $CH_4$ content<br>❖ Clogging due to bacterial growth<br>❖ Possibility of foaming<br>❖ Biogas drying needed |
| **Chemical absorption (amines)** | ❖ High $CH_4$ content efficiency (> 99%)<br>❖ Low electricity demand<br>❖ Process without pressure<br>❖ More $CO_2$ dissolved per unit volume, compared to water<br>❖ Very low $CH_4$ losses (< 0.1%) | ❖ Relatively extensive investment<br>❖ High energy demand for regeneration<br>❖ Corrosion<br>❖ Decomposition and poisoning of amines by $O_2$ or other chemicals<br>❖ Precipitation of salts<br>❖ Possibility of foaming<br>❖ Pre-removal of $H_2S$ is normally required |
| **Membrane separation** | ❖ Simple construction, low weight and small footprint<br>❖ Simple operation, low maintenance<br>❖ No chemical or heat demand<br>❖ High reliability<br>❖ High pressure membrane separation system: removal efficiency (> 96% $CH_4$); $H_2O$ is removed<br>❖ Low pressure membrane separation system: removal efficiency (> 96% $CH_4$); cheap investment and operation | ❖ Low membrane selectivity: compromise between $CH_4$ purity and amount of upgraded biogas<br>❖ Multiple steps required to achieve high purity $CH_4$<br>❖ Middle $CH_4$ content<br>❖ Middle to high $CH_4$ losses depending on configuration<br>❖ Membrane durability unsure<br>❖ $H_2S$ removal step required<br>❖ Not suitable for biogas with many undefined contaminants (for example, biogas from waste water treatment plants and landfill gas)<br>❖ Membrane can be expensive |

## 2.2 Principles of Adsorption

This section covers the fundamental theories of adsorption that are used in this research for assessing the adsorption performances of the adsorbent bed. The adsorbent bed can be: (a) a packed bed of beads, pellets or granules, (b) a monolithic bed or (c) a foam-monolithic bed. Since the macrostructure of the foam-monoliths is the same as monoliths, their adsorption performance will be evaluated similar to the monolithic bed system. The adsorption performance of the adsorbent bed can be assessed by studying the dynamic, kinetic, gas flow and equilibrium behaviours of the adsorbate gas in the adsorbent bed.

The dynamic behaviour of adsorbate gas in the adsorbent bed is generally study from the breakthrough curves. A number of important adsorption properties of the adsorbent bed can be obtained by analysing their breakthrough curves. This includes their breakthrough and equilibrium times, breakthrough and equilibrium adsorption capacities, selectivity, effectiveness of adsorbent bed utilisation as well as mass transfer zone length and velocity (Yang, 1997). The descriptions of the breakthrough curves analysis and the equations used for determining the adsorption properties of the adsorbent bed are given in Section 2.2.1.

On the other hand, the kinetic behaviour of adsorbate gas in the adsorbent bed during adsorption can be studied from their mass and/or heat transfer characteristics depending on the condition of their system (Crittenden and Thomas, 1998). In this research, the entire system was assumed to be in an isotherm condition and this means the rate of adsorption was mainly governed by the mass transfer of adsorbate gas in the adsorbent bed. The mass transfer characteristics of adsorbate gas in the adsorbent bed to be studied in this work will focus on the mass transfer resistances and diffusion in the adsorbent bed. The theories of kinetic adsorption and equations used for estimating the mass transfer characteristics and diffusion of the adsorbate gas in the adsorbent bed are given in Section 2.2.2.

Moreover, the flow behaviour of adsorbate gas through the adsorbent bed is studied to evaluate the energy efficiency of the adsorbent beds. Usually, their energy efficiency is associated to the axial dispersion and pressure drop in the adsorbent bed (Crittenden and Thomas, 1998). The descriptions and equations used for calculating the axial dispersion and pressure drop can be found in Section 2.2.3.

The equilibrium behaviour of adsorbate gas in the adsorbent material is commonly studied from their adsorption isotherms. The equilibrium adsorption capacities of the adsorbate gas for the adsorbent material can also be obtained from their adsorption isotherms apart from their breakthrough curves (Reynolds *et al*, 2002). The basic concepts of equilibria adsorption are described in Section 2.2.4.

It has been mentioned previously (in Section 2.1.2.1) that adsorbents saturated with gas contaminants can be desorbed and regenerated either by reducing the pressure (Grande, 2011; Persson *et al.*, 2006; SEAI, 2012) and/or by heating them (Biernat and

Samson-Bręk, 2011). For this reason, the basic principles of both pressure and temperature swing regeneration methods are explained in Section 2.2.5.

### 2.2.1 Dynamics of adsorption

As mentioned earlier, the dynamic behaviour of the adsorbate gas in an adsorbent bed can be studied from their breakthrough curve (Yang, 1997). The shape of the breakthrough curve provides an indication on the efficiency of the mass transfer of adsorbate gas in the adsorbent bed. For efficient mass transfer, a sharp breakthrough curve is preferred (McCabe *et al.*, 2005). A more dispersive or less sharp breakthrough curve indicates mass transfer resistances and/or gas dispersions in the axial direction within the adsorbent bed (Yang, 1997).

To analyse the breakthrough curve quantitatively, a gas stream containing one or more adsorbate gases flowing through an adsorbent bed is considered. The adsorption of adsorbate gases starts at one end of the adsorbent bed and continues along the adsorbent bed until it reaches the breakthrough point at the breakthrough time $t_b$. The breakthrough time is the time at which the influent gas concentration $C_0$ is equal to the breakthrough concentration $C_b$ and the leading edge of the mass transfer front reaches the end of the adsorbent bed (Collins, 1967).

The breakthrough concentration is represented by the inflection point in the breakthrough curve at which the lowest achievable effluent gas concentration starts to increase by about 10% or more. For example, if the lowest achievable effluent gas concentration is zero, the breakthrough time is taken at $\frac{C}{C_0} \geq 0.1$. The effluent gas concentration $C$ will continue to increase gradually until it reaches the same concentration as the influent gas concentration, i.e. $\frac{C}{C_0} = 1$. The time at this point is called the equilibrium time $t_e$ and the adsorbent bed is said to be completely saturated with the adsorbate gas (Collins, 1967).

The initial adsorbent loading $q_0$ is zero and increases with the adsorption capacities of the adsorbate gases along the adsorbent bed until the adsorption reaches equilibrium at an equilibrium loading of $q_e$ (Collins, 1967). A typical breakthrough curve (represented by the effluent gas concentration trace) and the associated mass transfer profile in an adsorbent bed of length $L$ during adsorption are illustrated in Figure 2.2. The

breakthrough, stoichiometric and equilibrium times can be obtained directly from the breakthrough curve. The stoichiometric time $t_s$ is the time at which the area under the curve after the breakthrough time $t_b$ (represented by area ***A***) is equal to the area above the curve before the equilibrium time $t_e$ (represented by area ***B***) (Collins, 1967). Additionally, the breakthrough and equilibrium adsorption capacities, selectivity, effectiveness of adsorbent bed utilisation, mass transfer zone length and velocity for the adsorbent bed can also be determined from the breakthrough curve using equations given in Sections 2.2.1.1 to 2.2.1.4.

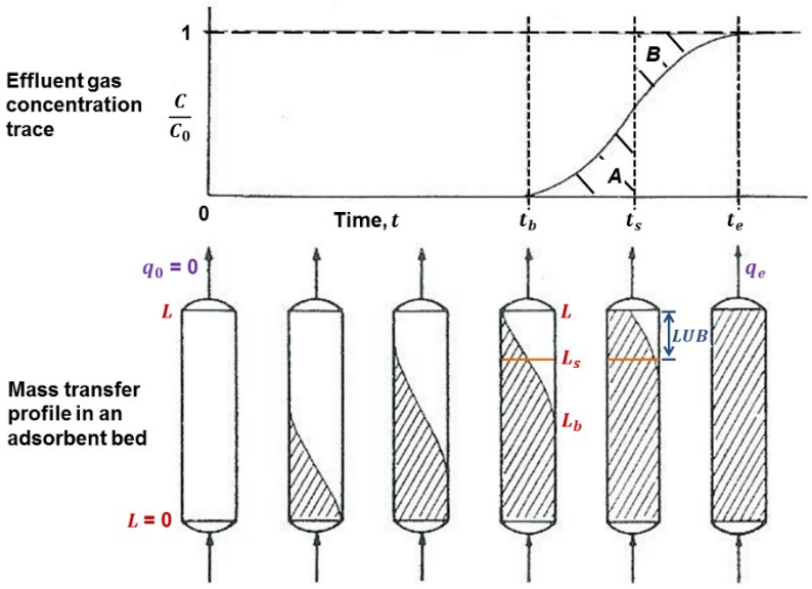


**Figure 2.2** Schematic diagram showing a typical breakthrough curve (represented by the effluent gas concentration trace) and the corresponding mass transfer profile in an adsorbent bed during adsorption. [Modified from Collins (1967).]

### 2.2.1.1 Breakthrough and equilibrium adsorption capacities

The breakthrough and equilibrium adsorption capacities of the adsorbate gas are defined as the amount of adsorbate gas adsorbed onto the adsorbent bed at breakthrough and equilibrium points, respectively. The breakthrough adsorption capacity, $\bar{q}_b$ (mmol g$^{-1}$), of adsorbate gas is represented by the area above the breakthrough curve from $t = 0$ to $t = t_b$ and they can be calculated using:

$$\bar{q}_b = \frac{\hat{Q}}{m_{ad}} \left( t_b - \sum_{t=0}^{t=t_b} \frac{C}{C_0} dt \right) \tag{2.4}$$

where $\hat{Q}$ is the molar flow rate of the influent gas (mmol s$^{-1}$) and $m_{ad}$ is the mass of the adsorbent (g) (Seader and Henley, 1998).

On the other hand, the equilibrium adsorption capacity, $\bar{q}_e$ (mmol g$^{-1}$), of adsorbate gas is represented by the area above the breakthrough curve from $t = 0$ to $t = t_e$ and they can be calculated using the equation developed by Seader and Henley (1998):

$$\bar{q}_e = \frac{\hat{Q}}{m_{ad}} \left( t_e - \sum_{t=0}^{t=t_e} \frac{C}{C_0} dt \right) \tag{2.5}$$

#### 2.2.1.2 Selectivity

The strength of an adsorbent solid to separate an adsorbate gas from another adsorbate gas in a mixed gas stream can be quantified by their selectivity. For efficient separation of $CO_2$ from the biogas stream, the adsorbent should have a high selectivity of $CO_2$ compared to $CH_4$ (Yang, 1997).

Adapting the separation factor reported by Yang (1997), the selectivity for adsorbing $CO_2$ over $CH_4$, $\alpha_{CO_2/CH_4}$, can be expressed as:

$$\alpha_{CO_2/CH_4} = \frac{\left(x_{CO_2}/y_{CO_2}\right)}{\left(x_{CH_4}/y_{CH_4}\right)} \tag{2.6}$$

where $x$ and $y$ are the mole fractions of the component in the adsorbed and gas phases, respectively. Note that $x$ can be substituted by $\bar{q}_e$ since both of them represent the amount of adsorbate gas been adsorbed onto the adsorbent solid (Yang, 1997).

#### 2.2.1.3 Effectiveness of adsorbent bed utilisation

Assuming that the adsorbent bed of length $L$ consists of equilibrium section and unused bed, the length of equilibrium section, $LES$ (m), can be expressed as (Collins, 1967; McCabe *et al.*, 2005):

$$LES = L - LUB \tag{2.7}$$

where $LUB$ is the length of unused bed (m).

As illustrated on the mass transfer profile in Figure 2.2, the length of unused bed is represented by the region from the stoichiometric front of bed length $L_s$ to the equilibrium front of bed length $L$. The length of unused bed is determined using the equation below:

$$LUB = L - L_s = L\left(\frac{t_s - t_b}{t_s}\right) \tag{2.8}$$

For efficient utilisation of the adsorbent bed, a short $LUB$ is preferred (Collins, 1967).

The effectiveness of adsorbent bed utilisation, $\varpi_{bed}$ (%), can then be estimated using the relation below:

$$\varpi_{bed} = \frac{LES}{L} \times 100\% \tag{2.9}$$

#### 2.2.1.4 Mass transfer zone length and velocity

The adsorbent bed region between the breakthrough time and the equilibrium time is known as the mass transfer zone (MTZ) (Collins, 1967). The length of MTZ, $L_{MTZ}$ (m), and the velocity of the adsorbate gas in the MTZ, $u_{MTZ}$ (m $s^{-1}$), can be determined using the equations developed by Kovach (1988):

$$L_{MTZ} = L\left(\frac{t_e - t_b}{t_e}\right) \tag{2.10}$$

$$u_{MTZ} = \frac{L_{MTZ}}{(t_e - t_b)} \tag{2.11}$$

The mass transfer zone length can also be expressed as the percentage length of MTZ in the adsorbent bed, $\bar{L}_{MTZ}$ (%), which is given by the equation below:

$$\bar{L}_{MTZ} = \frac{L_{MTZ}}{L} \times 100\% \tag{2.12}$$

For efficient mass transfer of adsorbate gas onto the adsorbent solid, it is favourable for the adsorbent bed to have a short $L_{MTZ}$ so that sharp mass transfer front and breakthrough curve can be produced. If the adsorbent bed has a short $L_{MTZ}$ with a relatively low $u_{MTZ}$, a single adsorption column can be used in the biogas upgrading system (Yang, 1997).

The biogas upgrading system can also have several adsorption columns in parallel if the adsorbent beds have a short $L_{MTZ}$ with a relatively high $u_{MTZ}$ or several adsorption columns in series if they have a long $L_{MTZ}$. So, if the adsorbent bed has a long $L_{MTZ}$ and a high $u_{MTZ}$, the biogas upgrading system is likely to have several adsorption columns in series and parallel (Crittenden and Thomas, 1998). The typical fixed-bed arrangement for biogas upgrading process employing PSA technology usually consists of four packed columns connected together in parallel to create a continuous operation and to reduce the energy demand for gas compression (Persson *et al.*, 2006).

### 2.2.2 Kinetics of adsorption

In addition to adsorption dynamics, the kinetic behaviour of the adsorbate gas in the adsorbent bed during adsorption will be studied in this research and it is related to the rate of adsorption in an equilibrium system. Considering that the heat transfer in the adsorbent bed is uniform and the entire system is in isothermal condition, then the rate of adsorption is mainly governed by the mass transfer in the adsorbent bed (Crittenden and Thomas, 1998).

The pores or channels of zeolitic adsorbents have precise dimensions and pore sizes are classified generally into three ranges: macropores (pore diameter larger than 50 nm), mesopores (pore diameter between 2 nm and 50 nm) and micropores (pore diameter smaller than 2 nm). As illustrated in Figure 2.3, the resistances that need to be overcome by the adsorbate gas during adsorption are (Crittenden and Thomas, 1998; Sircar and Myers, 2003):

a) external gas film resistance of the adsorbate gas to and from the external surface of the adsorbent particles,

b) diffusional resistances through the pore network to the surface of the adsorbent crystals and

c) intra-crystalline diffusional resistances through the micropores of the adsorbent crystals to the adsorption sites.

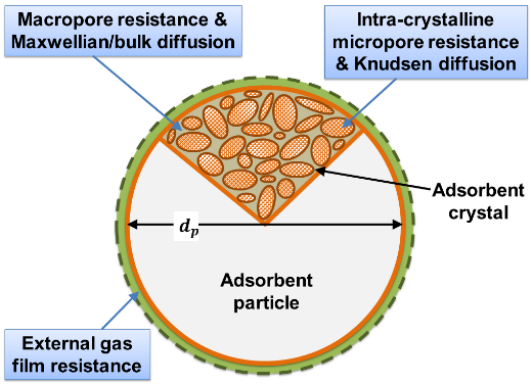


**Figure 2.3** Schematic diagram of an adsorbent particle with the associated resistances to mass transfer. [Redrawn from Crittenden and Thomas (1998).]

The next section will provide the general equations and experimental correlations reported in the literature that can be used for evaluating the mass transfer resistances in a packed bed of adsorbent beads, pellets or granules and in a monolithic adsorbent bed.

#### 2.2.2.1 Mass transfer resistances in porous adsorbent materials

According to Crittenden and Thomas (1998), the mass transfer rate of an adsorbate gas from the bulk gas phase to the external surface of the adsorbent, $R_m$ (mol m$^{-3}$ s$^{-1}$), through a thin layer of laminar gas film is driven by a concentration gradient, $\Delta C$ (mol m$^{-3}$), and the mass transfer rate can be expressed as:

$$R_m = kA_s\Delta C = kA_s(C_b - C_s) \tag{2.13}$$

where $k$ is the overall mass transfer coefficient (m s$^{-1}$), $A_s$ is the external specific surface area of the adsorbent bed (m$^2$ m$^{-3}$), $C_b$ is the adsorbate gas concentration in the bulk gas phase (mol m$^{-3}$) and $C_s$ is the adsorbate gas concentration at the external surface of the adsorbent (mol m$^{-3}$). Assuming that the value of $C_b$ is significantly larger than the value of $C_s$, the above mass transfer rate equation can be simplified into:

$$R_m = kA_sC_b \tag{2.14}$$

The external specific surface area for a packed bed of spherical adsorbent beads is estimated using:

$$A_s = \frac{6(1-\varepsilon)}{d_p} \tag{2.15}$$

where $\varepsilon$ is the dimensionless bed porosity (or voidage) and $d_p$ is the particle diameter (m) (Richardson *et al.*, 2002). For a monolithic bed, the external specific surface area is estimated using:

$$A_s = \frac{4\left(\sqrt{\varepsilon}-\varepsilon\right)}{t_w} \tag{2.16}$$

where $t_w$ is the wall thickness of the monolith (m) (Deluca and Campbell, 1977).

The bed porosity can either be measured physically using pore characterisation methods such as mercury intrusion porosimetry (MIP) or determined using the equations developed by Deluca and Campbell (1977). For a packed bed of adsorbent beads, pellets or granules, their bed porosity is calculated using:

$$\varepsilon = 1 - \frac{\rho_b}{\rho_p} \tag{2.17}$$

where $\rho_b$ is the bulk density of the packed bed (kg m$^{-3}$) and $\rho_p$ is the density of the adsorbent particle (kg m$^{-3}$). For a monolith, their bed porosity is calculated using:

$$\varepsilon = \frac{d_c^2}{(d_c + t_w)^2} \tag{2.18}$$

where $d_c$ is the channel diameter of the monolith (m).

The overall mass transfer coefficient takes into account on the contributions of the external and internal mass transfer resistances in an adsorbent bed, which is given by:

$$k = \frac{k_f k_p}{(k_f + k_p)} \tag{2.19}$$

where $k_f$ is the external gas film mass transfer coefficient (m $s^{-1}$) and $k_p$ is the pore mass transfer coefficient (m $s^{-1}$).

The external gas film mass transfer coefficient can be derived from the dimensionless Sherwood number, $Sh$, and it is represented by the experimental correlation below, which was developed by Wakao and Funazkri (1978) for a packed bed system with a gas flow of $Re$ < 10 000:

$$Sh = \frac{k_f d_p}{D_M} = 2.0 + 1.1\, Sc^{0.33}\, Re^{0.6} \tag{2.20}$$

where $D_M$ is the Maxwellian diffusion coefficient ($m^2$ $s^{-1}$) for the transport of adsorbate gas from the bulk gas phase to the adsorbent solid (equation of Maxwellian diffusion coefficient is given in Section 2.2.2.2), $Sc$ is the dimensionless Schmidt number and $Re$ is the dimensionless Reynolds number.

For a monolithic bed consisting of square channels with a laminar gas flow ($Re$ < 2 300), the expression of $Sh$ for estimating the external gas film mass transfer coefficient is given by the relation developed by Hawthorn (1974):

$$Sh = \frac{k_f d_c}{D_M} = 2.98\left[1 + 0.095\, Re\, Sc\, \left(\frac{d_c}{L}\right)\right]^{0.45} \tag{2.21}$$

Rezaei and Webley (2009) reported that the pore mass transfer coefficient for a packed bed system can be determined using:

$$k_p = \frac{10 D_e}{d_p} \tag{2.22}$$

where $D_e$ is the effective diffusivity ($m^2$ $s^{-1}$) (equation of effective diffusivity is given in Section 2.2.2.2) and that for a monolithic bed could be determined using:

$$k_p = \frac{2 D_e d_c}{d_c t_w + t_w^2} \tag{2.23}$$

### 2.2.2.2 Diffusion in porous adsorbent materials

As mentioned earlier, the mass transfer in an adsorbent bed is also limited by diffusional resistances through the pore network to the surface of the adsorbent crystals and through the micropores of the adsorbent crystals to the adsorption sites. Usually, the Maxwellian or bulk molecular diffusion occurs in the macropores (large pores of diameter greater than 50 nm) and the Knudsen diffusion occurs in the micropores (pores diameter smaller than the mean free path of the adsorbate gas molecules, i.e., small pores of diameter less than 2 nm) (Crittenden and Thomas, 1998; Sircar and Myers, 2003). The Maxwellian/bulk molecular diffusion and Knudsen diffusion in straight cylindrical pores are shown schematically in Figure 2.4.

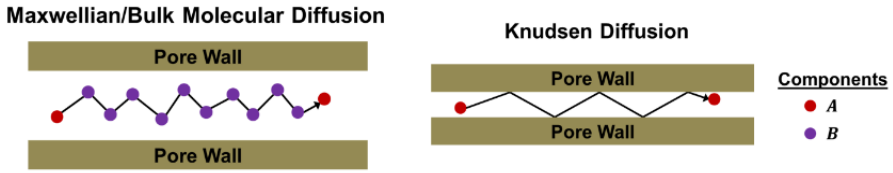


**Figure 2.4** Schematic diagram illustrating the Maxwellian/bulk molecular diffusion and Knudsen diffusion. [Redrawn from Welty *et al.* (2007).]

The Maxwellian diffusion coefficient (also known as molecular diffusivity) for binary gas mixture of components $A$ and $B$, can be represented by the relation below according to Chapman and Cowling (1951):

$$D_M = \frac{(1.8583\times10^{-9})T^{\frac{3}{2}}\left[\left(\frac{1}{M_{w,A}}\right)+\left(\frac{1}{M_{w,B}}\right)\right]^{\frac{1}{2}}}{P\vartheta^2{}_{AB}\Omega_{AB}} \tag{2.24}$$

where $T$ is the temperature of the flowing gas (K), $M_w$ is the molecular mass (g mol$^{-1}$), $P$ is the pressure of the flowing gas (bar), $\vartheta$ is a constant in the Lennard-Jonas potential function (also known as the average collision diameter) (nm), $\Omega$ is the dimensionless collision integral and the subscripts $A$ and $B$ denotes the individual components in the gas stream.

According to Bird *et al.* (2002), the average collision diameter and collision integral for binary gas mixture of components $A$ and $B$ can be estimated using the empirical equations below:

$$\vartheta_{AB} = \frac{\vartheta_A + \vartheta_B}{2} \tag{2.25}$$

$$\Omega_{AB} = \frac{1.06036}{\left(\frac{k_B T}{\xi_{AB}}\right)^{0.1561}} + \frac{0.193}{e^{\left(\frac{0.47635 k_B T}{\xi_{AB}}\right)}} + \frac{1.03587}{e^{\left(\frac{1.52996 k_B T}{\xi_{AB}}\right)}} + \frac{1.76474}{e^{\left(\frac{3.89411 k_B T}{\xi_{AB}}\right)}} \quad (2.26)$$

where $\vartheta_A$ and $\vartheta_B$ are the collision diameters for pure gases of components $A$ and $B$, respectively, $k_B$ is the Boltzmann constant (≈ 1.3807 × $10^{-23}$ J $K^{-1}$) and $\xi_{AB}$ is the characteristic energy of the binary gas mixture of components $A$ and $B$ that is equal to $\sqrt{\xi_A \xi_B}$.

The collision diameter and characteristic energy for pure gases can be calculated using the correlation below:

$$\vartheta = 2.44 \left(\frac{T_c}{P_c}\right)^{\frac{1}{3}} \quad (2.27)$$

$$\xi / k_B = 0.77 T_c \quad (2.28)$$

where $T_c$ is the critical temperature (K) and $P_c$ is the critical pressure of the gas (atm). Note that $\vartheta$ is in Ångstroms. Poling *et al.* (2008) reported that $CO_2$ has a critical temperature of 304.21 K and a critical pressure of 72.86 atm whereas $CH_4$ has a critical temperature of 190.56 K and a critical pressure of 45.39 atm.

On the other hand, the Knudsen diffusion coefficient (also known as Knudsen diffusivity), $D_K$ ($m^2$ $s^{-1}$), can be determined using:

$$D_K = \frac{\left(d_{pore} \times 10^4\right)}{3} \left(\frac{8 R_g T}{\pi M_w}\right)^{\frac{1}{2}} = 48.5 d_{pore} \left(\frac{T}{M_w}\right)^{\frac{1}{2}} \quad (2.29)$$

where $d_{pore}$ is the mean pore diameter of the adsorbent solid (m), $R_g$ is the Universal gas constant (= 8.314 × $10^{-5}$ $m^3$ bar $mol^{-1}$ $K^{-1}$) and $M_w$ is the molecular mass of the dominant adsorbate gas (g $mol^{-1}$) (Crittenden and Thomas, 1998). The mean pore diameter of an adsorbent solid can be measured using pore characterisation techniques such as MIP.

Pollard and Present (1948) stated that the sum of the resistances due to Maxwellian diffusion and Knudsen diffusion corresponds to the overall diffusional resistances. Then, the overall diffusion coefficient in an adsorbent bed, $D_o$ ($m^2$ $s^{-1}$), can be represented by the equation below with the assumption of adsorbate gas being transported in a straight cylindrical pore:

$$\frac{1}{D_o} = \frac{1}{D_M} + \frac{1}{D_K} \quad (2.30)$$

However, in porous materials, the diffusion of adsorbate gas molecules into the internal surface of a porous adsorbent material travels tortuously along the pore network and is hindered by inaccessible adsorbent particles. So, the overall diffusivity in porous materials can be represented by the effective diffusivity, $D_e$ ($m^2$ $s^{-1}$), that is defined by:

$$D_e = \frac{\varepsilon D_o}{\tau} \tag{2.31}$$

where $\tau$ is a dimensionless tortuosity factor of the adsorbent bed, which ranges from 1.5 to 10.0 for most porous materials according to Crittenden and Thomas (1998). The tortuosity factor can be estimated using the relation reported by Wakao and Smith (1962):

$$\tau = \frac{1}{\varepsilon} \tag{2.32}$$

By substituting equation (2.32) into equation (2.31), the effective diffusivity equation can be re-written into a simplified form:

$$D_e = \varepsilon^2 D_o \tag{2.33}$$

### 2.2.3 Dynamics of gas flow through adsorbent beds

The flow behaviour of the adsorbate gas through the adsorbent bed is also studied in this research and it is related to the axial dispersion and pressure drop in the adsorption column. A schematic diagram of the axial dispersion and pressure drop in a packed bed of adsorbent particles and a monolithic bed is illustrated in Figure 2.5. Both the axial dispersion and pressure drop in an adsorbent bed are influenced by the size of the adsorbent particles, velocity of the flowing gas and the dimensions of the adsorbent bed (Crittenden and Thomas, 1998).

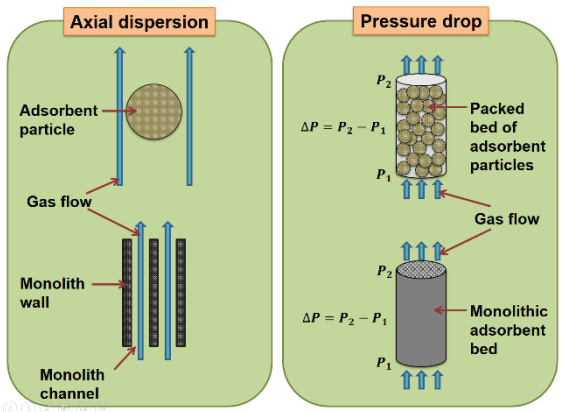


**Figure 2.5** Schematic diagram showing the axial dispersion and pressure drop in a packed bed of adsorbent particles and a monolithic adsorbent bed.

The next section will provide the empirical equations reported in the literature that are used in this research for determining the axial dispersion and pressure drop in a packed bed of adsorbent beads, pellets or granules and those in an adsorbent monolith.

#### 2.2.3.1 Axial dispersion

When a gas stream flows through an adsorbent bed, axial dispersion of the gas is likely to occur as a consequence of molecular diffusion and turbulent mixing that develops from the splitting and recombination of gas flows around the adsorbent particles, which will decrease the efficiency of the gas separation. So, it is necessary to reduce the axial dispersion in the adsorbent bed (Ruthven, 1984).

The extent of axial dispersion in an adsorbent bed is represented by the axial dispersion coefficient, $D_{ax}$ ($m^2\ s^{-1}$). For a packed bed of adsorbent particles, the axial dispersion coefficient can be estimated using the equation developed by Wakao and Funazkri (1978):

$$D_{ax} = \frac{D_M}{\varepsilon}(20 + 0.5\ Re\ Sc) \tag{2.34}$$

Generally, for a known bed porosity, the axial dispersion in a packed bed of adsorbent particles decreases with decreasing particle diameters.

For a monolithic adsorbent bed, Froment *et al.* (2010) reported that the axial dispersion coefficient can be calculated using:

$$D_{ax} = D_M + \frac{u_s^2 d_c^2}{192\varepsilon^2 D_M} \tag{2.35}$$

where $u_s$ is the superficial velocity of the flowing gas ($m\ s^{-1}$). For a fixed bed porosity, the axial dispersion in a monolithic bed decreases with decreasing superficial gas velocity and channel diameter.

According to Levenspiel (1999), the contribution of axial dispersion to the mass transfer of adsorbate gas in an adsorbent bed can be evaluated by the dimensionless Vessel Dispersion number, $VD$:

$$VD = \frac{\varepsilon D_{ax}}{u_s L} \tag{2.36}$$

The effect of axial dispersion on the mass transfer of adsorbate gas in the adsorbent bed can be neglected if the value of $VD$ is less than 0.01 but their effect on the mass transfer needs to be considered if the value of $VD$ is greater than 0.01 (Levenspiel, 1999).

#### 2.2.3.2 Pressure drop

In addition to axial dispersion, the pressure drop in the adsorbent bed will also be evaluated in this research as it is related to the energy efficiency of the system and the economics of the biogas upgrading process (Ruthven, 1984). So, it is important to make sure that the pressure drop in an adsorbent bed is not too low or too high. An adsorption system with a very low pressure drop will have a poor gas flow distribution in the adsorbent bed. On the other hand, an adsorption system with a high pressure drop will require a more pressurized gas stream to be fed into the adsorption column. This means the gas compressor will consume more energy during operation (Keller-II, 1987).

The pressure drop, $\Delta P$ (Pa), in a unit length of packed bed containing adsorbent particles can be estimated using the experimental correlation developed by Ergun (1952):

$$\frac{\Delta P}{L} = \frac{150(1-\varepsilon)^2 \mu u_s}{\varepsilon^3 d_p^2} + \frac{1.75(1-\varepsilon)\rho u_s^2}{\varepsilon^3 d_p} \tag{2.37}$$

where $\mu$ is the dynamic viscosity of the flowing gas (N s m$^{-2}$).

The above pressure drop equation indicates that adsorbent solids with small particle diameters will result in high pressure drop despite having better mass transfer between the adsorbate gas contaminants (such as $CO_2$, $H_2O$ vapour and $H_2S$) and the adsorbent solids. Although the pressure drop in the packed bed system can be reduced by using adsorbent solids of large particle diameters, the packed bed has a low mass transfer rate and this can be compromised by increasing the adsorbent bed diameters (Keller-II, 1987).

The pressure drop issue in packed beds can be overcome by using novel adsorbent structures such as monoliths. The pressure drop in a unit length of a monolithic bed of square channels can be estimated using the relation reported by Lee (1997):

$$\frac{\Delta P}{L} = \frac{28.4 \mu u_s}{\varepsilon d_c^2} \tag{2.38}$$

### 2.2.4 Equilibria of adsorption

The equilibrium behaviour of the adsorbate gas in an adsorbent material can be studied from their adsorption isotherms. The equilibria of adsorption are related to the amount of adsorbate gas adsorbed onto the adsorbent material at which equilibrium is established in the system (also known as the equilibrium adsorption capacity of the adsorbate gas, $\bar{q}_e$) under a given temperature $T$ and pressure $P$. The shape of the adsorption isotherms can vary since the pore structure of the adsorbent and the interaction between the adsorbate gas and the adsorbent solid at the surface of the adsorbent crystals and at the adsorption sites are complex (Crittenden and Thomas, 1998; Reynolds *et al*, 2002).

As shown in Figure 2.6, the International Union of Pure and Applied Chemistry (IUPAC) classified adsorption isotherms into six types, namely, Types I to VI. Type I isotherm indicates monolayer adsorption of adsorbate gas molecules on the adsorbent surface in the micropores of the adsorbent by micropore filling. They also correspond to the completion of a molecular monolayer when the micropores are completely filled (Crittenden and Thomas, 1998).

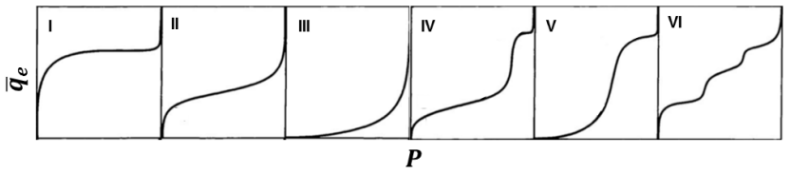


**Figure 2.6** Adsorption isotherms classified by IUPAC. [Adapted from Rouquerol *et al.* (1999).]

Type I isotherm is usually observed in microporous adsorbents (such as zeolites) with pore diameters not significantly larger than the molecular diameter of adsorbate gas molecules (Crittenden and Thomas, 1998). Several studies, for examples, Férey *et al.* (2005) and Zhang *et al.* (2011) have reported that gas adsorption onto MIL-101(Cr) exhibits type I isotherm because they possess two kinds of microporous pores. Both types II and III isotherms apply to adsorbents with a wide distribution of pore diameters. Monolayer adsorption occurs initially followed by multilayer adsorption of adsorbate gas molecules on the adsorbent surface and finally to capillary condensation of adsorbate condensate in larger pores, which increase the adsorption capacity at high pressure (Crittenden and Thomas, 1998).

Type IV isotherm shows that adsorption leads to the formation of two surface layers, i.e., either on a plane surface or on the wall of a pore significantly wider than the

molecular diameter of the adsorbate gas molecules. Type V isotherm is similar to type III isotherm at low pressure but the remaining large pores after the multilayer adsorption are completely filled with the adsorbate condensate during capillary condensation at high pressure. The isotherm of type VI suggests that adsorption progresses from monolayer to multilayer and ultimately to capillary condensation with complete pore filling at each layer (Crittenden and Thomas, 1998).

The adsorption isotherms for porous adsorbent materials can either be measured using the gravimetric gas sorption method or dynamic gas flow method. For the gravimetric gas sorption, the adsorption isotherm is determined gravimetrically using an electro-microbalance. This method measures the equilibrium adsorption capacity of the adsorbate gas. As for the dynamic gas flow method, a gas stream containing one or more adsorbate gases flows through an adsorbent bed and the effluent gas concentration is recorded. When the system has reached equilibrium, the effluent gas concentration stays constant. The equilibrium adsorption capacity of the adsorbate gas can then be calculated from their breakthrough curves using the equation given in Section 2.2.1.1.

In this research, both gravimetric gas sorption and dynamic gas flow methods will be used. The adsorption of $CO_2$, $CH_4$, $H_2O$ and $H_2S$ onto zeolite and MIL-101(Cr) monoliths and carbonate based zeolite foam-monoliths developed in this work will be studied using the dynamic gas flow method. Because MIL-101(Cr) is a new adsorbent material and they will be synthesized in this research, pure $CO_2$ adsorption on the prepared MIL-101(Cr) powders and monoliths will be studied using the gravimetric gas sorption method.

### 2.2.5 Regeneration of Adsorbents

This section describes some of the common regeneration methods such as temperature or pressure swing regenerations that can be used to desorb and regenerate the saturated adsorbents for reuse. The effect of pressure and temperature on the adsorption equilibrium of an adsorbate gas with a type I isotherm is shown schematically in Figure 2.7.

In temperature swing regeneration, the adsorbent bed is desorbed and regenerated by heating it either directly using a hot gas stream or indirectly using an external double jacket and an internal heating surface. Normally, an inert purge gas and/or vacuum is needed to remove the thermally desorbed gas components from the adsorbent bed as

well as a cooling step to reduce the temperature of the adsorbent bed to the adsorption condition. The temperature swing regeneration is suitable for a system containing strongly adsorbed gas components that can be desorbed and recovered at high concentrations. However, repeated temperature swing regeneration can reduce the adsorption capacity or life of the adsorbent (Crittenden and Thomas, 1998).

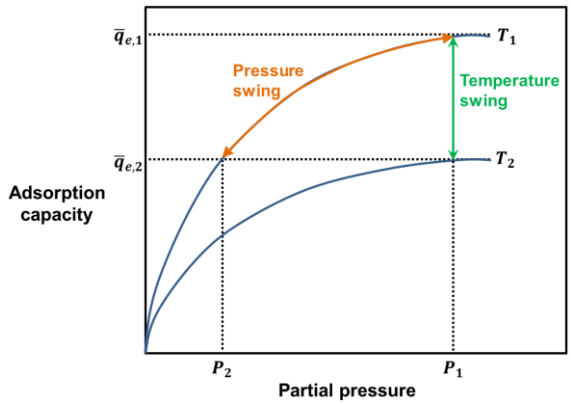


**Figure 2.7** Schematic diagram of temperature and pressure swing regenerations. [Redrawn from Crittenden and Thomas (1998).]

In pressure swing regeneration, the adsorbent bed is desorbed and regenerated by decreasing the pressure at the same temperature as the adsorption step. The pressure swing regeneration is favourable for a system with weakly adsorbed gas components that needs to be in high purity but very low pressure may be required to remove the gas contaminants from the adsorbent bed, which means the energy consumption by the vacuum pump may be increased that will in turn make the pressure swing regeneration more expensive to operate than the temperature swing regeneration (Crittenden and Thomas, 1998).

The choice of regeneration methods for adsorbents in biogas upgrading application depends on their technical (i.e., heat of adsorption and binding strength of the adsorbate gas molecules at the adsorption sites) and economic (i.e., cost of adsorbent, cost of supplying thermal energy in temperature swing process and cost of electricity for gas compressors or vacuum pumps in pressure swing process) aspects (Bart and Gemmingen, 2012). To ensure efficient desorption of gas contaminants (such as $CO_2$, $H_2O$ vapour and $H_2S$) from the adsorbent, a combination of temperature and pressure swing regeneration will be used in this research to desorb and regenerate the adsorbent, i.e. by heating them under atmospheric pressure. The reason is because adsorbents saturated with $H_2O$ vapour and $H_2S$ are normally harder to regenerate compared to those saturated with $CO_2$. Although this method has been reported in literatures (for examples,

Alonso-Vicario *et al.*, 2010 and Biernat and Samson-Bręk, 2011), it is still not been employed in current biogas upgrading plants. Details on adsorbents are given in the next section.

## 2.3 Adsorbents

Inefficient adsorption performance of the existing adsorption technology in biogas upgrading process is primarily caused by the adsorbent that is used in the system. The adsorbent may not be stable after frequent adsorption-desorption cycles due to degradation on long-term usage, difficulties in regeneration and poor tolerance to acidic/toxic contaminants such as $CO_2$, $H_2O$ vapour and $H_2S$. All these issues will result in slow adsorption and desorption kinetics as well as gradual loss in adsorption capacity and selectivity (Choi *et al.*, 2009). So, it is very important to select and use appropriate adsorbents for removing unwanted contaminants such as $CO_2$, $H_2O$ vapour and $H_2S$ from the biogas efficiently.

Ideally, the adsorbent for biogas upgrading application should have fast adsorption and desorption kinetics to minimize energy consumption, high adsorption capacities for $CO_2$, $H_2O$ vapour and $H_2S$, strong selectivity of $CO_2$ over $CH_4$ to enrich the $CH_4$ content in biogas, good regenerability, stability in repeated adsorption-desorption cycles and tolerance to contaminants present in the biogas (Choi *et al.*, 2009; Sayari *et al.*, 2011). To meet these conditions, structural characteristics (such as pore size and surface polarity) of the adsorbent and physical properties (such as molecular size and polarity) of the contaminants will need to be taken into consideration (Sircar and Myers, 2003).

Adsorbents can also be categorized based on the adsorption forces involved. They can either be physical adsorbents or chemical sorbents. The adsorption process using physical adsorbents such as zeolites and metal-organic frameworks (MOFs) involves weak intermolecular forces. Conversely, the adsorption process using chemical sorbents such as alkali metal carbonates involves the formation of chemical bonds between the gas molecules and the adsorbent surfaces (Crittenden and Thomas, 1998).

In the selection of suitable adsorbents for biogas upgrading, this research will focus on zeolites since they are one of the most commonly used adsorbents in current biogas upgrading technology, owing to their unique molecular sieving capabilities, relatively high adsorption capacities for $CO_2$, $H_2O$ vapour and $H_2S$, good regenerability, high thermal

stabilities and structurally stable to humid conditions (Choi *et al.*, 2009; Grande, 2011; EPRI, 2006). Additionally, this research will look into new adsorbent materials such as metal-organic frameworks (MOFs) and alkali metal carbonates for biogas upgrading applications. The suitability of all these adsorbents for biogas upgrading will be discussed in Sections 2.3.1 to 2.3.3.

### 2.3.1 Zeolites

Zeolites are microporous crystalline aluminosilicates of exchangeable alkali metal or alkaline earth metal cations (such as sodium, potassium and calcium) that are represented by the general chemical formula:

$$\mathbf{M}_{\frac{x}{n}}\left[(\mathrm{AlO_2})_x(\mathrm{SiO_2})_y\right]\cdot z\mathrm{H_2O}$$

where $\mathbf{M}$ is the metal cation, $n$ is the charge of the cation, $x$ and $y$ are integers and $z$ is the number of water molecules in the cavities that can be reversibly removed by heating (Roland and Kleinschmit, 2012; Yang, 1997).

For instance, the typical chemical formula for 5A zeolite with calcium cation ($Ca^{2+}$) prevalence is $Ca_3Na_2[(AlO_2)_{12}(SiO_2)_{12}]\cdot 27H_2O$ (Barrer, 1978; Li, 1998). The typical chemical formula for the low silica type X zeolite with lithium cation ($Li^+$) prevalence (represented by LiLSX) is $Li_{96}[(AlO_2)_{96}(SiO_2)_{96}]\cdot 32H_2O$ (Jiang *et al.*, 2002) and that for 13X zeolite with sodium cation ($Na^+$) prevalence is $Na_{86}[(AlO_2)_{86}(SiO_2)_{106}]\cdot 264H_2O$ (Ruthven, 2005). For natural zeolites such as clinoptilolite with $Na^+$ prevalence, its typical chemical formula is given by $(Na,K)_6[(AlO_2)_6(SiO_2)_{30}]\cdot 24H_2O$ (Barrer, 1978).

The framework structure of zeolites is made of a group of silicon ($SiO_4$) and aluminium ($AlO_4$) tetrahedra connected to oxygen atoms and charge balanced by exchangeable metal cations to form an open crystal lattice. The crystal lattice consists of hydrated cavities linked through pores of molecular dimensions that permit gas molecules to enter (Crittenden and Thomas, 1998). The three-dimensional framework structures of the commonly used types A and X zeolites and clinoptilolite are presented in Figure 2.8.

The framework structures of types A and X zeolites show that they are constructed from assemblies of polyhedra consisting of several $SiO_4$ and $AlO_4$ tetrahedra joined through six-membered oxygen rings to form type A zeolite or twelve-membered oxygen rings to form type X zeolite (Crittenden and Thomas, 1998). In contrast to types A and X

zeolites, the framework structure of clinoptilolite shows that it is built from groups of polyhedra consisting of several $SiO_4$ and $AlO_4$ tetrahedra connected through an interconnected eight-, ten- and eight-membered oxygen rings (IZA-SC, 2008).

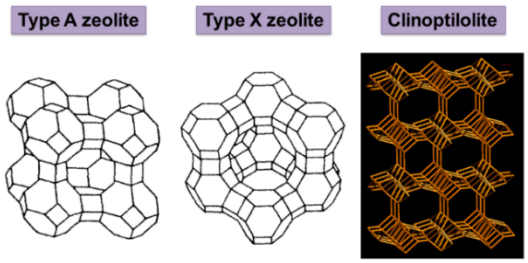


**Figure 2.8** Schematic representation showing the framework structures of types A and X zeolites and clinoptilolite. [Adapted from Ruthven (1984) and IZA-SC (2008).]

The pore sizes of zeolites can be designed to allow only gas molecules of smaller sizes to penetrate and get adsorbed in the cavities depending on the type of zeolite and the size of the exchangeable cations (Bart and Gemmingen, 2012). For instances, 5A zeolite (consisting of $Ca^{2+}$ ions) has a pore size of approximately 0.50 nm (Li, 1998; Sokolova and Kazanskii, 2005), LiLSX zeolite has a pore size of about 0.74 nm (Sokolova and Kazanskii, 2005) whereas 13X zeolite and clinoptilolite (consisting of $Na^+$ ions) have pore sizes of about 0.75 nm (Sircar and Myers, 2003) and 0.45 nm (Bogdanov *et al.*, 2009), respectively. This means that they are able to remove contaminants such as $CO_2$, $H_2O$ vapour and $H_2S$ from biogas by molecular sieving since the molecular sizes of these contaminants are smaller than the pore sizes of the zeolites mentioned in this example.

In addition, the Si/Al ratio of the zeolite structure can affect their selectivity, for instance, low silica zeolites with Si/Al ratio close to 1.0 have high affinity for polar molecules such as $H_2O$, $CO_2$ and $H_2S$ because there are strong adsorptive forces in the zeolite as a consequence of more cations been exposed within the crystal lattice (Ruthven, 1984). Considering 5A, 13X, LiLSX zeolites and clinoptilolite as examples, the adsorptive forces in these zeolites to attract polar contaminants such $CO_2$, $H_2O$ vapour and $H_2S$ in biogas are stronger than that in clinoptilolite because they have less silicon and more aluminium in their structures (Si/Al ratio of 1.0 for 5A and LiLSX zeolites and 1.2 for 13X zeolite) compared to clinoptilolite (Si/Al ratio of 5.0).

As a result of low silicon content in 5A, LiLSX and 13X zeolites, they exhibit high adsorption capacities for $H_2O$. For examples, international zeolite manufacturers such as UOP Ltd. (UK) claimed that both 5A and 13X zeolites have high adsorption capacities for

$H_2O$, which can be as high as 14.44 mmol $g^{-1}$ for 5A zeolite and 16.67 mmol $g^{-1}$ for 13X zeolite at 1 bar and 25 °C. LiLSX zeolite also has a high $H_2O$ adsorption capacity, i.e., 14.89 mmol $g^{-1}$ at 1 bar and 25 °C according to Buhl *et al.* (2004). Since the silicon content in clinoptilolite is higher than that in 5A, LiLSX and 13X zeolites, it was reported by Ward and McKague (1994) that clinoptilolite has a moderate $H_2O$ adsorption capacity of 8.06 mmol $g^{-1}$ at 1 bar and 25 °C.

Due to the unique molecular sieving effect and surface polarity of zeolites, they have reasonably high adsorption capacities for contaminants such as $CO_2$, $H_2O$ vapour and $H_2S$ compared to $CH_4$. For instance, the adsorption isotherms of pure $CO_2$ and $CH_4$ gases reported by Pakseresht *et al.* (2002) indicate that 5A zeolite has a high adsorption capacity of $CO_2$ (i.e., 2.85 mmol $g^{-1}$ at 1 bar and it can go up to 3.55 mmol $g^{-1}$ at 10 bar and 30 °C) compared to $CH_4$ (i.e., 0.72 mmol $g^{-1}$ at 1 bar and it can go up to 1.78 mmol $g^{-1}$ at 10 bar and 30 °C).

The pure component $CO_2$ and $CH_4$ adsorption isotherms presented by Cavenati *et al.* (2004) demonstrate that 13X zeolite also has a high adsorption capacity of $CO_2$ (ranging from 4.59 mmol $g^{-1}$ at 1 bar to 6.50 mmol $g^{-1}$ at 10 bar and 25 °C) compared to $CH_4$ (ranging from 0.62 mmol $g^{-1}$ at 1 bar to 3.05 mmol $g^{-1}$ at 10 bar and 25 °C). Based on the pure component $CO_2$ adsorption isotherm reported by Stuckert and Yang (2011), LiLSX zeolite can achieve a $CO_2$ adsorption capacity of 1.34 mmol $g^{-1}$ at 1 bar and 25 °C. To date, there is no $CH_4$ adsorption data for LiLSX zeolite been reported in the literature.

Moreover, the pure $CO_2$ adsorption isotherm presented by Siriwardane *et al.* (2003) reveals that clinoptilolite has a $CO_2$ adsorption capacity of 0.45 mmol $g^{-1}$ at 1 bar and it can increase up to 0.90 mmol $g^{-1}$ at 10 bar and 25 °C. Although clinoptilolite has a low adsorption capacity of $CO_2$ compared to 5A and 13X zeolites, Yaşyerli *et al.* (2002) demonstrated that they have a high adsorption capacity of $H_2S$ (i.e., 2.56 mmol $g^{-1}$ at 1 bar) even at a high temperature of 100 °C. This level of adsorption capacity may not be achievable by other adsorbents, for example, the 13X zeolite that was used by Melo *et al.* (2006) for removing $H_2S$ at 25 °C exhibits a low $H_2S$ adsorption capacity of 1.56 mmol $g^{-1}$ at 4.9 bar. So far, no $H_2S$ adsorption data has been reported in the literature for both 5A and LiLSX zeolites.

Besides having high adsorption capacity, zeolites also have good regenerability properties owing to their high thermal stability, which varies with the type of zeolite, nature

of the exchangeable cations and Si/Al ratio. For instances, the structures of 5A zeolite containing $Ca^{2+}$ with Si/Al ratio of 1.0 and 13X zeolite containing $Na^{+}$ with Si/Al ratio of 1.2 collapse at temperature above 800 °C (Li, 1998; Li and Rees, 1986) while the structure of clinoptilolite containing $Na^{+}$ with Si/Al ratio of 5.0 collapses at about 920 °C (Cruciani, 2006). This indicates that these zeolites are structurally stable when they are heated at temperatures below their thermal stability during activation (to remove water molecules from the cavities) and regeneration (to remove adsorbed gas molecules from the cavities).

So, it is possible to use zeolites for numerous adsorption-desorption cycles and they can be thermally regenerated, for example, at temperatures between 200 °C and 300 °C, without major degradation on their structure (Choi *et al.*, 2009). Additionally, zeolites are not combustible materials so they are safe to use in biogas upgrading application.

### 2.3.2 Metal-organic frameworks (MOFs)

An emerging new class of porous crystalline materials that can be used as physical adsorbents in biogas upgrading application is metal-organic frameworks (MOFs). Their structures comprise of metal ions or clusters connected by organic linkers to form a network. MOFs have large pore sizes, high porosities, large surface areas, good thermal and chemical stabilities, low framework densities and high adsorption capacities for contaminants such as $CO_2$, $H_2O$ vapour and $H_2S$ compared to other adsorbents such as zeolites so they are potentially suitable for this application (Férey *et al.*, 2005; Hamon *et al.*, 2009; Millward and Yaghi, 2005).

For example, MIL-101(Cr) [$Cr_3O(OH)(H_2O)_2(bdc)_3$; bdc = 1,4-benzenedicarboxylate] is a mesoporous crystalline material that has a three-dimensional framework structure consisting of trimeric chromium(III) ($Cr_3O$) clusters joined to 1,4-benzenedicarboxylate (bdc) ligands to form microporous super-tetrahedral unit. According to Férey *et al.* (2005), this super-tetrahedral unit has a pore size of 0.86 nm, which linked together with several other super-tetrahedral units to form a polyhedral unit.

The polyhedral unit of MIL-101(Cr) consists of two types of mesoporous quasi-spherical cavities that are filled with guest molecules such as water. The smaller cavity of 20 super-tetrahedra has a pore size of about 2.9 nm that is accessible through pentagonal windows of size 1.2 nm whereas the larger cavity of 28 super-tetrahedra has a pore of about 3.4 nm that is accessible through both pentagonal and hexagonal windows of sizes

1.45 nm by 1.6 nm (Férey *et al.*, 2005). The construction of the framework structure of MIL-101(Cr) is illustrated schematically in Figure 2.9.

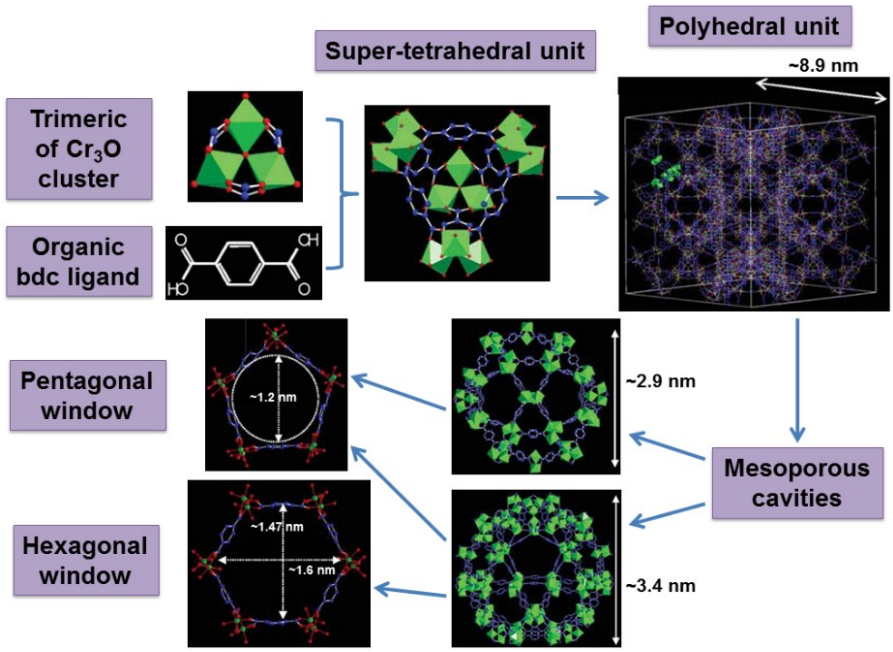


**Figure 2.9** Schematic diagram showing the construction of the framework structure of MIL-101(Cr). (Note: Chromium atoms were denoted in green colour, oxygen atoms were denoted in red colour while fluorine and carbon atoms were denoted in blue colour.) [Adapted from Férey *et al.* (2005).]

Férey *et al.* (2005) also reported that MIL-101(Cr) has a cubical crystal structure with a large cell volume of about 702 $nm^3$ and a large Langmuir surface area for nitrogen of about 5900 ± 300 $m^2$ $g^{-1}$. The large cell volume of MIL-101(Cr) will allow more adsorbate gas contaminants such as $CO_2$, $H_2O$ vapour and $H_2S$ to be stored in their mesoporous cavities. In addition to the large cell volume, the large surface area of MIL-101(Cr) will enable more adsorption sites to be exposed for adsorbing gas contaminants from the biogas stream.

Due to the large pore sizes of MIL-101(Cr), small-sized gas contaminants such as $CO_2$, $H_2O$ vapour and $H_2S$ can penetrate through the pentagonal and hexagonal pores and adsorb in the mesoporous cavities. Besides the molecular sieving effect, the open pore structure and large cavities of MIL-101(Cr) also cause more chromium clusters to be exposed within the crystal framework. This results in high affinity for polar molecules such as $H_2O$, $CO_2$ and $H_2S$ due to strong adsorptive forces in their structure between the contaminant gas molecules and the surface of MIL-101(Cr) as the chromium centre was activated (Chowdhury *et al.*, 2009).

For this reason, MIL-101(Cr) exhibits high adsorption capacities of $CO_2$, $H_2O$ vapour and $H_2S$ and they are more selective for $CO_2$ adsorption over $CH_4$. From the pure $CO_2$ and $CH_4$ adsorption isotherms presented by Chowdhury *et al.* (2009), MIL-101(Cr) shows a preferential adsorption for $CO_2$ over $CH_4$ with a high $CO_2$ adsorption capacity that ranges from 2.20 mmol $g^{-1}$ at 1 bar to 8.00 mmol $g^{-1}$ at 5.3 bar and 10 °C and a low $CH_4$ adsorption capacity that ranges from 0.65 mmol $g^{-1}$ at 1 bar to 2.20 mmol $g^{-1}$ at 5.3 bar and 10 °C.

The study carried out by Férey *et al.* (2005) found that MIL-101(Cr) has a high adsorption capacity of $H_2O$, i.e. 22.22 mmol $g^{-1}$ at 1 bar. This suggests that the framework structure of MIL-101(Cr) are stable in the presence of water unlike most MOFs (for example, HKUST-1 [$Cu_3(btc)_2$; btc = benzene-1,3,5-tricarboxylate]), which will degrade after $H_2O$ vapour adsorption (Küsgens *et al.*, 2009). The special hydrothermal stability of MIL-101(Cr) makes it suitable for use as an adsorbent in biogas upgrading since $H_2O$ vapour is likely to be present in the biogas stream.

Moreover, MIL-101(Cr) also exhibits higher adsorption capacity of $H_2S$ compared to other adsorbents such as zeolites. Based on the pure $H_2S$ adsorption isotherm reported by Hamon *et al.* (2009), MIL-101(Cr) has a high $H_2S$ adsorption capacity of 8.00 mmol $g^{-1}$ at 1 bar and it can increase up to 33.50 mmol $g^{-1}$ at 10 bar and 30 °C. This demonstrates that MIL-101(Cr) can be a better adsorbent than zeolites for capturing the poisonous $H_2S$ gas from the biogas stream.

The thermal analysis carried out by Férey *et al.* (2005) indicates that the structure of MIL-101(Cr) is stable up to 275 °C. Although the thermal stability temperature of MIL-101(Cr) is much lower than other adsorbents such as zeolites, this can be an advantage in an energy perspective. The temperature used in the activation and regeneration of MIL-101(Cr) should be below 275 °C (for example, 150 °C) to prevent/minimize structural changes in their crystal framework. By using a low activation and regeneration temperature, the energy consumption in the biogas upgrading process can be reduced. This will result in a more energy efficient adsorption technology for the system (Munusamy *et al.*, 2012).

### 2.3.3 Alkali metal carbonates

Apart from the physical adsorbents mentioned in previous sections, contaminants such as $CO_2$, $H_2O$ vapour and $H_2S$ in biogas can also be removed by chemical sorbents such as alkali metal carbonates, for examples, sodium carbonate ($Na_2CO_3$) and potassium carbonate ($K_2CO_3$) (Samantha *et al.*, 2011). These alkali metal carbonates are usually coated on the adsorbent to improve the physical adsorptive characteristics of the adsorbent with chemical reaction (EPRI, 2006; Petersson *et al.*, 2009). A lot of studies on alkali metal carbonates-based solid sorbents are carried out for $CO_2$ capture from flue gas. For example, Esmaili and Ehsani (2014) developed $K_2CO_3$ (33.1% wt.) on alumina support sorbent for $CO_2$ capture from flue gas with 8% vol. $CO_2$ and 12% vol. $H_2O$ in a fixed-bed reactor at 65 °C. Their sorbent showed an adsorption capacity of 1.50 mmol $g^{-1}$.

Lee *et al.* (2008) prepared several $Na_2CO_3$ (20% wt. to 50% wt.)-based solid sorbents for $CO_2$ capture from simulated flue gas with 14.4% vol. $CO_2$, 5.4% vol. $O_2$, 10% vol. $H_2O$ and 70.2% vol. $N_2$. The test was carried out by thermogravimetric analysis with sorption temperature from 50 °C to 70 °C and the regeneration temperature was 120 °C. They found that their sorbent (with 30% wt. $Na_2CO_3$) has better $CO_2$ sorption capacity (2.27 mmol $g^{-1}$; > 80% sorbent utilisation) than MEA solution (30.3% MEA solution was used as a reference and its $CO_2$ sorption capacity was 1.36 mmol $g^{-1}$; 33% sorbent utilisation). So far, there is no studies being reported on the use of these alkali metal carbonates-based solid sorbents for biogas upgrading application.

The framework structure of alkali metal carbonates consists of a set of carbonate ($CO_3^{2-}$) ions that is charge balanced by alkali metal ions, either sodium ($Na^+$) or potassium ($K^+$) ions. Each $CO_3^{2-}$ ion contains one carbon atom and three oxygen atoms, which are connected to the sodium or potassium atoms to form octahedral units. The sodium or potassium atoms are arranged such that they are located at the centre of a hexagon of oxygen atoms from different carbonate groups (Gatehouse and Lloyd, 1973). The framework structure of alkali metal carbonates is illustrated schematically in Figure 2.10.

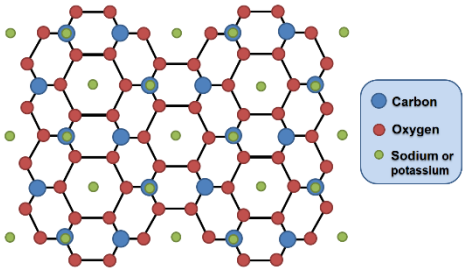


**Figure 2.10** Schematic representation of the framework structure of alkali metal carbonates. [Redrawn from Gatehouse *et al.* (1973) and PubChem (2015a, b).]

$Na_2CO_3$ and $K_2CO_3$ can be obtained by heating their respective alkali metal bicarbonates, i.e., $NaHCO_3$ (at 250 °C to 300 °C) and $KHCO_3$ (at 100 °C to 400 °C) (All Reactions, 2015a, b):

$$2NaHCO_3 \rightarrow Na_2CO_3 + CO_2 + H_2O \quad (2.39)$$

$$2KHCO_3 \rightarrow K_2CO_3 + CO_2 + H_2O \quad (2.40)$$

During adsorption, the alkali metal carbonates form chemical bonds with the adsorbate gas contaminants. For example, the reactions of $Na_2CO_3$ and $K_2CO_3$ with $CO_2$ and $H_2O$ vapour at low temperature (between 30 °C and 40 °C) (All Reactions, 2015a, b) can be represented by the following chemical equations, which are the reverse of reactions 2.39 and 2.40.

$$Na_2CO_3 + CO_2 + H_2O \rightarrow 2NaHCO_3 \quad (2.41)$$

$$K_2CO_3 + CO_2 + H_2O \rightarrow 2KHCO_3 \quad (2.42)$$

From these chemical equations, it is estimated that $Na_2CO_3$ and $K_2CO_3$ have a respective maximum theoretical capacity of 9.43 mmol $g^{-1}$ and 7.24 mmol $g^{-1}$ for both $CO_2$ and $H_2O$ vapour adsorption (Samantha *et al.*, 2011).

Moreover, the reactions of $Na_2CO_3$ and $K_2CO_3$ with $H_2S$ are also reversible and they take place at moderately low temperature (between 70 °C and 130 °C) (Field *et al.*, 1960):

$$Na_2CO_3 + H_2S \rightleftarrows NaHCO_3 + NaHS \quad (2.43)$$

$$K_2CO_3 + H_2S \rightleftarrows KHCO_3 + KHS \quad (2.44)$$

Based on these chemical equations, the maximum theoretical capacity for $H_2S$ adsorption on $Na_2CO_3$ and $K_2CO_3$ is similar to those estimated for $CO_2$ and $H_2O$ vapour adsorption (i.e., 9.43 mmol $g^{-1}$ of $Na_2CO_3$ and 7.24 mmol $g^{-1}$ of $K_2CO_3$).

Due to the low temperature involved in the reactions, the adsorption of gas contaminants such as $CO_2$, $H_2O$ vapour and $H_2S$ from the biogas stream can be operated at low temperature and the alkali metal carbonates can be regenerated at temperature below 200 °C (Samantha *et al.*, 2011). This means that the heat energy demanded by the biogas upgrading system can be reduced and hence lowering the cost of supplying heat energy to the system (Liang *et al.*, 2004).

## 2.4 Binders: Clays

In addition to the review of potential adsorbents for biogas upgrading that was described in Section 2.3, this section covers the selection of suitable binders that can be added to the adsorbent powders so that the resulting structured adsorbents possess adequate mechanical strength to withstand bulk handling and friction when they are used in the industries, for example, in biogas upgrading plants. This research will concentrate on clays since they have unique properties, i.e., plastic and mouldable when wet, rigid when dry and hard when fired at high temperature (Li, 1998; Murray, 2012).

One of the commercially important clays is bentonite, which is a smectite clay mineral containing montmorillonite. The framework structure of bentonite consists of units that contain two silica ($SiO_2$) tetrahedral sheets with a central alumina ($Al_2O_3$) octahedral sheet joined through oxygen atoms (see Figure 2.11). The aluminium atoms are often replaced by the substitution of iron or magnesium and the silicon atoms are sometimes replaced by the substitution of aluminium atoms. These substitutions create an unbalanced charge within the three-layer framework and they are balanced by the absorption of exchangeable cations such as sodium ($Na^+$) and calcium ($Ca^{2+}$) ions and water molecules at the interlayer, which cause the hexagonal crystal lattice to expand (Murray, 2012).

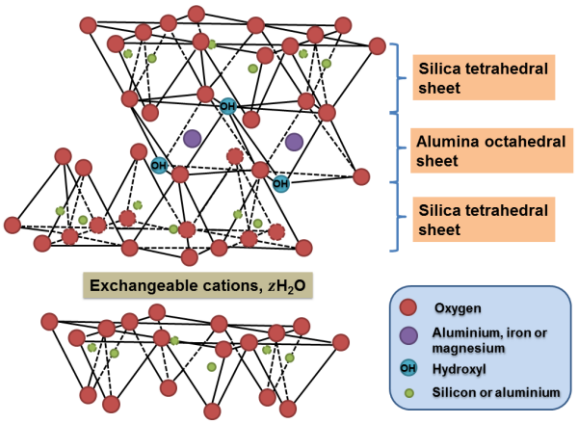


**Figure 2.11** Schematic diagram showing the framework structure of bentonite. [Redrawn from Murray (2012).]

The hydration and swelling capacities of bentonite depend on the type of exchangeable cations contained in their lattice. For examples, sodium bentonite (also termed as Wyoming sodium bentonite), containing mainly $Na^+$ ions, has high water adsorption and swelling capacities whereas calcium bentonite, containing mainly $Ca^{2+}$ ions, has lower water adsorption and swelling capacities due to the higher positive charge of the cations (CETCO, 2013; Murray, 2012).

When water is absorbed by the bentonite, several layers of water are created at the interlayer to form a rigid network. The hydrogen bonds connecting the hydrogen atoms of the water molecules and the oxygen atoms of the silica tetrahedra through these thin layers of water can partially break when mechanical stress or pressure is applied, allowing the silica tetrahedral sheets to slide over one another more freely and thus, forming the plasticity effect of the bentonite (CETCO, 2013; Murray, 2012).

With an appropriate amount of water in the crystal lattice, bentonite can bind strongly with other particles such as adsorbents by retaining water molecules in the highly rigid network, providing more mechanical strength to the green extrudate as well as more heat resistance since bentonite has higher thermal stability than other type of clays. [Green extrudate means the extrudate before drying or in the drying process.] Apart from the high plasticity and binding effects, bentonite also has relatively high dry compression strength (CETCO, 2013; Murray, 2012).

## 2.5 Structured Adsorbents

The discussion in previous section indicated that it is possible to manufacture structured adsorbents with high mechanical strengths by adding bentonite to the adsorbent powders. The shape of the structured adsorbents can range from the current state-of-the-art adsorbent structures such as beads (spherical), pellets (cylindrical) and granules (irregular) to novel structures such as monoliths and foams. These different types of structures are illustrated Figure 2.12.

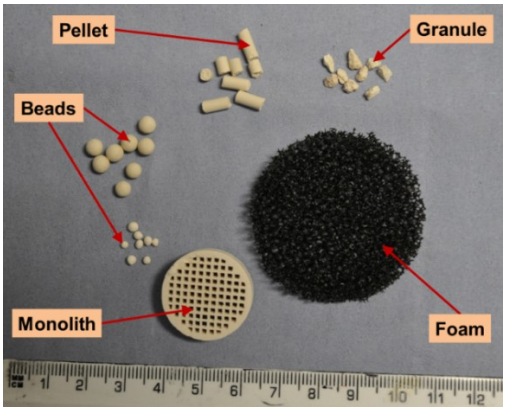


**Figure 2.12** A photograph showing various type of structured adsorbents/polymers: 4.0 mm 5A zeolite beads, 2.1 mm 13X zeolite beads, 3.2 mm 13X zeolite pellets, 5.0 mm clinoptilolite granules, 30 cells $cm^{-2}$ 5A zeolite monolith and 20 pores per inch (ppi) polyester foam.

In most industrial applications, it is preferable to use structured adsorbents in adsorption columns than powdered adsorbents. The reasons for this are:

a) structured adsorbents can be settled easily in adsorption columns compared to powdered adsorbents during no gas flow,

b) movement of adsorbent beds and fluidization of adsorbent particles in adsorption columns during gas flow can be avoided using structured adsorbents instead of powdered adsorbents,

c) better gas flow distribution can be achieved in structured adsorbent beds compared to powdered adsorbent beds, and

d) it is easier to handle structured adsorbents than powdered adsorbents when removing them from adsorption columns for replacement, regeneration or disposal.

For efficient adsorption in biogas upgrading, it is important to choose suitable structured adsorbents (i.e., beads, pellets, granules, monoliths or foams) that will produce a high adsorption performance with low energy consumption and low cost. The current state-of-the-art adsorbents (such as beads, pellets and granules) and novel adsorbent structures (such as monoliths and foams) will be reviewed in Sections 2.5.1 to 2.5.3, focussing on the mass transfer and pressure drop in these adsorbent structures as they are related to the adsorption performance, energy efficiency and economic of the system.

### 2.5.1 Current state-of-the-art adsorbents: Beads, pellets and granules

Beads, pellets and granules are the current state-of-the-art adsorbents and they are commonly used in industries, including biogas upgrading plants due to their availability from commercial sources and low cost (Yon and Sherman, 2003). Some of the processing methods used in shaping these adsorbents from powdered adsorbents into various sizes and geometries (such as spherical and cylindrical) are extrusion and granulation, followed by drying and calcination. Binders such as clays (for examples, bentonites) are also added to the adsorbent powders so that the shaped bodies have sufficient mechanical stability (Akhtar *et al.*, 2014; Li, 1998). Adsorbent beads, pellets and granules are usually packed randomly in adsorption columns to provide a high contact area between the flowing gas and adsorbent surfaces (Petersson and Wellinger, 2009).

Depending on their particle diameters and bed porosities, the gas flow distribution and pressure in the adsorbent bed will vary so considerations on the pressure drop and

mass transfer in packed beds of adsorbent beads, pellets or granules need to be taken. The pressure drop in a packed bed of adsorbent beads, pellets or granules is mainly caused by skin friction and form drag. The skin friction occurs when the gas flows over the adsorbent surfaces and increases if the surfaces are rough. On the other hand, the form drag occurs when the gas flows over the adsorbent solids and increases if the adsorbent solids are bluff (for examples, spherical beads and cylindrical pellets) (Newcamp, 2002). Figure 2.13 illustrates the formation of skin friction and form drag as the gas flow around a spherical adsorbent bead.

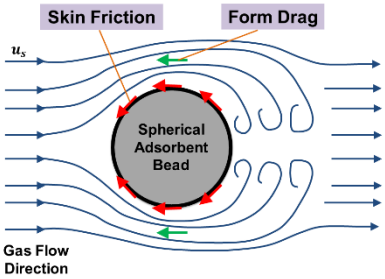


**Figure 2.13** Schematic diagram showing the skin friction and form drag when the gas flows around a spherical adsorbent bead. [Redrawn from Newcamp (2002).]

Since the adsorbent beads, pellets and granules have rough surfaces and bluff shape (spherical or cylindrical), they usually have large skin friction and form drag when the gas flows around them. For these reasons, the gas flow distribution around the adsorbents is not uniform and this causes the pressure in a packed bed of adsorbent beads, pellets or granules to fluctuate. As a result of large skin friction and form drag on the adsorbent beads, pellets or granules, packed bed of these structured adsorbents often have high pressure drop. This means the adsorption process using the packed bed system would require more energy for operating the gas compressors or vacuum pumps to maintain the desired pressure in the packed column. This also means that the cost of electricity will increase and thus causing the adsorption process to be less economical (Crittenden and Thomas, 1998).

The skin friction and form drag resist the gas flow around the adsorbent beads, pellets or granules and this cause some energy to be lost. In a packed bed of adsorbent beads, pellets or granules, energy is lost during skin friction as the gas flows over the adsorbent surfaces and during form drag as the gas flows through the tortuous paths between the adsorbent beads, pellets or granules. This implies that the use of packed bed system for adsorption process is not energy efficient (Crittenden and Thomas, 1998). To reduce the energy loss, this research will develop adsorbent monoliths of straight channels that will minimize the form drag when the gas flows along the channels.

The packed bed adsorbent beads, pellets or granules also have poor mass transfer between the adsorbate gas contaminants (such as $CO_2$, $H_2O$ vapour and $H_2S$) and the adsorbent particles. This is as a result of slow gas diffusion into and out of the adsorbent particles (Akhtar *et al.*, 2014; Rezaei and Webley, 2010). Generally, the particle size of the adsorbent beads, pellets or granules is reduced to increase the rate of gas diffusion into and out of the adsorbent particles and this will improve the mass transfer in the packed bed system (Rezaei and Webley, 2010).

### 2.5.2 Monoliths

The problems of high pressure drop and poor mass transfer in packed beds of adsorbent beads, pellets and granules can be avoided by using novel structures such as monoliths. The structure of monoliths consists of parallel channels with various cross-sectional shapes, for examples, circular, square, triangular and hexagonal. The most common and simplest channel shape to manufacture is square (Patton *et al.*, 2004). Adsorbent monoliths are normally manufactured by extrusion, followed by drying and firing. It is also essential to include binders such as clays (for examples, bentonites) to the adsorbent powders to provide adequate mechanical stability to the extruded monoliths (Akhtar *et al.*, 2014; Li, 1998).

Monoliths can be packed easily in adsorption columns with gas streams flowing along the parallel channels. Similar to the packed bed of adsorbent beads, pellets or granules, the pressure drop in a monolithic bed is contributed by skin friction and form drag. The skin friction is caused by the gas flowing over the surfaces of the monolith walls and increases when the surfaces are rough. On the contrary, the form drag is caused by the gas flowing over the monolith walls in the straight channels and decreases when the channels are straight and small. Figure 2.14 illustrates the formation of skin friction and form drag as the gas flows around the monolithic walls along a straight channel.

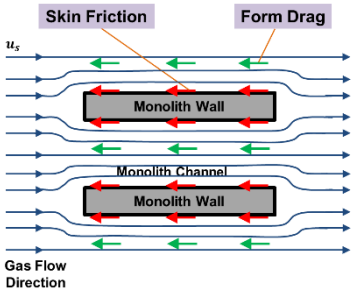


**Figure 2.14** Schematic diagram showing the skin friction and form drag when the gas flows around the monolith walls in a straight channel.

The surfaces of the monolith walls are usually rough so they tend to produce skin friction during gas flows. As mentioned earlier, the adsorbent monoliths to be developed in this research will consist of straight channels that will reduce the form drag when the gas flows over the monolith walls in the channels. By minimizing the form drag in the adsorbent monoliths, the gas flow distribution around the monolith walls will be more uniform and this will reduce the pressure fluctuations in monolithic beds.

For these reasons, the adsorbent monoliths normally have lower pressure drop compared to the packed bed of adsorbent beads, pellets or granules. This means the adsorption process will demand less energy since there is less work to be performed by the gas compressors or vacuum pumps to maintain the desired pressure in the column. As a result, the cost of electricity for operating the gas compressors or vacuum pumps is reduced and this makes the adsorption process more economical to run (Crittenden and Thomas, 1998).

The resistance of gas flows in the adsorbent monoliths during skin friction and form drag cause some energy to be lost. Since the adsorbent monoliths of straight channels have small form drag, the source of gas resistance in the monolithic bed is mainly dominated by the skin friction. This implies that energy is mostly lost during skin friction as the gas flows over the surfaces of the monolith walls rather than during form drag as the gas flows over the monolith walls in the straight channels. Because of this, the adsorbent monoliths are more energy efficient than the packed bed of adsorbent beads, pellets or granules when used for adsorption in the biogas upgrading process.

Depending on the design of the adsorbent monoliths, the mass transfer in monolithic beds can be better than packed beds of adsorbent beads, pellets or granules. For efficient mass transfer of gases in adsorbent monoliths, the gas diffusion into and out of the adsorbent particles should be fast. This can be achieved by having thin-walled monoliths. To develop adsorbent monoliths of low pressure drop and good mass transfer, they should have small channel diameters and thin walls. By reducing the channel diameters and wall thicknesses of the adsorbent monoliths, their cell densities will increase accordingly. This means they have high adsorbent loading per volume. Several studies (for examples, Patton *et al.* (2004) and Rezaei and Webley (2010)) showed that adsorbent monoliths with high cell densities, small channel diameters and thin walls have fast mass transfer rates and low pressure drop.

In addition, the studies carried out by Crittenden *et al.* (2005) and Li *et al.* (2009) demonstrated that high cell densities and thin-walled adsorbent monoliths have lower pressure drop and faster mass transfer rates than packed beds of beads, pellets or granules. Although monoliths have been researched for various adsorption processes, they are still not being used industrially because of mass transfer issues. For instance, the 5A zeolite monoliths manufactured by Li (1998) for air separation application have mass transfer resistances in the monolithic beds in spite of having almost the same adsorption capacities for oxygen and nitrogen and three to five times lower pressure drop than the commercial 5A zeolite pellets.

One way of overcoming the mass transfer issue in monoliths is to improve the macroporosity of the monoliths (Lee, 1997). This can be achieved by adding a pore former such as wax into their paste formulations that will decompose upon thermal treatment to create macropores within the monolithic structure. The presence of these macropores in the monolithic structure will allow more adsorption sites to be exposed for adsorbing gas contaminants such as $CO_2$, $H_2O$ vapour and $H_2S$ from the biogas stream. This means the mass transfer between the adsorbate gas contaminants and the adsorbent solids can be enhanced.

This innovative approach of incorporating a pore former to enhance the macroporosities of the monolithic structure for improving the mass transfer in adsorbent beds will be studied in this research. The inclusion of a pore former in various adsorbent paste formulations for the production of zeolite monoliths will be described in Chapter 3 while those for the production of MOFs (such as MIL-101(Cr)) monoliths and carbonate-based zeolite monoliths will be described individually in Chapters 4 and 5.

### 2.5.3 Foams

Besides monoliths, novel structures such as foams can also overcome the problems of high pressure drop and poor mass transfer in the packed bed system. Foams are structures containing a network of pores and struts (or cell walls) that can be produced by foam extrusion. The pores in foams are created by adding foaming agents, which are either in the forms of physical (such as air, $CO_2$, $N_2$ and butane) or chemical (such as sodium bicarbonate that will decompose to produce $CO_2$ gas) (Weber *et al.*, 2012).

The bed porosity and surface area of the foams can be optimised to meet the system requirements by either controlling the gas flow rates of the physical foaming agents or the amount of chemical foaming agents. To minimize the pressure drop and mass transfer resistances in foam adsorbent beds, it is favourable to have a high bed porosity and large surface area within the foam structure (Rezaei and Webley, 2010).

For industrial usage, it is necessary for the foams to possess good mechanical stability so that they can withstand bulk handling and friction in industrial vessels. Due to high bed porosities of the foam structure, their mechanical strengths are very weak. Normally, ceramic or metal foam structure are made and then coated with adsorbent materials. Although this method resolved the mechanical stability issue of the foams, their adsorption performance is limited by the low adsorbent loading per unit mass or volume of the foams.

A pioneering manufacturing strategy will be introduced in this research that will resolve not only the mechanical stability issue of the foam structure but also the limitation of their adsorption performance. The strategy is to embed the foams into the monoliths and this will create a novel structure known as a foam-monolith for the biogas upgrading application. Since this new adsorbent structure is a combination of foams and monoliths, they will have lower pressure drop and better mass transfer than the packed bed of adsorbent beads, pellets or granules.

In this research, the novel foam-monoliths will be manufactured using a unique extrusion technique based on the special formulations described in Chapter 5. In addition to the chosen adsorbent (i.e., 13X zeolite), chemical foaming agents such as sodium and potassium bicarbonates are included in their paste formulations. These chemical foaming agents will decompose when heated to produce $CO_2$ gas within the foam-monolith walls and this creates pores or foam structure in the foam-monolith walls. Clays such as calcium bentonite will also be added to the adsorbent mixture as a binder to provide mechanical stability to the foam-monolithic structures.

To improve the macroporosity of the foam-monoliths, a decomposable pore forming agent such as Licowax C micropowder PM (an amine wax) will be incorporated to their paste formulations. This will further enhance the mass transfer between the adsorbate gas contaminants (such as $CO_2$, $H_2O$ vapour and $H_2S$) and the adsorbent solids. The details of their manufacturing procedures are given in Chapter 5.

## 2.6 Conclusions

The background information of the research has been provided in this chapter. Biogas is used as a model gas in this research since it is a clean renewable fuel that can be utilised in many applications (such as to generate heat and electricity or use as transport fuels). Typically, a raw biogas contains about 50% vol. to 75% vol. $CH_4$, 25% vol. to 45% vol. $CO_2$ and other trace gases such as $H_2O$ vapour and $H_2S$. The biogas quality can be improved by enriching its $CH_4$ content through the removal of its gas contaminants such as $CO_2$, $H_2O$ vapour and $H_2S$. Various biogas upgrading technologies are available and their technical, energy, environmental and economic performance have been compared. It was concluded that pressure swing adsorption could be the most suitable technology for biogas upgrading compared to water scrubbing, chemical absorption with amine solutions and membrane separation.

For this reason, the principles of adsorption that are applicable to the research were described in this chapter. It was shown that the dynamic behaviour of adsorbate gas contaminants in the adsorbent bed could be studied by analysing their breakthrough curves. Adsorption properties that could be determined from their breakthrough curves were breakthrough, stoichiometric and equilibrium times, breakthrough and equilibrium adsorption capacities, selectivity, effectiveness of adsorbent bed utilisation as well as mass transfer zone length and velocity. Additionally, the kinetic behaviour of adsorbate gas in the adsorbent bed during adsorption could be studied by determining their mass transfer and diffusion coefficients. It was shown that the flow behaviour of adsorbate gas contaminants in the adsorbent bed could be studied by evaluating their axial dispersion and pressure drop. It was also shown that the equilibrium behaviour of adsorbate gas contaminants in the adsorbent bed could be studied from their adsorption isotherm.

Common regeneration methods such as temperature and pressure swing regeneration have been described. Normally, adsorbents saturated with $H_2O$ vapour and $H_2S$ are harder to regenerate than those saturated with $CO_2$. In order to make sure that all these gas contaminants can be effectively desorbed from the adsorbent, saturated adsorbents can be regenerated by heating them under atmospheric pressure. This method is a combination of temperature and pressure swing regeneration and it will be used in this research to demonstrate the possibility of employing this regeneration method for biogas upgrading process since it is still not been adapted on biogas upgrading plants.

Physical adsorbents (such as zeolites and MOFs) and chemical sorbents (such as alkali metal carbonates) suitable for biogas upgrading were described in this chapter. Generally, these adsorbents/sorbents were chosen because they have high $CO_2$, $H_2O$ vapour and/or $H_2S$ adsorption capacities, relatively high $CO_2/CH_4$ selectivity to increase the concentration of $CH_4$ in the upgraded biogas stream, fast adsorption and desorption kinetics to reduce energy consumption, good regenerability, stability in repeated adsorption-desorption cycles and good tolerance to contaminants present in the biogas. Examples of potential adsorbents for biogas upgrading to be studied in this research are 5A zeolite, 13X zeolite, LiLSX zeolite, clinoptilolite, MIL-101(Cr), $Na_2CO_3$ and $K_2CO_3$. The use of carbonates-based solid sorbents for biogas upgrading will be studied in this research because, to date, there is no study being reported in the literature on this area.

Clays such as calcium and Wyoming sodium bentonites are usually added to the adsorbent powders to provide mechanical stability to the adsorbent structures. The structure and properties of these bentonites have been described. Various types of structured adsorbents such as the current state-of-the-art adsorbents (beads, pellets and granules) and novel adsorbent structures (monoliths and foams) were reviewed. The mass transfer and pressure drop associated with these adsorbent structures were discussed. Although monoliths have lower pressure drop than packed of beads, pellets or granules, they are still not being used industrially as they have mass transfer issues. An innovative way to reduce the mass transfer resistances in the monolithic beds is to improve its structural macroporosity. In this research, a decomposable pore former such as wax will be incorporated into their paste formulations to create macropores within the monolithic structure.

A new adsorbent structure to be developed in this research for biogas upgrading was also introduced, it was known as ‘foam-monolith’. Chemical foaming agents such as $NaHCO_3$ or $KHCO_3$ will be included in their adsorbent paste formulations. When heated, these chemical foaming agents will decompose to produce $Na_2CO_3$ or $K_2CO_3$ and $CO_2$ gas within the foam-monolith walls. The carbonates will be retained within the foam-monolith structure while the $CO_2$ gas creates pores or foam structure in the foam-monolith walls. Similar to monolith, a decomposable pore former such as wax could be added to enhance their structural macroporosity. This produces carbonate-based adsorbent foam-monoliths. It was suggested that the mass transfer and pressure drop issues in current adsorption technology that still use the packed bed system could be mitigated by using novel adsorbent structures such as monoliths and foam-monoliths.

# Chapter 3 Fabrication and Characterisation of Zeolite Monoliths

This chapter will describe the fabrication of zeolite monoliths and their physical characterisation. The materials and equipment used in this study are given in Section 3.1. A unique paste extrusion technique will be employed in this study to fabricate zeolite monoliths according to the specially invented formulations. The procedure described in this thesis for fabricating zeolite monoliths is different from those reported in the literature (for examples, Lee (1997) and Li (1998)), in which the materials used in the study are treated differently. In this work, zeolites such as 13X zeolite, LiLSX zeolite, 5A zeolite and clinoptilolite are selected and used as model adsorbents for biogas upgrading. The reasons are because they have unique molecular sieving capabilities, relatively high adsorption capacities for $CO_2$, $H_2O$ vapour and $H_2S$, good regenerability, high thermal stabilities and good resistances to humid conditions. The details of their fabrication procedures are provided in Section 3.2.

As discussed in previous chapter, clays such calcium (Ca) bentonite and Wyoming sodium (Na) bentonite could make the adsorbent pastes mouldable and impart mechanical strength to the extruded monoliths. So, they are chosen and used as model binders in this study. An amine wax such as Licowax C micropowder PM, which will decompose at temperature above 200 °C, will also be added to the paste formulations of zeolite monoliths as pore forming agent to enhance their structural macroporosity.

Physical characteristics such as thermal stabilities, crystal structures, pore structures, surface morphologies and mechanical compression strengths of the prepared zeolite monoliths and some of the materials used in this study will be determined and compared with commercially available zeolite beads or granules. The characterisation methods that will be used in this study are simultaneous thermogravimetry and differential scanning calorimetry (TG-DSC), powder X-ray diffraction (PXRD), mercury intrusion porosimetry (MIP), scanning electron microscopy (SEM) and mechanical strength tests. The descriptions of these characterisation methods are provided in Section 3.3.

The results obtained from the fabrication and characterisation of the prepared zeolite monoliths will be provided and discussed in Section 3.4. Lastly, the work described in this chapter will be concluded in Section 3.5.

## 3.1 Materials and Equipment Used in the Study

The materials used in the fabrication of zeolite monoliths are listed in Table 3.1, which consist of the powdered adsorbents, binders, a pore forming agent and a solvent. The selected model adsorbents used in this study were 13X zeolite, LiLSX zeolite, 5A zeolite and clinoptilolite. Clays such as calcium bentonite and Wyoming sodium bentonite were used as model binders. The pore forming agent used in the study was Licowax C micropowder PM and the solvent was water.

**Table 3.1** Materials required in this study and their commercial sources.

| Categories | Materials | Particle diameter | Sources |
|---|---|---|---|
| Powdered adsorbents | 13X zeolite | 3 μm – 5 μm | Zeochem AG (Switzerland) |
| | LiLSX zeolite | 4.5 μm | Süd-Chemie (UK) |
| | 5A zeolite | 3 μm – 5 μm | UOP LLC (USA) |
| | Clinoptilolite | < 5 μm | Milled from granules supplied by Euremica Environmental Ltd. (UK) |
| Powdered binders | Calcium bentonite | < 0.5 μm | Bath Potters' Supplies Ltd. (UK) |
| | Wyoming sodium bentonite | < 0.5 μm | RS Minerals Ltd. (UK) |
| Powdered pore forming agent | Licowax C micropowder PM | 15.1 μm | Clariant (UK) |
| Solvent | Water | – | Wessex Water (UK) |
| Structured adsorbents | 13X zeolite beads | 1.6 mm – 2.5 mm | Süd-Chemie (Germany) |
| | LiLSX zeolite beads | 1.0 mm – 2.0 mm | Zeochem AG (Switzerland) |
| | 5A zeolite beads | 4.0 mm | Acros Organics (USA) |
| | Clinoptilolite granules | 3.0 mm – 8.0 mm | Euremica Environmental Ltd. (UK) |
| Non-wetting liquid for MIP | Mercury | – | Sigma-Aldrich Co. (USA) |

For characterisation, powdered samples of 13X zeolite, LiLSX zeolite, 5A zeolite, clinoptilolite, calcium bentonite and Wyoming sodium bentonite were used in TG-DSC, PXRD and SEM tests. Zeolite monoliths prepared in this study were characterised and the monolith samples used in each of the characterisation methods are listed in Table 3.2. The paste compositions of the zeolite monolith samples are expressed in terms of weight percentage (% wt.) of the total dry mass. For example, if the total dry mass is 100 g, the paste sample no. 4 requires 75 g of 13X zeolite, 25 g of calcium bentonite, 4 g of Licowax C micropowder PM and 116 g of water. The firing temperatures and wall thicknesses of the zeolite monolith samples used in the characterisation were also stated in Table 3.2. Commercial zeolite beads and granules were also used in this work for comparative

purposes. Mercury, which is a non-wetting liquid, was used in the MIP analysis. All materials listed in Table 3.1 were used as obtained from suppliers and no further purification was made.

**Table 3.2** Zeolite monolith samples prepared and used in each of the characterisation methods. [Note: Firing temperatures and wall thicknesses of the monolith are given in brackets in the table.]

| Sample | Zeolite monolith (paste composition) | PXRD | MIP | SEM | Mechanical compression |
|---|---|---|---|---|---|
| 1 | 13X zeolite monolith (80% wt. 13X zeolite:20% wt. Ca bentonite + 113% wt. water) | No | No | No | Yes (400 °C; 0.9 mm) |
| 2 | 13X zeolite monolith (75% wt. 13X zeolite:25% wt. Ca bentonite + 116 % wt. water) | No | Yes (400 °C; 0.9 mm) | Yes (400 °C & 650 °C; 0.9 mm) | Yes (400 °C; 0.7 mm & 0.9 mm; 650 °C; 0.9 mm) |
| 3 | 13X zeolite monolith (70% wt. 13X zeolite:30% wt. Ca bentonite + 119% wt. water) | No | No | No | Yes (400 °C; 0.9 mm) |
| 4 | 13X zeolite monolith with pore former (75% wt. 13X zeolite:25% wt. Ca bentonite + 4% wt. Licowax C micropowder PM + 116 % wt. water) | Yes (400 °C & 650 °C; 0.9 mm) | Yes (400 °C & 650 °C; 0.9 mm) | No | Yes (400 °C; 0.9 mm) |
| 5 | 13X zeolite monolith (80% wt. 13X zeolite:20% wt. Wyoming Na bentonite + 123% wt. water) | No | No | Yes (650 °C; 0.9 mm) | Yes (650 °C; 0.9 mm) |
| 6 | 13X zeolite monolith with pore former (80% wt. 13X zeolite:20% wt. Wyoming Na bentonite + 2% wt. Licowax C micropowder PM + 123% wt. water) | No | No | No | Yes (650 °C; 0.9 mm) |
| 7 | 13X zeolite monolith with pore former (80% wt. 13X zeolite:20% wt. Wyoming Na bentonite + 4% wt. Licowax C micropowder PM + 123% wt. water) | No | No | Yes (650 °C; 0.9 mm) | Yes (650 °C; 0.9 mm) |
| 8 | 13X zeolite monolith (75% wt. 13X zeolite:25% wt. Wyoming Na bentonite + 126% wt. water) | No | No | No | Yes (400 °C; 0.9 mm) |
| 9 | LiLSX zeolite monolith (75% wt. LiLSX zeolite:25% wt. Ca bentonite + 125% wt. water) | No | No | No | Yes (400 °C; 0.9 mm) |
| 10 | LiLSX zeolite monolith (70% wt. LiLSX zeolite:30% wt. Ca bentonite + 128% wt. water) | No | Yes (400 °C; 0.9 mm) | No | Yes (400 °C; 0.7 mm & 0.9 mm; 650 °C; 0.9 mm) |

**Table 3.2** Zeolite monolith samples prepared and used in each of the characterisation methods. [Note: Firing temperatures and wall thicknesses of the monolith are given in brackets in the table.] (continued)

| Sample | Zeolite monolith (paste composition) | PXRD | MIP | SEM | Mechanical compression |
|---|---|---|---|---|---|
| 11 | LiLSX zeolite monolith (65% wt. LiLSX zeolite:35% wt. Ca bentonite + 131% wt. water) | No | No | No | Yes (400 °C; 0.9 mm) |
| 12 | LiLSX zeolite monolith with pore former (70% wt. LiLSX zeolite:30% wt. Ca bentonite + 4% wt. Licowax C micropowder PM + 128% wt. water) | No | Yes (400 °C; 0.9 mm) | No | Yes (400 °C; 0.9 mm) |
| 13 | LiLSX zeolite monolith (80% wt. LiLSX zeolite:20% wt. Wyoming Na bentonite + 132% wt. water) | No | No | Yes (650 °C; 0.9 mm) | No |
| 14 | LiLSX zeolite monolith (70% wt. LiLSX zeolite:30% wt. Wyoming Na bentonite + 138% wt. water) | No | No | No | Yes (400 °C; 0.9 mm) |
| 15 | LiLSX zeolite monolith (60% wt. LiLSX zeolite:40% wt. Wyoming Na bentonite + 144% wt. water) | No | No | Yes (400 °C; 0.9 mm) | No |
| 16 | LiLSX zeolite monolith with pore former (70% wt. LiLSX zeolite:30% wt. Wyoming Na bentonite + 4% wt. Licowax C micropowder PM + 138% wt. water) | Yes (400 °C; 0.9 mm) | No | Yes (650 °C; 0.9 mm) | No |
| 17 | 5A zeolite monolith (85% wt. 5A zeolite:15% wt. Ca bentonite + 92% wt. water) | No | No | No | Yes (400 °C; 0.9 mm) |
| 18 | 5A zeolite monolith (80% wt. 5A zeolite:20% wt. Ca bentonite + 95% wt. water) | No | Yes (400 °C; 0.9 mm) | No | Yes (400 °C; 0.7 mm & 0.9 mm; 650 °C; 0.9 mm) |
| 19 | 5A zeolite monolith (75% wt. 5A zeolite:25% wt. Ca bentonite + 98% wt. water) | No | No | No | Yes (400 °C; 0.9 mm) |
| 20 | 5A zeolite monolith with pore former (80% wt. 5A zeolite:20% wt. Ca bentonite + 4% wt. Licowax C micropowder PM + 95% wt. water) | No | Yes (400 °C; 0.9 mm) | No | No |
| 21 | 5A zeolite monolith (80% wt. 5A zeolite:20% wt. Wyoming Na bentonite + 105% wt. water) | No | No | Yes (400 °C & 650 °C; 0.9 mm) | Yes (400 °C; 0.9 mm) |

**Table 3.2** Zeolite monolith samples prepared and used in each of the characterisation methods. [Note: Firing temperatures and wall thicknesses of the monolith are given in brackets in the table.] (continued)

| Sample | Zeolite monolith (paste composition) | PXRD | MIP | SEM | Mechanical compression |
|---|---|---|---|---|---|
| 22 | 5A zeolite monolith with pore former (80% wt. 5A zeolite:20% wt. Wyoming Na bentonite + 4% wt. Licowax C micropowder PM + 105% wt. water) | Yes (400 °C; 0.9 mm) | No | Yes (650 °C; 0.9 mm) | Yes (400 °C; 0.9 mm) |
| 23 | Clinoptilolite monolith (85% wt. clinoptilolite:15% wt. Ca bentonite + 80% wt. water) | No | Yes (400 °C; 0.9 mm) | No | Yes (400 °C; 0.7 mm & 0.9 mm; 650 °C; 0.9 mm) |
| 24 | Clinoptilolite monolith (80% wt. clinoptilolite:20% wt. Ca bentonite + 83% wt. water) | No | No | No | Yes (400 °C; 0.9 mm) |
| 25 | Clinoptilolite monolith (75% wt. clinoptilolite:25% wt. Ca bentonite + 86% wt. water) | No | No | No | Yes (400 °C; 0.9 mm) |
| 26 | Clinoptilolite monolith with pore former (85% wt. clinoptilolite:15% wt. Ca bentonite + 4% wt. Licowax C micropowder PM + 80% wt. water) | No | Yes (400 °C; 0.9 mm) | No | Yes (400 °C; 0.9 mm) |
| 27 | Clinoptilolite monolith (85% wt. clinoptilolite:15% wt. Wyoming Na bentonite + 90% wt. water) | No | No | Yes (400 °C & 650 °C; 0.9 mm) | Yes (400 °C; 0.9 mm) |
| 28 | Clinoptilolite monolith with pore former (85% wt. clinoptilolite:15% wt. Wyoming Na bentonite + 4% wt. Licowax C micropowder PM + 90% wt. water) | Yes (400 °C; 0.9 mm) | No | Yes (650 °C; 0.9 mm) | No |

The equipment used in the fabrication of zeolite monoliths were:

a) an electric mixer (Clatronic, model KM 3067) consisting of a 5 Litre stainless steel bowl and a special stainless steel stirrer for blending the wet powder mixtures to produce adsorbent pastes,

b) a horizontal, single-screw extruder (model BETOL 2520J) with a barrel length, $L_b$, of 62 cm and a screw diameter, $D_s$, of 2.3 cm provided by Plasplant Machinery Ltd. (UK) for extruding the zeolite adsorbent pastes,

c) a stainless steel extruder die manufactured by South Western Tools Ltd. (UK) for shaping the monolithic extrudates and

d) an electric kiln (Rohde, model Ecotop 43L) with programmable temperatures purchased from Bath Potters' Supplies Ltd. (UK) for firing the zeolite adsorbent monoliths.

The schematic diagrams showing the extruder equipment and cross-section of an extruder die are presented in Figures 3.1 (a) and (b), respectively. In this research, two stainless steel extruder dies of different geometrical properties (Table 3.3) were used for optimising the design of the zeolite monoliths. Their photographs are shown in Figure 3.2.

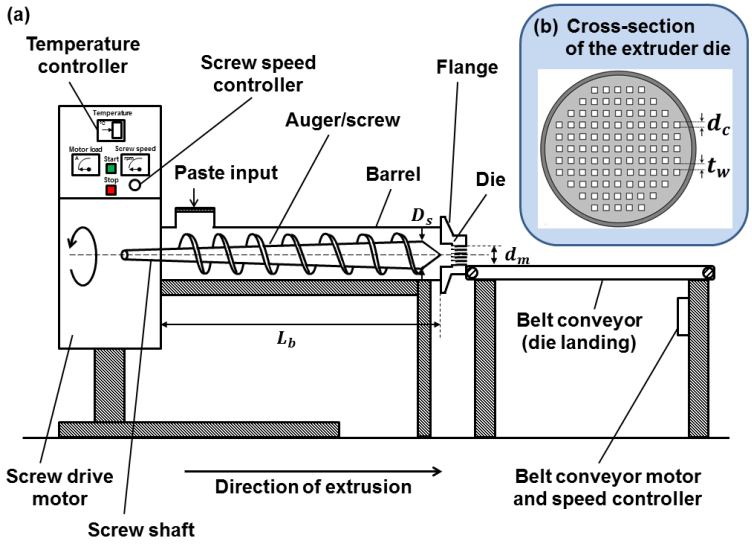


**Figure 3.1** Schematic diagrams of the (a) extruder equipment and (b) cross-section of an extruder die (see inserted picture).

**Table 3.3** Geometrical properties of extruder dies.

| Extruder die | Die A | Die B |
|---|---|---|
| Cell density, $\rho_{cell}$ (cells cm$^{-2}$) | 34 | 30 |
| Channel diameter, $d_c$ (mm) | 1.0 | 0.9 |
| Wall thickness, $t_w$ (mm) | 0.7 | 0.9 |

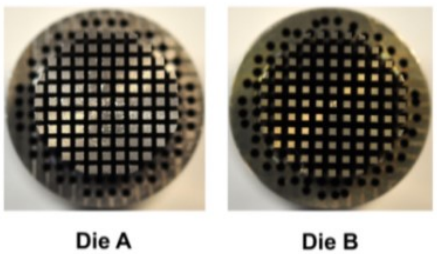


**Figure 3.2** Photographs of the two extruder dies used in the research.

For the characterisation of zeolite monoliths and materials, the following apparatus were used in this study:

a) a simultaneous thermogravimetric and differential scanning calorimetric analyser (model Setaram TGA 92) equipped with a microbalance, a furnace and a 100 $mm^3$ alumina crucible (5 mm in diameter and 9.9 mm in height) for analysing their thermal properties,

b) a diffractometer (model Bruker AXS D8 Advance) consisting of an X-ray generator, a vertical goniometer (angular range: $-110° < 2Theta \leq 168°$), a 50 mm diameter silicon sample cup (with a 20 mm diameter and 0.5 mm depth sample reception) and an X-ray detector for analysing their crystal structures,

c) a mercury penetrometer (model Micromeritics AutoPore III) with a 3 $cm^3$ bulb glass penetrometer (stem volume of 1.19 $cm^3$) for determining their pore properties,

d) an Edwards sputter coater (model S150B) and an electron microscope (model JEOL JSM-6480 LV) built in a vacuum chamber that contains a stainless steel sample holder, a sample stage, an electron gun and an electron sensor for examining their morphologies and

e) an Instron universal tester (model 3369) assembled with a 1 kN or 50 kN load cell for evaluating their mechanical compressive strengths.

## 3.2 Experimental Procedures for the Fabrication of Zeolite Monoliths

In this study, the zeolite monoliths will be fabricated using a unique paste extrusion technique that is different from those reported in the literature, for examples, Lee (1997) and Li (1998). The fabrication process employed in this work comprises of several steps, i.e., paste preparation, pre-drying, extrusion, drying and firing. The schematic flow diagram in Figure 3.3 summarized the processing steps of producing adsorbent monoliths. Issues such as surface tearing, cracking and bending can happen if the fabrication procedures are not followed properly. The detailed processing steps and possible defects that may occur in each step are provided in Sections 3.2.1 to 3.2.5.

The selected materials for this study were treated differently depending on the properties of the materials (such as particle size and particle size distribution) and the pastes (such as plasticity and consistency). To ensure close packing of particles, all the powdered materials used in this work have fine particle sizes (considerably < 5 μm for the

chosen zeolites and < 0.5 μm for the chosen bentonites). It was important to use fine powders because they could reduce the tendency of phase separation in the extrusion step and improve the sintering rate in the firing step (Benbow *et al.*, 1987).

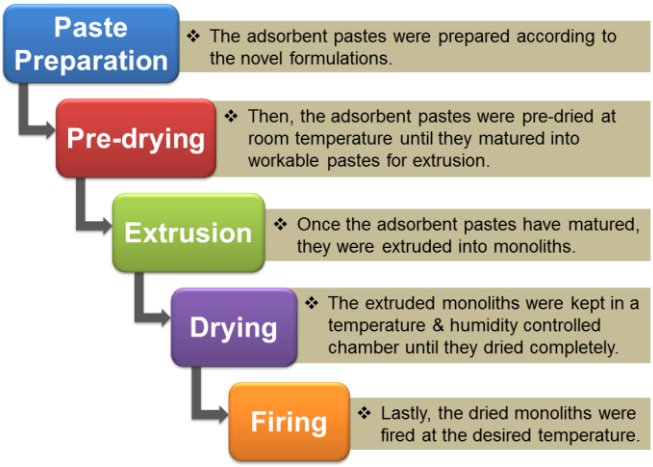


**Figure 3.3** A schematic flow diagram showing the steps involved in the fabrication process.

### 3.2.1 Paste preparation

In this study, the adsorbent pastes were prepared by mixing and kneading dry powders of zeolites, bentonites and/or pore forming agent with sufficient amount of water on an electric mixer to form homogenous adsorbent pastes that were plastic and mouldable. To find the suitable plasticity of the adsorbent pastes for the extrusion process, right proportions of the starting materials need to be obtained. Ideally, the adsorbent pastes should have low water content and high plasticity to prevent surface tearing or solid-liquid phase separation of the adsorbent pastes during extrusion and to ensure slow drying of the extruded monoliths (Lee, 1997; Ryan, 1978).

For these reasons, a number of adsorbent pastes with different compositions were prepared and the adsorbent paste formulations that have the suitable plasticity for extrusion are listed in Table 3.2. According to Table 3.3, it seems that the extrudable adsorbent pastes could contain maximum amounts of 80% wt. of 13X zeolite, 75% wt. of LiLSX zeolite and 85% wt. of both 5A zeolite and clinoptilolite in the adsorbent paste formulations, which were balanced by the appropriate amounts of bentonites and water. In addition, a maximum amount of 4% wt. of Licowax C micropowder PM was incorporated to the adsorbent paste formulations to minimize the effect of the pore forming agent on the mechanical strength of the adsorbent monoliths. For comparison, 2% wt. of Licowax C micropowder PM was included in the 13X zeolite paste formulation (i.e., Sample no. 6).

### 3.2.2 Pre-drying

When the homogenous adsorbent pastes have been prepared, they were placed and wrapped in a cloth to allow the water molecules to evaporate by gravity at room temperature until they matured into workable adsorbent pastes with high plasticity for extrusion. Depending on the water content of the zeolite pastes, the pre-drying step could take at least 48 hours to achieve the right plasticity and consistency of the zeolite pastes for extrusion.

### 3.2.3 Extrusion

Once the adsorbent pastes had matured, they were manipulated and divided into small lumps to ensure there were no air pockets in the pastes, which could critically influence their mechanical strength. Prior to the start of the extrusion process, it was essential to check all internal surfaces of the extruder that would come into contact with the adsorbent pastes, including the screw, internal wall of the barrel and die were cleaned. This was to make sure there were no particulates remained in the extruder from previous extrusion otherwise cracking could happen on the extrudates due to the blockage of the flow of adsorbent pastes through the extruder die.

In this study, the extrusion process was carried out at room temperature and the speed of the rotating screw of the extruder was set at 5 revolutions per minute (rpm) at the start of the extrusion. Lumps of zeolite pastes were fed into the paste input of the extruder continuously to avoid the entrapment of air and separation of the zeolite pastes. By forcing the zeolite pastes to flow forward along the barrel and through the extruder die, the green (i.e., wet) zeolite monoliths were formed.

The extruded green zeolite monoliths of diameter, $d_m$, of about 24 mm were landed on a wax paper that was attached to the belt conveyor. The speed of the belt conveyor was the same as the extruder screw. The purpose of the belt conveyor was to reduce the force required by the extruder to push the zeolite pastes out of the extruder die.

The extruded green zeolite monoliths were cut using a thin copper wire of diameter 0.1 mm into the preferred lengths. These sectioned green zeolite monoliths were then placed carefully onto a perforated aluminium tray so that they could be handled easily with minimal skin contacts.

### 3.2.4 Drying

To prevent rapid evaporation of water molecules, the tray of green zeolite monoliths was immediately kept in a chamber of controlled temperature (5 °C) and humidity (> 95% relative humidity) for at least a week depending on the water content of the green zeolite monoliths. In the drying process, the green zeolite monoliths tend to shrink as a consequence of water molecules been evaporated from the cavities and through the pores of the zeolite crystals and from the interlayers of the bentonite crystals.

With the use of perforated aluminium tray as well as controlled temperature and humidity in the chamber, uneven and fast evaporation of the water molecules from the surface of the green zeolite monoliths could be avoided. This means the drying effect and stress on the green zeolite monoliths could be reduced, which would minimize the risks of cracking and bending of the green zeolite monoliths.

### 3.2.5 Firing

When the green zeolite monoliths have fully dried, they were placed on the ceramic plates in the electric kiln and ready for firing, which was the last step of the fabrication process. In this study, the green zeolite monoliths were fired under compressed air according to the temperature programmes, as shown in Figure 3.4. The temperature programmes for the firing step were determined empirically such that the resulting fired zeolite monoliths were not cracked and they were strong enough to be used in the experiments of this research.

In this study, the firing temperature was ramped slowly at several stages until it reached the desired high temperature of 400 °C or 650 °C. These firing temperatures were selected such that they were below the thermal stability temperature of both the zeolites and bentonites. This was to prevent their crystal structures from collapsing, which would affect their adsorption properties.

In the first stage of the firing process, the green zeolite monoliths were heated from room temperature of 20 °C to 130 °C at a slow rate of 0.08 °C $min^{-1}$ to gradually remove any remaining water molecules from the pores of the zeolite crystals and from the interlayers of the bentonite crystals. This was to reduce the risk of cracking on zeolite monoliths. In the second stage, the temperature in the kiln was increased from 130 °C to

either 300 °C or 400 °C at a rate of 0.30 °C $min^{-1}$ with a holding time of 1 hour to ensure any impurities in bentonites and the pore forming agent were burnt off.

In the final stage, the temperature of the kiln was increased from either 300 °C or 400 °C to their respective chosen temperature of 400 °C or 650 °C at a rate of 0.80 °C $min^{-1}$ with a holding time of 1 hour. This was to bind zeolite and bentonite crystals together. The chosen temperature of 400 °C or 650 °C was kept constant by holding them for 5 hours so that the necessary mechanical strength could be provided to the fired zeolite monoliths.

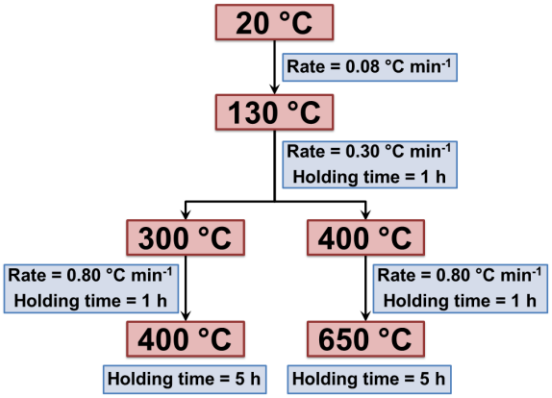


**Figure 3.4** Flow diagram of the firing temperature programmes for zeolite monoliths.

After the firing process has completed, the fired zeolite monoliths were cooled to room temperature naturally in the kiln. This was to prevent the sudden drop in temperature that would cause rapid contraction of the fired zeolite monoliths, which in turn would lead to the cracking of the zeolite monoliths. Zeolite monoliths prepared in this study were refined by cutting both of their ends using a saw prior to characterisation and use in the experiments described in this thesis.

## 3.3 Methods of Characterizing the Zeolite Monoliths

The materials and zeolite monoliths studied in this work were characterised using: (a) simultaneous TG-DSC for investigating their thermal properties, (b) PXRD for analysing their crystal structures, (c) MIP for determining their pore properties, (d) SEM for observing their morphologies and (e) mechanical compression tests for evaluating their compressive strengths. The experimental procedures of each of these characterisation methods are provided in Sections 3.3.1 to 3.3.5.

### 3.3.1 Simultaneous thermogravimetry and differential scanning calorimetry

A sample of either zeolite or bentonite powder was loaded into a small alumina crucible and weighed on a microbalance inside an insulated furnace at room temperature. The environment in the furnace was controlled by flowing cool water to the system and purging them with argon gas while the temperature in the furnace was measured by a thermocouple. A temperature programme for this analysis was set such that the air supplied into the furnace was heated from 20 °C to 900 °C at a rate of 10 °C $min^{-1}$.

The sample was then analysed using a simultaneous thermogravimetric and differential scanning calorimetric analyser. After the analysis has completed, the samples were allowed to cool naturally to room temperature before removing them from the furnace. The thermal data of the sample was recorded on a computer using a SetSoft2000 programme and they were used to generate the thermogravimetric (TG – i.e., a plot of weight against temperature) and differential scanning calorimetric (DSC – i.e., a plot of heat flow against temperature) curves. A blank test was also carried out using an empty alumina crucible under similar operating conditions as mentioned above. The TG and DSC curves of the blank test was given in Appendix 1. All the TG and DSC curves presented in this thesis were corrected by subtracting the sample thermal data with the blank thermal data.

### 3.3.2 Powder X-ray diffraction

Zeolite monoliths (Samples no. 4, 16, 22 and 28) were crushed into fine powder prior to analysis. Each powder sample of the zeolites, bentonites or zeolite monoliths was placed on a silicon sample cup and mounted onto the sample stage. The sample was then examined using a diffractometer with copper radiation (Cu Kα) as a source of X-rays at 21 °C in atmospheric pressure. All powder samples were analysed with a scan step size of 0.016° and scan angles from 3° to 60°. The diffracted X-rays were detected and recorded on a computer. The intensities of the diffracted X-rays were plotted as a function of their angular positions.

### 3.3.3 Mercury intrusion porosimetry

A sample of zeolite either in the forms of beads, granules or monoliths (Samples no. 2, 4, 10, 12, 18, 20, 23 and 26) was loaded into a glass penetrometer. The loaded penetrometer was then installed onto the low pressure port of the mercury penetrometer to evacuate gases from the sample. After the low pressure (0 bar to 3.45 bar) data was collected, they were transferred to the high pressure port where mercury was forced into

the evacuated sample pores with hydraulic pressure up to about 4 137 bar. A blank test was also carried out using an empty penetrometer and the result was provided in Appendix 1. All MIP data presented in the thesis have been automatically corrected by the machine with the blank test result. Using the data collected from this analysis, important pore properties of the sample such as total pore surface area, mean pore diameter, porosity, bulk density and pore size distribution could be obtained.

For example, the pore diameter $d_{pore}$ (mm) of the solid sample was determined using the Washburn equation (Washburn, 1921) by assuming the pores are cylindrical:

$$d_{pore} = \frac{4\,\gamma \cos\varphi}{P} \tag{3.1}$$

where $\gamma$ is the surface tension of mercury (= 485 mN m$^{-1}$), $\varphi$ is the contact angle between the solid and mercury (= 130°) and $P$ is the applied pressure (Pa). Then, the total pore surface area $S_{pore,t}$ (mm$^2$) of the sample could be estimated using the equation derived by Rootare and Prenzlow (1967):

$$S_{pore,t} = -\frac{1}{\gamma\,\cos\varphi}\int_{0}^{V_{pore,t}} P\,dV \tag{3.2}$$

where $V_{pore,t}$ is the total pore volume (mm$^3$) or the total intruded volume of mercury at the highest pressure.

In addition, the mean pore diameter $d_{mean}$ (mm) of the sample could be calculated using the relation suggested by Liabastre and Orr (1978) with the assumption that the sample has cylindrical pores of length $L_{pore}$ with a pore volume of $V_{pore} = \frac{\pi(d_{mean})^2 L_{pore}}{4}$ and a pore surface area of $S_{pore} = \pi d_{mean} L_{pore}$:

$$d_{mean} = \frac{4V_{pore}}{S_{pore}} \tag{3.3}$$

### 3.3.4 Scanning electron microscopy

The samples of zeolites in the forms of powders, beads, granules and monoliths (Samples no. 2, 5, 7, 13, 15, 16, 21, 22, 27 and 28) and bentonite powders were attached individually at different locations on the stainless steel sample holder using carbon adhesive. They were kept in a vacuum desiccator overnight to evacuate gases from the samples. All samples were coated with a thin layer of gold using an Edwards sputter

coater to produce electrically conductive surfaces on the samples that would deflect the electron beam.

For the SEM experiments, the sample holder containing the gold-coated samples was mounted onto the sample stage in a small vacuum chamber at room temperature. Then, a beam of electrons was projected to the surfaces of the samples. The deflected electrons were detected by an electron sensor to form images of the surface of the samples, which were viewed using an electron microscope. The scanning electron micrographs of the samples were recorded on a computer.

### 3.3.5 Mechanical compression tests

A sample of zeolite either in the forms of beads, granules or monoliths (Samples no. 1 to 12, 14, 17 to 19 and 21 to 27) of length between 1.5 cm and 7.0 cm was tested using an Instron universal tester by applying radial and axial compressions on the sample until they fail. The mechanical compression tests were carried out with a compression rate of 0.5 mm $min^{-1}$ at 22 °C under atmospheric pressure. The orientation of the monolith samples on radial and axial compressive loadings is shown schematically in Figure 3.5. The applied compressive load on the sample and their deformation were recorded on a computer using a Bluehill software.

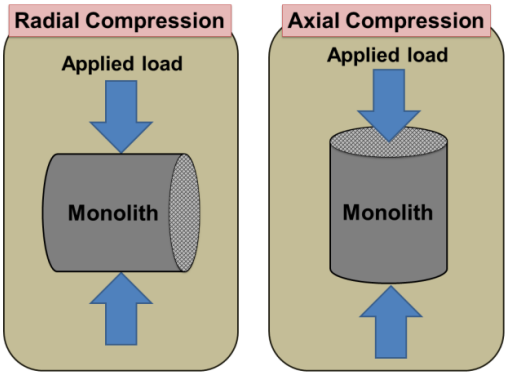


**Figure 3.5** Schematic diagram of the orientation of the monolith samples on radial and axial compressions.

From the recorded mechanical strength data, the compressive strength/stress $\sigma$ (Pa), compressive strain $\epsilon$ (m $m^{-1}$), and elastic modulus $E$ (Pa), of the sample could be determined using the Hooke's law equations, which are:

$$\sigma = \frac{F_c}{A} \tag{3.4}$$

$$\epsilon = \frac{\Delta l}{L_c} \tag{3.5}$$

$$E = \frac{\text{Stress}}{\text{Strain}} = \frac{\sigma}{\epsilon} \tag{3.6}$$

where $F_c$ is the applied compressive load (N), $A$ is the cross-sectional area of the sample ($m^2$), $\Delta l$ is the extension of the sample (m) and $L_c$ is the original length of the sample (m).

## 3.4 Results and Discussion for the Fabrication and Characterisation of Zeolite Monoliths

This section provides the results for the fabrication and characterisation of the zeolite monoliths prepared in this study and their discussion. The first part of this section (i.e., Section 3.4.1) covers the results and discussion for the fabrication of zeolite monoliths. The fabrication challenges encountered in this work are also included. The second part of this section (i.e., Section 3.4.2) covers the characterisation results of zeolite monoliths and the discussion of their physical properties in comparison to zeolite powders and beads/granules and bentonite powders.

### 3.4.1 Fabrication of zeolite monoliths

Monoliths of 13X, LiLSX and 5A zeolites and clinoptilolite with adsorbent content ranged between 65% wt. and 85% wt. of zeolites (Samples no. 1 to 28) were successfully fabricated according to the novel formulations described in this study. These zeolite monoliths have wall thicknesses of either 0.7 mm or 0.9 mm. As seen in Figure 3.6, 13X, LiLSX and 5A zeolite monoliths were white in colour and clinoptilolite monoliths were brown in colour.

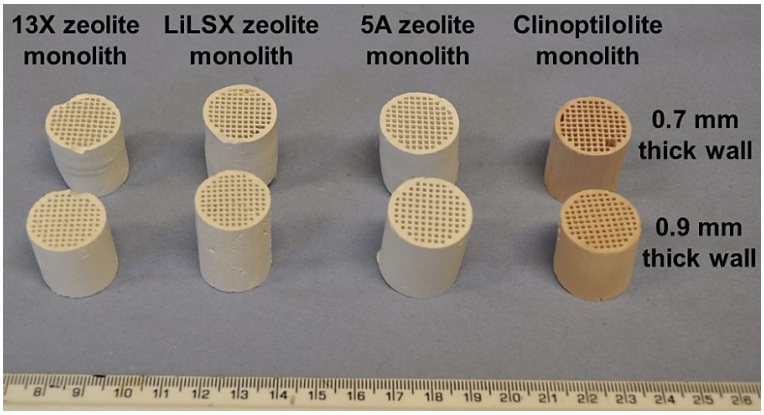


**Figure 3.6** Photograph of the manufactured 13X zeolite, LiLSX zeolite, 5A zeolite and clinoptilolite monoliths with 0.7 mm or 0.9 mm thick walls. Left to right: Samples no. 3, 10, 18 and 23.

Due to the different water adsorption capacities of both zeolites and bentonites, the adsorbent paste formulations described in this study required different amount of water depending on the types and amounts of zeolites and bentonites, as indicated in Table 3.2. The optimum ratios of water to dry powders (i.e., zeolites, bentonites and/or pore former) were discovered to be between 1.13 and 1.26 for 13X zeolite, between 1.25 and 1.44 for LiLSX zeolite, between 0.92 and 1.05 for 5A zeolite and between 0.80 and 0.90 for clinoptilolite paste formulations.

For the same type and amount of zeolite, adsorbent paste formulations that contain calcium bentonite were found to have 10% wt. less water compared to those containing Wyoming sodium bentonite. This was as a result of the strong positive charge of $Ca^{2+}$ that hold the framework structure of the bentonite more firmly, which limit the water adsorption capacity of the bentonite (Murray, 2012).

The main issues that occurred during the fabrication process are surface tearing, cracking and bending of the zeolite monoliths. As shown in Figure 3.7, both surface tearing and cracking of the zeolite monoliths could happen during extrusion as a consequence of poor cohesion and insufficient plasticity that prevent the adsorbent pastes from binding together after they were sheared by the extruder screw and the extruder die. To solve these fabrication issues, the water content of the adsorbent paste needs to be adjusted and the plasticity of the adsorbent paste needs to be improved.

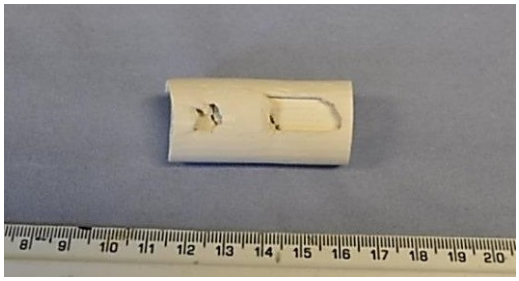

**Figure 3.7** Photograph of a 5A zeolite monolith (Sample no. 19) showing the occurrence of surface tearing and cracking during extrusion.

Additionally, cracking could occur during drying if there were rapid evaporation of water molecules from the surface of the green zeolite monoliths, as demonstrated in Figure 3.8. So, it was important to keep the tray of green zeolite monoliths in a chamber of controlled temperature and humidity instantaneously after the extrusion to slow down the evaporation of water molecules.

**Figure 3.8** Photograph of a 5A zeolite monolith (Sample no. 17) showing the formation of cracks during drying.

During drying, bending of the zeolite monoliths could also arise as a result of uneven evaporation of water molecules from the surface of the green zeolite monoliths that leads to irregular stress on the green zeolite monoliths, as shown in Figure 3.9. To overcome this issue, it was necessary to make sure that the tray of green zeolite monoliths was placed in an unobstructed area inside the temperature and humidity controlled chamber so that the moisture gradient and evaporation rate of the water molecules is almost the same along the green zeolite monoliths. This would even out the stress induce on the green zeolite monoliths.

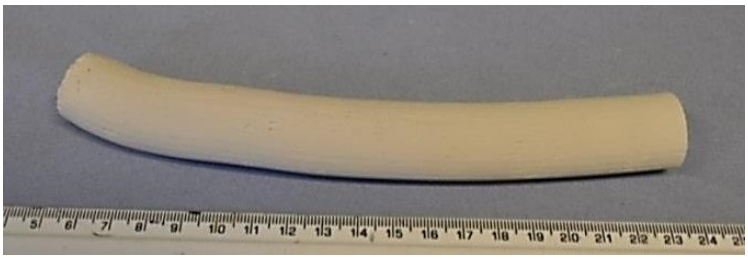

**Figure 3.9** Photograph of a bent 5A zeolite monolith (Sample no. 18) during drying.

### 3.4.2 Characterisation of zeolite monoliths and materials

As mentioned previously, this section covers the results and discussion for the characterisation of zeolite monoliths and some selected materials such zeolite powders, beads/granules and bentonite powders. This includes the analyses on their thermal properties, crystal structures, pore properties, morphologies and mechanical compressive strengths, which are provided and discussed individually in Sections 3.4.2.1 to 3.4.2.5.

#### 3.4.2.1 Thermal properties of zeolites and bentonites

First, the thermal properties of selected zeolites and bentonites were investigated. The TG and DSC curves of the studied zeolites presented in Figure 3.10 showed the changes in weight and heat flow as the zeolites were heated at elevated temperatures.

These thermal data were used to evaluate the weight loss (that is equivalent to their water content) and thermal stabilities of the zeolites.

Figure 3.10 (a) shows the TG and DSC curves of 13X zeolite powder. The TG curve indicated that there was a weight loss (or water content) of about 21% until 500 °C as water molecules was removed from the heated 13X zeolite. This weight loss is similar to that found by Mishra (2007). In the DSC curve, the endothermic peak that was resulted from dehydration was seen at 100 °C to 400 °C and the exothermic peak that was resulted from recrystallization was seen at 400 °C to 700 °C. Knowing the amount of weight loss, the unknown stoichiometry of the dehydration reaction for 13X zeolite can be determined. The equation of the dehydration reaction for 13X zeolite is provided in equation 3.4. The sharp exothermic peak observed at temperature above 800 °C in the DSC curve represents the structural collapse of 13X zeolite crystals and this is in agreement with the results reported by Li and Rees (1985). This means the crystal structure of the 13X zeolite was thermally stable at temperature below 800 °C.

$$Na_{86}[(AlO_2)_{86}(SiO_2)_{106}] \cdot 264H_2O \rightleftarrows Na_{86}[(AlO_2)_{86}(SiO_2)_{106}] \cdot 52H_2O + 212H_2O \qquad (3.7)$$

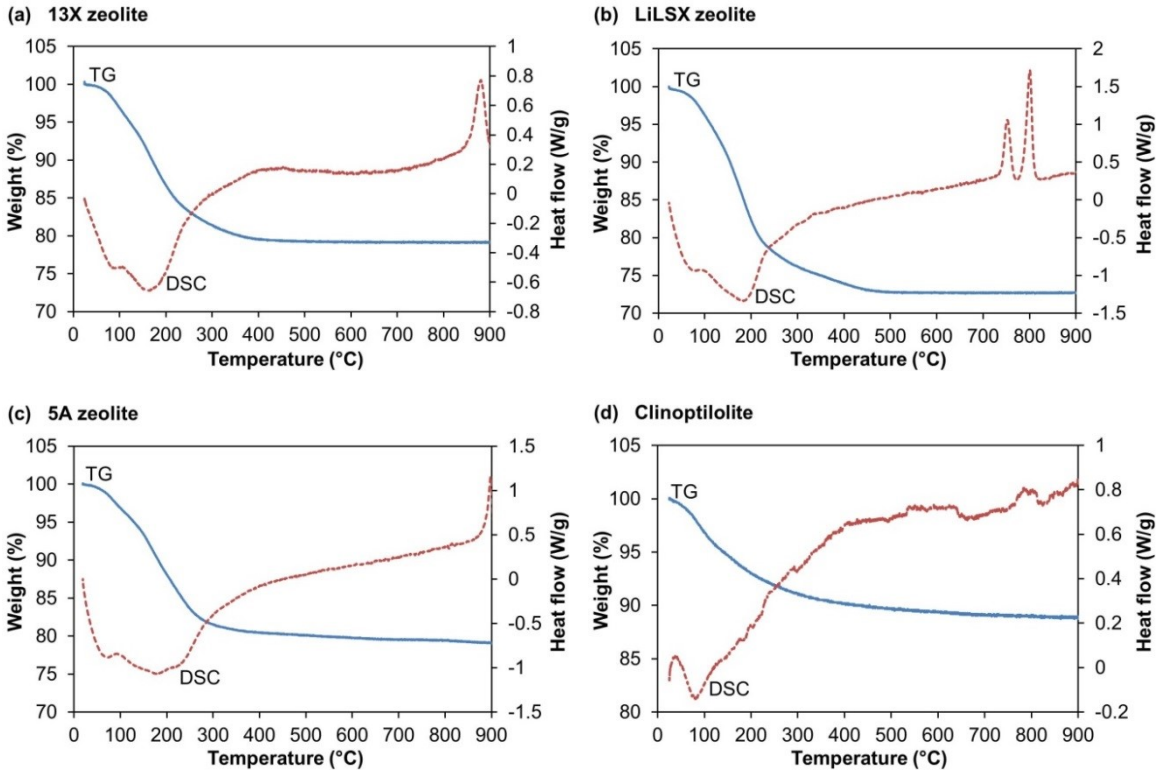


**Figure 3.10** The TG and DSC curves of the (a) 13X zeolite, (b) LiLSX zeolite, (c) 5A zeolite and (d) clinoptilolite powders.

In Figure 3.10 (b), the TG curve of the LiLSX zeolite shows that they have a weight loss (or water content) of about 27% until 500 °C as a consequence of dehydration when subjected to heat treatment. The thermal weight loss of LiLSX zeolite found in this study matches with that reported by Panezai *et al.* (2016). Using the weight loss, the unknown stoichiometric of the dehydration reaction for LiLSX zeolite can be determined and the equation of the dehydration reaction was given in equation 3.5. The dehydration of LiLSX zeolite was represented by the endothermic peak of its DSC curve at 100 °C to 500 °C. The exothermic peak resulted from recrystallization was observed at 500 °C to 770 °C and the exothermic peak resulted from structural collapse was observed at 770 °C to 820 °C. This implies that the structure of LiLSX zeolite crystals was thermally stable at temperature below 770 °C.

$$\mathrm{Li_{96}[(AlO_2)_{96}(SiO_2)_{96}]\cdot 250H_2O \rightleftarrows Li_{96}[(AlO_2)_{96}(SiO_2)_{96}]\cdot H_2O + 249H_2O} \quad (3.8)$$

The TG and DSC curves of the 5A zeolite are given in Figure 3.10 (c). Its TG curve demonstrated that they have a weight loss (or water content) of about 21% up to 500 °C upon heating as a result of dehydration. This thermal weight loss of 5A zeolite is close to that reported by Li (1998), which found that 5A zeolite has a weight loss of about 18%. Equation 3.6 shows the dehydration reaction for 5A zeolite that was determined from the thermal weight loss found in this study. In the DSC curve, the endothermic peak observed at 100 °C to 500 °C was due to dehydration while the exothermic peak at temperature above 800 °C was due to structural collapse of 5A zeolite crystals. This indicates that the crystal structure of the 5A zeolite was thermally stable at temperature below 800 °C.

$$\mathrm{Ca_3Na_2[(AlO_2)_{12}(SiO_2)_{12}]\cdot 27H_2O \rightleftarrows Ca_3Na_2[(AlO_2)_{12}(SiO_2)_{12}]\cdot 3H_2O + 24H_2O} \quad (3.9)$$

Additionally, the TG curve of the clinoptilolite in Figure 3.10 (d) reveals that they have a weight loss (or water content) of about 11% up to 500 °C due to dehydration, which is represented by the endothermic peak in their DSC curve at 60 °C to 500 °C. The thermal weight loss found in this study for clinoptilolite is close to that reported by Mansouri *et al.* (2013), which claimed that clinoptilolite has a weight loss of about 14%. The equation of the dehydration reaction for clinoptilolite was provided in equation 3.7 and it was determined using the thermal weight loss found in this study. The exothermic peaks at 500 °C to 820 °C were caused by recrystallization and the exothermic peak at temperature above 820 °C was caused by the structural collapse of clinoptilolite crystals. This denotes that the crystal structure of the clinoptilolite was thermally stable at temperature below 820 °C. The thermal data of clinoptilolite found in this study was about

the same as that reported by Cruciani (2006), which claimed that major dehydration occurs around 30 °C to 230 °C and the structural collapse occurs at about 920 °C.

$$(Na, K)_6[(AlO_2)_6(SiO_2)_{30}] \cdot 24H_2O \rightleftarrows (Na, K)_6[(AlO_2)_6(SiO_2)_{30}] \cdot 6H_2O + 18H_2O \quad (3.10)$$

The thermal data of the studied zeolites described above confirmed that the structure of these zeolites has high thermal stabilities and their crystal structures would not collapse when heated at the chosen temperature of 400 °C or 650 °C in the firing process. The thermal properties of the selected bentonites were also analysed in this study. Their TG and DSC curves are provided in Figure 3.11.

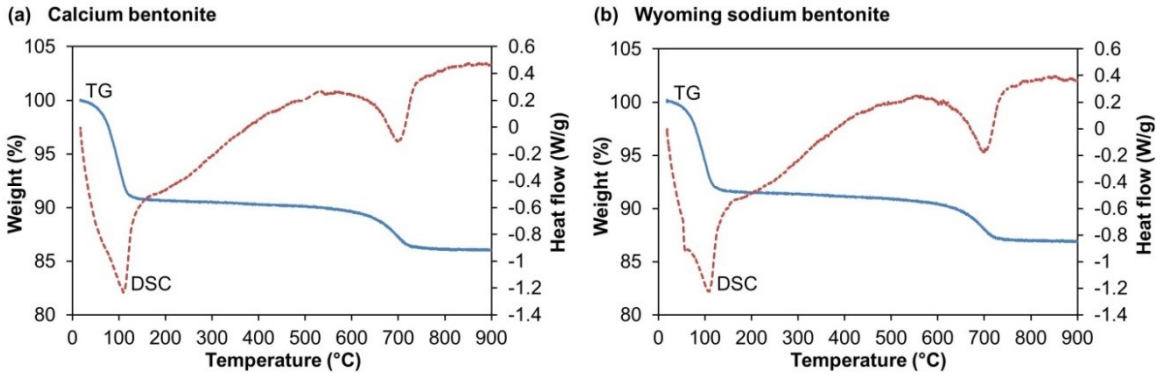


**Figure 3.11** The TG and DSC curves of the (a) calcium bentonite and (b) Wyoming sodium bentonite powders.

The TG curve of the calcium bentonite in Figure 3.11 (a) demonstrates that it has an initial weight loss of about 10% up to 500 °C due to dehydration and a second weight loss of about 4% at 500 °C to 800 °C due to dehydroxylation. The dehydration of the calcium bentonite was indicated by the endothermic peak in its DSC curve at 80 °C to 400 °C and their recrystallization was indicated by the exothermic peak at 400 °C to 600 °C. The endothermic peak at 600 °C to 800 °C was resulted from the dehydroxylation while the exothermic peak at 800 °C to 900 °C was resulted from recrystallization. According to Sarikaya *et al.* (2000), the crystal structure of calcium bentonite would collapse and recrystallize at 920 °C to 1050 °C so an exothermic peak was expected at these temperature range in its DSC curve.

Similar thermal behaviour was also exhibited by the Wyoming sodium bentonite, as presented in Figure 3.11 (b). Its TG curve revealed that they have an initial weight loss of about 9% until 400 °C as a result of dehydration and a second weight loss of about 4% at 400 °C to 800 °C as a result of dehydroxylation. The endothermic peak in their DSC curve that was caused by dehydration was observed at 80 °C to 400 °C and the exothermic

peak that was caused by recrystallization was observed at 400 °C to 600 °C. The endothermic peak at 600 °C to 800 °C was resulted from dehydroxylation whereas the exothermic peak at 800 °C to 900 °C was resulted from recrystallization. Due to the temperature limitation of the equipment, the exothermic peak resulted from the structural collapse of the Wyoming sodium bentonite was not seen in its DSC curve. But, the thermal stability of the Wyoming sodium bentonite was expected to be above 900 °C (Inglethorpe *et al.*; 1993).

The thermal data of the selected bentonites described above verified that the structure of these bentonites have high thermal stabilities and their crystal structures would not collapse when heated during the firing process at the chosen temperature of 400 °C or 650 °C.

#### 3.4.2.2 Crystal structures of zeolites and bentonites in pure powders and those in zeolite monoliths

In addition to the thermal analyses described in the previous section, the PXRD patterns of the studied zeolites and bentonites were compared with the zeolite monoliths prepared in this study. This was to validate that there was no structural collapse taking place in the firing process. All the tested zeolite monoliths contain 4% wt. Licowax C micropowder PM (a pore former) in their paste formulations and they have been fired at 400 °C or 650 °C.

The PXRD patterns of 13X zeolite monoliths in Figure 3.12 (a) show that they have the same peak positions as 13X zeolite and calcium bentonite powders. This means the crystal structures of both 13X zeolite and calcium bentonite were still maintained in the monoliths even after they were fired at 400 °C or 650 °C. Similarly, the PXRD patterns in Figures 3.12 (b) to (d) also demonstrate that the peak positions of LiLSX zeolite, 5A zeolite and clinoptilolite monoliths were the same as their respective zeolite powders and Wyoming sodium bentonite powder. This suggests that the original crystal structures of LiLSX zeolite, 5A zeolite, clinoptilolite and Wyoming sodium bentonite were retained in the monoliths when they were fired at 400 °C. The PXRD patterns of the tested zeolites and bentonites powders obtained in this study are similar to those reported in the literature, for examples, Mishra (2004) for 13X zeolite, Panezai *et al.* (2016) for LiLSX zeolite, Li (1998) for 5A zeolite, Mansouri *et al.* (2013) for clinoptilolite, Sarikaya *et al.* (2000) for calcium bentonite and Inglethorpe *et al.* (1993) for Wyoming sodium bentonite.

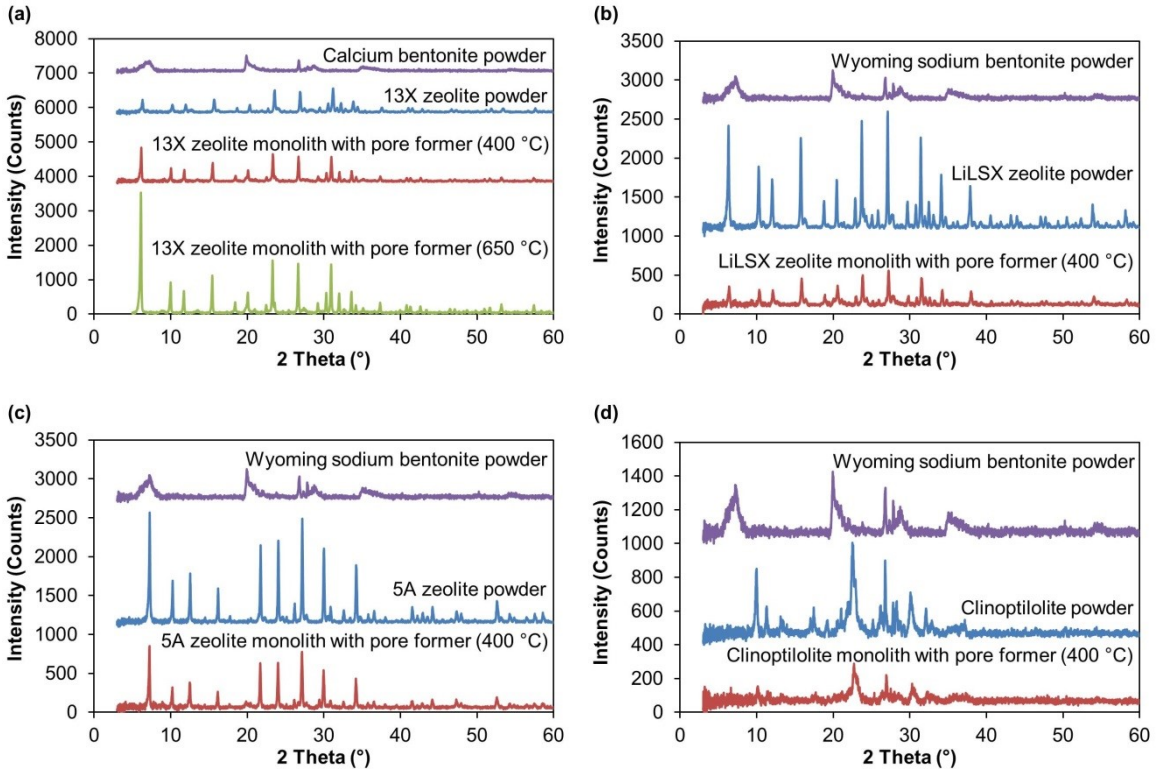


**Figure 3.12** The PXRD patterns of (a) 13X zeolite, (b) LiLSX zeolite, (c) 5A zeolite and (d) clinoptilolite powders with their respective bentonites powders and zeolite monoliths after been fired at 400 °C or 650 °C.

### 3.4.2.3 Pore properties of zeolite monoliths and beads/granules

The results and discussion of the MIP tests are cover in this section. The pore structures of the prepared zeolite monoliths (either with or without the inclusion of 4% wt. Licowax C micropowder PM as a pore former in their paste formulations) were analysed and compared with commercial zeolites that were either in the forms of beads or granules. Their pore properties such as total pore volume, total pore surface area, mean pore diameter, porosity and bulk density that are obtained using MIP are provided in Table 3.4. The data in Table 3.4 has experimental errors of about ± 0.027 mL $g^{-1}$ to 0.055 mL $g^{-1}$ for total pore volume, ± 8.6 $m^2$ $g^{-1}$ to 13.1 $m^2$ $g^{-1}$ for total pore surface area, ± 61.8 nm to 110.0 nm for mean pore diameter, ± 12.2% to 16.9% for porosity and ± 0.15 g $mL^{-1}$ to 0.54 g $mL^{-1}$ for bulk density.

The results in Table 3.4 show that the prepared zeolite monoliths have larger total pore volumes than the commercial zeolite beads/granules. This means the monolithic structure developed in this study have large storage capacities for adsorbate gas contaminants such as $CO_2$, $H_2O$ vapour and $H_2S$ compared to the beaded or granular structures. The total pore volumes of the prepared zeolite monoliths were found to be larger by about 63% for 13X zeolite, 46% for LiLSX zeolite, 76% for 5A zeolite and 33% for clinoptilolite when compared to their commercial zeolite beads/granules.

Although the prepared monoliths of 13X, LiLSX and 5A zeolites have larger pore volumes than their commercial zeolite beads, their total pore surface areas were lower than those in the commercial zeolite beads, as shown in Table 3.4. The reason for this was because of the variation in the arrangement of zeolite and bentonite crystals within the monolithic structure. In this study, the total pore surface areas of these zeolite monoliths were found to be lower by about 28% for 13X zeolite, 14% for LiLSX zeolite and 77% for 5A zeolite when compared with their respective zeolite beads. This indicates that the exposure of adsorption sites to adsorbate gas contaminants in the monolithic structure was lesser than that in the beaded structures.

Considering that the prepared monoliths of 13X, LiLSX and 5A zeolites have larger mean pore diameters than their commercial beads, their low total pore surface areas could be compensated. Their large mean pore diameter implies that adsorbate gas contaminants such as $CO_2$, $H_2O$ vapour and $H_2S$ could penetrate the pores and adsorb onto the adsorption sites at a faster rate. The results in Table 3.4 reveal that the mean pore diameters of these zeolite monoliths were larger by about 2.3 times for 13X zeolite, 1.9 times for LiLSX zeolite and 7.5 times for 5A zeolite compared to their commercial zeolite beads. Similar trend was also indicated by Li (1998), which reported that monoliths possess lower total pore surface area and larger mean pore diameter than commercial pellets.

Unlike monoliths of 13X, LiLSX and 5A zeolites, the prepared clinoptilolite monoliths have larger total pore surface areas (by about 38%) with slightly smaller mean pore diameters (by about 3%) than the commercial clinoptilolite granules, as demonstrated in Table 3.4. This suggests that more adsorption sites could be exposed for capturing adsorbate gas contaminants in the clinoptilolite monolithic structure compared to the granular structure with no major difference in their mass transfer or diffusion rates through the pores.

The total pore volumes of the structured zeolites (either in the forms of monoliths, beads or granules) are related to the porosities of their structures. Structured zeolites with large total pore volumes would have high structural porosities and vice versa. Since the prepared zeolite monoliths have larger total pore volumes than the commercial zeolite beads/granules, their porosities in the monolithic structure are higher than those in the beaded or granular structures, as shown in Table 3.4.

Their results indicate that the porosities of the prepared zeolite monoliths were higher by about 37% for 13X zeolite, 27% for LiLSX zeolite, 44% for 5A zeolite and 18% for clinoptilolite compared to their respective zeolite beads/granules. This implies that the novel monolithic structure developed in this study has a wider pore network for adsorbate gas contaminants such as $CO_2$, $H_2O$ vapour and $H_2S$ to diffuse into the zeolite crystals and adsorb onto the adsorption sites located at the surface of the pores as well as those inside the pores compared to the pore networks in the beaded or granular structures. The pore properties of monoliths found in this study show similar trend as that reported by Li (1998), which stated that monoliths possess higher total pore volume and porosity than commercial pellets.

The effect of incorporating a decomposable pore former (such as Licowax C micropowder PM) in the paste formulations of zeolite monoliths on their pore structures was also investigated in this work. The results in Table 3.4 show that the pore properties of the zeolite monoliths that have included a pore former in their paste formulations were improved compared to those without the inclusion of pore former. This was due to the formation of macropores within the monolithic structures when the pore former was decomposed upon heating.

For example, the inclusion of 4% wt. Licowax C micropowder PM in the paste formulations of zeolite monoliths was discovered to increase their total pore volumes slightly by about 11% for 13X zeolite, 16% for LiLSX zeolite, 10% for 5A zeolite and 19% for clinoptilolite. This means that monolithic structures could store more adsorbate gas contaminants. The total pore surface areas of zeolite monoliths were also increased by about 18% for 13X zeolite, 98% for LiLSX zeolite, 4% for 5A zeolite and 18% for clinoptilolite when 4% wt. Licowax C micropowder PM was added to their paste formulations. This implies that more adsorption sites could be exposed for capturing adsorbate gas contaminants such as $CO_2$, $H_2O$ vapour and $H_2S$ from the biogas stream.

Due to the difference in the arrangement of zeolite and bentonite crystals within the monolithic structure, the mean pore diameters of zeolite monoliths that have included a pore former in their paste formulations could be smaller or larger than those without any addition of the pore former. The results in Table 3.4 show that the mean pore diameters of the prepared zeolite monoliths with 4% wt. Licowax C micropowder PM in their paste formulations were smaller by about 5% for 13X zeolite and 42% for LiLSX zeolite but

larger by about 7% for 5A zeolite and 1% for clinoptilolite. Since the increment or reduction in their mean pore diameters was not very large, it was assumed that their influence on the mass transfer or diffusion rates of the adsorbate gas contaminants in the monoliths are negligible.

**Table 3.4** The pore properties of 13X zeolite, LiLSX zeolite, 5A zeolite and clinoptilolite beads/granules and monoliths.

| Materials (particle diameter/firing temperature; zeolite:Ca bentonite+Licowax C micropowder PM, in % wt.) | Total pore volume[a] (mL $g^{-1}$) | Total pore surface area[b] ($m^2$ $g^{-1}$) | Mean pore diameter[c] (nm) | Porosity[d] (%) | Bulk density[e] (g $mL^{-1}$) |
|---|---|---|---|---|---|
| **13X zeolite beads ($d_p$ = 1.6 mm – 2.5 mm)** | 0.272 | 21.9 | 49.7 | 35.7 | 1.31 |
| **13X zeolite monolith (400 °C; 75:25) – Sample no. 2** | 0.412 | 14.2 | 116.1 | 47.9 | 1.16 |
| **13X zeolite monolith with pore former (400 °C; 75:25+4) – Sample no. 4** | 0.464 | 15.7 | 118.0 | 50.8 | 1.10 |
| **13X zeolite monolith with pore former (650 °C; 75:25+4) – Sample no. 4** | 0.454 | 17.7 | 102.4 | 48.4 | 1.07 |
| **LiLSX zeolite beads ($d_p$ = 1.0 mm – 2.0 mm)** | 0.301 | 21.4 | 56.2 | 36.6 | 1.22 |
| **LiLSX zeolite monolith (400 °C; 70:30) – Sample no. 10** | 0.408 | 12.4 | 131.4 | 44.5 | 1.09 |
| **LiLSX zeolite monolith with pore former (400 °C; 70:30+4) – Sample no. 12** | 0.473 | 24.6 | 76.8 | 48.1 | 1.02 |
| **5A zeolite beads ($d_p$ = 4.0 mm)** | 0.290 | 32.3 | 35.9 | 34.7 | 1.20 |
| **5A zeolite monolith (400 °C; 80:20) – Sample no. 18** | 0.485 | 7.4 | 261.6 | 49.3 | 1.02 |
| **5A zeolite monolith with pore former (400 °C; 80:20+4) – Sample no. 20** | 0.535 | 7.7 | 278.9 | 50.9 | 0.95 |
| **Clinoptilolite granules ($d_p$ = 3.0 mm – 8.0 mm)** | 0.284 | 23.3 | 48.7 | 38.8 | 1.36 |
| **Clinoptilolite monolith (400 °C; 85:15) – Sample no. 23** | 0.344 | 29.4 | 46.8 | 43.4 | 1.26 |
| **Clinoptilolite monolith with pore former (400 °C; 85:15+4) – Sample no. 26** | 0.411 | 34.7 | 47.4 | 48.0 | 1.17 |

**Experimental errors:** [a] ± 0.027 mL $g^{-1}$ to 0.055 mL $g^{-1}$; [b] ± 8.6 $m^2$ $g^{-1}$ to 13.1 $m^2$ $g^{-1}$; [c] ± 61.8 nm to 110.0 nm; [d] ± 12.2% to 16.9% and [e] ± 0.15 g $mL^{-1}$ to 0.54 g $mL^{-1}$.

The formation of macropores in the monolithic structures after the thermal decomposition of the pore former improved the porosities of the zeolite monoliths. As indicated in Table 3.4, the porosities of the prepared zeolite monoliths that have included 4% wt. Licowax C micropowder PM in their paste formulations were slightly increased by

about 6% for 13X zeolite, 8% for LiLSX zeolite, 3% for 5A zeolite and 11% for clinoptilolite compared to those without any inclusion of the pore former. This means the mass transfer of adsorbate gas molecules within the monolithic structure could be enhanced by exposing more adsorption sites to capture contaminant gases such as $CO_2$, $H_2O$ vapour and $H_2S$ from the biogas stream.

Additionally, the effect of the firing temperature on the pore properties of the zeolite monoliths was tested in this study. Considering 13X zeolite monoliths that have included 4% wt. Licowax C micropowder PM as a pore former in their paste formulations as an example, the results in Table 3.4 demonstrate minor reductions in their total pore volumes (by about 2%) and mean pore diameters (by about 13%) when the firing temperature was raised from 400 °C to 650 °C. The reduction in their mean pore diameters was balanced by a small increment of about 13% in their total pore surface areas. The small reduction in their total pore volumes caused a slight decrease in their structural porosities, i.e., by about 5%. This indicates that some of the pores in the monolithic structure were covered by the bentonites, making them inaccessible for adsorbate gas contaminants such as $CO_2$, $H_2O$ vapour and $H_2S$ to enter and hence limiting the mass transfer between the adsorbate gas contaminants and the 13X zeolite.

From the MIP tests, the bulk densities of the samples were also obtained. The results in Table 3.4 show that the bulk densities of the prepared zeolite monoliths were almost the same as the commercial zeolite beads/granules. Since the zeolite monoliths prepared in this study only contain zeolites and bentonites, their bulk densities were slightly less dense than the commercial zeolite beads/granules, which often contain several types of clay and/or other additives apart from the zeolites. For example, this study found that the bulk densities of the zeolite monoliths were slightly lower by about 15% for 13X zeolite, 14% for LiLSX zeolite, 18% for 5A zeolite and 11% for clinoptilolite compared to their commercial zeolite beads/granules. Similar trend was also reported by Li (1998).

Next, the pore size distributions of the prepared zeolite monoliths were analysed and compared with the commercial zeolite beads/granules to evaluate the variation of the pore volumes with respect to their pore diameters. As seen on the pore size distributions in Figures 3.13 (a) to (c), the prepared monoliths of 13X, LiLSX and 5A zeolites have larger pore volumes than their commercial zeolite beads in the macropores (pore diameters > 50 nm) but not in the mesopores (pore diameters between 2 nm and 50 nm).

This means that adsorbate gas contaminants such as $CO_2$, $H_2O$ vapour and $H_2S$ in the biogas stream could be stored mostly in the macropores rather than in the mesopores for monoliths of 13X, LiLSX and 5A zeolites.

The collected pore data revealed that the pore volumes of 13X zeolite monoliths were about twice in the macropores and half in the mesopores compared to 13X zeolite beads. For LiLSX zeolite monoliths, their pore volumes were larger by about 1.7 times in the macropores and smaller by about 1.4 times in the mesopores than LiLSX zeolite beads. As for 5A zeolite monoliths, their pore volumes were about 2.8 times larger in the macropores and 7.9 times smaller in the mesopores compared to 5A zeolite beads. These results indicate that the adsorption of contaminant gases such as $CO_2$, $H_2O$ vapour and $H_2S$ on monoliths of 13X, LiLSX and 5A zeolites mainly takes place in the macropores unlike their commercial beads, which mainly takes place in the mesopores.

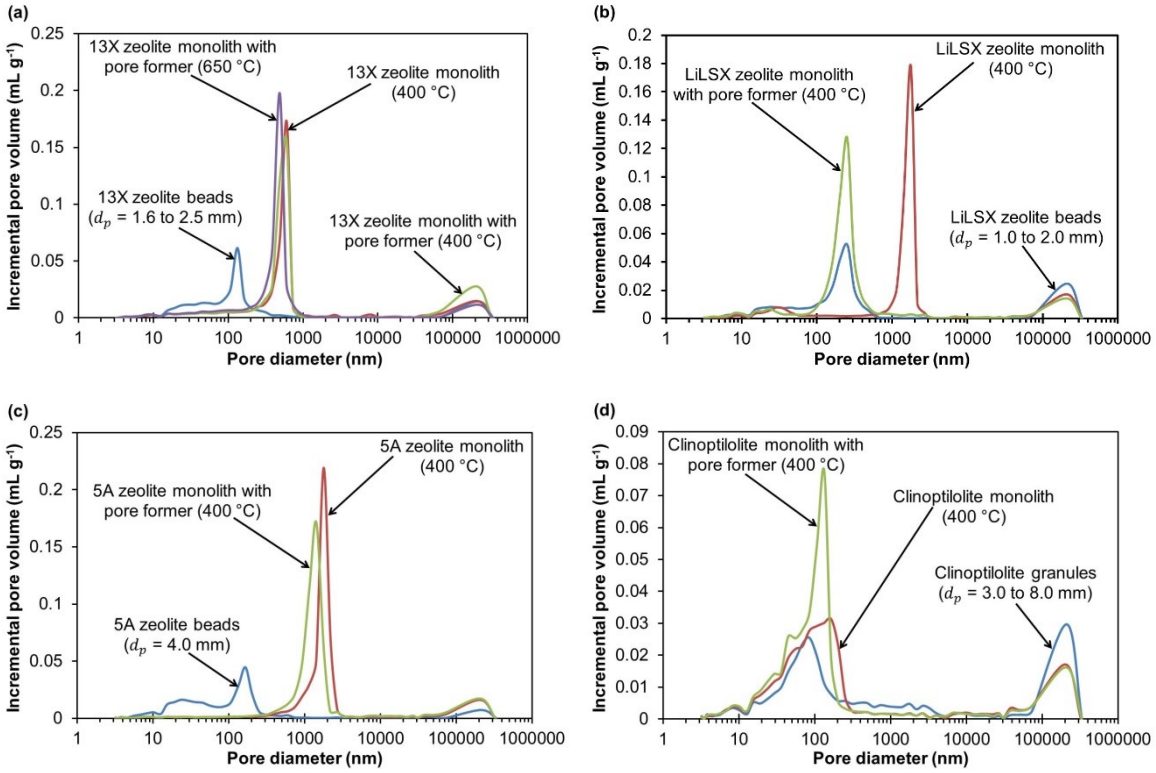


**Figure 3.13** The pore size distributions of (a) 13X zeolite, (b) LiLSX zeolite, (c) 5A zeolite and (d) clinoptilolite in the forms of beads, granules and monoliths.

The pore size distribution of LiLSX zeolite beads shown in Figure 3.13 (b) was about that same as that reported by Todd (2003), which used Zeochem LiLSX zeolite beads (diameter ~ 1.7 mm). It can be seen that the pore diameters of zeolite monoliths with and without pore former were generally in close range (as indicated by the first peak of the pore size distribution plot). However, the pore diameters of zeolite monoliths with and

without pore former could also be in different range, as indicated by Figure 3.13 (b). This was due to the random distribution of pore former in the monolith, which decomposed to create macropores of different sizes. The pore size distributions of 5A zeolite monoliths and beads in Figure 3.13 (c) agree well with the results reported by Li (1998).

Moreover, the pore size distribution in Figure 3.13 (d) show that the prepared clinoptilolite monoliths have larger pore volumes that the commercial clinoptilolite granules in both the macropores (by about 1.3 times) and mesopores (by about 1.4 times). This indicates that both the macropores and mesopores of clinoptilolite monoliths have higher storage capacities for adsorbate gas contaminants compared to those of clinoptilolite granules.

The influence of pore former on the pore volumes of the zeolite monoliths was also demonstrated by their pore size distributions, which are provided in Figures 3.13 (a) to (d). As observed in these pore size distributions, the pore volumes of the prepared zeolite monoliths were improved mainly in the macropores when Licowax C micropowder PM was included in their paste formulations as a pore former. In this case, the addition of 4% wt. Licowax C micropowder PM in the paste formulations of the zeolite monoliths was found to increase their pore volumes in the macropores by about 11% for 13X and 5A zeolites, 16% for LiLSX zeolite and 20% for clinoptilolite compared to those without the addition of the pore former. This clearly confirms the formation of macropores in the zeolite monolithic structure after the pore former was decomposed upon heating.

In addition, the influence of the firing temperature on the pore volumes of the zeolite monoliths was analysed from their pore size distributions. For example, the pore size distributions of 13X zeolite monoliths that contains 4% wt. Licowax C micropowder PM in their paste formulations shown in Figure 3.13 (a) indicate that their pore volumes were reduced in the macropores by about 3% but not in the mesopores (a small increment of about 11%) when their firing temperature was increased from 400 °C to 650 °C. This implies that the macropores tend to be covered by bentonites compared to the mesopores when 13X zeolite monoliths were fired at 650 °C.

#### 3.4.2.4 Morphologies of zeolites and bentonites in pure powders and those in zeolite monoliths and beads/granules

This section provides the SEM results of the chosen zeolites and bentonites powders, the fired zeolite monoliths and their commercial zeolite beads/granules. The

effects of firing temperature and pore former on the morphologies of the prepared zeolite monoliths are also investigated in this work. The observations on the scanning electron micrographs of the powdered calcium bentonite in Figure 3.14 (a) and Wyoming sodium bentonite in Figure 3.14 (b) show that they have non-homogeneous morphologies with particle sizes of about 5 μm to 150 μm. The morphology of Wyoming sodium bentonite obtained in this study was consistent with the SEM image reported by Li (1998).

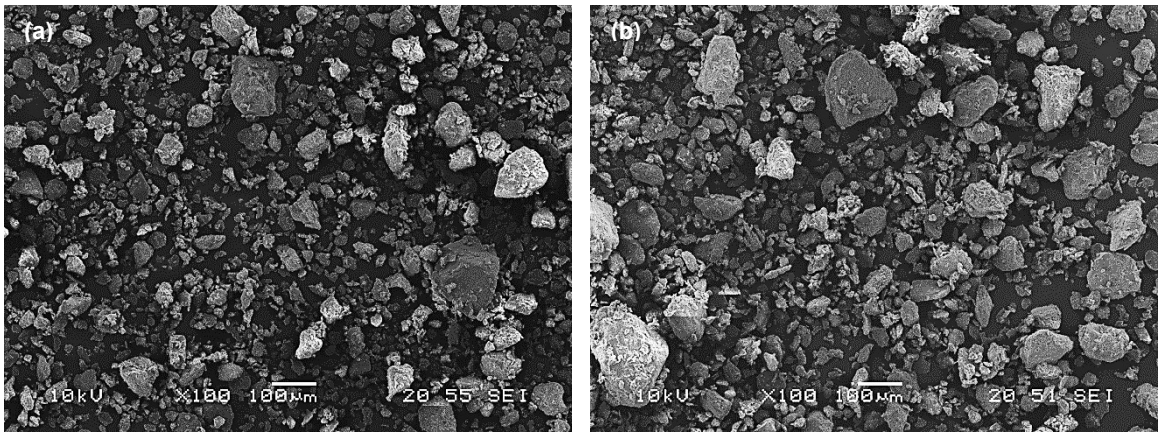


**Figure 3.14** The scanning electron micrographs of (a) calcium bentonite and (b) Wyoming sodium bentonite powders.

On the other hand, the scanning electron micrograph in Figure 3.15 (a) shows that 13X zeolite powder consists of cubical crystals with particle sizes ranging from 0.5 μm to 4.0 μm. The morphology of 13X zeolite crystals in Figure 3.15 (a) was the same as that reported by Akhtar and Bergström (2011). As seen in Figures 3.15 (b) and (c), the surface morphologies of the fired 13X zeolite monoliths comprises of cubical 13X zeolite crystals bounded by materials similar to calcium bentonite crystals. The crystal structures of both 13X zeolite and calcium bentonite seem to maintain their original crystalline forms even after been fired at 400 °C or 650 °C. This verifies that the selected firing temperatures for 13X zeolite monoliths were below the thermal stabilities of 13X zeolite and calcium bentonite. The morphologies of 13X zeolite monoliths (for example, Figure 3.15 (b)) appear to be the same as the morphology of 13X zeolite extrudates reported by Cavenati *et al.* (2004).

Similar surface morphology of the fired 13X zeolite monoliths was observed in Figure 3.15 (d) although they have slightly higher content of 13X zeolite and used Wyoming sodium bentonite as the binder. This indicates that a small increment of 5% wt. in the content of 13X zeolite and the change in the type of bentonite did not cause any difference on the surface morphology of the fired 13X zeolite monoliths. The surface morphologies of the fired 13X zeolite monoliths in Figures 3.15 (b) to (d) were compared

with that of the commercial 13X zeolite beads. Although there were differences in the type of binders and thermal treatments used in the production of these structured zeolites, the scanning electron micrograph of the commercial 13X zeolite beads in Figure 3.15 (e) shows very little difference in morphology compared to the fired 13X zeolite monoliths.

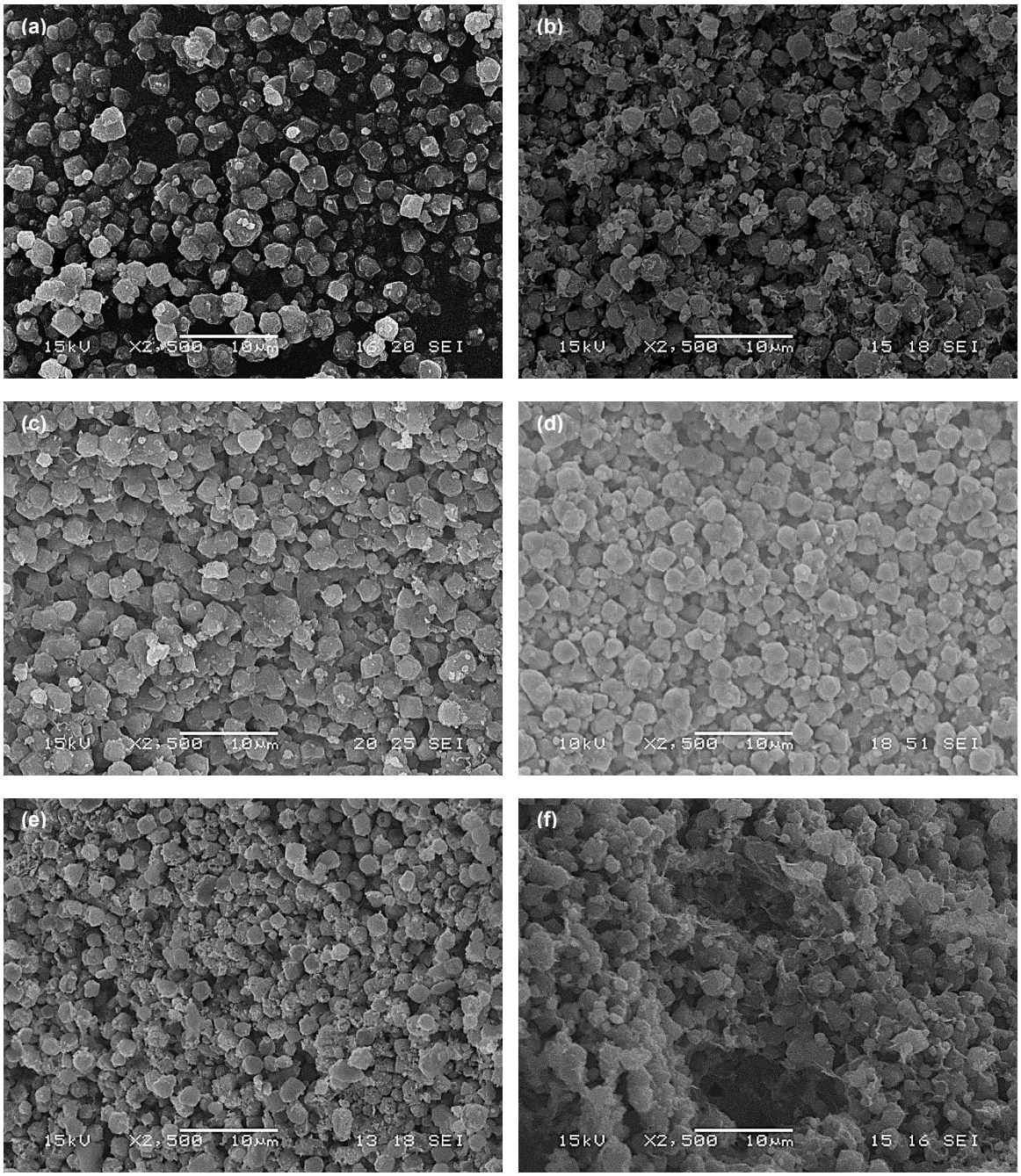


**Figure 3.15** The scanning electron micrographs of 13X zeolite (a) powder, (b) monolith after been fired at 400 °C [75% wt. 13X zeolite:25% wt. calcium bentonite], (c) monolith after been fired at 650 °C [75% wt. 13X zeolite:25% wt. calcium bentonite], (d) monolith after been fired at 650 °C [80% wt. 13X zeolite:20% wt. Wyoming sodium bentonite], (e) bead and (f) monolith with pore former after been fired at 650 °C [80% wt. 13X zeolite:20% wt. Wyoming sodium bentonite+4% wt. Licowax C micropowder PM].

The effect of including Licowax C micropowder PM as a pore former in the paste formulations of the 13X zeolite monoliths on their morphologies was also investigated in

this work. As observed in Figure 3.15 (f), some macropores were created on the surface of the fired 13X zeolite monoliths that have incorporated 4% wt. Licowax C micropowder in their paste formulations. This clearly confirms the formation of macropores in the 13X zeolite monolithic structure after the thermal decomposition of the pore former. The size of macropores shown in Figure 3.15 (f) was about 5 μm to 15 μm and these pore sizes were within the pore size distribution range of 13X zeolite monoliths with pore former, see Figure 3.13 (a). It was noticed that the macropores created in the monolithic structure are of slightly different sizes and this was mainly due to variation in the distribution of pore former in the monolith. By enhancing the macroporosity of the monolithic structure, more adsorption sites would be exposed for adsorbing gas contaminants such as $CO_2$, $H_2O$ vapour and $H_2S$ from the biogas stream. This would, in turn, improve the mass transfer in 13X zeolite monoliths.

For LiLSX zeolite, the scanning electron micrograph of its powder (Figure 3.16 (a)) shows that they consist of orthorhombical crystals with particle sizes ranging between 1 μm and 7 μm. The morphology of LiLSX zeolite powder in Figure 3.16 (a) matches with that reported by Kim (2003). The surface morphologies of the fired LiLSX zeolite monoliths show that the orthorhombical LiLSX zeolite crystals were interlinked with materials similar to Wyoming sodium bentonite crystals, as demonstrated in Figures 3.16 (b) and (c). The original crystal structures of both LiLSX zeolite and Wyoming sodium bentonite seem to be retained in the monoliths when they were fired at 400 °C or 650 °C. This proves that these firing temperatures were below the thermal stabilities of LiLSX zeolite and Wyoming sodium bentonite.

Figures 3.16 (b) and (c) also show that there was no difference in the surface morphologies of the fired LiLSX zeolite monoliths even though the adsorbent content was increased from 60% wt. to 80% wt. LiLSX zeolite. This implies that an increment of 20% wt. in the content of LiLSX zeolite was not large enough to change the surface morphologies of the fired LiLSX zeolite monoliths. The surface morphologies of the fired LiLSX zeolite monoliths were compared to the commercial LiLSX zeolite beads. The scanning electron micrograph of a commercial LiLSX zeolite bead in Figure 3.16 (d) shows some difference in morphology to the fired LiLSX zeolite monoliths. This was because of the different type of binder and firing conditions used in their production, which influence the binding and arrangement of LiLSX zeolite and Wyoming sodium bentonite crystals in monolithic and beaded structures.

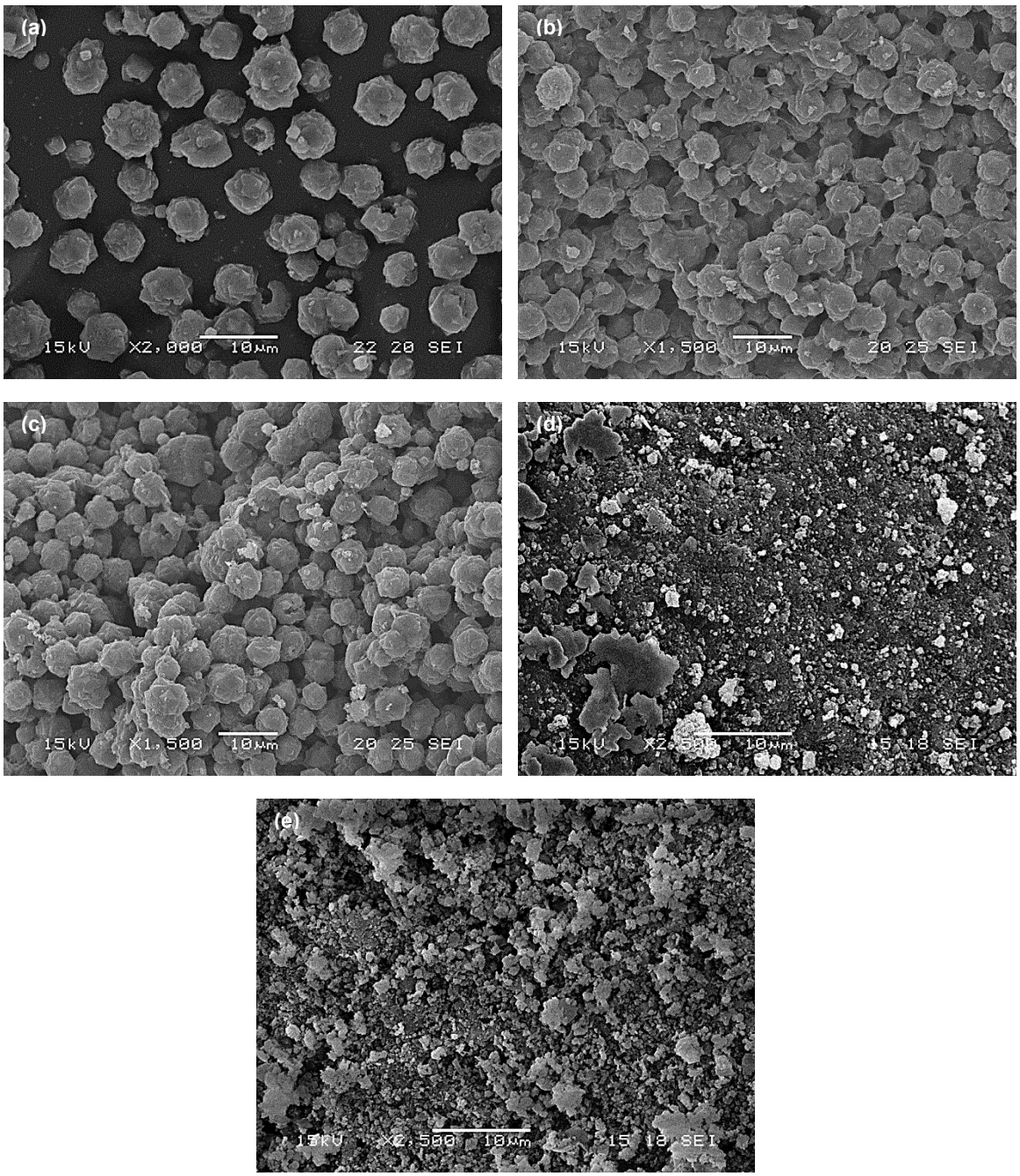


**Figure 3.16** The scanning electron micrographs of LiLSX zeolite (a) powder, (b) monolith after been fired at 400 °C [60% wt. LiLSX zeolite:40% wt. Wyoming sodium bentonite], (c) monolith after been fired at 650 °C [80% wt. LiLSX zeolite:20% wt. Wyoming sodium bentonite], (d) bead and (e) monolith with pore former after been fired at 650 °C [70% wt. LiLSX zeolite:30% wt. Wyoming sodium bentonite+4% wt. Licowax C micropowder PM].

The scanning electron micrograph of the fired LiLSX zeolite monoliths that have included 4% wt. Licowax C micropowder PM as a pore former in their paste formulations is given in Figure 3.16 (e). Some macropores were observed on their surface morphology and this validates the formation of macropores in the LiLSX zeolite monoliths after the burn out of the pore former. As a result of the random distribution of the pore former in LiLSX zeolite monoliths, macropores were created at random location within the monolithic structure and they were of variable sizes. The formation of additional

macroporosities in the LiLSX zeolite monolithic structure would improves the mass transfer between the adsorbate gas contaminants and the LiLSX zeolite since there was more adsorption sites exposed for adsorbing gas contaminants such as $CO_2$, $H_2O$ vapour and $H_2S$ from the biogas stream. The behaviour of Licowax C micropowder PM in this study was similar to that reported by Lee (1997), who used starch as a pore former to create a more open structure on the silicalite monolith.

Next, the scanning electron micrograph of the 5A zeolite powder was examined. As shown in Figure 3.17 (a), the 5A zeolite comprises of cubical crystals with particle sizes ranging from 0.5 μm to 6.0 μm. The surface morphologies of the fired 5A zeolite monoliths in Figures 3.17 (b) and (c) demonstrate that the cubical 5A zeolite crystals were surrounded by materials similar to Wyoming sodium bentonite crystals. There was no change in the crystal structures of 5A zeolite and Wyoming sodium bentonite when 5A zeolite monoliths were fired at 400 °C or 650 °C. This confirms that the selected firing temperatures of 5A zeolite monoliths were below the thermal stabilities of 5A zeolite and Wyoming sodium bentonite.

The scanning electron micrograph of the commercial 5A zeolite beads is also provided for comparison with the fired 5A zeolite monoliths. As seen in Figure 3.17 (d), the surface morphology of the commercial 5A zeolite beads is slightly different to the 5A zeolite monoliths prepared in this study. This was mainly because of the different type of binder and firing conditions used in their production that influence the binding and arrangement of 5A zeolite and Wyoming sodium bentonite crystals in monolithic and beaded structures. Several clusters of particles were observed in Figure 3.17 (d) and this was as a result of the binding between binder materials and 5A zeolite crystals. The morphologies of 5A zeolite powder, monoliths and beads shown in Figures 3.17 (a) to (d) were in good agreement with those reported by Li (1998).

The effect of including a pore former (such as Licowax C micropowder PM) on the morphologies of 5A zeolite monoliths was studied. The scanning electron micrograph in Figure 3.17 (e) shows that there were some macropores been created in the fired 5A zeolite monoliths that have included 4% wt. Licowax C micropowder PM in their paste formulations. This validates the formation of macropores in the 5A zeolite monolithic structure after the pore former was decomposed by heating. Similar to those observed in 13X zeolite and LiLSX zeolite monoliths, different sizes of macropores were created in 5A zeolite monoliths as a result of random distribution of the pore former within the structure.

By enhancing the macroporosities of 5A zeolite monoliths, the mass transfer in the monolithic structure could be improved as more adsorption sites were exposed to gas contaminants such as $CO_2$, $H_2O$ vapour and $H_2S$.

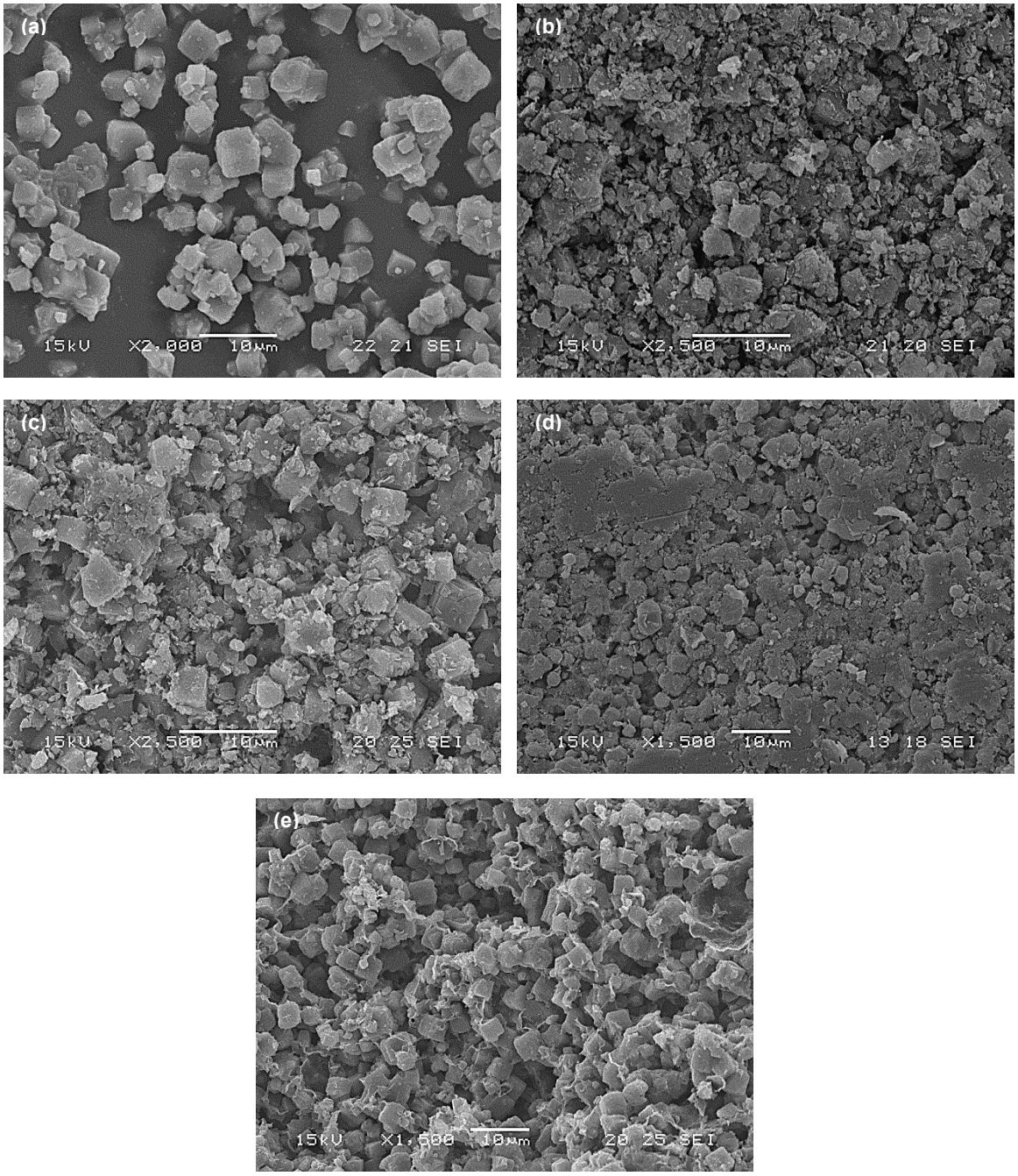


**Figure 3.17** The scanning electron micrographs of 5A zeolite (a) powder, (b) monolith after been fired at 400 °C [80% wt. 5A zeolite:20% wt. Wyoming sodium bentonite], (c) monolith after been fired at 650 °C [80% wt. 5A zeolite:20% wt. Wyoming sodium bentonite], (d) bead and (e) monolith with pore former after been fired at 650 °C [80% wt. 5A zeolite:20% wt. Wyoming sodium bentonite+4% wt. Licowax C micropowder PM].

Lastly, the morphology of clinoptilolite powder was examined. Its scanning electron micrograph in Figure 3.18 (a) shows that they consist of monoclinical crystals with particle sizes ranging from 5 µm to 50 µm. The SEM image of clinoptilolite powder obtained in this

study was similar to that reported by Verboekend *et al.* (2013). The surface morphologies of the fired clinoptilolite monoliths in Figures 3.18 (b) and (c) demonstrate that clinoptilolite crystals were bounded by materials similar to Wyoming sodium bentonite crystals. No change in crystal structures was seen after they were fired at 400 °C or 650 °C since these firing temperatures were below their thermal stability temperatures.

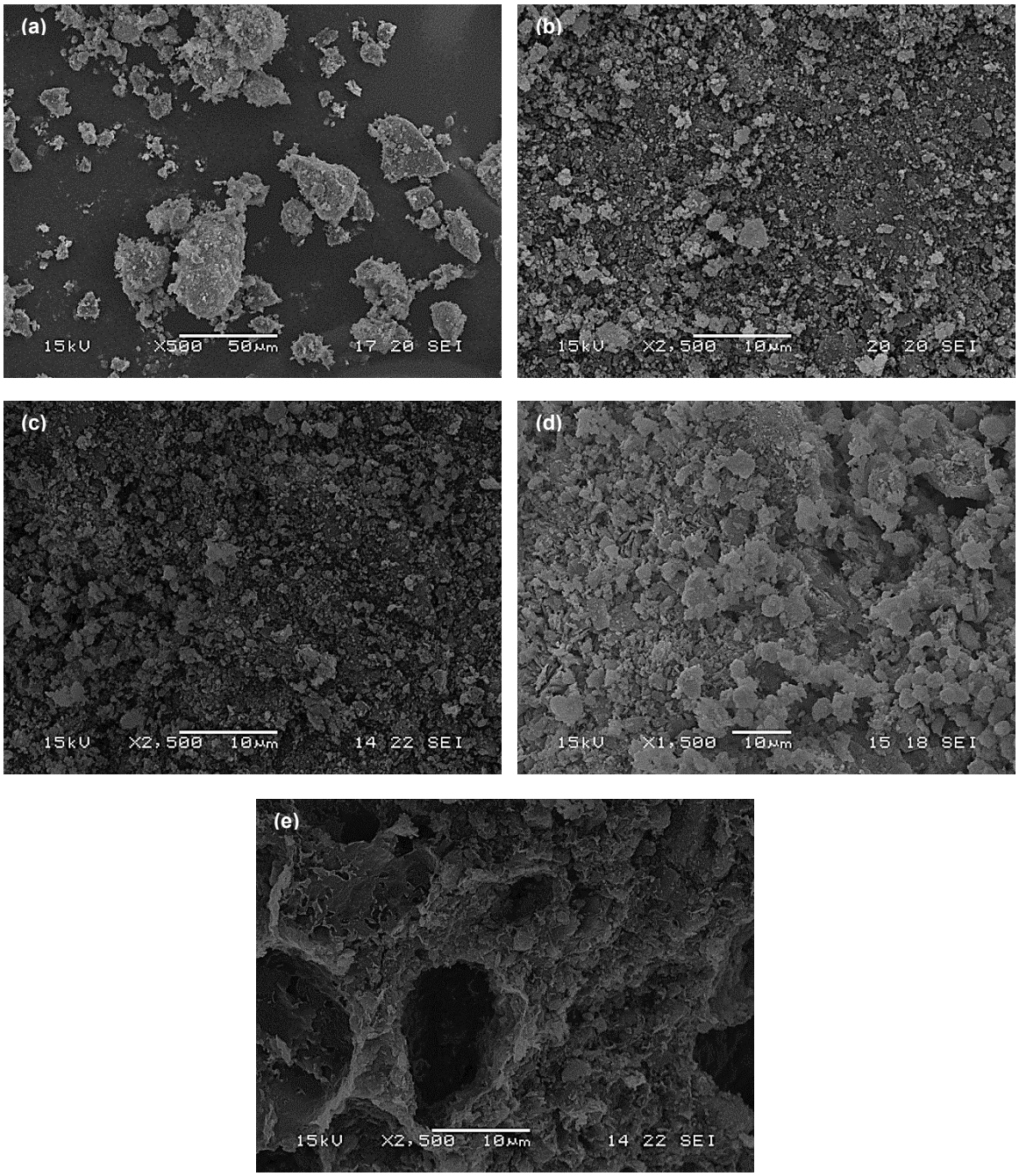


**Figure 3.18** The scanning electron micrographs of clinoptilolite (a) powder, (b) monolith after been fired at 400 °C [85% wt. clinoptilolite:15% wt. Wyoming sodium bentonite], (c) monolith after been fired at 650 °C [85% wt. clinoptilolite:15% wt. Wyoming sodium bentonite], (d) granule and (e) monolith with pore former after been fired at 650 °C [85% wt. clinoptilolite:15% wt. Wyoming sodium bentonite+4% wt. Licowax C micropowder PM].

The surface morphologies of the fired clinoptilolite monoliths were compared to the commercial clinoptilolite granules. Some difference was observed on the scanning electron micrograph of a commercial clinoptilolite granule in Figure 3.18 (d) when compared to the clinoptilolite monoliths prepared in this study. The reason for this was due to the different type of binder and firing conditions used in their production, which affect the binding and arrangement of clinoptilolite and Wyoming sodium bentonite crystals in monolithic and beaded structures. Some fracture was seen on the surface of the clinoptilolite granule and this was as a consequence of the shrinkage of binder materials after the firing process, according to Li (1998).

This study also investigates the effect of pore former on the morphologies of clinoptilolite monoliths. As revealed in Figure 3.18 (e), the surface morphology of the fired clinoptilolite monoliths that have included 4% wt. Licowax C micropowder PM as a pore former in their paste formulations shows that some macropores were created in the monolithic structure. This clearly confirms that the thermal decomposition of the pore former leads to the formation of macropores in clinoptilolite monoliths. As a result of the random distribution of pore former within the monolithic structure, macropores of different sizes were created. Clinoptilolite monoliths with enhanced macroporosities would allow more exposure of adsorption sites to capture contaminants such as $CO_2$, $H_2O$ vapour and $H_2S$ from the biogas stream. This means they would have improved mass transfer in the monolithic structure.

#### 3.4.2.5 Mechanical compressive strengths of zeolite monoliths and beads/granules

In the production of structured adsorbents (such as beads or granules), the mechanical strengths of commercial structured zeolites are often measure for quality control. This is because they need to be sufficiently strong to withstand bulk handling and friction in industrial vessels (Li, 1998). Due to this reason, the mechanical strengths of the prepared zeolite monoliths on either radial or axial compressive loadings were determined in this study and compared to the commercial zeolite beads/granules.

The effects of the types of zeolites and bentonites, content of bentonite (or zeolite to bentonite ratio), monolith wall thickness, firing temperature and content of the Licowax C micropowder PM (a pore former) on mechanical compressive strengths of the prepared zeolite monoliths were investigated. Their results are provided and discussed in this section. The mechanical compressive strengths of some commercial zeolite

beads/granules are also included in this work for comparative purposes. The mechanical compressive strength tests were repeated at least twice and experimental error in the compressive stresses obtained in this study was about 4% to 88%.

First, the mechanical (radial) compression tests were carried out on monoliths of 13X zeolite, LiLSX zeolite, 5A zeolite and clinoptilolite that have been fired at 400 °C. These zeolite monoliths contained 75% wt. adsorbent:25% wt. calcium bentonite and they have a wall thickness of 0.9 mm. As shown in Figure 3.19 (a), their radial compressive stresses vary with the type of zeolites, depending on the binding effect between the calcium bentonite and the zeolites as well as the water content of the green zeolite monoliths.

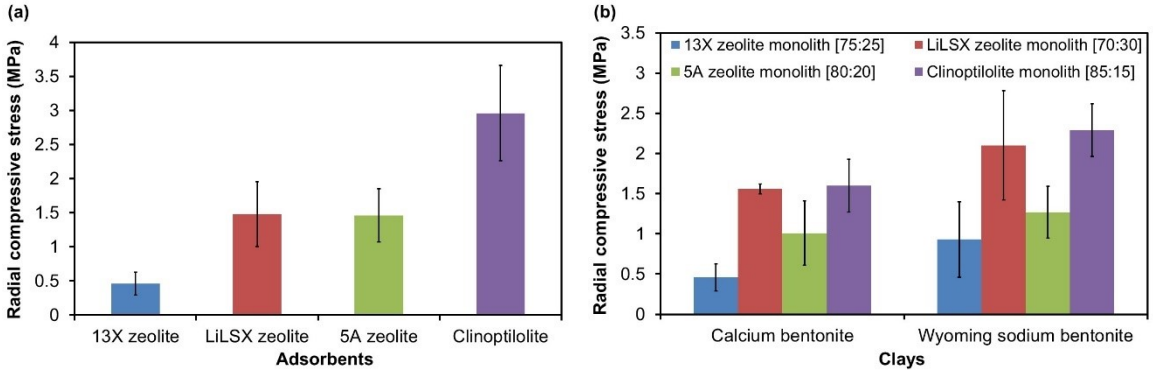


**Figure 3.19** The radial compressive stresses of zeolite monoliths that have been fired at 400 °C (a) with different type of zeolites [75% wt. adsorbent:25% wt. calcium bentonite] and those (b) with either calcium bentonite or Wyoming sodium bentonite as the binder. Note: Their paste compositions are denoted by [% wt. zeolite:% wt. bentonite] in the plots.

Mechanically strong zeolite monoliths could be produced if they have high binding effect and low water content. In this work, radial compressive strengths of the fired 75% wt. zeolite monoliths were discovered in order of (high to low): clinoptilolite, LiLSX zeolite, 5A zeolite and 13X zeolite. This indicates that the calcium bentonite binds more strongly with clinoptilolite, which has the lowest water content in the green clinoptilolite monoliths compared to 13X, LiLSX and 5A zeolites. In terms of elastic moduli, these fired 75% zeolite monoliths also demonstrate the same order as their radial compressive stresses. Experimentally, the fired 75% wt. zeolite monoliths were found to have elastic moduli of about 106.9 ± 1 MPa for 13X zeolite, 230.3 ± 3 MPa for LiLSX zeolite, 183.7 ± 2 MPa for 5A zeolite and 370.2 ± 4 MPa for clinoptilolite.

The relation between water content of the paste and mechanical strength of monoliths has been investigated by Forzatti *et al.* (1998) and their results showed similar

behaviour as this study. Their results indicate that a reduction in water content from 40% wt. to 30% wt. in their $TiO_2$-based ceramic pastes (containing 90% wt. tungsta/titania, ~ 6.5% wt. clays and 3.5% wt. glass fibres) increased the compressive strength of $TiO_2$-based ceramic monoliths by about 7 times (i.e., from 0.003 MPa to 0.02 MPa).

Second, the mechanical (radial) compression tests were carried out on the prepared zeolite monoliths that contained either calcium bentonite or Wyoming sodium bentonite as the binder. The tested zeolite monoliths have 0.9 mm thick walls and they have been fired at 400 °C. Each type of the zeolite monoliths (of the same adsorbent to clay ratio) was compared and their results are presented in Figure 3.19 (b). The results show that the radial compressive stresses of the prepared zeolite monoliths were increased by about twice for 13X zeolite, 1.3 times for LiLSX and 5A zeolites and 1.4 times for clinoptilolite when Wyoming sodium bentonite was used as a binder instead of the calcium bentonite.

These small improvements in the mechanical compressive strength of the zeolite monoliths were resulted from the difference in the ionic charges present in the framework structure of the bentonite, which affect the rate of dehydration in the firing process. For example, the strong positive charge of the $Ca^{2+}$ in the crystal structure of the calcium bentonite tends to hold water molecules more strongly at the interlayer of their structure compared to the positive charge of the $Na^{+}$ in the crystal structure of the Wyoming sodium bentonite. Due to the strong water retention in the crystal structure of calcium bentonite, the rate of dehydration was reduced and this caused less mechanical strength to be imparted to the monolithic structure during the firing process.

In contrast to the results obtained in this study, Sanabria *et al.* (2010) reported that the radial compressive stress of their Wyoming sodium bentonite extrudates (with water to bentonite ratio of 0.746) was slightly lower by about 7% than calcium bentonite extrudates (with water to bentonite ratio of 0.562), i.e., 4.1 MPa for Wyoming sodium bentonite extrudates and 4.4 MPa for calcium bentonite extrudates. Their bentonite extrudates have been fired at 400 °C and they were of 2 cm long and 2.5 mm in diameter. Since the difference in compressive strength between both types of bentonite extrudates was very small (same as this study), it can be considered that the types of bentonite have no major influence on the mechanical characteristics of the final product.

Third, the mechanical (radial) compression tests were carried out on the prepared zeolite monoliths containing different weight percentages of calcium bentonite (or

adsorbent to clay ratios). These zeolite monoliths have a wall thickness of 0.9 mm and they have been fired at 400 °C. The results in Figures 3.20 (a) to (d) demonstrate that the radial compressive stresses of 13X zeolite, LiLSX zeolite, 5A zeolite and clinoptilolite monoliths increase with increasing weight percentage of calcium bentonite. The reason for this was because the binding effect between the calcium bentonite and the zeolites are much stronger when the monolithic structure has a high content of bentonite as they would provide more mechanical stability to the fired zeolite monoliths.

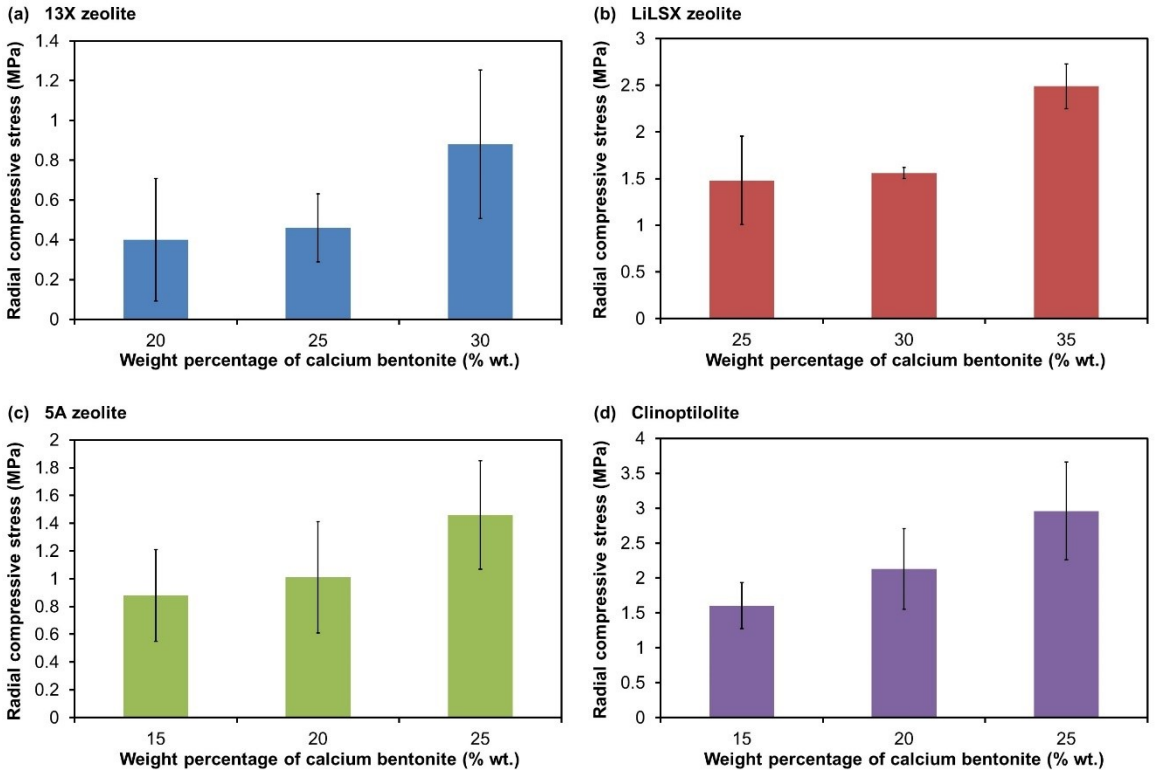


**Figure 3.20** The radial compressive stresses of (a) 13X zeolite, (b) LiLSX zeolite, (c) 5A zeolite and (d) clinoptilolite monoliths that been fired at 400 °C with different weight percentages of calcium bentonite.

For example, an increment of 20% wt. to 30% wt. of calcium bentonite was found to improve the radial compressive stresses of the fired 13X zeolite monoliths by about 2.2 times based on the results shown in Figure 3.20 (a). As for the fired LiLSX zeolite monoliths, their radial compressive stresses were found to increase by about 1.7 times when their bentonite content was increased from 25% wt. to 35% wt. calcium bentonite, as demonstrated in Figure 3.20 (b). The increment in radial compressive stresses of the fired 5A zeolite monoliths was the same as the fired LiLSX zeolite monoliths when their bentonite content was increased from 15% wt. to 25% wt. calcium bentonite, as indicated in Figure 3.20 (c).

With the same increment in bentonite content as 5A zeolite monoliths, the radial compressive stresses of the fired clinoptilolite monoliths was found to improve by about 1.9 times, as seen in Figure 3.20 (d). Similar behaviour has been reported by Lee (1997), who revealed that the compressive stress of square-channelled silicalite monoliths (with 1.25 mm wide channels and 0.59 mm thick walls) was increased by about 1.4 times (i.e., from 7.3 MPa to 10.0 MPa) when its bentonite content was increased from 15% wt. to 20% wt. sodium bentonite.

Next, the mechanical (radial) compression tests were carried out on zeolite monoliths of 0.7 mm or 0.9 mm thick walls that have been fired at 400 °C. Each type of the zeolite monoliths (of the same zeolite to bentonite ratio) was compared and their results are given in Figure 3.21 (a). The results demonstrate that the radial compressive stresses of the prepared zeolite monoliths increase with increasing monolith wall thickness. For example, the radial compressive stresses of the fired zeolite monoliths were discovered to be improved by about 1.4 times for 13X zeolite, 2.6 times for LiLSX zeolite, 1.8 times for 5A zeolite and 1.5 times for clinoptilolite when their monolith wall thickness was increased from 0.7 mm to 0.9 mm. This proved the fact that zeolite monoliths with thicker walls are mechanically stronger to withstand compressive loadings compared to those with thinner walls. Lee (1997) also observed the same trend, in which the compressive stress of its 80% wt. silicalite monoliths was increased by about 1.8 times (i.e., from 10.0 MPa to 17.6 MPa) when the monolith wall thickness was increased from 0.59 mm to 1.0 mm.

The effect of firing temperature on the mechanical strength of zeolite monoliths was investigated in this study. The mechanical (radial) compression tests were carried out on the prepared zeolite monoliths that have been fired at 400 °C or 650 °C. The tested zeolite monoliths have 0.9 mm thick walls and comparison was made for each type of zeolite monolith (of the same zeolite to calcium bentonite ratio). The results in Figure 3.21 (b) demonstrate that radial compressive stresses of the fired zeolite monoliths were improved by about 43% for 13X zeolite, 78% for LiLSX zeolite, 81% for 5A zeolite and 44% for clinoptilolite when their firing temperature was raised from 400 °C to 650 °C. This indicates that more mechanical strength could be imparted to the monolithic structure as the bentonite becomes more hardened at a higher firing temperature. According to Sanabria *et al.* (2010), the radial compressive stress of calcium bentonite extrudates was increased by about 86% (i.e., from 4.4 MPa to 8.2 MPa) when their firing temperature was increased from 400 °C to 500 °C.

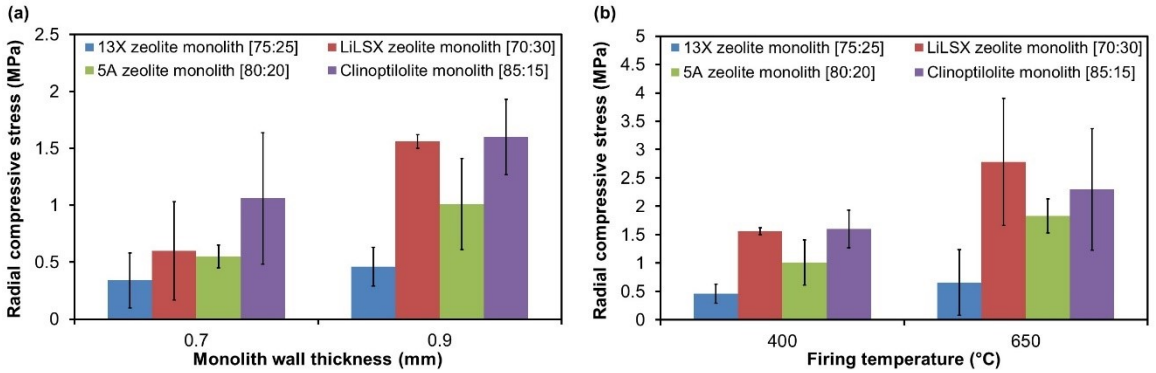


**Figure 3.21** The radial compressive stresses of the prepared zeolite monoliths (a) that have been fired at 400 °C with monolith wall thicknesses of 0.7 mm or 0.9 mm and those (b) that have been fired at 400 °C or 650 °C with a monolith wall thickness of 0.9 mm. Note: Their paste compositions are denoted by [% wt. zeolite:% wt. calcium bentonite] in the plots.

Additionally, the effect of pore former (such as Licowax C micropowder PM) on the mechanical strength of the prepared zeolite monoliths was studied for different content of pore former in their paste formulations. The mechanical (radial) compression tests were first carried out on 13X zeolite monoliths (containing 75% wt. 13X zeolite:25% wt. Wyoming sodium bentonite) without any pore former and those with 2% wt. and 4% wt. Licowax C micropowder PM. These 13X zeolite monoliths have 0.9 mm thick walls and they have been fired at 650 °C. The results in Figure 3.22 (a) reveal that the radial compressive stresses of the fired 13X zeolite monoliths were decreased by about 24% when 2% wt. Licowax C micropowder PM was included in their paste formulations compared to those without any inclusion of the pore former.

A further decrease of about 67% in radial compressive stresses of the fired 13X zeolite monoliths was seen in Figure 3.22 (a) when 4% wt. Licowax C micropowder PM was added in their paste formulations compared to those without any addition of the pore former. This shows that the higher the content of pore former been incorporated in the paste formulations of 13X zeolite monoliths, the more macropores are created within the monolithic structure when the pore former was thermally decomposed. The formation of additional macropores in zeolite monoliths with pore former has been confirmed previously by MIP and SEM tests (refer Sections 3.4.2.3 and 3.4.2.4, respectively). Their pore size distribution plots (refer Figures 3.13 (a) to (d) in Section 3.4.2.3) indicate increments in their pore volumes in the macropore region of about 11% for 13X zeolite and 5A zeolite, 16% for LiLSX zeolite and 20% for clinoptilolite monoliths with 4% wt. Licowax C micropowder PM as a pore former when compared to those without any pore former. A high number of macropores in the zeolite monoliths means that the monolithic structure has less mechanical stability on compressive loadings.

Similar effect of the pore former on the mechanical strength of zeolite monoliths was observed in Figure 3.22 (b). The mechanical (radial) compression tests were carried out on the prepared zeolite monoliths without and with 4% wt. Licowax C micropowder PM in their paste formulations. The tested zeolite monoliths have a wall thickness of 0.9 mm and they have been fired at 400 °C. Each type of zeolite monoliths (of the same zeolite to bentonite ratio) was compared. Their results reveal that the radial compressive stresses of the fired zeolite monoliths without any pore former were decreased by about 4% for 13X zeolite, 57% for LiLSX zeolite, 11% for 5A zeolite and 21% for clinoptilolite when their paste formulations have included 4% wt. Licowax C micropowder PM. This confirms that the formation of macropores in the monolithic structure after the thermal decomposition of the pore former reduces the mechanical compressive strength of zeolite monoliths. Same behaviour was observed by Lee (1997), who discovered that the compressive stress of 85% wt. silicalite monoliths (of 0.59 mm thick walls) was reduced by about 11% (i.e., from 7.3 MPa to 6.5 MPa) when 10% wt. starch was added into their formulations as a pore former.

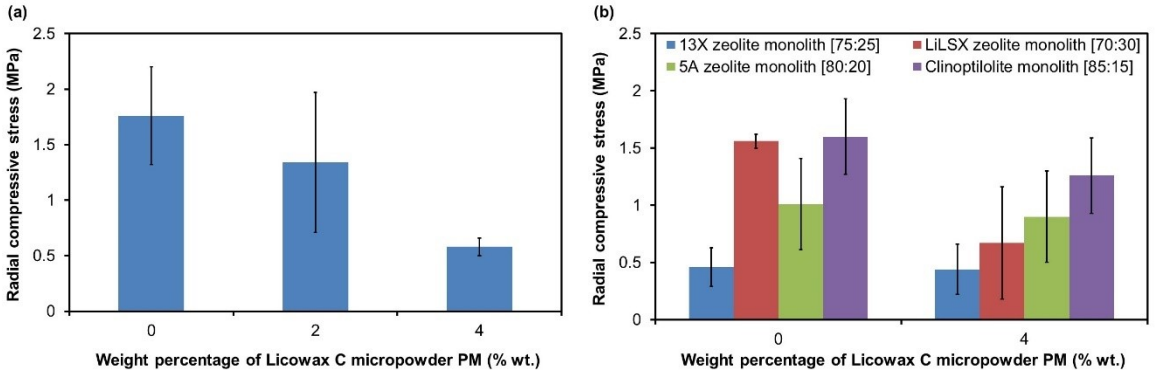


**Figure 3.22** The radial compressive stresses of (a) 80% wt. 13X zeolite monoliths that have been fired at 650 °C with different weight percentages of Licowax C micropowder PM (a pore former) and (b) the prepared zeolite monoliths that have been fired at 400 °C without or with 4% wt. Licowax C micropowder PM. Note: Their paste compositions are denoted by [% wt. zeolite:% wt. bentonite] in the plots.

Further mechanical (radial and axial) compression tests were carried out on the prepared zeolite monoliths to determine their compressive stresses on radial and axial compression loadings. The tested zeolite monoliths have 0.9 mm thick walls and they have been fired at 400 °C. Comparison between the radial and axial compressions was made for each type of zeolite monoliths (of the same zeolite to bentonite ratio). The results in Figure 3.23 (a) demonstrate that the compressive stresses of the fired zeolite monoliths were stronger by about 3.6 times for 13X zeolite, 1.8 times for LiLSX zeolite and 1.9 times for both the 5A zeolite and clinoptilolite when the compression loadings were applied in the axial direction compared to those in the radial direction. This implies that the

monolithic structure prepared in the study has high mechanical stability for axial compression compared to radial compression.

Similar trend was also reported by Li (1998), who found that their square-channelled 5A zeolite monoliths (containing 75% wt. 5A zeolite and 25% wt. sodium bentonite) have higher compressive stress of about 4 times for axial loading compared to radial loading. Their results revealed that the axial and radial compressive stresses of their 5A zeolite monoliths (with channel diameter of 2 mm and wall thickness of 0.98 mm) that have been fired at 800 °C were about 6.5 MPa and 1.6 MPa, respectively.

Lastly, the mechanical (axial) compression tests were carried out on the prepared zeolite monoliths without and with a pore former (such as Licowax C micropowder PM) as well as on their commercial zeolite beads/granules. The tested zeolite monoliths have a thickness of 0.9 mm and they have been fired at 400 °C. Each type of zeolite monoliths (of the same zeolite to bentonite ratio) was compared with their respective commercial zeolite beads/granules. Their results in Figure 3.23 (b) demonstrate that the axial compressive stresses of the prepared zeolite monoliths (without and with 4% wt. Licowax C micropowder PM) were higher by about 4.9 times for 13X zeolite, 2.7 times for LiLSX zeolite, 7.7 times for 5A zeolite and 5.4 times for clinoptilolite compared to their commercial zeolite beads/granules.

This shows that the zeolite monolithic structure prepared in the study was mechanically stronger than the commercially available zeolite beads/granules. This also means the prepared zeolite monoliths without and those with the inclusion of 4% wt. Licowax C micropowder PM in their paste formulations are strong enough to withstand the bulk handling and friction in adsorption columns for the biogas upgrading application. When comparing monoliths of the same structure, the mechanical compressive strength results from this study are higher than the activated carbon monoliths prepared by Yates *et al.* (2012), slightly lower than the 5A zeolite monoliths prepared by Li (1998) and lower than the silicalite monoliths prepared by Lee (1997).

According to Yates *et al.* (2012), their 75% wt. activated carbon monoliths (2.6 mm wide square-channels and 0.9 mm thick walls) that have been fired at 500 °C have a radial compressive stress of about 0.3 MPa. Their radial compressive stress value was lower than all the different types of zeolite monoliths prepared in this study. As mentioned before, the 75% wt. 5A zeolite monoliths (2 mm wide square-channels and 0.98 mm thick

walls, fired at 800 °C) prepared by Li (1998) have a radial compressive stress of about 1.6 MPa and an axial compressive stress of about 6.5 MPa. When compared to the results from this study (monoliths containing 75% wt. zeolite), its radial compressive stress value was slightly higher than 13X zeolite, LiLSX zeolite and 5A zeolite monoliths but lower than clinoptilolite monoliths. Its axial compressive stress value was higher than all the different types of zeolite monoliths prepared in this study. Lee (1997) reported that its 80% wt. silicalite monoliths with equal square-channels size and wall thickness of 1 mm (fired at 750 °C) have a radial compressive stress of 17 MPa and this value was higher than all the different types of zeolite monoliths made in this study.

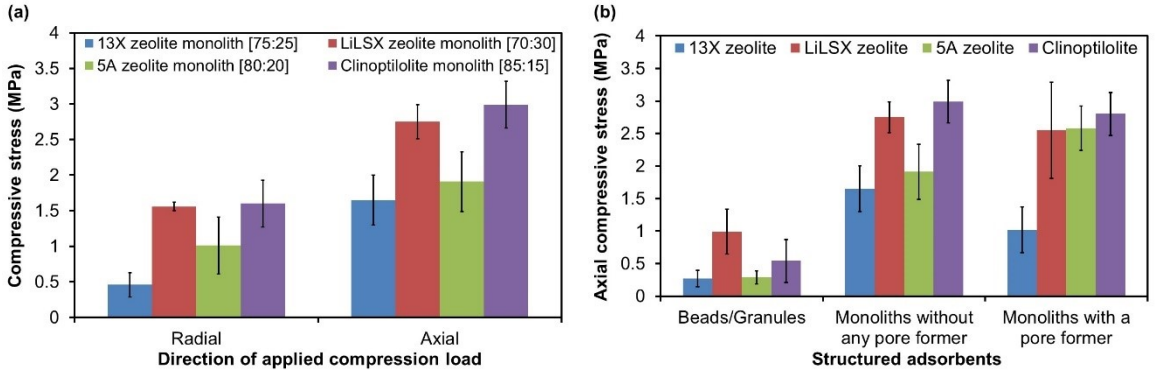


**Figure 3.23** (a) The radial and axial compressive stresses of the prepared zeolite monoliths that have been fired at 400 °C [Note: Their paste compositions are denoted by [% wt. zeolite:% wt. calcium bentonite] in the plots.] and (b) the axial compressive stresses of the 75% wt. 13X zeolite, 70% wt. LiLSX zeolite, 80% wt. 5A zeolite and 85% wt. clinoptilolite monoliths that have been fired at 400 °C without or with 4% wt. Licowax C micropowder PM (a pore former) in comparison to their commercial zeolite beads/granules.

## 3.5 Conclusions

The work described in this chapter has showed that 13X zeolite, LiLSX zeolite, 5A zeolite and clinoptilolite monoliths were fabricated successfully based on novel formulations using the unique paste extrusion technique. Clays such as calcium bentonite and Wyoming sodium bentonite were chosen and used as binder in this study because they have high plasticity and binding effects with the selected zeolites. These bentonites also give adequate mechanical stability to the monolithic structure.

The innovation of the work described in this chapter was demonstrated by the incorporation of a decomposable pore former such as Licowax C micropowder PM in the paste formulations of zeolite monoliths. When the Licowax C micropowder PM was decomposed, macropores are formed within the monolithic structure. This would enable more adsorption sites to be exposed for capturing gas contaminants such as $CO_2$, $H_2O$

vapour and $H_2S$ from the biogas stream and therefore improving the mass transfer between adsorbate gas contaminants and zeolites.

The main fabrication challenges such as surface tearing, cracking and bending of zeolite monoliths need to be overcame to produce zeolite monoliths of perfect structure. This study found that these fabrication issues could be avoided by adjusting the water content of the paste, improving the plasticity of the paste and controlling the evaporation rate of water molecules from the surface of the green zeolite monoliths.

The physical properties of the selected zeolites and bentonites powders have been characterised by simultaneous TGA and DSC, PXRD and SEM. The results reveal that the selected zeolites (i.e., 13X zeolite, LiLSX zeolite, 5A zeolite and clinoptilolite) and bentonites (i.e., calcium bentonite and Wyoming sodium bentonite) have high thermal stabilities and their crystal structures would not collapse when heated at 400 °C or 650 °C. Zeolite monoliths prepared in the study have been characterised by PXRD, MIP, SEM and mechanical compression tests. Their physical properties have also been compared with commercial zeolite beads/granules. The PXRD and SEM analyses showed that zeolite crystals were maintained in the fired zeolite monoliths. Both SEM and MIP tests proved the formation of macropores within the zeolite monoliths after the pore former was decomposed.

The MIP tests revealed that the prepared zeolite monoliths have higher porosities than the commercial zeolite beads/granules. This means adsorbate gas contaminants such as $CO_2$, $H_2O$ vapour and $H_2S$ could diffuse into the zeolite crystals and adsorb onto the adsorption sites much faster in the monolithic structure compared to the beaded or granular structures. The MIP tests also shown that the structural porosity of 13X zeolite monoliths was reduced slightly by about 5% when their firing temperature was increased from 400 °C to 650 °C, indicating that some of the pores were blocked by the bentonite.

As demonstrated by the mechanical compression tests, the prepared zeolite monoliths have better quality than the commercial zeolite beads/granules. Depending on the binding effect between bentonites and zeolites, the mechanical strengths of the prepared zeolite monoliths on radial or axial compressions were found to be varied with the types of zeolites and bentonites, content of bentonite (or zeolite to bentonite ratio), monolith wall thickness, firing temperature and content of the Licowax C micropowder PM. The study discovered that the radial compressive strengths of the fired 75% wt. zeolite

monoliths were in order of (high to low): clinoptilolite, LiLSX zeolite, 5A zeolite and 13X zeolite.

It was found that the mechanical compressive strengths of the prepared zeolite monoliths were improved slightly by using Wyoming sodium bentonite as the binder instead of calcium bentonite. Moreover, the radial compressive strengths of the prepared zeolite monoliths were discovered to increase with increasing content of bentonite (or lower zeolite to bentonite ratio), monolith wall thickness and firing temperature. The mechanical compression tests also have demonstrated that the mechanical compressive strengths of the prepared zeolite monoliths were reduced when the content of the Licowax C micropowder PM was increased. This was due to the increasing number of macropores been formed within the monolithic structure after the pore former was decomposed when heated.

Zeolite monoliths prepared in this study will be optimised for $CO_2$ adsorption, which is described later in Chapter 6 of this thesis. The best zeolite monoliths among the prepared zeolite monoliths will then be tested for single (such as $CO_2$, $CH_4$ and $H_2S$) and mixed (such as $CO_2/CH_4$ and $CO_2/CH_4/H_2O$ vapour) gas adsorption. Their adsorption performance for biogas upgrading will be assessed in Chapter 7 of this thesis. The mass transfer, axial dispersion and pressure drop in zeolite monoliths will also be evaluated, see Chapter 8 of this thesis.

# Chapter 4 Fabrication and Characterisation of Metal-Organic Framework (MOF) Monoliths

The development of metal-organic framework (MOF) monoliths for biogas upgrading application will be introduced in this chapter. One of the MOFs that is selected and used as a model adsorbent in this study is MIL-101(Cr) ($[Cr_3O(OH)(H_2O)_2(bdc)_3]\cdot xH_2O$; bdc = 1,4-benzenedicarboxylate). One of the reasons is because they have high adsorption capacities for $CO_2$, $H_2O$ vapour and $H_2S$ as a result of high porosities and large surface areas. They also have good tolerance in the presence of $H_2O$ and this distinctive property of MIL-101(Cr) makes them suitable for biogas upgrading since there are normally about 2% vol. to 7% vol. of $H_2O$ vapour in the biogas stream. In this work, MIL-101(Cr) monoliths will be fabricated using a unique paste extrusion technique based on novel formulations. The materials and equipment used in this study are given in Section 4.1.

Due to the high cost of MIL-101(Cr) from commercial sources, MIL-101(Cr) powders will be synthesized without the use of the hazardous hydrofluoric acid according to the special preparation methods described in Section 4.2. For use in industrial applications such as biogas upgrading, MIL-101(Cr) powders produced in this study will be structured in the form of monoliths so that they can be handled easily and used in the most efficient way during adsorption. The details of the fabrication of MIL-101(Cr) monoliths are provided in Section 4.3. So far, no work has been reported on MIL-101(Cr) monoliths by other research groups. This demonstrates the novelty of this research in the production of MIL-101(Cr) monoliths.

In the fabrication of MIL-101(Cr) monoliths, clay such as calcium (Ca) bentonite is chosen and used as a binder. The reasons for this are because they would make the adsorbent pastes mouldable and provide mechanical stability to the extruded MIL-101(Cr) monoliths. Previous study (Section 3.4.2.5) have indicated that the types of bentonite did not have major influence on the mechanical properties of the monolith so only calcium bentonite was used in this study as an example. As shown in previous chapter, the structural porosities of monoliths were improved by including a decomposable pore former such as Licowax C micropowder PM in the paste formulations. This would, in turn, enhance the mass transfer of adsorbate gas contaminants such as $CO_2$, $H_2O$ vapour and $H_2S$ in the monolithic structure. So, similar fabrication strategy will be used in this work to improve the structural porosities of MIL-101(Cr) monoliths so that the mass transfer in MIL-101(Cr) monoliths could be enhanced.

MIL-101(Cr) powders and monoliths produced in this study will then be characterised using established methods to determine their physical and adsorptive properties. The physical characteristics of MIL-101(Cr) to be determined in this study are thermal stabilities, crystal and pore structures, surface morphologies and mechanical compression strengths. Since $CO_2$ gas is the main contaminant in biogas (generally, about 25% vol. to 45% vol.) that needs to be removed from the biogas stream to upgrade its gas quality, the $CO_2$ adsorption characteristics of MIL-101(Cr) will be determined.

The thermal stabilities, PXRD patterns, morphologies and $CO_2$ adsorption capacities of the MIL-101(Cr) powders synthesized in this work will be compared to those reported in the literature. The characterisation methods to be employed in this study are simultaneous thermogravimetry and differential scanning calorimetry (TG-DSC), powder X-ray diffraction (PXRD), mercury intrusion porosimetry (MIP), scanning electron microscopy (SEM), mechanical strength tests and gravimetric sorption analysis. The details of the characterisation of MIL-101(Cr) powders and monoliths are given in Section 4.4.

The results for the production and characterisation of MIL-101(Cr) powders and monoliths will be provided and discussed in Section 4.5. Then, the work described in this chapter will be concluded at the end in Section 4.6.

## 4.1 Materials and Equipment Used in the Study

The materials used in the synthesis of MIL-101(Cr) powders were chromium(III) nitrate nonahydrate [$Cr(NO_3)_3{\cdot}9H_2O$; 99%, purchased from Acros Organics, UK], 1,4-benzenedicarboxylic acid [$HO_2C(C_6H_4)CO_2H$; ≥99%, purchased from Acros Organics, UK], ethanol [$C_2H_5OH$; ≥99.8%, purchased from Sigma-Aldrich Co., UK] and distilled water [$H_2O$]. All these chemicals and solvents were of the highest purity and they were used as received.

On the other hand, the materials used in the fabrication of MIL-101(Cr) monoliths were MIL-101(Cr) powders (synthesized in this study), calcium bentonite (purchased from Bath Potters' Supplies Ltd., UK), Licowax C micropowder PM (purchased from Clariant, UK) and water. For the characterisation of MIL-101(Cr) powders and monoliths, mercury (purchased from Sigma-Aldrich Co., UK) was used as a non-wetting liquid in the MIP

analysis and a pure $CO_2$ gas (purchased from BOC Ltd., UK) was used in the gravimetric sorption analysis. All these materials were used as obtained from commercial sources.

In this study, MIL-101(Cr) powders were synthesized in a 352 $cm^3$ Teflon-lined autoclave (5.3 cm inner diameter and 16 cm long) that was made at University of Bath workshop (UK). An electric oven (model UM 100) manufactured by Memmert (Germany) was used for heating the prepared MOF solutions during the hydrothermal reaction. The resulting MIL-101(Cr) solids were separated from the supernatant solution using a centrifuge (model IEC CL10) that was purchased from Thermo Electron Corporation (UK).

The equipment used in the preparation of MIL-101(Cr) pastes comprises of a 5 Litre stainless steel mixing bowl, a whisker and a spatula. The prepared MIL-101(Cr) pastes were extruded using a horizontal, single-screw extruder (model BETOL 2520J) provided by Plasplant Machinery Ltd. (UK). This extruder was similar to that used for extruding the zeolite pastes (see Figure 3.1 (a) of Chapter 3). In this work, a stainless steel extruder die manufactured by South Western Tools Ltd. (UK) was used for shaping the MIL-101(Cr) monolithic extrudates so that they have a cell density of 30 cells $cm^{-2}$ with a channel diameter of 0.9 mm and a wall thickness of 0.9 mm. An electric kiln (Rohde, model Ecotop 43L) of programmable temperatures purchased from Bath Potters' Supplies Ltd. (UK) was used for firing the MIL-101(Cr) monoliths.

Moreover, a simultaneous thermogravimetric and differential scanning calorimetric analyser (model Setaram TGA 92) was used for analysing the thermal stabilities of MIL-101(Cr) powders. This analyser consists of a microbalance, a furnace and a 100 $mm^3$ alumina crucible (5 mm in diameter and 9.9 mm in height). The crystal structures of MIL-101(Cr) powders were characterised using a diffractometer (model Bruker AXS D8 Advance). The equipment associated with the diffractometer are: an X-ray generator, a vertical goniometer (angular range: $-110° < 2\text{Theta} \leq 168°$), a 50 mm diameter silicon sample cup (with a 20 mm diameter and 0.5 mm depth sample reception) and an X-ray detector.

The pore properties of MIL-101(Cr) powders and monoliths were determined using a mercury penetrometer (model Micromeritics AutoPore III) in which the samples were loaded into a 3 $cm^3$ bulb glass penetrometer with a stem volume of 1.19 $cm^3$. For examining the morphologies of MIL-101(Cr) powders and monoliths, an Edwards sputter coater (model S150B) was used to coat the samples with a thin layer of conducting gold

so that the images of the sample's surfaces could be produced and viewed using an electron microscope (model JEOL JSM-6480 LV). The electron microscope was assembled in a vacuum chamber, which contains a stainless steel sample holder, a sample stage, an electron gun and an electron sensor.

In this study, an Instron universal tester (model 3369) equipped with a 1 kN load cell was used for determining the mechanical compressive strengths of MIL-101(Cr) monoliths. The $CO_2$ adsorption characteristics of MIL-101(Cr) powders and monoliths were analysed using an intelligent gravimetric analyser (model Hiden HAS022120L), which consists of a microbalance, a sample holder, a thermostat, a furnace and a vacuum/pressure vessel.

## 4.2 Experimental Procedures for Synthesizing MIL-101(Cr) Powders

Conventionally, MIL-101(Cr) was synthesized by hydrothermal reaction that involves the toxic and highly corrosive hydrofluoric acid. A different synthesizing strategy was applied in this study, in which no harmful hydrofluoric acid was used in the preparation of MIL-101(Cr) and the hydrofluoric acid was substituted by water. The elimination of the hazardous hydrofluoric acid in the synthesis of MIL-101(Cr) would simplify their hydrothermal reaction and reduce the cost of production.

This means that the synthesis of MIL-101(Cr) powders could be scaled-up for the fabrication of MIL-101(Cr) monoliths economically by using low cost and non-toxic starting materials and easier preparation methods. In addition, MIL-101(Cr) synthesized with or without the hydrofluoric acid exhibits almost the same adsorption properties and water stabilities according to the study carried out by Liang *et al.* (2013). The success of synthesizing MIL-101(Cr) without the use of any hydrofluoric acid has been reported by a few research groups.

For example, Khan *et al.* (2011) have reported the hydrothermal synthesis of nano-sized MIL-101(Cr) without using any hydrofluoric acid at 210 °C for 6 or 24 hours. Similarly, Huang *et al.* (2011) have reported the hydrofluoric acid-free synthesis of MIL-101(Cr) hydrothermally at 200 °C for 8 hours for the adsorption of volatile organic compounds. This new synthesizing approach for preparing MIL-101(Cr) hydrothermally without using any hydrofluoric acid was also reported by Bromberg *et al.* (2012), in which their MIL-101(Cr) was synthesized at 218 °C for 18 hours for catalytic applications.

Recently, our group, Hong *et al.* (2015), have reported the hydrothermal synthesis of MIL-101(Cr) without using any hydrofluoric acid at 220 °C for 8 hours for $CO_2$ adsorption.

In this study, the hydrothermal synthesis of MIL-101(Cr) powders did not include any hydrofluoric acid and the methods of treating the materials were different to those reported in the literature. The synthesis of MIL-101(Cr) powders presented in this work consists of several processing steps, namely: solution preparation, synthesis by heat treatment, centrifugation, washing and drying. This produces the as-synthesized MIL-101(Cr) powder. Additional processing steps were also employed in this work to produce the purified MIL-101(Cr) powder, in which the as-synthesized MIL-101(Cr) powder was treated with a solvent, followed by centrifugation, washing and drying. The processing steps involved in the production of as-synthesized and purified MIL-101(Cr) powders are shown schematically in Figure 4.1 and described individually in Sections 4.2.1 and 4.2.2.

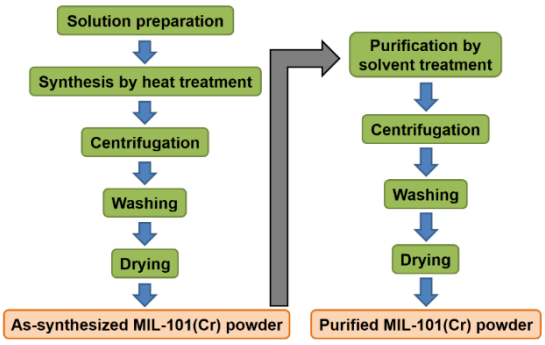


**Figure 4.1** A schematic flow diagram showing the processing steps involved in the production of as-synthesized and purified MIL-101(Cr) powders.

### 4.2.1 As-synthesized MIL-101(Cr) powder

As mentioned earlier, the processing steps for the production of as-synthesized MIL-101(Cr) powder comprises of: solution preparation, synthesis by heat treatment, centrifugation, washing and drying. The descriptions of each of these processing steps are provided in Sections 4.2.1.1 to 4.2.1.5.

#### 4.2.1.1 Solution preparation

First, the MOF solutions were prepared by mixing 4.2 g of chromium(III) nitrate nonahydrate and 1.6 g of 1,4-benzenedicarboxylic acid with 49.0 mL of water for small-scale synthesis of MIL-101(Cr). This specially formulation was scaled-up to 16.8 g of chromium(III) nitrate nonahydrate, 6.4 g of 1,4-benzenedicarboxylic acid and 196.0 mL of water for large-scale synthesis of MIL-101(Cr).

#### 4.2.1.2 Synthesis by heat treatment

Each of the prepared MOF solutions (either small- or large-scale synthesis) was transferred into a Teflon-lined autoclave, which was sealed and placed in an electric oven. The autoclave containing the MOF solution was heated at 220 °C for 8 hours. It was very important to make sure that the autoclave was sealed properly so that the autogenous pressure generated inside the vessel was maintained throughout the reaction time otherwise MIL-101(Cr) crystals would not be formed at the end of the reaction. In the synthesis, hydroxyl ions ($OH^-$) were incorporated onto chromium (III) trimers as terminal ligands. These chromium (III) trimers with $OH^-$ ligands were linked to the 1,4-benzenedicarboxylate (bdc) ligands to form the mesoporous MIL-101(Cr) crystals.

#### 4.2.1.3 Centrifugation

After the synthesis, the autoclave was cooled to room temperature and MIL-101(Cr) solids were separated from the supernatant solution using a centrifuge. The centrifugation was carried out at a speed of 5 000 rpm for 10 minutes. Some MIL-101(Cr) solids may be lost while removing the supernatant solution so they need to be handled carefully.

#### 4.2.1.4 Washing

The resulting green solids of MIL-101(Cr) were washed with water three times. This was to remove any remaining supernatant solution from the MIL-101(Cr) solids after the centrifugation. Again, some loss of MIL-101(Cr) solids may occur while removing the water so careful handling of the materials is required.

#### 4.2.1.5 Drying

Any residual water was then removed from MIL-101(Cr) solids by drying them at room temperature. This produces as-synthesized MIL-101(Cr) powder.

### 4.2.2 Purified MIL-101(Cr) powder

Generally, the as-synthesized MIL-101(Cr) solids contain impurities of unreacted or recrystallized 1,4-benzenedicarboxylic acid that were present outside or within the pores of MIL-101(Cr). The presence of these impurities reduces the quality of the MIL-101(Cr). So, a solvent such as ethanol was used to purify the as-synthesized MIL-101(Cr). The processing steps involved in the production of purified MIL-101(Cr) powder are: purification by solvent treatment, centrifugation, washing and drying. Each of these processing steps is described in Sections 4.2.2.1 to 4.2.2.4.

#### 4.2.2.1 Purification by solvent treatment

The as-synthesized MIL-101(Cr) powder was purified by treating them with hot ethanol at 80 °C for 4 hours. This was to remove any unreacted or recrystallized 1,4-benzenedicarboxylic acid from the pores of MIL-101(Cr) crystals by dissolving them in the hot ethanol.

#### 4.2.2.2 Centrifugation

After the purification, MIL-101(Cr) solids in solvent were cooled to room temperature and the pure MIL-101(Cr) solids were separated from the supernatant solvent using a centrifuge. The centrifugation was operated at a speed of 5000 rpm for 10 minutes. Careful handling was practiced to minimize the loss of MIL-101(Cr) solids while removing the supernatant solvent.

#### 4.2.2.3 Washing

Then, the pure MIL-101(Cr) solids were washed with ethanol three times to eliminate any remaining supernatant solvent from the pure MIL-101(Cr) solids after the centrifugation. Some MIL-101(Cr) solids may be lost while removing the supernatant solvent so they need to be handled carefully.

#### 4.2.2.4 Drying

Lastly, the collected green crystals of pure MIL-101(Cr) were dried at room temperature to remove the residual ethanol. This produces purified MIL-101(Cr) powder.

## 4.3 Fabrication Procedures for MIL-101(Cr) Monoliths

In this research, MIL-101(Cr) monoliths were fabricated using the as-synthesized and purified MIL-101(Cr) powders synthesized in this study. For the first time, MIL-101(Cr) monoliths were developed and their fabrication procedures are covered in this section. The novel MIL-101(Cr) monoliths were fabricated using a unique paste extrusion technique, which consists of several processing steps, i.e., paste preparation, pre-drying, extrusion, drying and firing. Although these processing steps were similar to those used in the fabrication of zeolite monoliths (refer Chapter 3), the materials involved in this work were treated differently.

Licowax C micropowder PM would also be incorporated to the paste formulations of MIL-101(Cr) monoliths as a pore forming agent to improve their structural porosities so that more adsorption sites could be exposed for adsorbing gas contaminants such as $CO_2$, $H_2O$ vapour and $H_2S$ from the biogas stream. This would, in turn, enhance the mass transfer of gas contaminants in the monolithic structure. The detailed processing steps for the fabrication of MIL-101(Cr) monoliths are given in Sections 4.3.1 to 4.3.5. The fabrication procedures need to be followed correctly to avoid problems such as surface tearing, cracking and bending that may occur during the fabrication process.

### 4.3.1 Paste preparation

Initially, MIL-101(Cr) pastes were prepared by mixing the dry powders of either as-synthesized or purified MIL-101(Cr), calcium bentonite and/or Licowax C micropowder PM with sufficient amount of water. The MIL-101(Cr) pastes should have low water content and high plasticity to avoid surface tearing or solid-liquid phase separation of the adsorbent pastes during extrusion and to reduce the evaporation rate of water from the extruded MIL-101(Cr) monoliths. So, it was very important to get the right amount of starting materials in the MIL-101(Cr) paste formulations.

Considering these factors, some MIL-101(Cr) pastes were prepared and their novel formulations are given in Table 4.1, which were expressed in weight percentage (% wt.) of the total dry mass. For example, if the total dry mass is 10 g, the paste sample M4 requires 7.5 g of purified MIL-101(Cr), 2.5 g of calcium bentonite and 0.04 g of Licowax C micropowder PM. In this work, MIL-101(Cr) pastes contained either 75% wt. or 60% wt. MIL-101(Cr) and they were balanced by the appropriate amounts of calcium bentonite and water. To minimize the effect of pore forming agent on the mechanical strength of MIL-101(Cr) monoliths, 4% wt. of Licowax C micropowder PM was added in their paste formulations to enhance their structural porosity.

**Table 4.1** Compositions of the prepared MIL-101(Cr) pastes.

| Paste sample | MIL-101(Cr):Bentonite (% wt.) + Pore forming agent (% wt.) | Water (% wt.) |
|---|---|---|
| M1 | As-synthesized MIL-101(Cr):Ca bentonite (60:40) | 159 |
| M2 | Purified MIL-101(Cr):Ca bentonite (60:40) | 159 |
| M3 | Purified MIL-101(Cr):Ca bentonite (75:25) | 150 |
| M4 | Purified MIL-101(Cr):Ca bentonite (75:25) + Licowax C micropowder PM (4) | 150 |

### 4.3.2 Pre-drying

After the MIL-101(Cr) pastes have been prepared, they were placed and wrapped in a greaseproof paper until they matured into workable pastes of high plasticity for the extrusion step. During this maturity period, excess water in the adsorbent pastes could evaporate slowly through the greaseproof paper. In order for the MIL-101(Cr) pastes to obtain the right plasticity and consistency for extrusion, the pre-drying step could take at least 24 hours depending on the water content of the adsorbent pastes.

### 4.3.3 Extrusion

Once the MIL-101(Cr) pastes had matured, they were kneaded and made into small lumps to eliminate any air pockets that may exist in the adsorbent pastes, which could impair the mechanical stability of the monolithic structure. Before starting the extrusion process, all internal surfaces of the extruder (i.e., the screw, internal wall of the barrel and die) that would be in contact with the MIL-101(Cr) pastes were inspected to make sure that they were properly cleaned. This was because any particulates in the extruder that were left behind from previous extrusion would cause cracking on the extrudates since the flow of the adsorbent pastes through the extruder die was obstructed. The schematic diagram of the extruder is provided in Figure 3.1 (a) of Chapter 3.

The speed of the rotating screw of the extruder was set at 5 rpm and the extrusion process was performed at room temperature. The extrusion process was started by inserting lumps of MIL-101(Cr) pastes into the paste input of the extruder continuously to prevent the entrapment of air and separation of MIL-101(Cr) pastes. The MIL-101(Cr) pastes were forced to flow forward along the barrel and through the extruder die to produce MIL-101(Cr) monoliths.

The extruded MIL-101(Cr) monoliths were landed on a wax paper, which was attached to the belt conveyor. The speed of the belt conveyor was controlled such that they were similar to the speed of the extruder screw. As the extruded MIL-101(Cr) monoliths moves forward with the belt conveyor, the force required by the extruder to push the MIL-101(Cr) pastes through the extruder die was reduced.

The extruded MIL-101(Cr) monoliths were cut into the desired lengths using a thin copper wire of 0.10 mm in diameter. Then, they were placed carefully onto a perforated aluminium tray so that they could be handled easily with minimal skin contacts.

### 4.3.4 Drying

The tray of MIL-101(Cr) monoliths was instantaneously kept in a cool chamber of controlled temperature (5 °C) and humidity (> 95% relative humidity) to avoid rapid evaporation of water. The drying process could take at least a week depending on the water content of MIL-101(Cr) monoliths. MIL-101(Cr) monoliths would shrink during the drying process since water molecules were evaporated from the cavities/pores of MIL-101(Cr) crystals and the interlayers of calcium bentonite crystals.

By placing MIL-101(Cr) monoliths on the perforated aluminium tray and keeping them in a temperature and humidity controlled chamber, the evaporation rate of water from the surface of MIL-101(Cr) monoliths could be regulated and minimized. This was to reduce the drying effect and stress on MIL-101(Cr) monoliths so that the occurrence of cracking and bending of monoliths could be prevented.

### 4.3.5 Firing

When MIL-101(Cr) monoliths have dried completely, they were placed on ceramic plates in the electric kiln for the firing process. In this work, MIL-101(Cr) monoliths were fired under compressed air according to the chosen temperature programmes, which are shown in Figure 4.2. The temperature programmes used in this work were determined empirically such that the resulting fired MIL-101(Cr) monoliths were not cracked and they were strong enough for use in the experiments described in this thesis. Due to these reasons, the firing process for MIL-101(Cr) monoliths was carried out by elevating the firing temperature slowly in several stages until they reached the desired temperature.

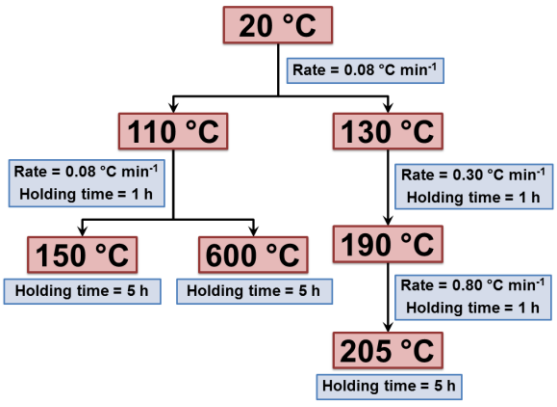


**Figure 4.2** Flow diagram of the firing temperature programmes for MIL-101(Cr) monoliths.

For comparative study, three firing temperatures were selected for the firing process and they were 150 °C, 205 °C and 600 °C. The first two firing temperatures were selected such that they were below the thermal stability temperature of both MIL-101(Cr) and calcium bentonite. The last firing temperature was selected such that it was above the thermal stability temperature of MIL-101(Cr) but below the thermal stability temperature of calcium bentonite, for comparative purposes. The temperature programmes for 150 °C and 600 °C involved two stages whereas that for 205 °C involved three stages.

In the first stage of the firing process, MIL-101(Cr) monoliths were heated slowly at a rate of 0.08 °C $min^{-1}$ from 20 °C to 110 °C or 130 °C to remove water molecules from the pores of MIL-101(Cr) crystals and from the interlayers of calcium bentonite crystals slowly. This was to avoid cracking of MIL-101(Cr) monoliths. In the second stage, the temperature in the kiln was elevated either from 110 °C to 150 °C or 600 °C at the same heating rate of 0.08 °C $min^{-1}$ with a holding time of 1 hour or from 130 °C to 190 °C at a rate of 0.30 °C $min^{-1}$ with a holding time of 1 hour. The purpose of the second stage was to burn off any impurities that are present in calcium bentonite.

In the third stage, the temperature in the kiln was further elevated from 190 °C to 205 °C at a rate of 0.80 °C $min^{-1}$ with a holding time of 1 hour to burn off the pore forming agent. The selected firing temperature of 150 °C, 205 °C or 600 °C was kept constant by holding the firing process for 5 hours. This was to sinter MIL-101(Cr) and calcium bentonite crystals together to give the necessary mechanical strength to the fired MIL-101(Cr) monoliths. After the firing process has completed, the fired MIL-101(Cr) monoliths were cooled to room temperature and they were refined by cutting both ends of the monoliths using a saw. The fired MIL-101(Cr) monoliths are now ready for characterisation and use in the experiments described in this thesis.

## 4.4 Characterisation Methods for MIL-101(Cr) Powders and Monoliths

The MIL-101(Cr) powders and monoliths prepared in this study were characterised using: (a) simultaneous TG-DSC for investigating their thermal properties, (b) PXRD for analysing their crystal structures, (c) MIP for determining their pore properties, (d) SEM for examining their morphologies, (e) mechanical compression tests for evaluating their compressive strengths and (f) gravimetric sorption analysis for determining their $CO_2$ adsorption properties. The experimental procedures of each of these characterisation methods are provided in Sections 4.4.1 to 4.4.6.

### 4.4.1 Simultaneous thermogravimetry and differential scanning calorimetry

A sample (either as-synthesized or purified MIL-101(Cr) powders) was loaded into a small alumina crucible and weighed on a microbalance in an insulated furnace at room temperature. The environment in the furnace was controlled using cool water and the system was cleaned using argon gas. The furnace has a built-in thermocouple for measuring the temperature in the furnace. A temperature programme was created for heating the sample in air from 20 °C to 900 °C at a rate of 10 °C $min^{-1}$.

The thermal analysis of the sample was carried out using a simultaneous thermogravimetric and differential scanning calorimetric analyser. This analyser was connected to a computer, which record the thermal data of the sample using a SetSoft2000 programme. At the end of the analysis, the sample was cooled to room temperature naturally before removing them from the furnace. Thermogravimetric (TG) and differential scanning calorimetric (DSC) curves of the tested sample were then generated from the collected thermal data. The TG curves were obtained by plotting the sample weight against the temperature while the DSC curves were obtained by plotting the heat flow against the temperature. All the TG and DSC curves presented in this study have been subtracted from the TG and DSC curves of the blank test (thermal data of an empty alumina crucible), which was given in Appendix 1.

### 4.4.2 Powder X-ray diffraction

The prepared MIL-101(Cr) monoliths (Samples M1 to M4) were crushed into fine powder before the analysis. Each powder sample of the MIL-101(Cr) monoliths or calcium bentonite was placed on a silicon sample cup and mounted onto the sample stage. Then, the sample was examined using a diffractometer with copper radiation (Cu Kα) as a source of X-rays. The analysis was performed at 21 °C in atmospheric pressure. All powder samples were analysed with a scan step size of 0.016° and scan angles from 3° to 60°. The X-rays that were diffracted from the samples were detected and recorded on a computer. The intensities of the diffracted X-rays were then plotted as a function of their angular positions to produce the PXRD patterns of the samples.

### 4.4.3 Mercury intrusion porosimetry

A sample of the prepared MIL-101(Cr) monoliths (Samples M1 to M4) was loaded into a glass penetrometer. Then, the loaded penetrometer was fitted onto the low pressure port of the mercury penetrometer to evacuate gases from the sample. Once the low pressure (0 bar to 3.45 bar) analysis had completed, the loaded penetrometer was

transferred to the high pressure port of the mercury penetrometer. In the high pressure analysis, mercury was forced into the evacuated sample pores with hydraulic pressure up to about 4 137 bar. The data from the MIP tests was recorded on a computer and they were used to obtain important pore properties such as total pore volume, total pore surface area, mean pore diameter, porosity, bulk density and pore size distribution of the sample. All MIP data presented in this study have been automatically corrected by the machine with the blank test (of an empty penetrometer) result, which was provided in Appendix 1.

### 4.4.4 Scanning electron microscopy

The MIL-101(Cr) powders and monoliths (Samples M1, M3 and M4) prepared in this study were placed and attached on the stainless steel sample holder using carbon adhesive. They were kept in a vacuum desiccator overnight to evacuate gases from the samples. Prior to the SEM examinations, all samples were coated with a thin layer of electrically conductive gold surface using the Edwards sputter coater. Then, they were mounted onto the sample stage in a small vacuum chamber at room temperature and ready for the SEM tests. The SEM tests were started by projecting a beam of electrons onto the surfaces of the samples. The deflected electrons were detected by an electron sensor and formed images of the surface of the samples. These images were observed using an electron microscope and the scanning electron micrographs of the samples were recorded on a computer.

### 4.4.5 Mechanical compression tests

A sample of the prepared MIL-101(Cr) monoliths (Samples M1, M3 and M4) of length ranging between 0.7 cm and 3.5 cm was tested on an Instron universal tester. Radial compression was applied to each sample at a rate of 0.5 mm $min^{-1}$ until they fracture. The compression tests were carried out at 22 °C under atmospheric pressure. The compression testing equipment was connected to a computer, which records the applied compressive load on the sample and their deformation using a Bluehill software.

### 4.4.6 Gravimetric sorption analysis

A sample of the prepared MIL-101(Cr) powder or monolith (Sample M2) was loaded onto a sample holder. The mass of the sample was weighed using a microbalance at room temperature. The reactor chamber was sealed and decontaminated overnight under vacuum. To make sure that there was no gas remained in the system after the decontamination step, the reactor was purged with $CO_2$ gas. The sample was then

outgassed at a rate of 10 mbar $min^{-1}$ to about $10^{-6}$ mbar and heated to 180 °C at a rate of 2 °C $min^{-1}$ for 12 hours. This was to remove any water molecules and gas contaminants from the samples. Once the sample preparation step had completed, the sample was cooled to room temperature and the dry mass of the sample was recorded.

Then, the $CO_2$ adsorption isotherm measurements were carried out up to about 4.4 bar at 20 °C or 25 °C. A series of adsorption pressure steps was involved in the isotherm measurements. The sample weight was measured at each pressure step and they were allowed to reach equilibrium during adsorption before moving to the next pressure point. The data was collected at each pressure point with a minimum equilibrium time of 20 min and a maximum equilibrium time of 240 min. This was to ensure that all the isotherm points were collected when the sample attained equilibrium during adsorption. When all the adsorption pressure steps have completed, equilibrium adsorption capacity of $CO_2$ gas was plotted as a function of pressure.

## 4.5 Results and Discussion for the Production and Characterisation of MIL-101(Cr) Powders and Monoliths

This section covers the results and discussion of the MIL-101(Cr) powders and monoliths prepared and characterised in this study. The results and discussion for the synthesis of MIL-101(Cr) powders are given in Section 4.5.1 while those for the fabrication of MIL-101(Cr) monoliths are given in Section 4.5.2. The characterisation results of the MIL-101(Cr) powders and monoliths are provided and discussed in Section 4.5.3.

### 4.5.1 Synthesis of MIL-101(Cr) powders

As seen in Figure 4.3 (a), the mixture of chromium(III) nitrate nonahydrate, 1,4-benzenedicarboxylic acid and water formed a dark purple starting solution, which changed to green colour after the heat treatment at 220 °C for 8 hours. MIL-101(Cr) solids were observed in the resulting green solution and this confirms the formation of MIL-101(Cr). The green MIL-101(Cr) crystals were collected, washed and dried to produce fine green powder of MIL-101(Cr), as shown in Figure 4.3 (b). These photographs demonstrate that MIL-101(Cr) were synthesized successfully according to the novel chemical formulations and preparation procedures described in this work.

The amount of MIL-101(Cr) produced in the synthesis (either small- or large-scale) was about 0.6 g to 0.9 g of MIL-101(Cr) per gram of chromium(III) nitrate nonahydrate.

Depending on the amount of MIL-101(Cr) lost at each processing steps, the amount of MIL-101(Cr) produced in the synthesis would vary. For example, the product yield of the as-synthesized MIL-101(Cr) powder was found to be about 76.5% whereas that of the purified MIL-101(Cr) powder was found to be about 62.4%. This indicates that the loss of MIL-101(Cr) crystals was slightly more when the as-synthesized MIL-101(Cr) was purified by performing the additional processing steps, which involved the purification by solvent treatment, centrifugation, washing and drying.

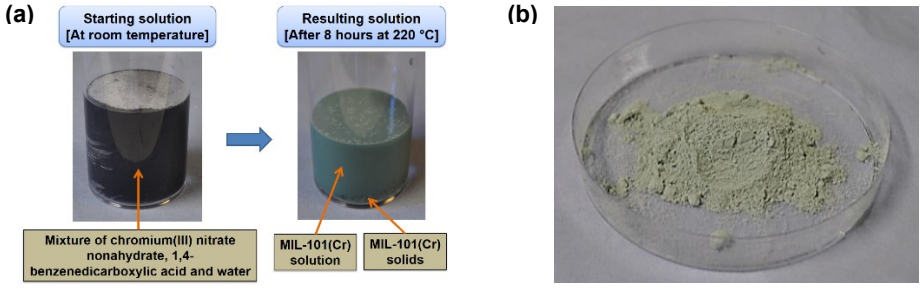


**Figure 4.3** Photographs of (a) the starting and resulting solutions in the synthesis of MIL-101(Cr) and (b) the synthesized MIL-101(Cr) powder (~ 3 g).

### 4.5.2 Fabrication of MIL-101(Cr) monoliths

MIL-101(Cr) monoliths with containing 60% wt. and 75% wt. of either as-synthesized or purified MIL-101(Cr) were successfully fabricated according to the novel paste formulations described in this study. These MIL-101(Cr) monoliths were made up of square channels of 0.9 mm wide with wall thickness of 0.9 mm. The colour of the fired MIL-101(Cr) monoliths was green, as seen in Figure 4.4. It was found that the amount of water used in the MIL-101(Cr) paste formulations varies with the amounts of MIL-101(Cr) and calcium bentonite and this was because they have different water adsorption capacities. In this study, the optimum ratio of water to dry powders (i.e., MIL-101(Cr), calcium bentonite and/or pore former) was found to be between 1.50 and 1.59.

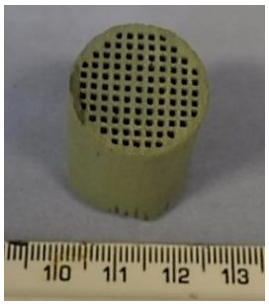


**Figure 4.4** Photograph of a manufactured MIL-101(Cr) monolith (Sample M4) with 0.9 mm thick walls.

As mentioned previously, common fabrication problems such as surface tearing, cracking and bending could occur if the fabrication procedures are not followed correctly. In this work, the MIL-101(Cr) monoliths were prepared carefully according to the fabrication procedures described in Section 4.3. As a result, the issues on surface tearing, cracking and bending were avoided during the fabrication of MIL-101(Cr) monoliths.

### 4.5.3 Characterisation of MIL-101(Cr) powders and monoliths

This section provides the results and discussion for the characterisation of the prepared MIL-101(Cr) powders and monoliths. Their physical characteristics such as thermal properties, crystal structures, pore properties, morphologies, mechanical compressive strengths and $CO_2$ adsorption properties are covered in Sections 4.5.3.1 to 4.5.3.5.

#### 4.5.3.1 Thermal properties of MIL-101(Cr)

The TG and DSC curves of the prepared MIL-101(Cr) powders are provided in Figure 4.5 (a) for the as-synthesized MIL-101(Cr) and Figure 4.5 (b) for the purified MIL-101(Cr). The changes in weight and heat flow of the heated MIL-101(Cr) samples were interpreted to determine their weight losses and thermal stabilities. The TG curves of as-synthesized and purified MIL-101(Cr) powders show that they both have two-steps weight loss when heated. The first weight loss of about 16% up to 279 °C for the as-synthesized MIL-101(Cr) and about 39.4% up to 277 °C for the purified MIL-101(Cr) was due to the loss of water molecules. The second weight loss of about 62.2% from 280 °C to 500 °C for the as-synthesized MIL-101(Cr) and about 45.2% from 280 °C to 480 °C for the purified MIL-101(Cr) was due to the removal of hydroxyl (OH) groups and the decomposition of their frameworks. The TG curve of purified MIL-101(Cr) powder in Figure 4.5 was consistent with that reported by Liang *et al.* (2013).

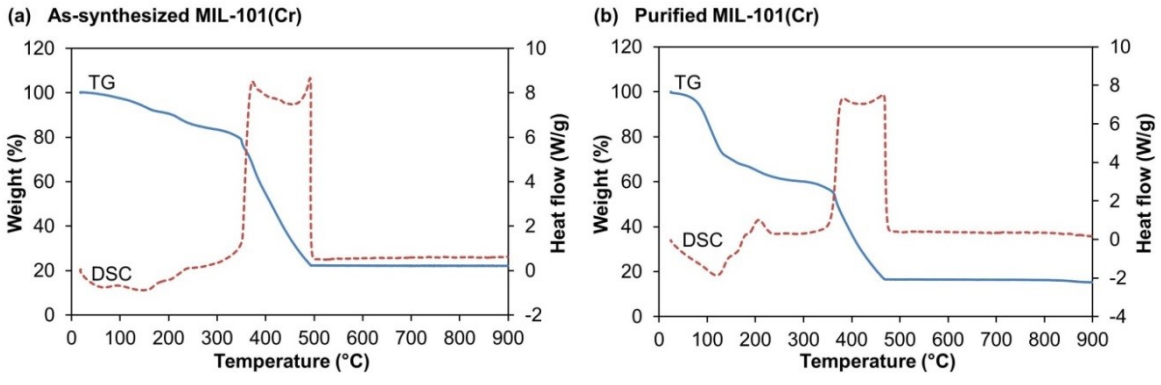


**Figure 4.5** The TG and DSC curves of (a) as-synthesized and (b) purified MIL-101(Cr) powders.

The loss of water molecules from MIL-101(Cr) crystals was also indicated by the endothermic peak of their DSC curves at 100 °C to 200 °C for the as-synthesized and purified MIL-101(Cr). On the other hand, the loss of hydroxyl groups and decomposition of the crystal structure of the MIL-101(Cr) were represented by the exothermic peak of their DSC curves, which was observed at temperature above 370 °C for the as-synthesized MIL-101(Cr) and above 380 °C for the purified MIL-101(Cr). This means the crystal structure of the MIL-101(Cr) was thermally stable at temperature below 370 °C for the as-synthesized MIL-101(Cr) and below 380 °C for the purified MIL-101(Cr). These thermal stability temperatures of the MIL-101(Cr) are the same as those reported in the literature, for example, in Liang *et al.* (2013).

The dehydration of MIL-101(Cr) can be represented by the equation below:

$$\mathrm{Cr_3O(OH)(H_2O)_2(bdc)_3} \rightarrow \mathrm{Cr_3O(OH)(bdc)_3} + 2\mathrm{H_2O} \tag{4.1}$$

where $\mathrm{bdc}$ is 1,4-benzenedicarboxylate. As indicated by their TG and DSC curves in Figures 4.5 (a) and (b), further increase in temperature leads to the loss of hydroxyl groups and decomposition of MIL-101(Cr). The dihydroxylation and decomposition reactions of MIL-101(Cr) can be represented by equations 4.2 and 4.3, respectively. According to Férey *et al.* (2005), the resulting solids for MIL-101(Cr) was $Cr_3O$.

$$\mathrm{Cr_3O(OH)(bdc)_3} \rightarrow \mathrm{Cr_3O(bdc)_3} + \mathrm{OH^-} \tag{4.2}$$

$$\mathrm{Cr_3O(bdc)_3} \rightarrow \mathrm{Cr_3O} + 3\mathrm{bdc} \tag{4.3}$$

#### 4.5.3.2 Crystal structures of MIL-101(Cr) and calcium bentonite in pure powders and those in MIL-101(Cr) monoliths

The PXRD patterns of the prepared MIL-101(Cr) powders shown in Figure 4.6 (a) for the as-synthesized MIL-101(Cr) and in Figure 4.6 (b) for the purified MIL-101(Cr) are similar to those reported in the literature, for example, in Khan *et al.* (2011). This confirms the formation of MIL-101(Cr) crystals during the hydrothermal synthesis. The PXRD patterns of as-synthesized and purified MIL-101(Cr) monoliths are also illustrated in Figures 4.6 (a) and (b), respectively. Their peak positions seem to be a combination of their respective MIL-101(Cr) and calcium bentonite powders.

It was noticed that the PXRD patterns of as-synthesized and purified MIL-101(Cr) monoliths (without or with 4% wt. Licowax C micropowder PM as a pore former) that have been fired at 150 °C or 205 °C show the same peak positions as their respective MIL-101(Cr) and calcium bentonite powders. This indicates that the crystal structures of MIL-

101(Cr) and calcium bentonite retained their original crystalline forms even when they were fired at 150 °C or 205 °C.

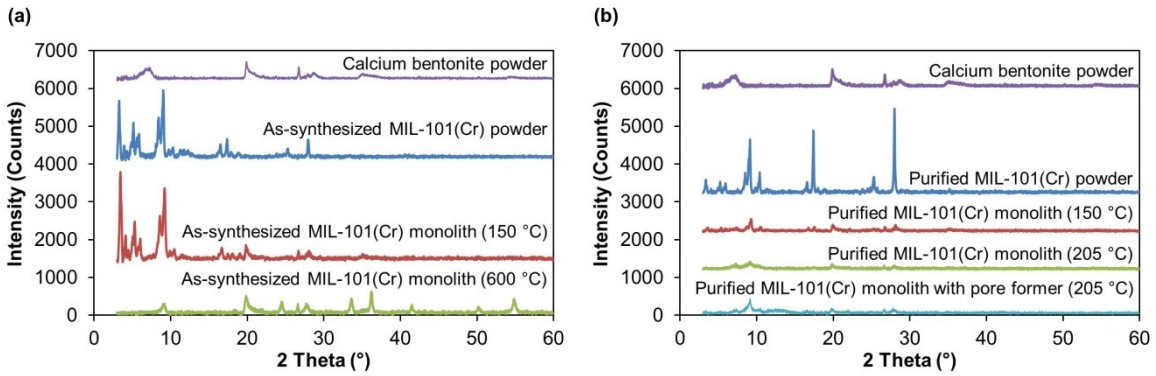


**Figure 4.6** The PXRD patterns of (a) as-synthesized and (b) purified MIL-101(Cr) powders with calcium bentonite powders and their respective MIL-101(Cr) monoliths after been fired at 150 °C, 205 °C or 600 °C.

The PXRD patterns of as-synthesized MIL-101(Cr) monoliths in Figure 4.6 (a) demonstrate that they have slightly different peak positions to the as-synthesized MIL-101(Cr) powder but they have the same peak positions as the calcium bentonite when they were fired at 600 °C. This implies that the crystal structure of the calcium bentonite was maintained but not the crystal structure of the MIL-101(Cr). This shows that the firing temperature of 600 °C was not suitable for MIL-101(Cr) monoliths because it is above the thermal stability temperature of the MIL-101(Cr), i.e., 370 °C.

### 4.5.3.3 Pore properties of MIL-101(Cr) monoliths

The pore properties of the prepared MIL-101(Cr) monoliths either without or with the inclusion of 4% wt. Licowax C micropowder PM as a pore former in their paste formulations are given in Table 4.2. The data in Table 4.2 has experimental errors of about ± 0.023 mL $g^{-1}$ to 0.142 mL $g^{-1}$ for total pore volume, ± 2.8 $m^2$ $g^{-1}$ to 27.9 $m^2$ $g^{-1}$ for total pore surface area, ± 0.3 nm for mean pore diameter, ± 1.9% to 2.6% for porosity and ± 0.05 g $mL^{-1}$ to 0.06 g $mL^{-1}$ for bulk density. The prepared MIL-101(Cr) monoliths containing 60% wt. of either as-synthesized or purified MIL-101(Cr) that have been fired at 150 °C show some difference in their pore properties and this was due to the variation in the arrangement of MIL-101(Cr) and bentonite crystals within the monolithic structure.

The MIP experiments found that their total pore volumes vary slightly by about 0.432 mL $g^{-1}$ with a small difference in their total surface areas by about 46.6 $m^2$ $g^{-1}$, which results in a minor change in their mean pore diameters by about 4.3 nm. As a consequence of these variations, the porosities of as-synthesized and purified MIL-

101(Cr) monoliths were differed by about 12.3%. This shows that the use of either as-synthesized or purified MIL-101(Cr) powders in the fabrication of MIL-101(Cr) monoliths did not have significant influence on the pore properties of the monolithic structure.

**Table 4.2** The pore properties of as-synthesized and purified MIL-101(Cr) monoliths.

| Materials (firing temperature; MIL-101(Cr):Ca bentonite+Licowax C micropowder PM, in % wt.) | Total pore volume[a] ($mL\ g^{-1}$) | Total pore surface area[b] ($m^2\ g^{-1}$) | Mean pore diameter[c] (nm) | Porosity[d] (%) | Bulk density[e] ($g\ mL^{-1}$) |
|---|---|---|---|---|---|
| **As-synthesized MIL-101(Cr) monolith (150 °C; 60:40) – Sample M1** | 1.144 | 229.4 | 19.9 | 68.6 | 0.60 |
| **Purified MIL-101(Cr) monolith (150 °C; 60:40) – Sample M2** | 0.712 | 182.8 | 15.6 | 56.3 | 0.79 |
| **Purified MIL-101(Cr) monolith (205 °C; 75:25) – Sample M3** | 0.992 | 69.8 | 56.9 | 62.5 | 0.63 |
| **Purified MIL-101(Cr) monolith with pore former (205 °C; 75:25+4) – Sample M4** | 1.164 | 195.0 | 23.9 | 65.4 | 0.56 |

**Experimental errors:** [a] ± 0.023 mL $g^{-1}$ to 0.142 mL $g^{-1}$; [b] ± 2.8 $m^2\ g^{-1}$ to 27.9 $m^2\ g^{-1}$; [c] ± 0.3 nm; [d] ± 1.9% to 2.6% and [e] ± 0.05 g $mL^{-1}$ to 0.06 g $mL^{-1}$.

The effect of firing temperature on the pore properties of the prepared MIL-101(Cr) monoliths was also investigated in this study. Assuming that there is no major change in the pore properties for MIL-101(Cr) monoliths of different compositions, the results in Table 4.2 reveal that purified MIL-101(Cr) monoliths have some improvements in their total pore volumes (by about 39%) and mean pore diameters (by about 3.6 times) when their firing temperature was increased from 150 °C to 205 °C. The increment in their mean pore diameters was balanced by the reduction in their total pore surface areas (by about 62%).

It was found that the increment in the total pore volumes of purified MIL-101(Cr) monoliths enhanced their structural porosities by about 11%. This indicates that the impurities present in the calcium bentonite could be burnt off more effectively at 205 °C than at 150 °C, resulting in more accessibility of the pores in the monolithic structure for gas contaminants such as $CO_2$, $H_2O$ vapour and $H_2S$ to penetrate. This would then improve the mass transfer between the gas contaminants and the MIL-101(Cr).

In addition, the effect of incorporating a decomposable pore former (such as Licowax C micropowder PM) in the paste formulations of MIL-101(Cr) monoliths on their pore structures was tested in this work. The results in Table 4.2 show that the pore

properties of purified MIL-101(Cr) monoliths that have included a pore former in their paste formulations were improved compared to those without the inclusion of pore former. This was as a result of additional pores been created within the monolithic structures after the thermal decomposition of the pore former.

In this case, the inclusion of 4% wt. Licowax C micropowder PM in the paste formulation of purified MIL-101(Cr) monoliths was found to increase their total pore volumes slightly by about 17%. This means they have additional storage capacity for gas contaminants. The total pore surface areas of purified MIL-101(Cr) monoliths were also found to increase by about 2.8 times when 4% wt. Licowax C micropowder PM was added to their paste formulations. This means more adsorption sites could be exposed for capturing gas contaminants such as $CO_2$, $H_2O$ vapour and $H_2S$ from the biogas stream.

The results in Table 4.2 show that the mean pore diameters of purified MIL-101(Cr) monoliths that have included 4% wt. Licowax C micropowder PM in their paste formulations were about 2.4 times smaller than those without any addition of the pore former. This was balanced by the increment in their total pore surface areas. The reduction in their mean pore diameters was due to the difference in the arrangement of MIL-101(Cr) and calcium bentonite crystals within the monolithic structure. Since the magnitudes between the increment in their total surface areas and the reduction in their mean pore diameters were almost the same, their influence on the mass transfer or diffusion rates of gas contaminants in the monoliths is assumed to be negligible.

The porosities of purified MIL-101(Cr) monoliths were discovered to increase slightly by about 5% when 4% wt. Licowax C micropowder PM was incorporated in their paste formulations compared to those without any inclusion of the pore former, as indicated in Table 4.2. This confirms the formation of additional pores in the monolithic structure after the pore former was decomposed when heated. By improving the structural porosities of MIL-101(Cr) monoliths, the mass transfer of adsorbate gas molecules in the monolithic structure could be enhanced since more adsorption sites was exposed for adsorbing contaminant gases such as $CO_2$, $H_2O$ vapour and $H_2S$ from the biogas stream.

The bulk densities of MIL-101(Cr) monoliths were also obtained from the MIP experiments. The results in Table 4.2 show that the MIL-101(Cr) monoliths prepared in this study have almost the same bulk densities, i.e., between 0.56 g $mL^{-1}$ and 0.79 g $mL^{-1}$.

Because MIL-101(Cr) is a low density material, the resulting MIL-101(Cr) monoliths have lower bulk densities when compared to zeolite monoliths (refer Section 3.4.2.3).

The pore size distributions of the prepared MIL-101(Cr) monoliths in Figure 4.7 show the variation of pore volumes with their pore diameters. From the pore size distributions of MIL-101(Cr) monoliths that have been fired at 150 °C, as-synthesized MIL-101(Cr) monoliths seems to have slightly larger pore volumes than purified MIL-101(Cr) monoliths in both macropores (by about 1.8 times) and mesopores (by about 1.4 times). These small differences in their pore volumes indicate that as-synthesized and purified MIL-101(Cr) monoliths have almost similar storage capacities for gas contaminants in macropores and mesopores.

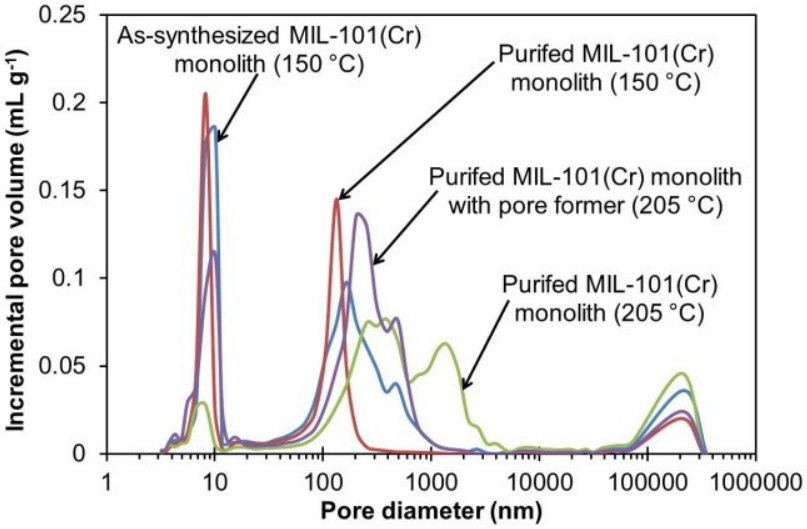


**Figure 4.7** The pore size distributions of as-synthesized and purified MIL-101(Cr) monoliths.

The effect of firing temperature on pore volumes of purified MIL-101(Cr) monoliths is also demonstrated in Figure 4.7. As seen on their pore size distributions, the pore volumes of purified MIL-101(Cr) monoliths was increased by about 2.4 times in macropores and reduced by about 3.2 times in mesopores when their firing temperature was elevated from 150 °C to 205 °C. This shows that the impurities of calcium bentonite in the macropores could be burnt off more effectively at 205 °C than at 150 °C. These results also indicate that the adsorption of contaminant gases such as $CO_2$, $H_2O$ vapour and $H_2S$ on purified MIL-101(Cr) monoliths occur mainly in the macropores.

The pore size distributions of the purified MIL-101(Cr) monoliths with and without the inclusion of a pore former in their paste formulations in Figure 4.7 show that their pore volumes were mainly improved in the mesopores, i.e., by about 3.4 times when their paste

formulations contain 4% wt. Licowax C micropowder PM as a pore former. This clearly confirms the formation of mesopores in MIL-101(Cr) monoliths after the pore former was decomposed upon heating. The results from this study indicate that the pore former generates more mesopores as opposed to zeolite monoliths where more macropores were observed after the pore former was decomposed (refer Section 3.4.2.3). The reason was because most of the pore former aggregates on MIL-101(Cr) monoliths were smaller than those on zeolite monoliths.

#### 4.5.3.4 Morphologies of MIL-101(Cr) powders and monoliths

The scanning electron micrographs of as-synthesized and purified MIL-101(Cr) powders are provided in Figure 4.8 (a) and (b), respectively. The cluster of either as-synthesized or purified MIL-101(Cr) particles seems to be made up of cubical crystals that range from 0.1 μm to 1 μm. The crystal morphology of the MIL-101(Cr) prepared in this study agrees well to those reported in the literature, for example, in Khan *et al.* (2011).

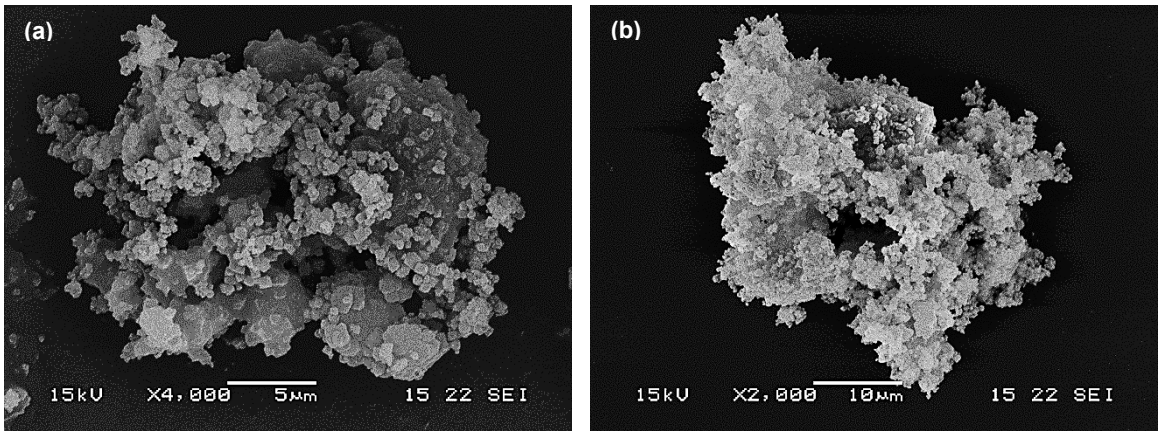


**Figure 4.8** The scanning electron micrographs of (a) as-synthesized and (b) purified MIL-101(Cr) powders.

As seen in Figure 4.9 (a), the surface morphology of the fired as-synthesized MIL-101(Cr) monoliths comprises of cubical MIL-101(Cr) crystals surrounded by materials similar to calcium bentonite crystals. The crystal structures of both MIL-101(Cr) and calcium bentonite seem to maintain their original crystalline forms after they were fired at 150 °C. This shows that the selected firing temperature of 150 °C was below the thermal stabilities of MIL-101(Cr) and calcium bentonite.

When the firing temperature was increased from 150 °C to 600 °C, a different surface morphology of the fired as-synthesized MIL-101(Cr) monoliths was observed, as shown in Figure 4.9 (b). The cubical crystal structure of the MIL-101(Cr) was not seen and the surface morphology was non-homogenous, similar to that in the calcium bentonite,

refer Figure 3.14 (a) in Chapter 3. This means the original crystal structure of the calcium bentonite was retained but not the MIL-101(Cr) when they were heated at 600 °C. This verifies that the selected firing temperature of 600 °C was not suitable for MIL-101(Cr) monoliths because it is above its thermal stability temperature.

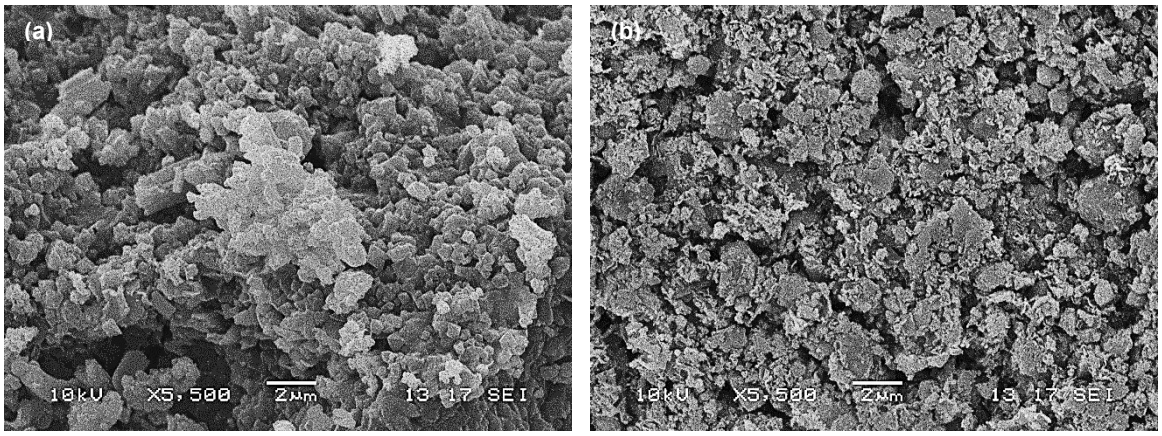


**Figure 4.9** The scanning electron micrographs of as-synthesized MIL-101(Cr) monoliths [60% wt. as-synthesized MIL-101(Cr):40% wt. calcium bentonite] after been fired at (a) 150 °C and (b) 600 °C.

The scanning electron micrographs of purified MIL-101(Cr) monoliths that have been fired at 150 °C and 205 °C are shown individually in Figures 4.10 (a) and (b). The observations on their surface morphologies demonstrate that the cubical MIL-101(Cr) crystals were surrounded by materials resembling that of calcium bentonite crystals. The original crystal structures of MIL-101(Cr) and calcium bentonite were maintained after they were fired at 150 °C or 205 °C. This confirms that the chosen firing temperature of 150 °C or 205 °C was below the thermal stabilities of both MIL-101(Cr) and calcium bentonite.

The effect of including Licowax C micropowder PM as a pore former in the paste formulations of MIL-101(Cr) monoliths on their morphologies was also investigated in this work. The scanning electron micrograph in Figure 4.10 (c) reveals that some macropores have been created on the surface of purified MIL-101(Cr) monoliths when 4% wt. Licowax C micropowder was incorporated in their paste formulations. This proves the formation of macropores in MIL-101(Cr) monoliths after the thermal decomposition of the pore former.

Figure 4.10 (c) also shows that the macropores formed in MIL-101(Cr) monoliths were of different sizes and this was as a result of the random distribution of the pore former within the monolithic structure. A large cluster of pore former at a particular location in the monolithic structure would create a large macropore and vice versa. By enhancing the structural porosity of MIL-101(Cr) monoliths, more adsorption sites could be exposed

for capturing gas contaminants such as $CO_2$, $H_2O$ vapour and $H_2S$ from the biogas stream. This would then result in improved mass transfer between the adsorbate gas contaminants and the MIL-101(Cr).

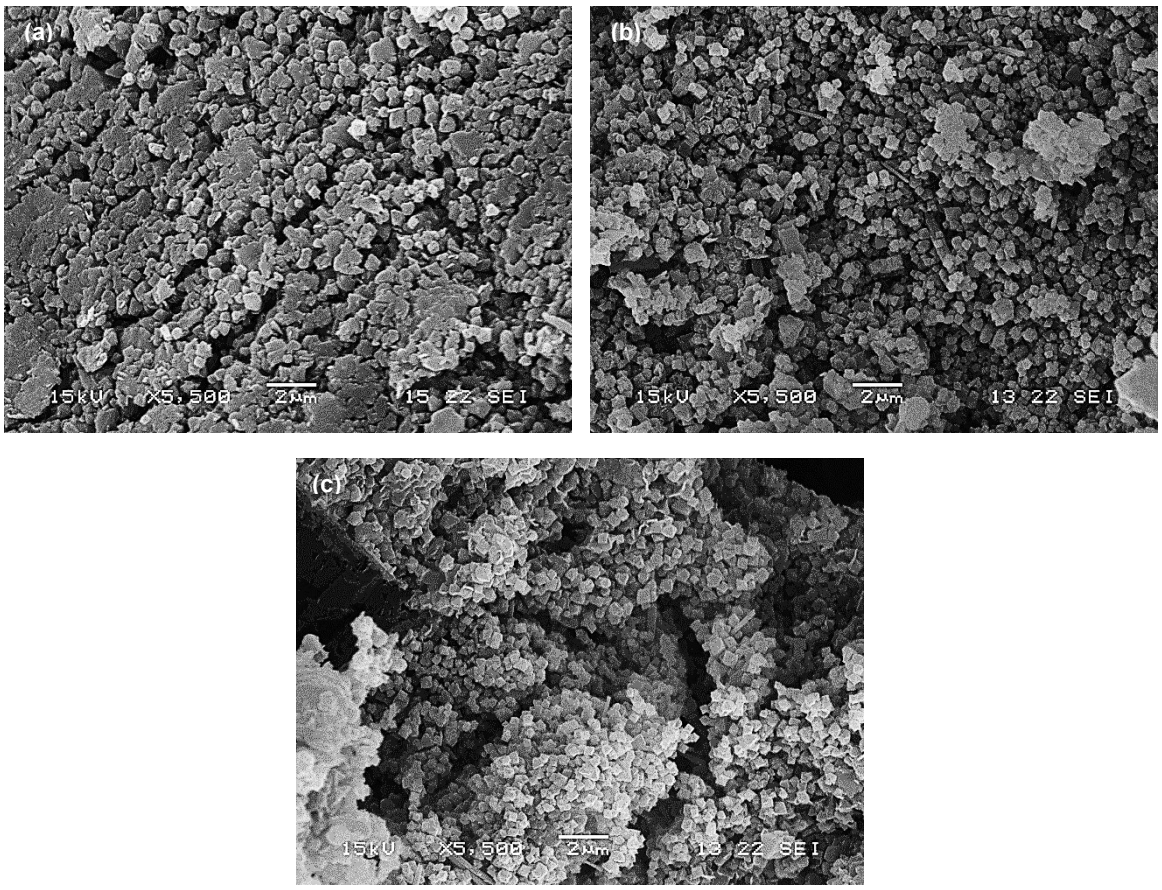


**Figure 4.10** The scanning electron micrographs of purified MIL-101(Cr) monoliths [75% wt. purified MIL-101(Cr):25% wt. calcium bentonite] after been fired at (a) 150 °C or (b) 205 °C and (c) those with pore former [75% wt. purified MIL-101(Cr):25% wt. calcium bentonite+4% wt. Licowax C micropowder PM] after been fired at 205 °C.

#### 4.5.3.5 Mechanical compressive strengths of MIL-101(Cr) monoliths

The MIL-101(Cr) monolith samples used in the mechanical compressive strength tests were run once due to the limitation of MIL-101(Cr) monoliths and the error of the compressive stresses was about 0.9%. The mechanical compressive strengths of the prepared MIL-101(Cr) monoliths containing different weight percentages of calcium bentonite (or adsorbent to clay ratios) on radial compression are shown in Figure 4.11 (a). These MIL-101(Cr) monoliths have been fired at 150 °C and their results indicate that their radial compressive stresses were improved by about 16.5 times when the clay content was increased from 25% wt. to 40% wt. calcium bentonite. The reason for this was because the binding effect between MIL-101(Cr) and calcium bentonite are much stronger when the monolithic structure has a high content of calcium bentonite. As a result, more mechanical stability was imparted to the monolithic structure during the firing process.

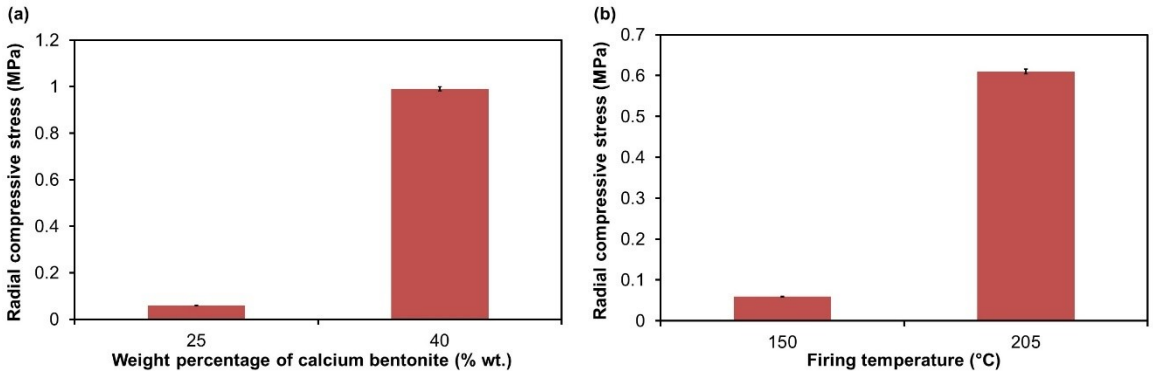


**Figure 4.11** The radial compressive stresses of (a) the prepared MIL-101(Cr) monoliths that have been fired at 150 °C with different weight percentages of calcium bentonite and (b) the purified MIL-101(Cr) monoliths [75% wt. purified MIL-101(Cr):25% wt. calcium bentonite] that have been fired at 150 °C or 205 °C.

Next, the effect of firing temperature on mechanical compressive strengths of the prepared MIL-101(Cr) monoliths was investigated. The mechanical (radial) compression tests were carried out on 75% wt. purified MIL-101(Cr) monoliths that have been fired at 150 °C or 205 °C. The results in Figure 4.11 (b) demonstrate that their radial compressive stresses were improved by about 10.2 times when their firing temperature was raised from 150 °C to 205 °C. This shows that more mechanical strength could be imparted to the monolithic structure as the calcium bentonite becomes more harden at a higher firing temperature.

The effect of pore former (such as Licowax C micropowder PM) on mechanical compressive strengths of the prepared MIL-101(Cr) monoliths was also investigated in this study. The mechanical (radial) compression tests were carried out on 75% wt. purified MIL-101(Cr) monoliths without and with 4% wt. Licowax C micropowder PM in their paste formulations. These MIL-101(Cr) monoliths have been fired at 205 °C. Experimentally, the radial compressive stress of purified MIL-101(Cr) monoliths without any pore former was found to be about 0.6 ± 0.05 MPa while those with 4% wt. Licowax C micropowder PM was found to be about 1.1 ± 0.1 MPa.

These results show very small difference (i.e., ± 0.5 MPa) in their radial compressive stresses and this indicates that the inclusion of 4% wt. Licowax C micropowder PM in the paste formulations of MIL-101(Cr) monoliths did not have major influence on the mechanical compressive strengths of MIL-101(Cr) monoliths. This means MIL-101(Cr) monoliths either without or with 4% wt. Licowax C micropowder PM in their paste formulations are strong enough to be used in the experiments described in this thesis.

#### 4.5.3.6 $CO_2$ adsorption properties of MIL-101(Cr) powder and monolith

In addition to physical characterisation, the $CO_2$ adsorption properties of MIL-101(Cr) powder and monolith were determined by carrying out the gravimetric $CO_2$ sorption analysis. Purified MIL-101(Cr) powder and monolith were used as examples in this work. The purified MIL-101(Cr) monolith contains 60% wt. purified MIL-101(Cr) and 40% wt. calcium bentonite and they have been fired at 150 °C. Pure $CO_2$ adsorption onto purified MIL-101(Cr) powder and monolith was performed up to about 4.4 bar at 20 °C or 25 °C. The pure $CO_2$ adsorption isotherms of purified MIL-101(Cr) powder and monolith at 20 °C and 25 °C are shown in Figure 4.12, with error bars around an average run.

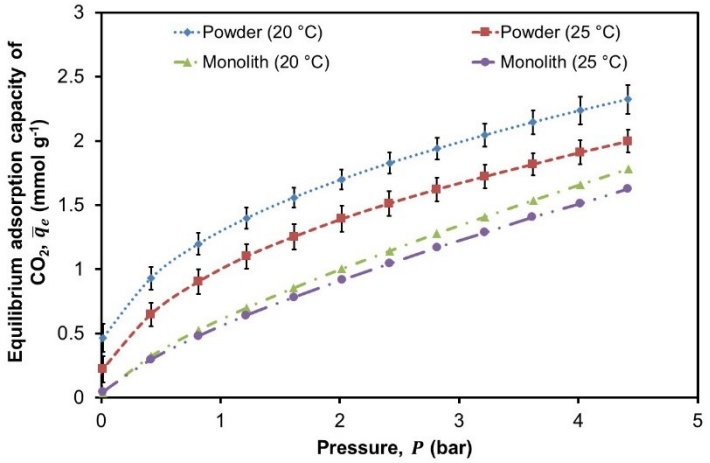


**Figure 4.12** The $CO_2$ adsorption isotherms of purified MIL-101(Cr) powder and monolith [60% wt. purified MIL-101(Cr):40% wt. calcium bentonite; fired at 150 °C] at 20 °C and 25 °C.

The results show that their equilibrium adsorption capacities of $CO_2$ increase with increasing pressure. For example, the equilibrium adsorption capacity of $CO_2$ for the purified MIL-101(Cr) powder at 20 °C was found to increase from 0.52 mmol $g^{-1}$ at 0.01 bar to 2.38 mmol $g^{-1}$ at 4.4 bar. On the other hand, the equilibrium adsorption capacity of $CO_2$ for the purified MIL-101(Cr) monolith at 20 °C was found to increase from 0.04 mmol $g^{-1}$ at 0.01 bar to 1.78 mmol $g^{-1}$ at 4.4 bar. This indicates that more $CO_2$ gas molecules could be forced into the pores and adsorbed onto the adsorption sites of the MIL-101(Cr) at high pressure.

Similar trend was also observed in the study carried out by Zhang *et al.* (2015). They found out that at 20 °C their MIL-101(Cr) powder has an equilibrium adsorption capacity of $CO_2$ of about 1 mmol $g^{-1}$ at 1 bar and it can increase to about 5.6 mmol $g^{-1}$ at 7.4 bar. Figure 4.12 indicates that the MIL-101(Cr) powder synthesized in this study has an equilibrium adsorption capacity of $CO_2$ of 1.3 ± 0.1 mmol $g^{-1}$ at 1 bar and 20 °C. This

value of equilibrium adsorption capacity of $CO_2$ was close to the value reported by Zhang *et al.* (2015).

The results demonstrated that the equilibrium adsorption capacity of $CO_2$ for the purified MIL-101(Cr) monolith was lower than the purified MIL-101(Cr) powder at the same temperature and pressure. For example, it was found that the equilibrium adsorption capacity of $CO_2$ at 20 °C and 1 bar for the purified MIL-101(Cr) monolith was about half of that for the purified MIL-101(Cr) powder. This implies that there were less adsorption sites available for $CO_2$ adsorption in the MIL-101(Cr) monolith compared to the MIL-101(Cr) powder and this was due to the blockage of some pores of MIL-101(Cr) by the calcium bentonite. Munusamy *et al.* (2011) also reported the same behaviour, in which their MIL-101(Cr) granules showed lower equilibrium adsorption of $CO_2$ than MIL-101(Cr) powder. Their results indicate that the equilibrium adsorption of $CO_2$ was 1.68 mmol $g^{-1}$ for MIL-101(Cr) granules and 2.90 mmol $g^{-1}$ for MIL-101(Cr) powder at 10 bar and 30 °C.

The $CO_2$ adsorption isotherms in Figure 4.12 show that the equilibrium adsorption capacities of $CO_2$ for purified MIL-101(Cr) powder and monolith were influenced by the adsorption temperature. When adsorption temperature was increased, the equilibrium adsorption capacity of $CO_2$ was decreased. This was due to the fast desorption of molecules from the surface, which caused the system to reach equilibrium faster (Munusamy *et al.*, 2011). The results reveal that the equilibrium adsorption capacity of $CO_2$ for the purified MIL-101(Cr) powder was reduced by about 48% at 0.01 bar and 14% at 4.2 bar when their adsorption temperature was increased from 20 °C to 25 °C. As for the purified MIL-101(Cr) monolith, its equilibrium adsorption capacity of $CO_2$ starts to decrease at 0.4 bar by about 6% and decrease slightly more by about 8% at 4.4 bar when the adsorption temperature was elevated from 20 °C to 25 °C. These results validate the fact that adsorption is an exothermic process. Several studies, for examples, Munusamy *et al.* (2011), Zhang *et al.* (2011) and Zhang *et al.* (2015), have also reported the same trend.

Repeatability tests for the $CO_2$ adsorption onto purified MIL-101(Cr) powder and monolith were also carried out in this study to verify the experimental adsorption data. The results in Figure 4.12 indicate a minor difference/error of about 0.10 mmol $g^{-1}$ in the equilibrium adsorption capacity of $CO_2$ for the purified MIL-101(Cr) powder when the $CO_2$ adsorption was repeated at 20 °C or 25 °C. For the purified MIL-101(Cr) monolith, its equilibrium adsorption capacity of $CO_2$ was the same when the $CO_2$ adsorption was run for the second time. These results demonstrate that the experimental adsorption data

obtained in this study was accurate and they showed true representation of the $CO_2$ adsorption onto purified MIL-101(Cr) powder and monolith.

## 4.6 Conclusions

This chapter demonstrated that MIL-101(Cr) was produced successfully by hydrothermal reaction according to the novel chemical formulations, which did not contain any harmful hydrofluoric acid. Depending on the processing steps involved in the production of MIL-101(Cr), MIL-101(Cr) powders can be in as-synthesized or purified forms. For the first time, the work described in this chapter showed the possibility of structuring the powdered MIL-101(Cr) into monoliths. The study showed that MIL-101(Cr) monoliths were fabricated successfully based on novel paste formulations using the unique paste extrusion technique. Clay such as calcium bentonite was selected and used as a binder in this study because they have high plasticity and binding effects with MIL-101(Cr). It also provides mechanical stability to the monolithic structure.

An innovative strategy for improving the mass transfer in MIL-101(Cr) monoliths was introduced in this chapter, which was the incorporation of a decomposable pore former such as Licowax C micropowder PM in their paste formulations. When the Licowax C micropowder PM was thermally decomposed, additional pores were formed within the monolithic structure. Therefore, exposing more adsorption sites for capturing gas contaminants such as $CO_2$, $H_2O$ vapour and $H_2S$ from the biogas stream.

Characterisation methods such as simultaneous TGA-DSC, PXRD and SEM have been used to characterise the physical properties of the prepared MIL-101(Cr) powders. The results showed that the prepared MIL-101(Cr) powders have relatively high thermal stabilities, i.e., up to about 370 °C for the as-synthesized MIL-101(Cr) and up to about 380 °C for the purified MIL-101(Cr). The results also showed that their crystal structures would collapse when heated at 600 °C but not at 150 °C or 205 °C.

For the prepared MIL-101(Cr) monoliths, their physical properties were determined by PXRD, MIP, SEM and mechanical compression tests. The PXRD and SEM analyses showed that MIL-101(Cr) crystals were retained in the monolithic structure when they were fired at 150 °C or 205 °C but not at 600 °C. The results of the MIP experiments revealed that the impurities in calcium bentonite were removed more effectively when MIL-101(Cr) monoliths were fired at 205 °C compared to those at 150 °C. Both SEM and

MIP tests have validated the formation of macropores and mesopores within the prepared MIL-101(Cr) monoliths after the pore former was burnt off.

The mechanical compression tests demonstrated that the prepared MIL-101(Cr) monoliths were strong enough to be used in the experiments described in this thesis. It was found that their mechanical strengths on radial compressions increase with increasing content of calcium bentonite (or lower adsorbent to clay ratio) as a result of high binding effect between the calcium bentonite and MIL-101(Cr). The radial compressive strengths of the fired 75% wt. purified MIL-101(Cr) monoliths were found to improve by about 10.2 times when their firing temperature was increased from 150 °C to 205 °C.

The study also demonstrated that there was no significant change in the radial compressive strengths of the fired 75% wt. purified MIL-101(Cr) monoliths when 4% wt. of Licowax C micropowder PM was incorporated in their paste formulations compared to those without any pore former. This implies that the inclusion of 4% wt. of Licowax C micropowder PM in the paste formulations of the MIL-101(Cr) monoliths did not have an influence on their mechanical compressive strengths.

The $CO_2$ adsorption characteristics of the prepared MIL-101(Cr) powder and monolith have also been determined in this study using the gravimetric $CO_2$ gas sorption method. Their $CO_2$ adsorption isotherms showed that their equilibrium adsorption capacity of $CO_2$ increase with increasing pressure and decrease temperature. Their $CO_2$ adsorption isotherms indicated that the maximum equilibrium adsorption capacity of $CO_2$ at 4.4 bar and 20 °C for the purified MIL-101(Cr) powder was about 2.38 mmol $g^{-1}$ and that for the purified MIL-101(Cr) monolith was about 1.78 mmol $g^{-1}$.

Both as-synthesized and purified MIL-101(Cr) monoliths prepared in this study will be optimised for $CO_2$ adsorption, which will be presented later in Chapter 6 of this thesis. The adsorption performance of MIL-101(Cr) monoliths for biogas upgrading will also be assessed by testing them with single (such as $CO_2$, $CH_4$ and $H_2S$) and mixed (such as $CO_2/CH_4$ and $CO_2/CH_4/H_2O$ vapour) gases, see Chapter 7 of this thesis.

# Chapter 5 Fabrication and Characterisation of Carbonate-based Zeolite Foam-Monoliths

In addition to zeolite and MIL-101(Cr) monoliths, this chapter will present the development of a novel adsorbent structure called foam-monolith using an innovative manufacturing approach, in which the foam structure is embedded into the monolithic structure. This invention aims to produce adsorbent foam-monoliths of low pressure drop and enhanced mass transfer properties that would improve the energy efficiency and adsorption performance of the biogas upgrading process. The materials and equipment used in this study are listed in Section 5.1.

The unique extrusion technique described in Chapter 3 will be employed in this study to fabricate the carbonate-based zeolite foam-monoliths according to the specially invented formulations. The model physical adsorbent used in this work is 13X zeolite and it is chosen because they have distinctive molecular sieving properties, reasonably high adsorption capacities for $CO_2$, $H_2O$ vapour and $H_2S$, ease of regeneration, high thermal stability and good tolerance to moisture. Clay such as calcium (Ca) bentonite is selected and use as a binder since they can make the adsorbent pastes mouldable and give mechanical stability to the foam-monolithic structure.

An important ingredient used in this work is the chemical foaming agent such as sodium bicarbonate ($NaHCO_3$) or potassium bicarbonate ($KHCO_3$), which will decompose to produce $CO_2$ gas to create foam structure within the walls of the foam-monoliths. The decomposition of sodium or potassium bicarbonates also produces sodium carbonate ($Na_2CO_3$) or potassium carbonate ($K_2CO_3$), which is incorporated in the foam-monoliths as a chemical sorbent. This type of chemical sorbent can improve the adsorption capacities of $CO_2$, $H_2O$ vapour and $H_2S$ and they are regenerable at temperature below 200 °C (Samantha *et al.*, 2011).

To improve the structural porosity of the foam-monolithic structure, a pore forming agent such as Licowax C micropowder PM will be added to the paste formulations of carbonate-based zeolite foam-monoliths. This type of pore forming agent will decompose upon heating and generate additional pores in the foam-monolithic structure. The presence of these additional pores in carbonate-based zeolite foam-monoliths will enable more adsorption sites to be exposed for capturing gas contaminants such as $CO_2$, $H_2O$ vapour and $H_2S$ from the biogas stream and therefore enhancing the mass transfer in the

foam-monolithic structure. The detailed fabrication procedures used in the preparation of carbonate-based zeolite foam-monoliths are given in Section 5.2.

The physical characteristics of the prepared carbonate-based zeolite foam-monoliths and some of the starting materials will be determined and compared to the 13X zeolite monoliths prepared earlier in the research. Their thermal stabilities, crystal and pore structures, surface morphologies and mechanical compression strengths will be determined using established characterisation methods. This includes the simultaneous thermogravimetry and differential scanning calorimetry (TG-DSC), powder X-ray diffraction (PXRD), mercury intrusion porosimetry (MIP), scanning electron microscopy (SEM) and mechanical strength tests. The experimental procedures of these characterisation methods are given in Section 5.3.

The results for the fabrication and characterisation of carbonate-based zeolite foam-monoliths will be provided and discussed in Section 5.4. Lastly, the work described in this chapter will be concluded in Section 5.5.

## 5.1 Materials and Equipment Used in the Study

The materials used in the fabrication of carbonate-based zeolite foam-monoliths were 13X zeolite powder supplied by Zeochem AG (Switzerland), calcium bentonite powder supplied by Bath Potters' Supplies Ltd. (UK), Licowax C micropowder PM supplied by Clariant (UK), sodium bicarbonate supplied by Sigma-Aldrich Chemie GmbH (Germany), potassium bicarbonate supplied by Sigma-Aldrich Co. (UK) and water. For the comparative study, 13X zeolite monoliths prepared in the research were used. Mercury purchased from Sigma-Aldrich Co. (USA) was used a non-wetting liquid in the MIP analysis. All materials were used as obtained from commercial sources.

The equipment used in this study were the same as those used in the fabrication and characterisation of zeolite monoliths, as outlined in Section 3.1. To produce mechanically strong foam-monoliths, a stainless steel extruder die with a cell density of 30 cells $cm^{-2}$, a channel diameter of 0.9 mm and a wall thickness of 0.9 mm (i.e., Die B) was selected and used for shaping the carbonate-based zeolite foam-monolithic extrudates in this work.

## 5.2 Experimental Procedures for the Fabrication of Carbonate-based Zeolite Foam-Monoliths

The unique foam-extrusion technique used in this study for fabricating carbonate-based zeolite foam-monoliths involved several processing steps, which were: paste preparation, pre-drying, extrusion, drying and firing. These processing steps were the same as those used in the fabrication of zeolite monoliths (refer Chapter 3) but with some modifications. The details of these processing steps are given in Sections 5.2.1 to 5.3.5. The fabrication procedures described in this work must be followed in the right sequence to prevent problems such as surface tearing, cracking and bending, which may occur during the fabrication process.

### 5.2.1 Paste preparation

First, the carbonate-based zeolite pastes were prepared by mixing and kneading dry powders of 13X zeolite, calcium bentonite, sodium or potassium bicarbonate and/or Licowax C micropowder PM with sufficient amount of water on an electric mixer to form homogenous pastes that were plastic and mouldable. To possess the suitable plasticity and consistency for extrusion, it was very important for the carbonate-based zeolite pastes to have the right proportions of starting materials. The carbonate-based zeolite pastes should have low water content with high plasticity so that the occurrence of surface tearing or solid-liquid phase separation during extrusion could be avoided and the drying rate of the extruded foam-monoliths could be reduced. Since the main adsorbent in carbonate-based zeolite foam-monoliths was 13X zeolite, their paste formulations were developed using the 13X zeolite paste formulations (refer Chapter 3) as a starting point.

Normally, structured adsorbents (either in the forms of beads, pellets or granules) produced in the industries contain at least 75% wt. of adsorbent (Li, 1998). Using this adsorbent content as a reference, the carbonate-based zeolite paste formulations would contain 75% wt. 13X zeolite and 25% wt. calcium bentonite with a small amount of the chemical foaming agent and/or pore forming agent as well as a balanced amount of water. The carbonate-based zeolite paste formulations prepared in this work are provided in Table 5.1 and their compositions were expressed in terms of weight percentage (% wt.) of the total dry mass. For example, if the total dry mass is 100 g, sample C2 requires 75 g of 13X zeolite, 25 g of calcium bentonite, 4 g of sodium bicarbonate, 4 g of Licowax C micropowder PM and 106 g of water. To reduce the effect of chemical foaming agent and/or pore forming agent on the mechanical strength of the foam-monolithic structure, a

reasonable amount of 4% wt. sodium or potassium bicarbonates and/or Licowax C micropowder PM was added to the carbonate-based zeolite paste formulations.

**Table 5.1** Compositions of the carbonate-based zeolite pastes prepared in this study.

| Paste sample | 13X zeolite:Bentonite (% wt.) + Foaming agent (% wt.) + Pore forming agent (% wt.) | Water (% wt.) |
|---|---|---|
| C1 | 13X zeolite:Ca bentonite (75:25) + $NaHCO_3$ (4) | 106 |
| C2 | 13X zeolite:Ca bentonite (75:25) + $NaHCO_3$ (4) + Licowax C micropowder PM (4) | 106 |
| C1 | 13X zeolite:Ca bentonite (75:25) + $KHCO_3$ (4) | 95 |
| C2 | 13X zeolite:Ca bentonite (75:25) + $KHCO_3$ (4) + Licowax C micropowder PM (4) | 95 |

### 5.2.2 Pre-drying

When carbonate-based zeolite pastes have been prepared, they were pre-dried in the same manner as zeolite pastes (refer Section 3.2.2) in which the pre-drying process was carried out at room temperature for at least 48 hours. These pre-drying conditions would enable the carbonate-based zeolite pastes to achieve the right plasticity and consistency for extrusion, depending on their water content.

### 5.2.3 Extrusion

Once the carbonate-based zeolite pastes had matured, they were extruded using similar methods as that described for the extrusion of zeolite pastes in Section 3.2.3. In this work, small lumps of carbonate-based zeolite pastes were fed into the paste input of the extruder continuously so that there were no entrapment of air and separation of the carbonate-based zeolite pastes. The carbonate-based zeolite pastes were forced to flow forward along the barrel and through the extruder die to form the carbonate-based zeolite foam-monoliths, which landed on a wax paper.

Then, the extruded carbonate-based zeolite foam-monoliths were cut into the desired lengths using a thin 0.10 mm diameter copper wire. They were placed carefully onto a perforated aluminium tray for ease of handling and reducing skin contacts with the carbonate-based zeolite foam-monoliths.

### 5.2.4 Drying

The drying conditions described in Section 3.2.4 were employed in this study such that carbonate-based zeolite foam-monoliths were dried slowly in a chamber of controlled

temperature (5 °C) and humidity (> 95% relative humidity). Depending on the water content of carbonate-based zeolite foam-monoliths, their drying step could take about a week for them to dry completely.

The carbonate-based zeolite foam-monoliths would shrink slightly because water molecules were evaporated from the pores of 13X zeolite crystals and the interlayers of calcium bentonite crystals during drying. With the controlled drying conditions used in this work, the drying effect and stress on carbonate-based zeolite foam-monoliths could be reduced and hence alleviating the possibilities of cracking and bending of foam-monoliths.

### 5.2.5 Firing

When carbonate-based zeolite foam-monoliths have totally dried, they were placed on ceramic plates in the electric kiln and ready for the firing process. The carbonate-based zeolite foam-monoliths were fired under compressed air using the same firing temperature programmes as those used for firing zeolite monoliths (refer Figure 3.4). The firing temperature was ramped slowly in three stages until the desired high temperature (i.e., 400 °C or 650 °C) was reached. These firing temperatures have been confirmed in Chapter 3 that they were below the thermal stability temperatures of both 13X zeolite and calcium bentonite. This means their crystal structures would not collapse after the firing process.

In the first stage of the firing process, carbonate-based zeolite foam-monoliths were heated slowly from room temperature of 20 °C to 130 °C at a rate of 0.08 °C $min^{-1}$ to remove any remaining water molecules gradually from the pores of zeolite crystals and from the interlayers of bentonite crystals. This was to prevent the formation of cracks on the foam-monolithic structure. In the second stage of the firing process, the temperature in the kiln was increased from 130 °C to either 300 °C or 400 °C at a rate of 0.30 °C $min^{-1}$ with a holding time of 1 hour. The purpose of the second firing stage was to burn off any impurities present in calcium bentonite as well as the chemical forming agent and/or pore forming agent in foam-monoliths.

The $CO_2$ gas produced from the thermal decomposition of the chemical forming agent would create foams within the walls of the foam-monoliths. In addition to the foam structure, additional pores on the foam-monoliths were also created after the thermal decomposition of the pore forming agent that would improve their structural porosity. According to the literature (All Reactions, 2015a, b), sodium bicarbonate decomposes at

temperature between 250 °C and 300 °C whereas potassium bicarbonate decomposes at temperature between 100 °C and 400 °C. This means sodium bicarbonate would decompose in the second firing stage and potassium bicarbonate would decompose either in the first or second firing stage. Sodium or potassium carbonates that were produced from the decomposition of their bicarbonates would be incorporated in the foam-monolithic structure.

Lastly, in the third stage of the firing process, the temperature in the kiln was raised from either 300 °C or 400 °C to their respective chosen temperature of 400 °C or 650 °C at a rate of 0.80 °C $min^{-1}$ with a holding time of 1 hour. In the final firing stage, 13X zeolite, sodium or potassium carbonates and calcium bentonite crystals were bounded together in the foam-monolithic structure. To provide the necessary mechanical strength to the fired carbonate-based zeolite foam-monoliths, the firing temperature of 400 °C or 650 °C was kept constant for 5 hours.

After the firing process has completed, the fired carbonate-based zeolite foam-monoliths was cooled to room temperature naturally in the kiln. This was to avoid rapid contraction on the foam-monoliths as a result of the sudden drop in temperature, which would lead to the formation of cracks on the foam-monolithic structure. The carbonate-based zeolite foam-monoliths were refined by cutting both ends of the foam-monoliths using a saw for characterisation and use in the experiments described in this thesis.

## 5.3 Methods of Characterizing the Carbonate-based Zeolite Foam-Monoliths and Materials

The characterisation methods used in this study were the same as those used in the characterisation of zeolite monoliths (refer Section 3.3). This includes simultaneous TG-DSC, PXRD, MIP, SEM and mechanical compression tests. In this work, the prepared carbonate-based zeolite foam-monoliths and some selected materials such as sodium and potassium bicarbonates were characterised. The experimental procedures of these characterisation methods are given in Sections 5.3.1 to 5.3.5.

### 5.3.1 Simultaneous thermogravimetry and differential scanning calorimetry

First, a powder sample of sodium or potassium bicarbonates was loaded into a small alumina crucible and weighed on a microbalance inside an insulated furnace at room temperature. The environment in the furnace was controlled by flowing cool water to

the system. Argon gas was used to clean the system. The furnace has a built-in thermocouple that was used for measuring the temperature inside the furnace. Prior to the analysis, a temperature programme was created such that the air supplied into the furnace was heated from 20 °C to 900 °C at a rate of 10 °C $min^{-1}$.

The sample was analysed using a simultaneous thermogravimetric and differential scanning calorimetric analyser, which was connected to a computer. After the analysis has completed, the sample was cooled naturally to room temperature before removing them from the furnace. The thermal data of the sample was recorded using a SetSoft2000 programme and they were used to generate the thermogravimetric (TG – i.e., a plot of weight against temperature) and differential scanning calorimetric (DSC – i.e., a plot of heat flow against temperature) curves. All the TG and DSC curves presented in this study have been corrected with the TG and DSC curves of the blank test (thermal data of an empty alumina crucible), which was provided in Appendix 1.

### 5.3.2 Powder X-ray diffraction

Prior to the analysis, carbonate-based zeolite foam-monoliths (Samples C1 to C4) were crushed into fine powder. Each powder sample of sodium bicarbonate, potassium bicarbonate, 13X zeolite, calcium bentonite or carbonate-based zeolite foam-monoliths was placed on a silicon sample cup and mounted onto the sample stage. Then, the sample was examined using a diffractometer with copper radiation (Cu Kα) as a source of X-rays at 21 °C in atmospheric pressure. All powder samples were analysed with a scan step size of 0.016° and scan angles from 3° to 60°. The diffracted X-rays were detected and recorded on a computer. The intensities of the diffracted X-rays were plotted as a function of their angular positions.

### 5.3.3 Mercury intrusion porosimetry

A sample of the prepared carbonate-based zeolite foam-monoliths (Samples C1 to C4) or 13X zeolite monoliths (Samples 2 and 4) was loaded into a glass penetrometer. Then, the loaded penetrometer was assembled onto the low pressure port of the mercury penetrometer to evacuate gases from the sample. Once the low pressure analysis (0 bar to 3.45 bar) had completed, the loaded penetrometer was transferred to the high pressure port of the mercury penetrometer. In the high pressure analysis, mercury was forced into the evacuated sample pores with hydraulic pressure up to about 4 137 bar. The data from the MIP tests was recorded on a computer and they were used to obtain important pore properties such as total pore volume, total pore surface area, mean pore diameter,

porosity, bulk density and pore size distribution of the sample. All MIP data presented in this study have been automatically corrected by the machine with the blank test (of an empty penetrometer) result, which was provided in Appendix 1.

### 5.3.4 Scanning electron microscopy

The samples of carbonate-based zeolite foam-monoliths (Samples C1 to C4), sodium and potassium bicarbonates powders and 13X zeolite powder were placed and attached on the stainless steel sample holder using carbon adhesive. They were kept in a vacuum desiccator overnight to evacuate gases from the samples. Before the SEM examinations, all samples were coated with a thin layer of electrically conductive gold surface using the Edwards sputter coater. Then, they were mounted onto the sample stage in a small vacuum chamber at room temperature and ready for the SEM tests. The SEM tests were started by projecting a beam of electrons onto the surfaces of the samples. The deflected electrons were detected by an electron sensor and formed images of the surface of the samples. These images were observed using an electron microscope and the scanning electron micrographs of the samples were recorded on a computer.

### 5.3.5 Mechanical compression tests

A sample of the prepared carbonate-based zeolite foam-monoliths (Samples C1 to C4 with length between 1.5 cm and 4.0 cm) or 13X zeolite monoliths (Samples 2 and 4 with length between 2.4 cm and 2.7 cm) was tested on an Instron universal tester. Radial or axial compressions were applied to each sample at a constant rate of 0.5 mm $min^{-1}$ until they rupture. The compression tests were carried out at 22 °C under atmospheric pressure. The applied compressive load on the sample and their deformation were recorded on a computer using a Bluehill software.

## 5.4 Results and Discussion for the Fabrication and Characterisation of Carbonate-based Zeolite Foam-Monoliths

This section provides the results and discussion for the carbonate-based zeolite foam-monoliths prepared and characterised in this study. The fabrication results of carbonate-based zeolite foam-monoliths as well as their fabrication challenges are cover and discuss in Section 5.4.1. Then, the results and discussion for the characterisation of carbonate-based zeolite foam-monoliths and some selected materials such as sodium and potassium bicarbonates powders, 13X zeolite powder/monoliths and calcium

bentonite powder are given in Section 5.4.2. In this work, the physical characteristics of carbonate-based zeolite foam-monoliths are compared to those of 13X zeolite monoliths.

### 5.4.1 Fabrication of carbonate-based zeolite foam-monoliths

Foam-monoliths of sodium carbonate-based 13X zeolite ($Na_2CO_3$/13X zeolite) and potassium carbonate-based 13X zeolite ($K_2CO_3$/13X zeolite) were successfully fabricated according to the novel paste formulations described in this study. The prepared carbonate-based zeolite foam-monoliths have square channels of 0.9 mm wide and their walls were 0.9 mm thick. As seen in Figure 5.1, the colour of the fired carbonate-based zeolite foam-monoliths was white.

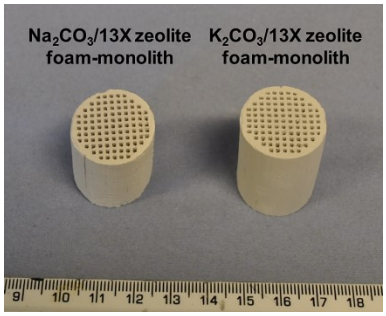


**Figure 5.1** Photograph of the manufactured $Na_2CO_3$/13X zeolite and $K_2CO_3$/13X zeolite foam-monoliths (Samples C2 and C4, respectively) with 0.9 mm thick walls.

It was found that the amount of water used in the carbonate-based zeolite paste preparation (refer Table 5.1) varies with the type of bicarbonates and this was because they have different solubilities in water. This work discovered that the paste formulations containing 4% wt. $NaHCO_3$ required 11% wt. more water than those containing 4% wt. $KHCO_3$, indicating that $NaHCO_3$ is less soluble in water than $KHCO_3$. The optimum ratios of water to dry powders (i.e., 13X zeolite, calcium bentonite, $NaHCO_3$ or $KHCO_3$ and/or pore former) were discovered to be 1.06 for $Na_2CO_3$/13X zeolite and 0.95 for $K_2CO_3$/13X zeolite paste formulations.

The photographs in Figure 5.2 (a) and (b) show the occurrence of cracking and bending on the prepared carbonate-based zeolite foam-monoliths during the drying step of the fabrication process. The cracking of carbonate-based zeolite foam-monoliths was due to the rapid evaporation of water from the surfaces of the foam-monoliths, which induces uneven stress on the foam-monolithic structure. To prevent cracking from happening during the drying step, the tray of carbonate-based zeolite foam-monoliths needs to be kept in a chamber of controlled temperature and humidity immediately after the foam-extrusion to slow down the evaporation of water.

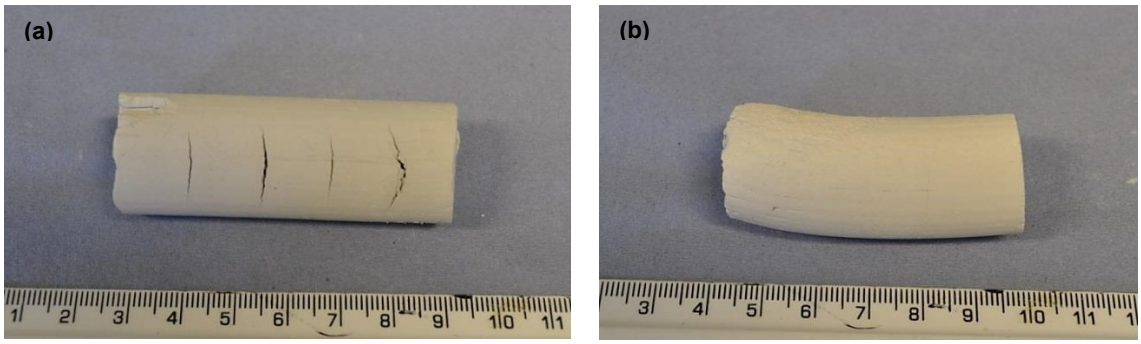


**Figure 5.2** Photographs of (a) a cracked $K_2CO_3$/13X zeolite foam-monolith (Sample C4) and (b) a bent $Na_2CO_3$/13X zeolite foam-monolith (Sample C2).

On the other hand, the bending of carbonate-based zeolite foam-monoliths during the drying step was caused by the uneven drying and stress on carbonate-based zeolite foam-monoliths. The bending issue could be overcome by drying them at a slow rate so that the induced stress on the foam-monolithic structure could be minimized and even out all over the foam-monoliths.

### 5.4.2 Characterisation of carbonate-based zeolite foam-monoliths and materials

This section provides the characterisation results of the prepared carbonate-based zeolite foam-monoliths and some selected materials such as sodium and potassium bicarbonates powders, 13X zeolite powder/monoliths and calcium bentonite powder. Their physical properties such as thermal properties, crystal structures, pore properties, morphologies and mechanical compressive strengths are provided and discussed in Sections 5.4.2.1 to 5.4.2.5. The physical characteristics of carbonate-based zeolite foam-monoliths are also compared to those of 13X zeolite monoliths.

#### 5.4.2.1 Thermal properties of sodium and potassium bicarbonates

The TG and DSC curves of the sodium bicarbonate powder are shown in Figure 5.3 (a) while those of the potassium bicarbonate powder are shown in Figure 5.3 (b). The changes in weight and heat flow during heating were analysed to determine their weight losses and thermal stabilities. As seen in Figure 5.3 (a), the TG curve of the $NaHCO_3$ shows that there was a weight loss of about 38.9% up to 200 °C due to decomposition. The TG curve of $NaHCO_3$ obtained in this study was in good agreement with that reported by Park *et al.* (2006). Their results showed that $NaHCO_3$ has a weight loss of about 36.4% up to 211 °C when heated. Their results were close to the values found in this study.

The thermal decomposition of $NaHCO_3$ to produce $Na_2CO_3$, $CO_2$ gas and $H_2O$ vapour was indicated by the endothermic peak of their DSC curve at 80 °C to 220 °C. In their DSC curve, the endothermic peaks observed at temperature above 700 °C were resulted from the melting and decomposition of $Na_2CO_3$ to form sodium oxide ($Na_2O$) and $CO_2$ gas. This means $NaHCO_3$ starts to decompose at 80 °C to form $Na_2CO_3$, $CO_2$ gas and $H_2O$ vapour and the decomposition reaction completes at 220 °C. These decomposition temperature values were close to those reported by Chaiwang *et al.* (2016), who found that $NaHCO_3$ began to decompose at 100 °C and terminated in the range between 150 °C and 250 °C. The firing temperature for $Na_2CO_3$/13X zeolite foam-monoliths must not be higher than 700 °C to prevent the conversion of $Na_2CO_3$ to $Na_2O$.

Similar to the thermal behaviour of $NaHCO_3$, the TG curve in Figure 5.3 (b) shows that $KHCO_3$ has a weight loss of about 31.6% up to 220 °C when they are heated as a result of decomposition. This corresponds to the endothermic peak of their DSC curve at 100 °C to 260 °C. In their DSC curve, the endothermic peak seen at temperature above 880 °C was resulted from the melting and decomposition of $K_2CO_3$ to form potassium oxide ($K_2O$) and $CO_2$ gas. This means that $KHCO_3$ starts to decompose at 100 °C to form $K_2CO_3$, $CO_2$ gas and $H_2O$ vapour and the decomposition reaction completes at 260 °C. The starting decomposition temperature of $KHCO_3$ found in this study was similar to the value reported by All Reactions (2015b). The decomposition temperature ranges found in this study were close to those reported by Chaiwang *et al.* (2016), who found that $KHCO_3$ began to decompose at 120 °C and terminated in the range between 200 °C and 300 °C. The firing temperature for $K_2CO_3$/13X zeolite foam-monoliths should be below 880 °C to avoid the decomposition of $K_2CO_3$ to $K_2O$.

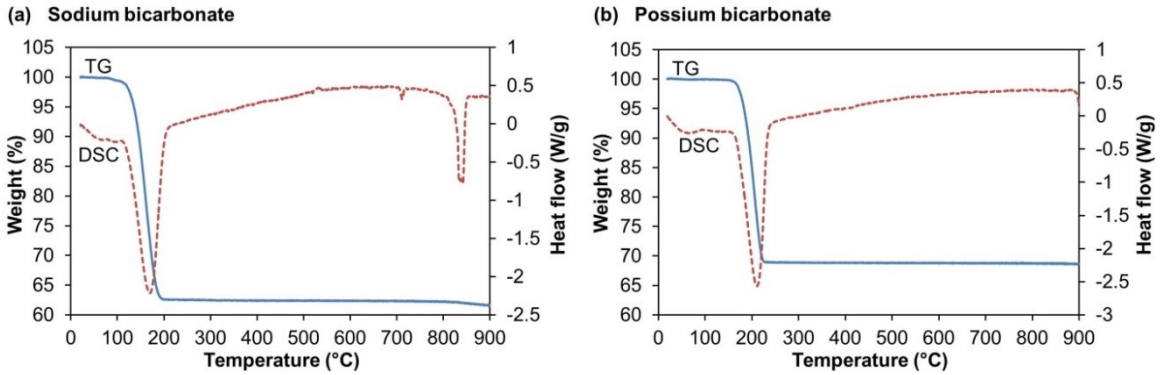


**Figure 5.3** The TG and DSC curves of the (a) sodium bicarbonate and (b) potassium bicarbonate powders.

### 5.4.2.2 Crystal structures of carbonate-based zeolite foam-monoliths and some of their starting materials

The PXRD patterns of sodium and potassium carbonate-based foam-monoliths in Figures 5.4 (a) and (b) show that they possess the same peak positions as 13X zeolite and calcium bentonite powders. This means the crystal structures of both 13X zeolite and calcium bentonite were retained after they were fired at 400 °C or 650 °C. The PXRD patterns of $Na_2CO_3$/13X zeolite and $K_2CO_3$/13X zeolite foam-monoliths seem to be different to their respective bicarbonates (i.e. $NaHCO_3$ and $KHCO_3$ powders). This indicates that the crystal structures of $NaHCO_3$ and $KHCO_3$ collapsed when they decomposed thermally in the firing process at 400 °C or 650 °C.

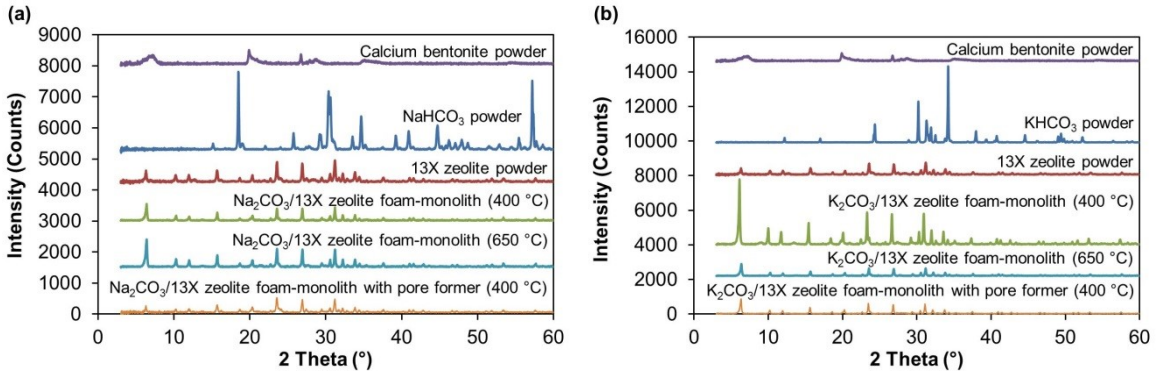


**Figure 5.4** The PXRD patterns of (a) sodium carbonate/13X zeolite and (b) potassium carbonate/13X zeolite foam-monoliths after been fired at 400 °C or 650 °C as well as those of the sodium and potassium bicarbonates, calcium bentonite and 13X zeolite powders.

### 5.4.2.3 Pore properties of carbonate-based zeolite foam-monoliths in comparison to 13X zeolite monoliths

The pore properties of the prepared carbonate-based zeolite foam-monoliths and 13X zeolite monoliths are provided in Table 5.2. The data in Table 5.2 has experimental errors of about ± 0.055 mL $g^{-1}$ to 0.210 mL $g^{-1}$ for total pore volume, ± 8.6 $m^2$ $g^{-1}$ to 53.5 $m^2$ $g^{-1}$ for total pore surface area, ± 101 nm to 110 nm for mean pore diameter, ± 12.2% to 24.3% for porosity and ± 0.01 g $mL^{-1}$ to 0.15 g $mL^{-1}$ for bulk density. The results show that the prepared carbonates based zeolite foam-monoliths have almost the same pore properties, irrespective to the type of carbonates ($Na_2CO_3$ or $K_2CO_3$) been incorporated in the foam-monolithic structure. This indicates that the type of carbonates did not have major influence on the pore properties of the foam-monoliths.

Although the results in Table 5.2 show that the prepared carbonate-based zeolite foam-monoliths have almost the same total pore volumes, total surface areas, porosities and bulk densities as 13X zeolite monoliths, their mean pore diameters were slightly

bigger (by about 13% for $Na_2CO_3$/13X zeolite and 7% for $K_2CO_3$/13X zeolite) compared to 13X zeolite monoliths. This small difference in their mean pore diameters verifies the formation of foams within the walls of the foam-monoliths. The enlargement in the mean pore diameters of carbonate-based zeolite foam-monoliths would enable more penetration of the adsorbate gas contaminants such as $CO_2$, $H_2O$ vapour and $H_2S$ through the pores, which would increase the mass transfer rate within the foam-monolithic structures.

**Table 5.2** The pore properties of carbonate-based zeolite foam-monoliths and 13X zeolite monoliths.

| **Materials (firing temperature; 13X zeolite:Ca bentonite+$NaHCO_3$/$KHCO_3$+Licowax C micropowder PM, in % wt.)** | **Total pore volume[a] (mL $g^{-1}$)** | **Total pore surface area[b] ($m^2$ $g^{-1}$)** | **Mean pore diameter[c] (nm)** | **Porosity[d] (%)** | **Bulk density[e] (g $mL^{-1}$)** |
|---|---|---|---|---|---|
| **13X zeolite monolith (400 °C; 75:25) – Sample 2** | 0.412 | 14.2 | 116.1 | 47.9 | 1.16 |
| **13X zeolite monolith with pore former (400 °C; 75:25+4) – Sample 4** | 0.464 | 15.7 | 118.0 | 50.8 | 1.10 |
| **$Na_2CO_3$/13X zeolite foam-monolith (400 °C; 75:25+4) – Sample C1** | 0.390 | 11.3 | 138.0 | 44.6 | 1.15 |
| **$Na_2CO_3$/13X zeolite foam-monolith (650 °C; 75:25+4) – Sample C1** | 0.402 | 15.4 | 104.2 | 45.2 | 1.13 |
| **$Na_2CO_3$/13X zeolite foam-monolith with pore former (400 °C; 75:25+4+4) – Sample C2** | 0.463 | 14.7 | 126.1 | 49.1 | 1.06 |
| **$K_2CO_3$/13X zeolite foam-monolith (400 °C; 75:25+4) – Sample C3** | 0.391 | 12.0 | 130.8 | 44.9 | 1.15 |
| **$K_2CO_3$/13X zeolite foam-monolith (650 °C; 75:25+4) – Sample C3** | 0.428 | 14.1 | 121.2 | 46.6 | 1.09 |
| **$K_2CO_3$/13X zeolite foam-monolith with pore former (400 °C; 75:25+4+4) – Sample C4** | 0.490 | 16.4 | 119.4 | 50.6 | 1.03 |
| **Experimental errors:** [a] ± 0.055 mL $g^{-1}$ to 0.210 mL $g^{-1}$; [b] ± 8.6 $m^2$ $g^{-1}$ to 53.5 $m^2$ $g^{-1}$; [c] ± 101 nm to 110 nm; [d] ± 12.2% to 24.3% and [e] ± 0.01 g $mL^{-1}$ to 0.15 g $mL^{-1}$. | | | | | |

The effect of firing temperature on the pore properties of carbonate-based zeolite monoliths was investigated in this work. As indicated in Table 5.2, there were small improvements in the total pore volumes and total pore surface areas of carbonate-based zeolite foam-monoliths when their firing temperature was elevated from 400 °C to 650 °C. For example, $Na_2CO_3$/13X zeolite foam-monoliths was found to have a minor increment in their total pore volumes by about 3% and in their total pore surface areas by about 36%, which were balanced by a reduction in their mean pore diameters by about 25%. Similarly, $K_2CO_3$/13X zeolite foam-monoliths was found to have a slight increment in their total pore volumes by about 9% and in their total pore surface areas by about 18%, which were balanced by a small reduction of about 7% in their mean pore diameters.

The increment in their total pore volumes did not show significant changes on the porosities of the foam-monolithic structure because the results showed very small improvements in their structural porosities, i.e., by about 1% for $Na_2CO_3$/13X zeolite and 4% for $K_2CO_3$/13X zeolite foam-monoliths when the firing temperature was raised from 400 °C to 650 °C. This demonstrates that the pore properties of carbonate-based zeolite foam-monoliths were not influenced by the firing temperature.

The effect of pore former on the pore properties of carbonate-based zeolite foam-monoliths was also studied in this work. The results in Table 5.2 reveal that the addition of a pore former in the paste formulation of carbonate-based zeolite foam-monoliths would increase their total pore volumes, total pore surface areas and porosities. In this case, the inclusion of 4% wt. Licowax C micropowder PM in the paste formulations of $Na_2CO_3$/13X zeolite foam-monoliths was found to increase their total pore volumes by about 19% and their pore surface areas by about 30%, which were balanced by a small reduction of about 9% in their mean pore diameters.

Similar improvement in pore properties was also demonstrated by $K_2CO_3$/13X zeolite foam-monoliths when a pore former was added in their paste formulations. It was found that the inclusion of 4% wt. Licowax C micropowder PM in the paste formulations of $K_2CO_3$/13X zeolite foam-monoliths increases their total pore volumes by about 26% and their pore surface areas by about 37%, which were balanced by a small reduction of about 9% in their mean pore diameters. The increment in the total pore volumes and pore surface areas of carbonate-based zeolite foam-monoliths implies that more gas contaminants such as $CO_2$, $H_2O$ vapour and $H_2S$ could be stored in the foam-monolithic structure and more adsorption sites were exposed for adsorbing gas contaminants.

Additionally, the porosities of carbonate-based zeolite foam-monoliths were found to be improved by about 10% for $Na_2CO_3$/13X zeolite foam-monoliths and about 13% for $K_2CO_3$/13X zeolite foam-monoliths when 4% wt. Licowax C micropowder PM was incorporated in their paste formulations compared to those without any inclusion of the pore former, as indicated in Table 5.2. This confirms the formation of macropores in the foam-monolithic structure after the thermal decomposition of the pore former. The macropores created in carbonate-based zeolite foam-monoliths would enable more adsorption sites to be exposed for capturing contaminant gases such as $CO_2$, $H_2O$ vapour

and $H_2S$ from the biogas stream, which would in turn enhance the mass transfer in foam-monoliths.

The bulk densities of carbonate-based zeolite foam-monoliths obtained from the MIP experiments are listed in Table 5.2. The results show that all the carbonate-based zeolite foam-monoliths prepared in this study have almost the same bulk densities, which ranged from 1.03 g $mL^{-1}$ to 1.15 g $mL^{-1}$.

The variation in pore volumes of carbonate-based zeolite foam-monoliths with respect to their pore diameters was plotted to show the pore size distributions in the foam-monolithic structure. The pore size distributions in Figure 5.5 (a) show that the pore volumes of $Na_2CO_3$/13X zeolite foam-monoliths was about 12 times larger in the macropores than those in the mesopores. On the other hand, the pore size distributions in Figure 5.5 (b) show that the pore volumes of $K_2CO_3$/13X zeolite foam-monoliths was about 13 times larger in the macropores than those in the mesopores. These results indicate that more adsorbate gas contaminants such as $CO_2$, $H_2O$ vapour and $H_2S$ would be adsorbed and stored in the macropores compared to those in the mesopores of the carbonate-based zeolite foam-monoliths.

The pore size distributions in Figures 5.5 (a) and (b) also show that the variation in pore volumes with the pore diameters of carbonate-based zeolite foam-monoliths were identical to those of 13X zeolite monoliths, i.e., they have larger pore volumes in the macropores compared those in the mesopores. This implies that both foam-monolithic and monolithic structures would capture and store more adsorbate gas contaminants in the macropores and less in the mesopores.

The effect of firing temperature on the pore volumes of the prepared carbonate-based zeolite foam-monoliths was also demonstrated in Figure 5.5 (a) for $Na_2CO_3$/13X zeolite foam-monoliths and in Figure 5.5 (b) for $K_2CO_3$/13X zeolite foam-monoliths. Their pore size distributions did not show major changes in pore volumes when the firing temperature was raised from 400 °C to 650 °C although there were minor improvements in their pore volumes (in both macropores and mesopores). The study found that the pore volumes of $Na_2CO_3$/13X zeolite foam-monoliths were increased slightly by about 2% in the macropores and 13% in the mesopores when the firing temperature was elevated from 400 °C to 650 °C. For $K_2CO_3$/13X zeolite foam-monoliths, their pore volumes were found to increase slightly by about 10% in the macropores and 6% in the mesopores. These

results indicate that the pore volumes of carbonate-based zeolite foam-monoliths were not influenced by the firing temperature.

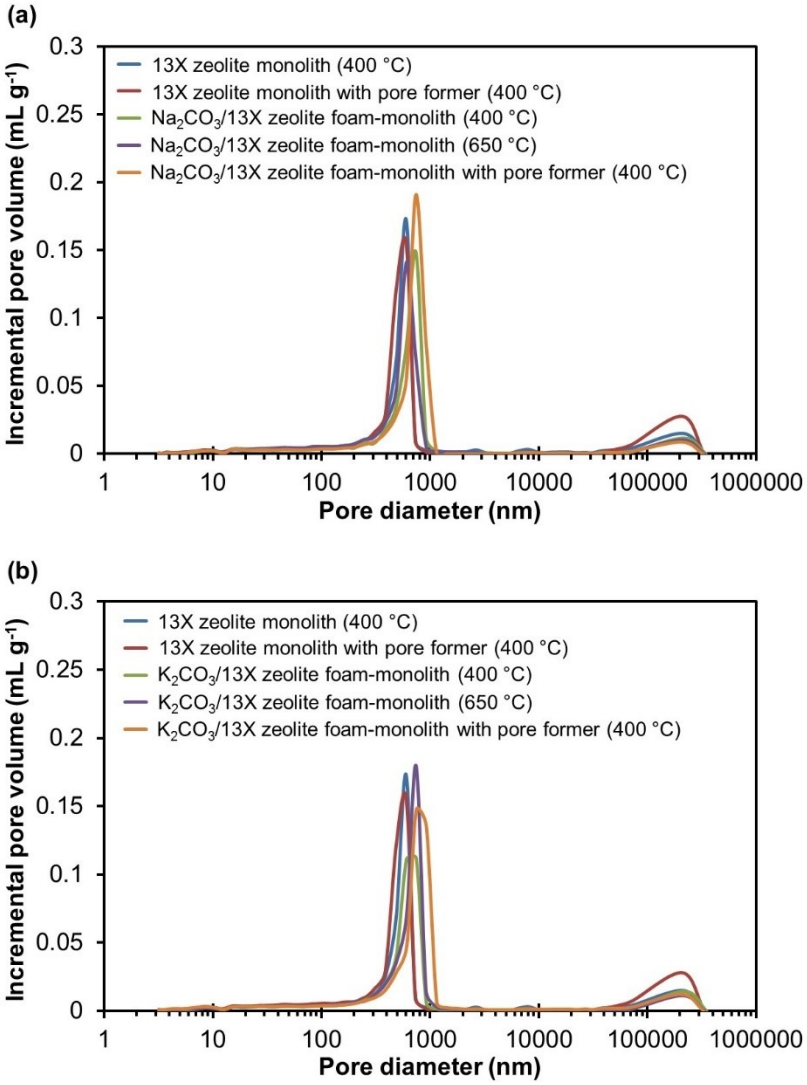


**Figure 5.5** The pore size distributions of (a) $Na_2CO_3$/13X zeolite and (b) $K_2CO_3$/13X zeolite foam-monoliths as well as those of the 13X zeolite monoliths.

The pore size distributions in Figures 5.5 (a) and (b) show that the pore volumes of carbonate-based zeolite foam-monoliths were improved in both macropores and mesopores when a pore former was included their paste formulations. In this work, the inclusion of 4% wt. Licowax C micropowder PM as a pore former in the paste formulations of $Na_2CO_3$/13X zeolite foam-monoliths was found to increase their pore volumes by about 20% in the macropores and 5% in the mesopores. For $K_2CO_3$/13X zeolite foam-monoliths, their pore volumes were found to increase by about 26% in the macropores and 17% in the mesopores when their paste formulations contained 4% wt. Licowax C micropowder PM. This confirms the formation of macropores and mesopores in carbonate-based zeolite foam-monoliths after the pore former was decomposed when heated.

#### 5.4.2.4 Morphologies of carbonate-based zeolite foam-monoliths, sodium bicarbonate and potassium bicarbonate powders

The scanning electron micrographs of sodium bicarbonate and potassium bicarbonate powders are shown separately in Figures 5.6 (a) and (b). Both of them seem to be made up of monoclinical crystals with particle sizes ranging between 25 μm and 400 μm for $NaHCO_3$ and between 25 μm and 600 μm for $KHCO_3$. These monoclinical crystals of sodium or potassium bicarbonates are not observed in the surface morphologies of the fired carbonate-based zeolite foam-monoliths (see Figures 5.7 (a) to (c) for $Na_2CO_3$/13X zeolite foam-monoliths and Figures 5.8 (a) and (c) for $K_2CO_3$/13X zeolite foam-monoliths). This verifies the decomposition of sodium or potassium bicarbonates when they were heated in the firing process to produce $Na_2CO_3$ or $K_2CO_3$, $CO_2$ gas and $H_2O$ vapour. The SEM image of $NaHCO_3$ shown in Figure 5.6 matches with that reported by Park *et al.* (2006).

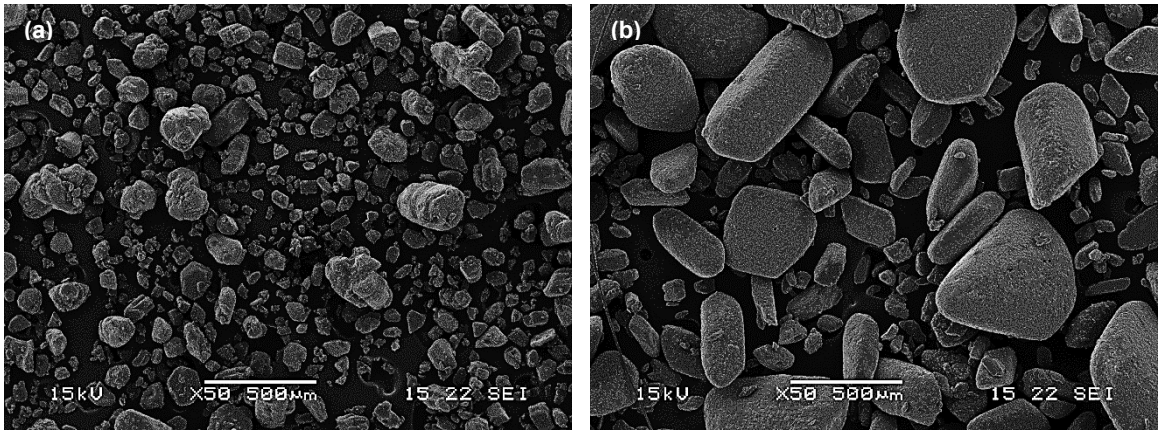


**Figure 5.6** The scanning electron micrographs of (a) sodium bicarbonate and (b) potassium bicarbonate powders.

As seen in Figures 5.7 (a) and (b), the surface morphologies of the fired $Na_2CO_3$/13X zeolite foam-monoliths consist of cubical 13X zeolite crystals surrounded by materials similar to calcium bentonite crystals but different to the monoclinical sodium bicarbonate crystals. The original crystal structures of both 13X zeolite and calcium bentonite were maintained but not the sodium bicarbonate when they were fired at 400 °C or 650 °C. This proves that these firing temperatures were below the thermal stabilities of both 13X zeolite and calcium bentonite and they were high enough for the sodium bicarbonate to decompose and produce sodium carbonate, $CO_2$ gas and $H_2O$ vapour.

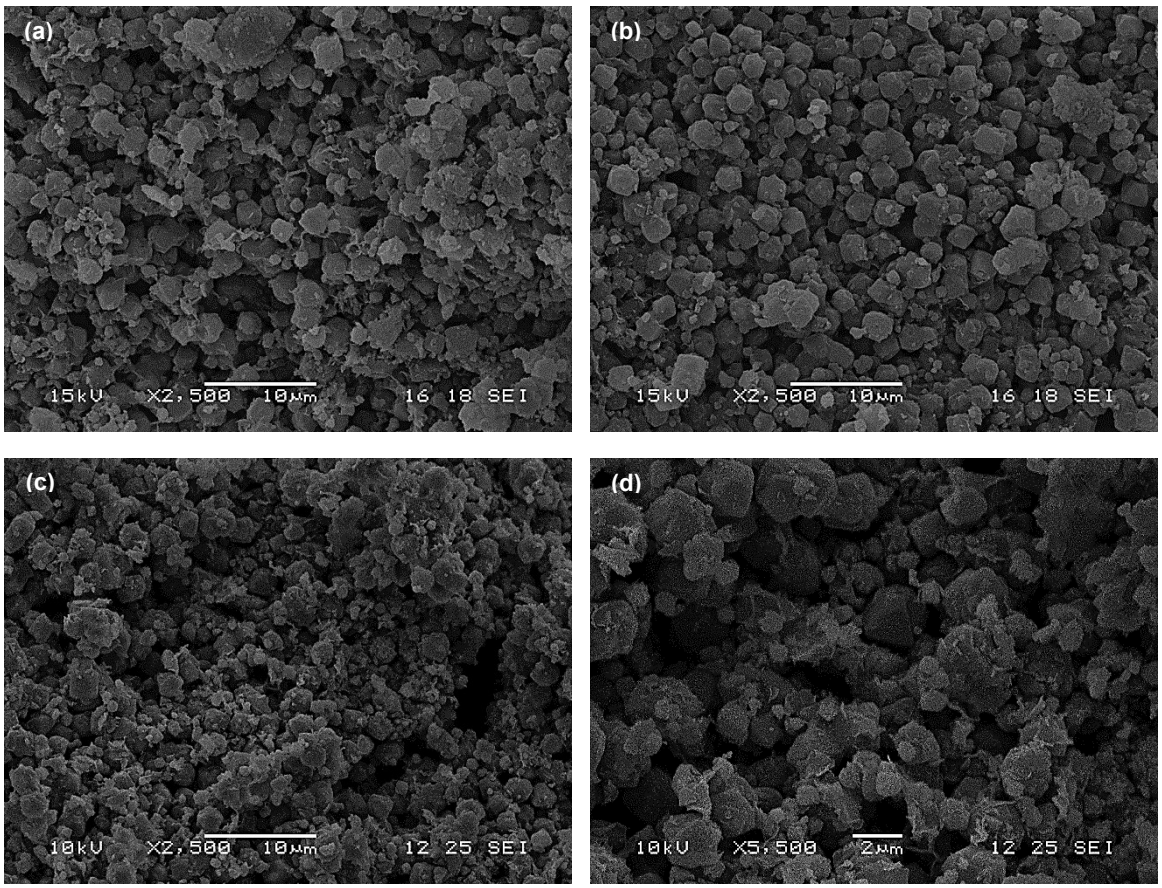


**Figure 5.7** The scanning electron micrographs of $Na_2CO_3$/13X zeolite foam-monoliths [75% wt. 13X zeolite:25% wt. calcium bentonite+4% wt. $NaHCO_3$] after been fired at (a) 400 °C or (b) 650 °C and (c and d) those with pore former [75% wt. 13X zeolite:25% wt. calcium bentonite+4% wt. $NaHCO_3$+4% wt. Licowax C micropowder PM] after been fired at 400 °C with magnifications of x2 500 and x5 500, respectively.

The effect of including Licowax C micropowder PM as a pore former in the paste formulations of $Na_2CO_3$/13X zeolite foam-monoliths on their morphologies was also investigated in this work. Figure 5.7 (c) reveals that some macropores were created on the surface of $Na_2CO_3$/13X zeolite foam-monoliths when 4% wt. Licowax C micropowder was incorporated in their paste formulations. This confirms the formation of macropores in $Na_2CO_3$/13X zeolite foam-monoliths after the thermal decomposition of the pore former. By improving the macroporosity of the foam-monolithic structure, more adsorption sites could be exposed for adsorbing the gas contaminants such as $CO_2$, $H_2O$ vapour and $H_2S$ from the biogas stream and therefore enhancing the mass transfer in $Na_2CO_3$/13X zeolite foam-monoliths. At higher magnification of x5 500, it can be seen in Figure 5.7 (d) that 13X zeolite and $Na_2CO_3$ crystals were bounded by calcium bentonite after the firing process. This behaviour was similar to that observed in Figures 5.7 (a) and (b).

Similar to $Na_2CO_3$/13X zeolite foam-monoliths, the surface morphologies of the fired $K_2CO_3$/13X zeolite foam-monoliths in Figures 5.8 (a) and (b) also show that the cubical 13X zeolite crystals were interlinked with materials similar to calcium bentonite crystals

but different to the monoclinical potassium bicarbonate crystals. The crystal structures of both 13X zeolite and calcium bentonite seems to be retained their original crystalline forms but this was not the case for the potassium bicarbonate when they were fired at 400 °C or 650 °C. This confirms that the firing temperatures used in this work were below the thermal stabilities of both 13X zeolite and calcium bentonite and they were high enough for the potassium bicarbonate to decompose to produce potassium carbonate, $CO_2$ gas and $H_2O$ vapour.

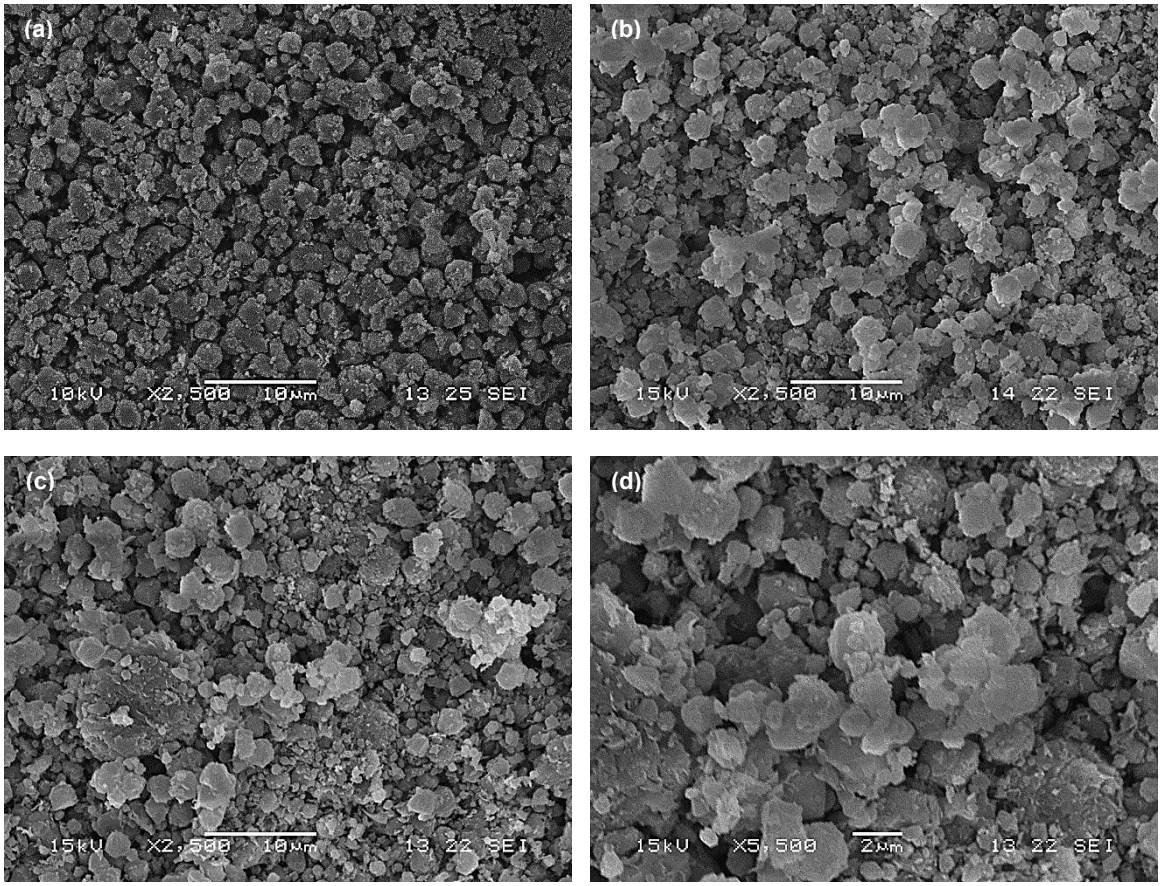


**Figure 5.8** The scanning electron micrographs of $K_2CO_3$/13X zeolite foam-monoliths [75% wt. 13X zeolite:25% wt. calcium bentonite+4% wt. $KHCO_3$] after been fired at (a) 400 °C or (b) 650 °C and (c and d) those with pore former [75% wt. 13X zeolite:25% wt. calcium bentonite+4% wt. $KHCO_3$+4% wt. Licowax C micropowder PM] after been fired at 400 °C with magnifications of x2 500 and x5 500, respectively.

The effect of incorporating a pore former in the paste formulations of $K_2CO_3$/13X zeolite foam-monoliths on their surface morphologies was also investigated. Although the scanning electron micrograph in Figure 5.8 (c) did not show very clearly the formation of macropores on the surface of $K_2CO_3$/13X zeolite foam-monoliths, the results from the MIP analyses (refer Section 5.4.2.3) have demonstrated improvement in their structural porosities when 4% wt. Licowax C micropowder was added to their paste formulations. This confirms the formation of macropores in their foam-monolithic structure. Observations on the SEM image of $K_2CO_3$/13X zeolite foam-monoliths with pore former at

higher magnification (Figure 5.8 (d)) reveal that macropores were indeed formed on the monolithic structure after the pore former was decomposed. 13X zeolite and $K_2CO_3$ aggregates were seen bounded by calcium bentonite in Figure 5.8 (d).

#### 5.4.2.5 Mechanical compressive strengths of carbonate-based zeolite foam-monoliths

The carbonate-based zeolite foam-monoliths prepared in this study were tested with radial or axial compressions to determine their mechanical compressive strengths. Each mechanical compressive strength test was repeated at least twice and experimental error in the compressive stresses obtained in this study was about 1% to 70%. First, the mechanical (radial) compression tests were carried out on carbonate-based zeolite foam-monoliths that have been fired at 400 °C or 650 °C. The results in Figure 5.9 (a) show that their radial compressive stresses were improved by about 3.7 times for $Na_2CO_3$/13X zeolite foam-monoliths and 1.6 times for $K_2CO_3$/13X zeolite foam-monoliths when their firing temperature was raised from 400 °C to 650 °C. This suggests that more mechanical strength could be imparted to the foam-monolithic structure as the calcium bentonite becomes more harden at a higher firing temperature (Sanabria *et al.*, 2010).

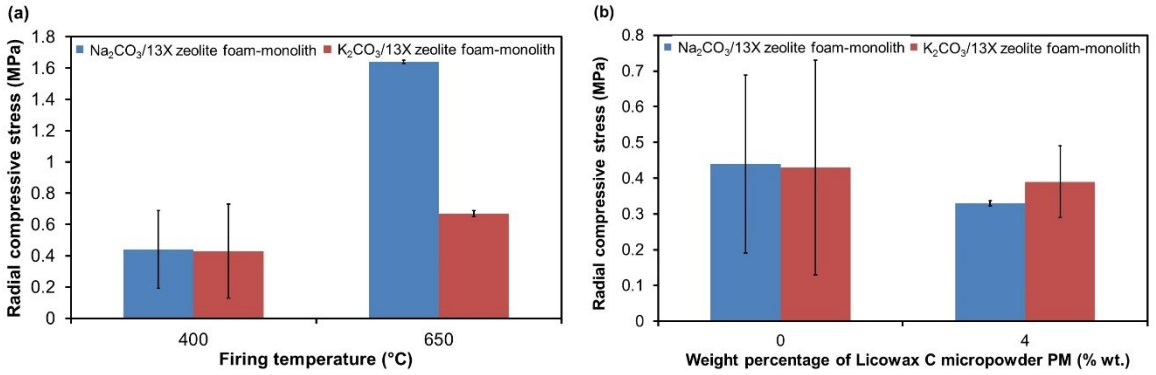


**Figure 5.9** The radial compressive stresses of $Na_2CO_3$/13X zeolite and $K_2CO_3$/13X zeolite foam-monoliths [75% wt. 13X zeolite:25% wt. calcium bentonite+4% wt. $NaHCO_3$/$KHCO_3$] (a) that have been fired at 400 °C or 650 °C and those (b) that have been fired at 400 °C without or with 4% wt. Licowax C micropowder PM (a pore former).

Second, the mechanical (radial) compression tests were carried out on carbonate-based zeolite foam-monoliths that have been fired at 400 °C without and with the inclusion of 4% wt. Licowax C micropowder PM as a pore former in their paste formulations. The results in Figure 5.9 (b) reveal that their radial compressive stresses were decreased by about 25% for $Na_2CO_3$/13X zeolite foam-monoliths and 9% for $K_2CO_3$/13X zeolite foam-monoliths when 4% wt. Licowax C micropowder PM was included in their paste formulations compared to those without any inclusion of the pore former. This indicates that the formation of macropores within the foam-monolithic structure after the thermal

decomposition of the pore former reduces their mechanical compressive strengths. This behaviour was similar to the zeolite monoliths prepared in earlier study (refer Section 3.4.2.5 of Chapter 3).

Next, the mechanical (radial and axial) compression tests were carried out on carbonate-based zeolite foam-monoliths that have been fired at 400 °C to determine their compressive stresses on radial and axial compression loadings. The results in Figure 5.10 (a) demonstrate that the compressive stresses were stronger by about 2.3 times for $Na_2CO_3$/13X zeolite foam-monoliths and 1.3 times for $K_2CO_3$/13X zeolite foam-monoliths when the compression loadings were applied in the axial direction compared to those in the radial direction. This implies that the foam-monolithic structure prepared in the study has high mechanical stability for axial compression compared to radial compression. Similar trend was also observed by Li (1998) and earlier study described in this thesis on zeolite monoliths (refer Section 3.4.2.5 of Chapter 3).

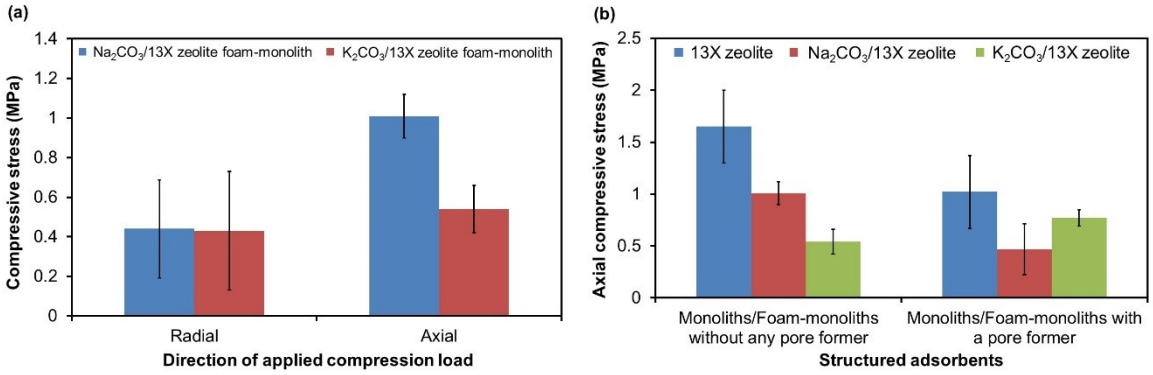


**Figure 5.10** (a) The radial and axial compressive stresses of the prepared carbonate-based zeolite foam-monoliths [75% wt. 13X zeolite:25% wt. calcium bentonite+4% wt. $NaHCO_3$/$KHCO_3$] that have been fired at 400 °C and (b) the axial compressive stresses of the prepared carbonate-based zeolite foam-monoliths and 13X zeolite monoliths that have been fired at 400 °C without or with 4% wt. Licowax C micropowder PM (a pore former).

Lastly, the mechanical (axial) compression tests were carried out on the prepared carbonate-based zeolite foam-monoliths and 13X zeolite monoliths that have been fired at 400 °C. Their paste formulations may or may not include 4% wt. Licowax C micropowder PM as a pore former. Their results in Figure 5.10 (b) show that the axial compressive stresses of the prepared carbonate-based zeolite foam-monoliths were slightly lower by about 1.8 times for $Na_2CO_3$/13X zeolite and 2 times for $K_2CO_3$/13X zeolite compared to 13X zeolite monoliths. This indicates that the prepared carbonate-based zeolite foam-monoliths were not as strong as the 13X zeolite monoliths prepared in the research but they are strong enough to be used in the experiments described in this thesis.

## 5.5 Conclusions

As a conclusion, the work presented in this chapter has demonstrated the possibility of creating foams in the monolithic structure to produce a novel adsorbent structure named as foam-monolith. The purpose of this invention was to reduce the pressure drop and enhance the mass transfer properties in the adsorbent beds so that the adsorption technology for biogas upgrading could be more energy efficient with improved adsorption performance. This innovative manufacturing strategy of producing a foam-monolithic structure was revealed for the first time in this thesis.

The study showed that the novel carbonate-based zeolite foam-monoliths were fabricated successfully according to the specially invented formulations using the unique extrusion technique proposed previously in Chapter 3. In this study, the model physical adsorbent was 13X zeolite and the model chemical sorbents were sodium and potassium carbonates, which were formed chemically from the thermal decomposition of their bicarbonates (i.e., $KHCO_3$ and $NaHCO_3$). Clay such as calcium bentonite was chosen and used as a binder in this work since they have high plasticity and binding effects on the physical adsorbent and chemical sorbents, which would provide the necessary mechanical stability to the foam-monolithic structure.

Using similar approach as that described previously for zeolite and MIL-101(Cr) monoliths (refer Chapters 3 and 4, respectively), Licowax C micropowder PM was incorporated into the paste formulations of carbonate-based zeolite foam-monoliths as a pore former to create macropores within the foam-monolithic structure after they decomposed. The presence of macropores in the foam-monolithic structure would allow more adsorption sites to be exposed for capturing gas contaminants such as $CO_2$, $H_2O$ vapour and $H_2S$ from the biogas stream. This would, in turn, improves the mass transfer in foam-monoliths. This method of adding a pore former in structured adsorbent have previously been reported by Lee (1997), who use starch as a pore former to enhance the macroporosity of their silicalite monoliths. In the fabrication of carbonate-based zeolite foam-monoliths, it was found that cracking and bending were likely to occur in the drying step of the fabrication process. To overcome these fabrication challenges, the drying rate needs to be slowed down to reduce the stress on the foam-monolithic structure.

The physical properties of sodium and potassium bicarbonates have been characterised by simultaneous TGA and DSC, PXRD and SEM. Their thermal analyses showed that they start to decompose at 80 °C for sodium bicarbonate and at 100 °C for

potassium bicarbonate. Their PXRD patterns and SEM results indicated that their crystal structures collapsed when they were heated at 400 °C or 650 °C and this confirms the decomposition of bicarbonates in the firing process.

The prepared carbonate-based zeolite foam-monoliths have been characterised using PXRD, MIP, SEM and mechanical compression tests. Their pore properties and mechanical strengths have also been compared with the 13X zeolite monoliths prepared the research. The PXRD and SEM analyses showed that 13X zeolite and calcium bentonite crystals were retained after they were fired at 400 °C or 650 °C. Both SEM and MIP examinations confirmed the formation of macropores within the prepared carbonate-based zeolite foam-monoliths after the pore former was decomposed. Additionally, the MIP examinations have verified the formation of foams in the foam-monolithic structure. The MIP examinations also found that the pore properties of carbonate-based zeolite form-monoliths were not influenced by the type of carbonates and firing temperature.

The mechanical compression tests demonstrated that the prepared carbonate-based zeolite foam-monoliths were strong enough to be used in the experiments described in this thesis. It was found that the radial compressive strengths of the fired carbonate-based zeolite foam-monoliths were improved by about 3.7 times for $Na_2CO_3$/13X zeolite and 1.6 times for $K_2CO_3$/13X zeolite when their firing temperature was elevated from 400 °C to 650 °C. Although the inclusion of 4% wt. of Licowax C micropowder PM in the paste formulations of carbonate-based zeolite foam-monoliths would enhance the macroporosity of the foam-monolithic structure, this study discovered that there was a trade-off with their mechanical strengths. The mechanical compression tests demonstrated that the radial compressive strengths of the fired carbonate-based zeolite foam-monoliths were reduced by about 25% for $Na_2CO_3$/13X zeolite and 9% for $K_2CO_3$/13X zeolite when 4% wt. of Licowax C micropowder PM was incorporated in their paste formulations compared to those without any pore former.

Similar to zeolite and MIL-101(Cr) monoliths, the carbonate-based zeolite foam-monoliths prepared in this study will be optimised for $CO_2$ adsorption. Their optimisation study will be covered in the next chapter. The adsorption performance of these carbonate-based zeolite foam-monoliths for biogas upgrading will also be evaluated by testing them with single (such as $CO_2$, $CH_4$ and $H_2S$) and mixed (such as $CO_2/CH_4$ and $CO_2/CH_4/H_2O$ vapour) gases, as described in Chapter 7 of this thesis.

# Chapter 6 Optimisation of Adsorbent Structures with $CO_2$ Adsorption

This chapter presents the optimisation of novel adsorbent structures (such as monoliths and foam-monoliths) prepared in the research for $CO_2$ adsorption. Comparison will be made with the current state-of-the-art adsorbent structure such as beads to determine the most suitable adsorbent structure for $CO_2$ adsorption. The optimisation study will focus on the adsorption of $CO_2$ since $CO_2$ is the main contaminant in biogas that needs to be removed to upgrade the biogas quality. Typically, biogas contains about 25% vol. to 45% vol. $CO_2$ so the model adsorbate gas concentration used in this study is 40% vol. $CO_2$. The materials and apparatus used in the optimisation study are provided in Section 6.1.

Adsorption experiments will be carried out to optimise the adsorbent monolithic and foam-monolithic structures prepared in the research. In this study, the one-factor-at-a-time approach will be used since it is the most conventional way of studying the influence of several factors/variables on the adsorption performance of the adsorbent monoliths and foam-monoliths. The experimental approach used in this study was quite similar to that used by Lee (1997), who optimised its silicalite monolith design (i.e., channel size, wall thickness and composition) by breakthrough curve analysis. In this study, various parameters will be considered and they are: the type of zeolites/MIL-101(Cr)/carbonates, the type of bentonites, the ratios of zeolite/MIL-101(Cr) to bentonite, effect of including a pore forming agent in their paste formulations, the firing temperature, the monolith wall thickness, the length of adsorbent beds and the regeneration temperature. Repeatability tests will also be carried out to verify the experimental adsorption data. The detailed experimental procedures for the optimisation study are described in Section 6.2.

The $CO_2$ adsorption breakthrough curves for the tested adsorbent structures will be analysed to evaluate their $CO_2$ adsorption performance. Adsorption properties such as breakthrough time ($t_b$), equilibrium time ($t_e$), adsorption capacities of $CO_2$ at breakthrough ($\bar{q}_b$) and equilibrium ($\bar{q}_e$), effectiveness of the adsorbent bed utilisation ($\omega_{bed}$), mass transfer zone velocity ($u_{MTZ}$) and percentage length of mass transfer zone in the adsorbent bed ($\bar{L}_{MTZ}$) will be determined from their breakthrough curves using equations given in Section 2.2.1. The optimisation results for zeolite monoliths, MIL-101(Cr) monoliths and carbonate-based zeolite foam-monoliths will be provided and discussed in Section 6.3. The comparative results between these novel monolithic or foam-monolithic

structures and the current state-of-the-art structure such as beads will also be included. Lastly, the work described in this chapter will be concluded in Section 6.4.

## 6.1 Materials and Equipment Used in the Optimisation Study

In the optimisation study, zeolite and MIL-101(Cr) monoliths and carbonate-based zeolite foam-monoliths prepared in the research were used as model adsorbent structures. The bed masses of zeolite monoliths were kept constant (i.e., about 31.5 g for the 10 cm long bed and 61.8 g for the 20 cm long bed). The zeolite monoliths considered in this study were of:

- different type of zeolites (13X zeolite, LiLSX zeolite, 5A zeolite or clinoptilolite). They have same zeolite to calcium bentonite ratio of 75:25 (in % wt.), bed length of 10 cm, wall thickness of 0.9 mm and firing temperature of 400 °C. [Samples 2, 9, 19 and 25.]
- different type of bentonites (calcium bentonite or Wyoming sodium bentonite) with same bed length of 10 cm, wall thickness of 0.9 mm and firing temperature of 400 °C. [Samples 2, 8, 10, 14, 18, 21, 23 and 27.]
- different zeolite to calcium bentonite ratio, ranging between 65:35 and 85:15 (in % wt.). They have equal bed length of 10 cm, wall thickness of 0.9 mm and firing temperature of 400 °C. [Samples 1 to 3, 9 to 11, 17 to 19 and 23 to 25.]
- same zeolite to calcium bentonite ratio without or with 4% wt. pore forming agent. They have equal bed length of 10 cm, wall thickness of 0.9 mm and firing temperature of 400 °C. [Samples 2, 4, 10, 12, 18, 20, 23 and 26.]
- different firing temperature (400 °C or 650 °C) with same bed length of 10 cm and wall thickness of 0.9 mm. [Samples 2, 10, 18 and 23.]
- different wall thickness (0.7 mm or 0.9 mm) with same bed length of 10 cm and firing temperature of 400 °C. [Samples 3, 10, 18 and 23.]
- different bed length (10 cm or 20 cm) with same wall thickness of 0.9 mm and firing temperature of 400 °C. [Samples 2, 10, 18 and 23.]
- different regeneration temperature (150 °C, 200 °C or 250 °C) with 4% wt. pore forming agent included in their paste formulations. They have same bed length of 10 cm, wall thickness of 0.9 mm and firing temperature of 400 °C. [Samples 4, 12, 20 and 26.]

Additionally, MIL-101(Cr) monoliths with 0.9 mm thick walls and 9 cm long beds were used in this study. Their bed masses were kept constant (i.e., about 14.0 g). MIL-101(Cr) monoliths of the following criteria were considered in this study, which were:

- different type of MIL-101(Cr) (as-synthesized or purified) with same MIL-101(Cr) to calcium bentonite ratio of 60:40 (in % wt.) and firing temperature of 150 °C. [Samples M1 and M2.]
- different MIL-101(Cr) to calcium bentonite ratio (60:40 or 75:25; in % wt.) with the same firing temperature of 150 °C. [Samples M2 and M3.]
- different firing temperature (150 °C or 205 °C) with the same purified MIL-101(Cr) to calcium bentonite ratio of 75:25 (in % wt.). [Sample M3.]
- same purified MIL-101(Cr) to calcium bentonite ratio (i.e., 75:25; in % wt.) without or with 4% wt. pore forming agent and they have the same firing temperature of 205 °C. [Samples M3 and M4.]
- different regeneration temperature (150 °C, 180 °C or 200 °C) with the same purified MIL-101(Cr) to calcium bentonite ratio of 75:25 (in % wt.) and have included 4% wt. pore forming agent in their paste formulations. They also have the same firing temperature of 205 °C. [Sample M4.]

Carbonate-based zeolite monoliths of 0.9 mm thick walls were used in this study. Their bed masses were kept constant (i.e., about 30.9 g for the 10 cm long bed and 62.7 g for the 20 cm long bed). They were of:

- different type of carbonates ($K_2CO_3$ or $Na_2CO_3$) with the same composition, i.e., 75% wt. 13X zeolite, 25% wt. calcium bentonite, 4% wt. $KHCO_3$ or $NaHCO_3$. They have equal bed length of 10 cm and firing temperature of 400 °C. [Samples C1 and C3.]
- same composition, i.e., 75% wt. 13X zeolite, 25% wt. calcium bentonite, 4% wt. $KHCO_3$ or $NaHCO_3$, without or with 4% wt. pore forming agent. They have equal bed length of 10 cm and firing temperature of 400 °C. [Samples C1 to C4.]
- different firing temperature (400 °C or 650 °C) with the same composition, i.e., 75% wt. 13X zeolite, 25% wt. calcium bentonite, 4% wt. $KHCO_3$ or $NaHCO_3$ and 4% wt. Licowax C micropowder PM. They have equal bed length of 10 cm. [Samples C1 and C3.]
- different bed length (10 cm or 20 cm) with the same composition, i.e., 75% wt. 13X zeolite, 25% wt. calcium bentonite, 4% wt. $KHCO_3$ or $NaHCO_3$ and 4% wt. Licowax C

micropowder PM. They have the same firing temperature of 400 °C. [Samples C1 and C3.]

- ❖ different regeneration temperature (150 °C, 200 °C or 250 °C) with the same composition, i.e., 75% wt. 13X zeolite, 25% wt. calcium bentonite, 4% wt. $KHCO_3$ or $NaHCO_3$ and 4% wt. Licowax C micropowder PM. They have equal bed length of 10 cm and firing temperature of 400 °C. [Samples C2 and C4.]

The $CO_2$ adsorption performances of 13X zeolite and purified MIL-101(Cr) monoliths and $K_2CO_3$/13X zeolite foam-monoliths were also compared with 13X zeolite beads of 1.6 mm to 2.5 mm diameter (purchased from Süd-Chemie, Germany). The adsorbent monoliths and foam-monoliths used in the comparative study were of the same compositions (i.e., 75% wt. 13X zeolite/MIL-101(Cr), 25% wt. calcium bentonite and 4% wt. Licowax C micropowder PM, with 4% wt. $KHCO_3$ for the foam-monolith). They have 0.9 mm thick walls and they have been fired at 400 °C. It was assumed that the commercial adsorbent beads contained 90% wt. 13X zeolite. The bed length of adsorbent monoliths and foam-monoliths was 10 cm long and the packed bed of 13X zeolite beads was 6.2 cm long. Their bed masses were kept constant (i.e., about 31.5 g).

In this study, $CO_2$ gas with a concentration of 40% vol. in air mixture (purchased from BOC Ltd., UK) was used as the model adsorbate gas and compressed air was used as the purging gas. For packing the adsorbent monolith/foam-monolith in an adsorption column, a high density polytetrafluoroethylene (PTFE) gas sealant tape of ½ inch wide (purchased from Sigma-Aldrich Co., UK) and nitrile O-rings of 24 mm internal diameter 4 mm cross-section or 22 mm internal diameter with 5 mm cross-section (purchased from Polymax Ltd., UK) were used.

The equipment used in this study were: (a) an electric oven (model MOV-112, manufactured by Sanyo Electric Co. Ltd., Japan) for drying and regenerating the structured adsorbents, (b) an electric balance (model KERN EG 220-3NM, manufactured by Kern & Sehn GmbH, Germany) for weighing the structured adsorbents, (c) a 500 mL glass soap-bubble flowmeter in 100 mL increments (purchased from Sigma Aldrich, UK) and a digital stopwatch (manufactured by Fisher Scientific, UK) for measuring the gas flow rate and (d) an adsorption flow-breakthrough apparatus (see Figure 6.1) for carrying out the adsorption experiments.

The apparatus consists of an influent gas flow system, an adsorption-breakthrough testing system and an effluent gas analytical system. All pipelines of the apparatus were built with ¼ inch diameter stainless steel tube and fittings (model 316, purchased from Swagelok Company, UK). The apparatus was also equipped with three 3-way ball valves (model SS-43S4, manufactured by Whitey Tool and Die Company, UK) for controlling the gas flow direction and two pressure relief valves (PRV, supplied by BOC Ltd., UK) for releasing pressure out of the system if there was a build-up of pressure in the system.

The influent gas flow system contains a $CO_2$ gas cylinder for providing the feed gas into the system and a compressed air vessel for providing the purge gas into the system. The gas flow rate was regulated using a mass flow controller (model 5850S, purchased from Brooks Instruments LLC., USA) and the desired gas flow rate could be set on a digital flow control box (purchased from Brooks Instruments LLC., USA). Both the $CO_2$ gas cylinder and compressed air vessel were equipped with pressure regulators and gauges for controlling and monitoring their gas pressures supplied to the system.

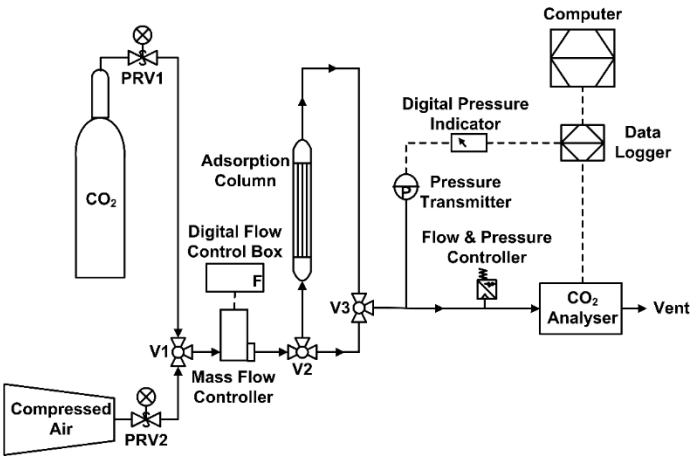


**Figure 6.1** Schematic diagram of an adsorption flow-breakthrough apparatus with $CO_2$ as the adsorbate gas.

In the adsorption-breakthrough testing system, a 25.5 cm long steel adsorption column (purchased from Agilent Technologies, UK) with an internal diameter of 3.1 cm was used for packing adsorbent monoliths, foam-monoliths or beads. Both ends of the column were fitted with 1¼ inches to ¼ inch reducers so that the column could be connected to the ¼ inch pipelines of the apparatus. The inlet reducer enables the gas flow to be distributed uniformly onto the adsorbent bed while the outlet reducer concentrates the gas flow from the adsorbent bed. Both the inlet and outlet reducers have built-in stainless steel frits to prevent fine particles and dust from entering or leaving the column that would block and damage the $CO_2$ analyser. The design of the adsorption column was shown in Figure 6.2. The column was assembled vertically on the adsorption apparatus

with the $CO_2$ gas flowing in an upward direction. This was to prevent the formation of gas flow maldistribution that may occur when adsorbent structures settled in the column.

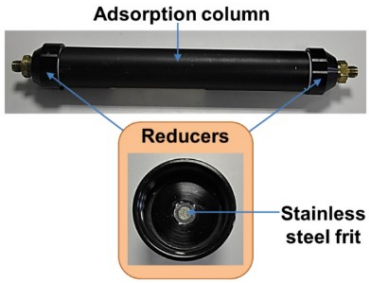


**Figure 6.2** The design of the adsorption column.

As seen in Figure 6.1, the effluent gas analytical system comprises of: (a) a bidirectional inline flow and pressure controller (model 9041202, manufactured by Metal Work Pneumatics, Italy) for tuning the flow and pressure of the supplied gas, (b) a pressure transmitter (model S-10, manufactured by WIKA Instruments Ltd., UK) for detecting the gas pressure, (c) a digital pressure indicator (model DPI 260, manufactured by Druck Ltd., UK) for producing a read-out of the pressure in bar (gauge) and (d) a digital $CO_2$ gas analyser (model Guardian Plus, purchased from Edinburgh Instruments Ltd., UK) for measuring the $CO_2$ gas concentration in % vol. (from 0% vol. to 100% vol.).

The output signals from the $CO_2$ analyser were communicated through a one-port data logger (model RS 232, manufactured by National Instruments Corporation, UK) and then to a computer, which records the $CO_2$ gas concentration in time using a LabVIEW programme.

## 6.2 Experimental Procedures for Optimising the Adsorbent Structures with $CO_2$ Adsorption

As mentioned earlier, the adsorbent monolithic and foam-monolithic structures prepared in the research were optimised by carrying out the adsorption experiments using $CO_2$ gas. The adsorption experiments involved the following steps, which were:

a) drying the structured adsorbent,

b) packing the structured adsorbent in a column,

c) setting the experimental operating conditions and checking the apparatus,

d) running the adsorption experiment,

e) stopping the adsorption experiment and unpacking the structured adsorbent and

f) regenerating the structured adsorbent.

The detailed experimental procedures of these steps are provided in Sections 6.2.1 to 6.2.6. To obtain correct experimental results from the adsorption experiments, the methods of handling the structured adsorbent and the apparatus must be followed properly in the right order.

### 6.2.1 Drying the structured adsorbent

First, the structured adsorbents either in the forms of monoliths, foam-monoliths or beads were dried in an electric oven at 150 °C for at least 18 hours. The purpose of this step was to remove water molecules from the pores of the adsorbent.

### 6.2.2 Packing the structured adsorbent in a column

After the drying step, the mass of the structured adsorbent was measured using an electric balance and they were packed in an empty adsorption column. The adsorbent monoliths and foam-monoliths were held tightly in the column by wrapping them with a high density polytetrafluoroethylene (PTFE) gas sealant tape and fitting a 24 mm or 22 mm diameter nitrile O-ring at the inlet end, see illustration in Figure 6.3 (a). This method of packing the adsorbent monoliths and foam-monoliths was to prevent the $CO_2$ gas from passing between the edge of the monolith/foam-monolith and the wall of the column.

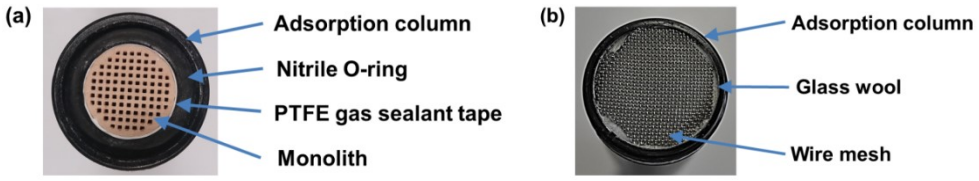


**Figure 6.3** Photographs showing the packing of adsorbent (a) monolith and (b) beads.

For packing adsorbent beads in an empty column, a two-layered fine wire meshes (with glass wool in between to prevent any dust particulates from entering the gas lines) was fitted on the inlet end of the column to hold the zeolite beads in place. Figure 6.3 (b) shows the fitting of the two-layered fine wire meshes at the inlet end of the adsorption column. Once the adsorption column was packed with the desired structured adsorbent, the column was assembled onto the apparatus such that the column was isolated from the

whole system (i.e., the 3-way valves at the inlet (V2) and outlet (V3) of the column were switched to direct the gas flow to bypassed the column). This was to make sure that there was no $CO_2$ gas present in the column before the start of the adsorption experiment.

### 6.2.3 Setting the experimental operating conditions and checking the apparatus

Next, the $CO_2$ gas was supplied to the adsorption flow-breakthrough apparatus by switching the 3-way valve (V1) so that the compressed air was isolated from the whole system. The flow rate and pressure of the $CO_2$ gas in the system were regulated by a mass flow controller and tuned using a flow and pressure controller. The desired $CO_2$ gas flow rate was set on the digital flow control box. For the optimisation study, the system was set to operate at an absolute pressure of 2 bar with $CO_2$ gas flowing at a rate of 500 mL $min^{-1}$ under an ambient temperature (i.e., between 19.5 °C and 24.5 °C). The entire apparatus was checked for leaks before starting the adsorption experiments. The maximum working pressure of the apparatus was about 7.5 bar absolute.

### 6.2.4 Running the adsorption experiment

When the $CO_2$ gas concentration, flow rate and pressure have stabilised, the adsorption flow-breakthrough apparatus was ready for running the adsorption experiment. The adsorption experiment was started by switching the 3-way valves at the inlet (V2) and outlet (V3) of the column to allow the $CO_2$ gas to flow through the packed column. The effluent $CO_2$ gas leaving the packed column was passed to a digital $CO_2$ gas analyser and discharged to the atmosphere through a vent. The concentration of the effluent $CO_2$ gas was recorded on a computer every second during the adsorption experiment until it reached the same concentration as the influent $CO_2$ gas.

### 6.2.5 Stopping the adsorption experiment and unpacking the structured adsorbent

Once a complete breakthrough curve had obtained, the adsorption experiment was stopped by switching the 3-way valves at the inlet (V2) and outlet (V3) of the column so that the packed column was isolated from the rest of the system. The packed column was disconnected from the apparatus to unpack the structured adsorbent. The whole system was then purged with compressed air by switching the 3-way valve (V1) such that $CO_2$ gas was not provided to the adsorption flow-breakthrough apparatus. This would clean the pipelines from any remaining $CO_2$ gas molecules.

### 6.2.6 Regenerating the structured adsorbent

The structured adsorbent that was removed from the column after the adsorption experiment was kept in an electric oven at 150 °C, 180 °C, 200 °C or 250 °C for at least 18 hours. This was to desorb the $CO_2$ gas molecules from the pores of the adsorbent solids and to regenerate the structured adsorbent for reuse.

## 6.3 Results and Discussion of the Optimisation Study

The breakthrough curves obtained from the $CO_2$ adsorption experiments were analysed to evaluate the adsorption performances of the tested structured adsorbents and their results are presented in this section. The sample calculations used in this study to determine the adsorption properties of adsorbent monoliths and foam-monoliths are provided in Appendix 2 (see Example 1). Since adsorption experiments in this study were carried out at low pressure (i.e., 2 bar), the holdup of gas in the adsorbent bed was assumed to be less significant relative to the amount adsorbed. So, the $CO_2$ gas accumulated in the particle voids and dead space was not considered in the calculations. The optimisation results and discussion for zeolite monoliths are given in Section 6.3.1 whereas those for MIL-101(Cr) monoliths are given in Section 6.3.2. As for the carbonate-based zeolite foam-monoliths, the results and discussion of their optimisation study are covered in Section 6.3.3.

To determine the most suitable adsorbent structure for $CO_2$ adsorption, the $CO_2$ adsorption breakthrough curves of the novel adsorbent monolithic and foam-monolithic structures prepared in the research were compared with the current state-of-the-art adsorbent structures such as beads. Their results and discussion are provided in Section 6.3.4. The error of the data reported in this chapter was estimated to be about 0.01% for breakthrough and equilibrium times ($t_b$ and $t_e$, respectively), effectiveness of adsorbent bed utilisation ($\varpi_{bed}$), mass transfer zone velocity ($u_{MTZ}$) and percentage length of mass transfer zone ($\bar{L}_{MTZ}$). The mass and volumetric adsorption capacities at breakthrough and equilibrium ($\bar{q}_b$ and $\bar{q}_e$) were estimated to have an error of about 2.6%.

### 6.3.1 Optimisation of zeolite monoliths

This section covers the results and discussion for the optimisation of zeolite monoliths. Various parameters were considered in optimising the zeolite monolithic structure prepared in the research. This includes their composition (such as types of

zeolites and bentonites, ratio of zeolite to bentonite and inclusion of a pore forming agent in their paste formulations), firing temperature, physical structure (such as monolith wall thickness and bed length) and regeneration temperature. The results of their $CO_2$ adsorption breakthrough curves analyses are provided and discussed in Sections 6.3.1.1 to 6.3.1.8. The $CO_2$ adsorption experiments for zeolite monoliths were also repeated to check the accuracy of their experimental adsorption data and their results are shown in Section 6.3.1.9.

### 6.3.1.1 Adsorption onto different type of zeolite monoliths

First, the adsorption of $CO_2$ onto different type of zeolite monoliths was compared to identify the most suitable zeolite monolith for adsorbing $CO_2$. In this investigation, $CO_2$ adsorption experiments were carried out using 13X zeolite, LiLSX zeolite, 5A zeolite and clinoptilolite monoliths of the same zeolite to calcium bentonite ratio of 75:25 (in % wt.). The tested zeolite monoliths have 0.9 mm thick walls and 10 cm long beds. All of them have been fired at 400 °C. The 40% vol. $CO_2$ adsorption breakthrough curves for these zeolite monoliths are shown in Figure 6.4. It was seen that they all have sharp breakthrough curves and this means that they have good mass transfer of $CO_2$ in the monolithic structure. The sharpest breakthrough curve was produced by the clinoptilolite monolith and this indicates that they have the most efficient mass transfer of $CO_2$ than the other tested zeolite monoliths.

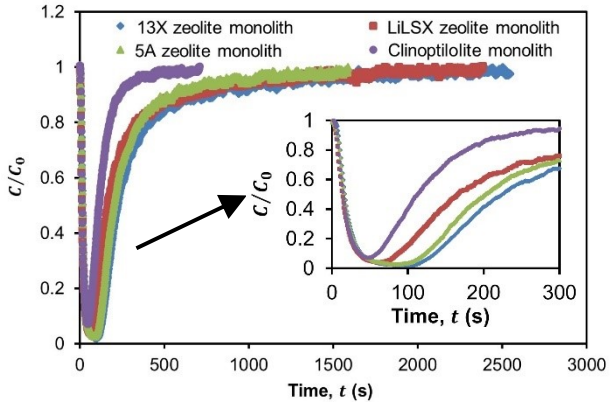


**Figure 6.4** Adsorption of 40% vol. $CO_2$ on different type of zeolite monoliths with the same composition (i.e., 75% wt. zeolite:25% wt. calcium bentonite).

Although the mass transfer of $CO_2$ was the most efficient in clinoptilolite monolith, they have the shortest breakthrough time (at 58 s) and equilibrium time (at 709 s) compared to 13X zeolite, LiLSX zeolite and 5A zeolite monoliths. It seems that the most suitable zeolite monolith to use for $CO_2$ adsorption was 13X zeolite monolith since they have the longest breakthrough time (at 112 s) and equilibrium time (at 2 237 s) among the tested zeolite monoliths. The long breakthrough and equilibrium times of 13X zeolite

monolith means that they could be used for a longer time (i.e., about twice as long as the clinoptilolite monolith until they breakthrough) for $CO_2$ adsorption before they need replacement or regeneration. The equilibrium time of 13X zeolite monolith achieved in this study was longer than 13X zeolite powder. According to Chen *et al.* (2014), 13X zeolite reaches equilibrium within 600 s. The reason was because of the blockage of some pores of 13X zeolite by the binder (i.e., calcium bentonite).

Corresponding to their long breakthrough and equilibrium times, 13X zeolite monolith also have the highest breakthrough and equilibrium adsorption capacities of $CO_2$ (both in terms of mass and volumetric) compared to other tested zeolite monoliths (see Table 6.1). Their adsorption capacities of $CO_2$ were found to be 0.52 mmol $g^{-1}$ at breakthrough and 2.01 mmol $g^{-1}$ at equilibrium. These results confirm that 13X zeolite monolith has more adsorption sites available for $CO_2$ adsorption compared to LiLSX zeolite, 5A zeolite and clinoptilolite monoliths. The lowest breakthrough and equilibrium adsorption capacities of $CO_2$ were found to be exhibited by the clinoptilolite monoliths since they have shortest breakthrough and equilibrium times among the tested zeolite monoliths. As indicated in Table 6.1, the adsorption capacities of $CO_2$ for clinoptilolite monolith were 0.21 mmol $g^{-1}$ at breakthrough and 0.64 mmol $g^{-1}$ at equilibrium.

When comparing the equilibrium adsorption capacity of $CO_2$ (on mass basis) obtained in this study with previously reported data (of similar/near operating pressure and temperature) in the literature, it was found that 13X zeolite and 5A zeolite monoliths prepared in this research have lower $\bar{q}_e$ values than 13X zeolite extrudates and 5A zeolite beads tested by Cavenati *et al.* (2004) and Mofarahi *et al.* (2014), respectively. Cavenati *et al.* (2004) reported their 13X zeolite extrudates have an equilibrium adsorption capacity of about 5.20 mmol $g^{-1}$ at 2 bar and 25 °C. Mofarahi *et al.* (2014) reported that their 5A zeolite beads have an equilibrium adsorption capacity of 3.25 mmol $g^{-1}$ at 2 bar and 30 °C. This was most likely due to the absence of binder in their zeolite extrudates/beads.

For LiLSX zeolite and clinoptilolite monoliths, their $\bar{q}_e$ values reported in Table 6.1 were slightly higher than those reported in the literature (i.e., 1.34 mmol $g^{-1}$ for LiLSX and 0.55 mmol $g^{-1}$ for clinoptilolite at 2 bar and 25 °C, according to Siriwardane *et al.* (2003) and Stuckert and Yang (2011), respectively). This was as a result of slightly lower experimental operating temperature used in this study for LiLSX zeolite and clinoptilolite monoliths (i.e., 22 ± 0.5 °C) compared to that used in their studies. The increase in $CO_2$ adsorption capacity with the decrease of temperature was associated with an increase of adsorbent-adsorbate interactions (site-adsorbate) induced by a decrease of the mobility of

adsorbed molecules into the zeolite cavities that might be caused by a decrease of thermal agitation (Khelifa *et al.*, 2001).

The results in Table 6.1 also show that the effectiveness of the monolithic bed utilised for $CO_2$ adsorption was about the same for all the tested zeolite monoliths. The most efficient use of the zeolite monolithic bed for $CO_2$ adsorption was exhibited by the clinoptilolite monolith, with a $\omega_{bed}$ value of about 41.1%. This confirms that they have the lowest mass transfer resistance compared to the other tested zeolite monoliths, as demonstrated by their sharp breakthrough curve. The order of the effective utilisation of zeolite monoliths for $CO_2$ adsorption was found to be (from high to low): clinoptilolite, 5A zeolite, 13X zeolite and LiLSX zeolite monoliths.

**Table 6.1** The adsorption properties of various type of zeolite monoliths for 40% vol. $CO_2$ adsorption at 2 bar.

| Adsorption properties | $t_b$ (s) | $t_e$ (s) | $\overline{q}_b$ (mmol g$^{-1}$) & (mmol cm$^{-3}$ in bracket) | $\overline{q}_e$ (mmol g$^{-1}$) & (mmol cm$^{-3}$ in bracket) | $\omega_{bed}$ (%) | $u_{MTZ}$ (cm min$^{-1}$) | $\overline{L}_{MTZ}$ (%) |
|---|---|---|---|---|---|---|---|
| **13X zeolite monolith** | 112 | 2 237 | 0.52 (0.32) | 2.01 (1.23) | 30.2 | 0.30 | 95.0 |
| **LiLSX zeolite monolith** | 76 | 1 806 | 0.40 (0.22) | 1.92 (1.06) | 26.0 | 0.33 | 95.8 |
| **5A zeolite monolith** | 99 | 1 586 | 0.47 (0.28) | 1.64 (0.99) | 33.7 | 0.38 | 93.8 |
| **Clinoptilolite monolith** | 58 | 709 | 0.21 (0.17) | 0.64 (0.53) | 41.1 | 0.85 | 91.8 |

As a result of the efficient mass transfer and utilisation of the clinoptilolite monolithic bed for $CO_2$ adsorption, they have faster mass transfer zone velocity and shorter mass transfer zone length compared to the other tested zeolite monoliths. In this case, it was found that clinoptilolite has a mass transfer zone velocity of 0.85 cm min$^{-1}$ and a percentage length of mass transfer zone in the monolith of 91.8%. For 13X zeolite, LiLSX zeolite and 5A zeolite monoliths, their mass transfer zone velocity was about the same (i.e., about 0.34 cm min$^{-1}$, on average) and this means that they have almost the same efficiency of mass transfer in the monolith. Among the tested zeolite monoliths, it was found that LiLSX zeolite monolith has the longest mass transfer zone length for $CO_2$ adsorption and this was due to their poor mass transfer and utilisation of the monolithic bed. Generally, a short mass transfer zone length is preferred for efficient mass transfer of $CO_2$ in the monolithic bed (Yang, 1997).

Considering the $CO_2$ adsorption properties of the tested zeolite monoliths, it seems that 13X zeolite monolith is the most suitable zeolite monolith for $CO_2$ adsorption. The reasons were because they have the longest breakthrough and equilibrium times for $CO_2$ adsorption and the highest adsorption capacities of $CO_2$ at breakthrough and equilibrium compared to LiLSX zeolite, 5A zeolite and clinoptilolite monoliths.

### 6.3.1.2 Adsorption onto zeolite monoliths of different type of bentonites

Then, the $CO_2$ adsorption experiments were carried out using 0.9 mm thick-walled zeolite monoliths of different type of bentonites (i.e., calcium bentonite or Wyoming sodium bentonite). This was to find out the most suitable bentonite binder for zeolite monoliths. In this study, 10 cm long 13X zeolite, LiLSX zeolite, 5A zeolite and clinoptilolite monoliths that have been fired at 400 °C were tested for $CO_2$ adsorption. Their 40% $CO_2$ adsorption breakthrough curves are illustrated separately in Figures 6.5 (a) to (d) for each type of zeolite monoliths (of the same zeolite to bentonite ratio). It was observed that the sharpness of the breakthrough curves was about the same for zeolite monoliths containing either type of bentonites. This indicates that the mass transfer in zeolite monoliths was not influenced by the type of bentonites.

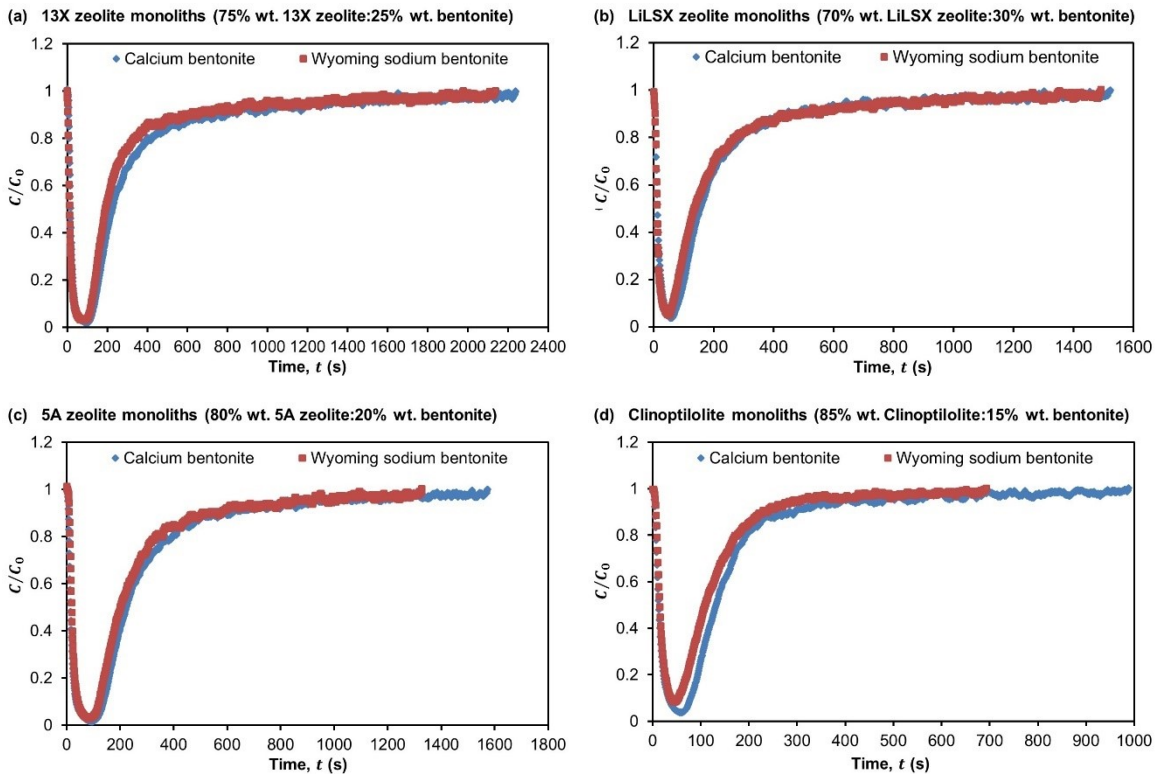


**Figure 6.5** Adsorption of 40% vol. $CO_2$ on (a) 13X zeolite, (b) LiLSX zeolite, (c) 5A zeolite and (d) clinoptilolite monoliths containing either calcium bentonite or Wyoming sodium bentonite as a binder.

It was also noticed that the breakthrough and equilibrium times were slightly longer for zeolite monoliths that used calcium bentonite as the binder rather than Wyoming sodium bentonite. This means zeolite monoliths using calcium bentonite as the binder could be used for a longer time for $CO_2$ adsorption. Additionally, some improvements on the breakthrough and equilibrium adsorption capacities of $CO_2$ (on mass basis and on volumetric basis, in most cases) were found when calcium bentonite was used as the binder for zeolite monoliths. This indicates that they have more adsorption sites available for $CO_2$ adsorption compared to those that used Wyoming sodium bentonite as the binder. In other words, the adsorption sites were less likely to be covered by calcium bentonite compared to Wyoming sodium bentonite as a result of the weak binding effect between calcium bentonite and zeolite.

All the tested zeolite monoliths demonstrate that there was no major difference in the utilisation of their monolithic beds for $CO_2$ adsorption by varying the type of bentonites (see Table 6.2). This means that the effectiveness of the zeolite monolithic bed utilised for $CO_2$ adsorption was not affected by the type of bentonites. Since the type of bentonites has no impact on the mass transfer and utilisation of the monolithic bed, the mass transfer zone velocity and length of the tested zeolite monoliths were about the same regardless of the type of bentonites. The minor difference in their $u_{MTZ}$ and $\bar{L}_{MTZ}$ values was due to the variation of mass transfer resistance and availability of adsorption sites in zeolite monoliths during $CO_2$ adsorption.

**Table 6.2** The adsorption properties of selected zeolite monoliths containing either calcium bentonite (Ca-B) or Wyoming sodium bentonite (W-Na-B) as a binder for 40% vol. $CO_2$ adsorption at 2 bar.

| Adsorption properties | | $t_b$ (s) | $t_e$ (s) | $\bar{q}_b$ (mmol g$^{-1}$) & (mmol cm$^{-3}$ in bracket) | $\bar{q}_e$ (mmol g$^{-1}$) & (mmol cm$^{-3}$ in bracket) | $\omega_{bed}$ (%) | $u_{MTZ}$ (cm min$^{-1}$) | $\bar{L}_{MTZ}$ (%) |
|---|---|---|---|---|---|---|---|---|
| **13X zeolite monolith** | **Ca-B** | 112 | 2 237 | 0.52 (0.32) | 2.01 (1.23) | 30.2 | 0.30 | 95.0 |
| | **W-Na-B** | 98 | 2 136 | 0.51 (0.33) | 1.92 (1.24) | 30.6 | 0.26 | 95.4 |
| **LiLSX zeolite monolith** | **Ca-B** | 65 | 1 523 | 0.39 (0.20) | 1.83 (0.96) | 26.4 | 0.39 | 95.7 |
| | **W-Na-B** | 56 | 1 492 | 0.32 (0.18) | 1.69 (0.94) | 24.1 | 0.40 | 96.2 |
| **5A zeolite monolith** | **Ca-B** | 110 | 1 573 | 0.54 (0.33) | 1.80 (1.09) | 34.4 | 0.38 | 93.0 |
| | **W-Na-B** | 108 | 1 328 | 0.53 (0.29) | 1.66 (0.90) | 37.7 | 0.45 | 91.9 |
| **Clinoptilolite monolith** | **Ca-B** | 72 | 988 | 0.24 (0.21) | 0.68 (0.60) | 41.4 | 0.62 | 92.7 |
| | **W-Na-B** | 54 | 693 | 0.16 (0.15) | 0.56 (0.52) | 38.9 | 0.81 | 92.2 |

The results from this investigation show that calcium bentonite was a more suitable binder for the zeolite monoliths compared to Wyoming sodium bentonite. The reason was because zeolite monoliths that used calcium bentonite as the binder could be used for $CO_2$ adsorption at a longer time and they have higher breakthrough and equilibrium adsorption capacities of $CO_2$ than those that used Wyoming sodium bentonite as the binder. The mechanical compressive strength tests results reported in previous chapter (i.e., Section 3.4.2.5 of Chapter 3) and those reported by Sanabria *et al.* (2010) indicate that the use of both types of bentonite did not have major impact on the mechanical characteristics of the final product.

#### 6.3.1.3 Adsorption onto zeolite monoliths of different zeolite to bentonite ratios

Next, the $CO_2$ adsorption onto 0.9 mm thick-walled zeolite monoliths of different zeolite to calcium bentonite ratios (ranging between 65:35 and 85:15) were investigated. In this study, 10 cm long 13X zeolite, LiLSX zeolite, 5A zeolite and clinoptilolite monoliths that have been fired at 400 °C were used. Their 40% $CO_2$ adsorption breakthrough curves are shown separately in Figures 6.6 (a) to (d) for each type of zeolite monoliths. The sharpness of the breakthrough curves was the same for all the different zeolite to calcium bentonite ratios of the tested zeolite monoliths. This indicates that the content of zeolite or calcium bentonite in the monolith did not have an influence on their mass transfer.

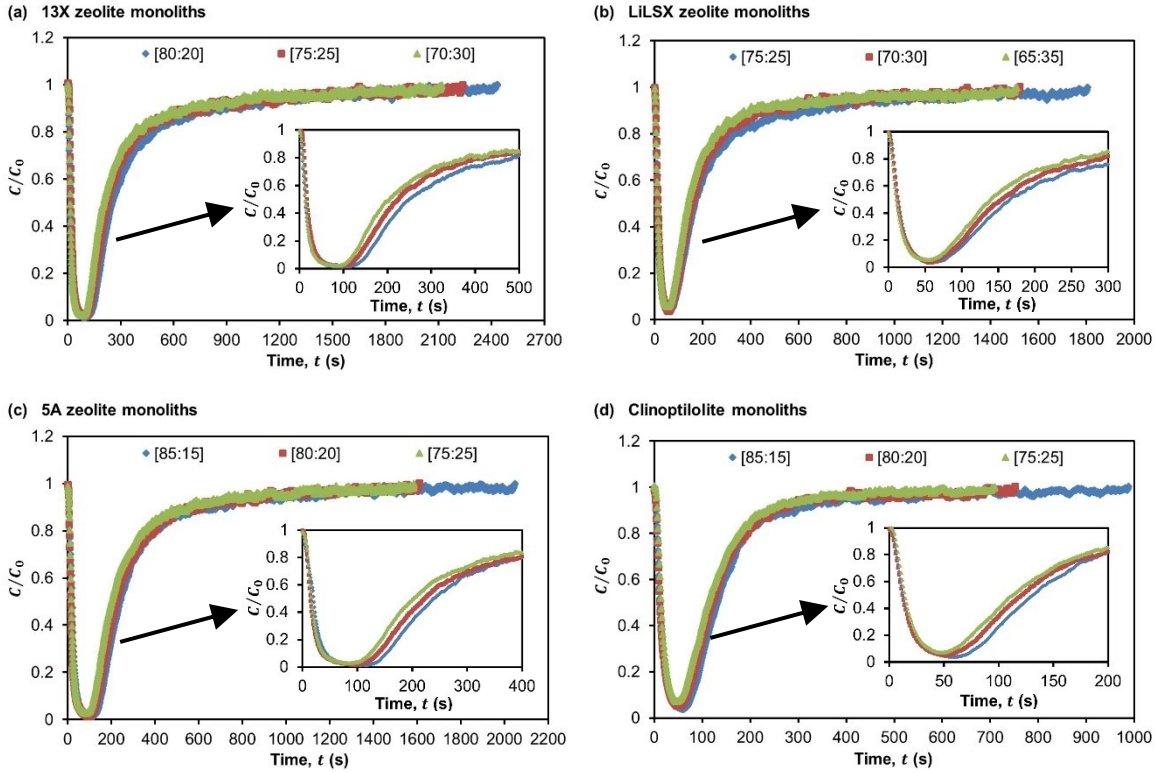


**Figure 6.6** Adsorption of 40% vol. $CO_2$ on (a) 13X zeolite, (b) LiLSX zeolite, (c) 5A zeolite and (d) clinoptilolite monoliths with different zeolite to bentonite ratios, which are denoted by [% wt. zeolite:% wt. calcium bentonite] in the plots.

It was observed that zeolite monoliths of higher zeolite to calcium bentonite ratio have longer breakthrough and equilibrium times compared to those of lower zeolite to calcium bentonite ratio. This was because the mass transfer front takes a longer time to reach the end of the monolithic bed and for the bed to get saturated with $CO_2$ when they have high zeolite content. Generally, a longer breakthrough time was preferred as this would mean that the zeolite monoliths could be used for a longer time before they need to be replaced or regenerated.

The study found that the breakthrough and equilibrium adsorption capacities of $CO_2$ (both in terms of mass and volumetric) were slightly higher for zeolite monoliths of high zeolite to calcium bentonite ratio. The reason was because monoliths with a high zeolite content have more adsorption sites available for $CO_2$ adsorption than those with a low zeolite content. For example, the $CO_2$ adsorption capacities (on mass basis) for 13X zeolite monoliths were found to improve by about 13% at breakthrough and 6% at equilibrium when their zeolite content was increased from 70% wt. to 80% wt. 13X zeolite (refer Table 6.3). The results also show that calcium bentonite did not contribute to the adsorption of $CO_2$ as there was no increase in adsorption capacities of $CO_2$ when the weight percentage of calcium bentonite was increased.

The trend of the results obtained in this study was similar to that reported by Lee (1997). Although zeolite monoliths of high zeolite to calcium bentonite ratio have longer breakthrough and equilibrium times for $CO_2$ adsorption and higher breakthrough and equilibrium adsorption capacities of $CO_2$ compared to those of low zeolite to calcium bentonite ratio, it has been demonstrated in Chapter 3 (Section 3.4.2.5) that there was a trade-off with the mechanical compressive strengths of the monolith.

The results in Table 6.3 indicate that the effectiveness of the monolithic bed utilised for $CO_2$ adsorption was about the same for all the different zeolite to calcium bentonite ratios considered in this study. On average, the effectiveness of the monolithic bed utilised for $CO_2$ adsorption was found to be about 29.6% for 13X zeolite, 26.3% for LiLSX zeolite, 34.5% for 5A zeolite and 40.9% for clinoptilolite monoliths. This validates the fact that the mass transfer in zeolite monoliths was not affected by the zeolite to calcium bentonite ratio. For this reason, the mass transfer zone velocity and length of the tested zeolite monoliths did not show significant change when their zeolite to calcium bentonite ratios were varied (see Table 6.3).

**Table 6.3** The adsorption properties of selected zeolite monoliths with different zeolite to bentonite ratios (represented by [% wt. zeolite:% wt. calcium bentonite] in the table) for 40% vol. $CO_2$ adsorption at 2 bar.

| Adsorption properties | | $t_b$ (s) | $t_e$ (s) | $\overline{q}_b$ (mmol $g^{-1}$) & (mmol $cm^{-3}$ in bracket) | $\overline{q}_e$ (mmol $g^{-1}$) & (mmol $cm^{-3}$ in bracket) | $\omega_{bed}$ (%) | $u_{MTZ}$ (cm $min^{-1}$) | $\bar{L}_{MTZ}$ (%) |
|---|---|---|---|---|---|---|---|---|
| **13X zeolite monolith** | **[80:20]** | 123 | 2 434 | 0.54 (0.35) | 2.04 (1.30) | 29.6 | 0.27 | 94.9 |
| | **[75:25]** | 112 | 2 237 | 0.52 (0.32) | 2.01 (1.23) | 30.2 | 0.30 | 95.0 |
| | **[70:30]** | 98 | 2 118 | 0.48 (0.30) | 1.93 (1.18) | 29.0 | 0.31 | 95.4 |
| **LiLSX zeolite monolith** | **[75:25]** | 76 | 1 806 | 0.40 (0.22) | 1.92 (1.06) | 26.0 | 0.33 | 95.8 |
| | **[70:30]** | 65 | 1 523 | 0.39 (0.20) | 1.83 (0.96) | 26.4 | 0.39 | 95.7 |
| | **[65:35]** | 60 | 1 510 | 0.37 (0.19) | 1.75 (0.92) | 26.5 | 0.40 | 96.0 |
| **5A zeolite monolith** | **[85:15]** | 126 | 2 048 | 0.57 (0.36) | 1.84 (1.16) | 35.6 | 0.30 | 93.8 |
| | **[80:20]** | 110 | 1 610 | 0.54 (0.33) | 1.80 (1.10) | 34.2 | 0.37 | 93.2 |
| | **[75:25]** | 99 | 1 586 | 0.47 (0.28) | 1.64 (0.99) | 33.7 | 0.38 | 93.8 |
| **Clinoptilolite monolith** | **[85:15]** | 72 | 988 | 0.24 (0.21) | 0.68 (0.60) | 41.4 | 0.62 | 92.7 |
| | **[80:20]** | 62 | 752 | 0.22 (0.18) | 0.65 (0.55) | 40.2 | 0.79 | 91.8 |
| | **[75:25]** | 58 | 709 | 0.21 (0.17) | 0.64 (0.53) | 41.1 | 0.85 | 91.8 |

#### 6.3.1.4 Effect of 4% wt. pore forming agent on the adsorption properties of zeolite monoliths

The effect of 4% wt. Licowax C micropowder (a pore former) on the $CO_2$ adsorption properties of zeolite monoliths was also investigated. In this study, 0.9 mm thick-walled monoliths of 13X zeolite, LiLSX zeolite, 5A zeolite and clinoptilolite prepared without or with the inclusion of 4% wt. Licowax C micropowder in their paste formulations were tested for $CO_2$ adsorption. The tested zeolite monoliths were of 10 cm long and they have been fired at 400 °C. Their 40% vol. $CO_2$ adsorption breakthrough curves are presented individually in Figures 6.7 (a) to (d) for each type of zeolite monoliths (of the same zeolite to bentonite ratio). It was seen that the sharpness of the breakthrough curves was slightly improved by adding 4% wt. Licowax C micropowder in their paste formulations, indicating better mass transfer in the monolithic bed. This was as a result of enhanced structural macroporosity of monoliths after the pore former was decomposed.

The breakthrough and equilibrium times for zeolite monoliths with 4% wt. Licowax C micropowder were found to be slightly longer compared to those without any pore former. The reason was because their mass transfer front takes a longer time to reach the end of

the monolithic bed and for the bed to get saturated with $CO_2$. This means that zeolite monoliths that have incorporated a pore former in their paste formulations could be used for a longer time for $CO_2$ adsorption before they need replacement or regeneration. Lee (1997) also observed the same results, in which a slightly improvement in both breakthrough and equilibrium times was obtained by adding 10% wt. starch into the paste formulations of their silicalite monoliths.

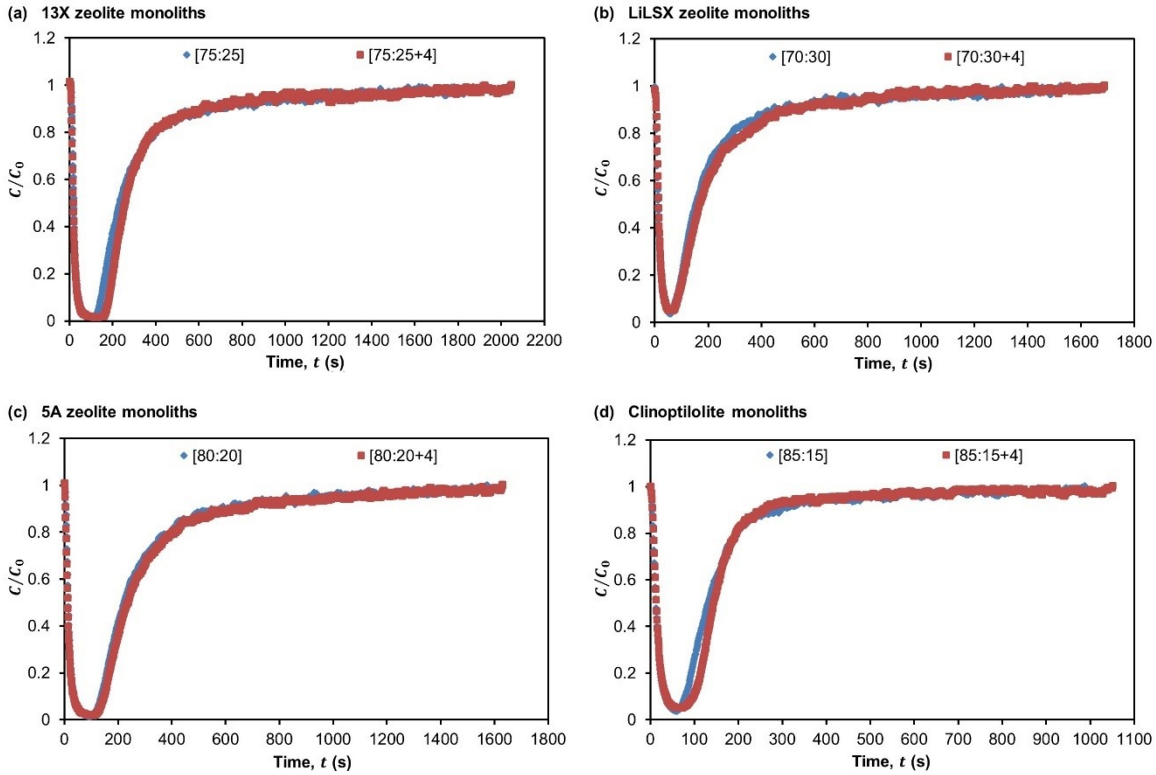


**Figure 6.7** Adsorption of 40% vol. $CO_2$ on (a) 13X zeolite, (b) LiLSX zeolite, (c) 5A zeolite and (d) clinoptilolite monoliths without or with the inclusion of 4% wt. Licowax C micropowder PM as a pore former. Note: Their paste compositions are denoted by [% wt. zeolite:% wt. calcium bentonite+% wt. pore former] in the plots.

As revealed in Table 6.4, the inclusion of a pore former in the paste formulations of zeolite monoliths was found to improve their breakthrough and equilibrium adsorption capacities of $CO_2$ (both in terms of mass and volumetric). For example, it was found that the adsorption capacities of $CO_2$ (on mass basis) for 13X zeolite monoliths were improved by about 40% at breakthrough and 8% at equilibrium when their paste formulations contained 4% wt. Licowax C micropowder. This was because more adsorption sites were exposed for $CO_2$ adsorption when the structural macroporosity of the monolith was enhanced by burning off the pore former to create macropores in the monolithic structure.

The study also shows that zeolite monoliths with a pore former were utilised more effectively for $CO_2$ adsorption than those without any pore former (see Table 6.4). For

example, the effectiveness of 13X zeolite monoliths utilised for $CO_2$ adsorption was found to improve by about 22% when 4% wt. Licowax C micropowder was included in their paste formulations compared to those without any pore former. This was mainly due to the improved mass transfer in the monolithic structure.

**Table 6.4** The adsorption properties of selected zeolite monoliths without or with the inclusion of 4% wt. Licowax C micropowder PM as a pore former for 40% vol. $CO_2$ adsorption at 2 bar. Note that their paste compositions are denoted by [% wt. zeolite:% wt. calcium bentonite+% wt. pore former] in the table.

| Adsorption properties | | $t_b$ (s) | $t_e$ (s) | $\overline{q}_b$ (mmol $g^{-1}$) & (mmol $cm^{-3}$ in bracket) | $\overline{q}_e$ (mmol $g^{-1}$) & (mmol $cm^{-3}$ in bracket) | $\omega_{bed}$ (%) | $u_{MTZ}$ (cm $min^{-1}$) | $\overline{L}_{MTZ}$ (%) |
|---|---|---|---|---|---|---|---|---|
| **13X zeolite monolith** | **[75:25]** | 126 | 1 916 | 0.58 (0.35) | 1.87 (1.14) | 35.9 | 0.35 | 93.4 |
| | **[75:25+4]** | 162 | 2 046 | 0.81 (0.49) | 2.02 (1.21) | 43.9 | 0.33 | 92.1 |
| **LiLSX zeolite monolith** | **[70:30]** | 65 | 1 523 | 0.39 (0.20) | 1.83 (0.96) | 26.4 | 0.39 | 95.7 |
| | **[70:30+4]** | 72 | 1 688 | 0.42 (0.22) | 1.89 (0.98) | 27.4 | 0.36 | 95.7 |
| **5A zeolite monolith** | **[80:20]** | 110 | 1 573 | 0.54 (0.33) | 1.80 (1.09) | 34.4 | 0.38 | 93.0 |
| | **[80:20+4]** | 126 | 1 800 | 0.61 (0.39) | 1.82 (1.14) | 37.3 | 0.38 | 92.3 |
| **Clinoptilolite monolith** | **[85:15]** | 72 | 988 | 0.24 (0.21) | 0.68 (0.60) | 41.4 | 0.62 | 92.7 |
| | **[85:15+4]** | 80 | 1 051 | 0.30 (0.24) | 0.78 (0.64) | 44.1 | 0.58 | 92.4 |

Although the inclusion of a pore former in the paste formulations of zeolite monoliths improves their breakthrough and equilibrium times for $CO_2$ adsorption, breakthrough and equilibrium adsorption capacities of $CO_2$ and utilisation of the monolithic bed, it has been demonstrated in Chapter 3 (Section 3.4.2.5) that the mechanical compressive strengths of zeolite monoliths were reduced by about 4% for 13X zeolite, 57% for LiLSX zeolite, 11% for 5A zeolite and 21% for clinoptilolite when 4% wt. Licowax C micropowder PM was incorporated into their paste formulations.

The results in Table 6.4 indicate that there was no significant change in mass transfer zone velocity and length of the tested zeolite monoliths by adding 4% wt. Licowax C micropowder PM in the paste formulations of zeolite monoliths. The reason was because the amount of pore former added to their paste formulations was not large enough to give major impact on their mass transfer zone velocity and length.

#### 6.3.1.5 Adsorption onto zeolite monoliths that have been fired at different temperatures

Additionally, the effect of firing temperature on the $CO_2$ adsorption properties of zeolite monoliths was studied to determine a suitable firing temperature for zeolite monoliths. In this study, the $CO_2$ adsorption experiments were carried out using 0.9 mm thick-walled 13X zeolite, LiLSX zeolite, 5A zeolite and clinoptilolite monoliths that have been fired at 400 °C or 650 °C. The tested zeolite monoliths were of 10 cm long. Their 40% vol. $CO_2$ adsorption breakthrough curves are shown separately in Figures 6.8 (a) to (d) for each type of zeolite monoliths (of the same zeolite to calcium bentonite ratio). Generally, the sharpness of the breakthrough curves was about the same for both firing temperatures. This indicates that the mass transfer in zeolite monoliths was not affected by the firing temperature.

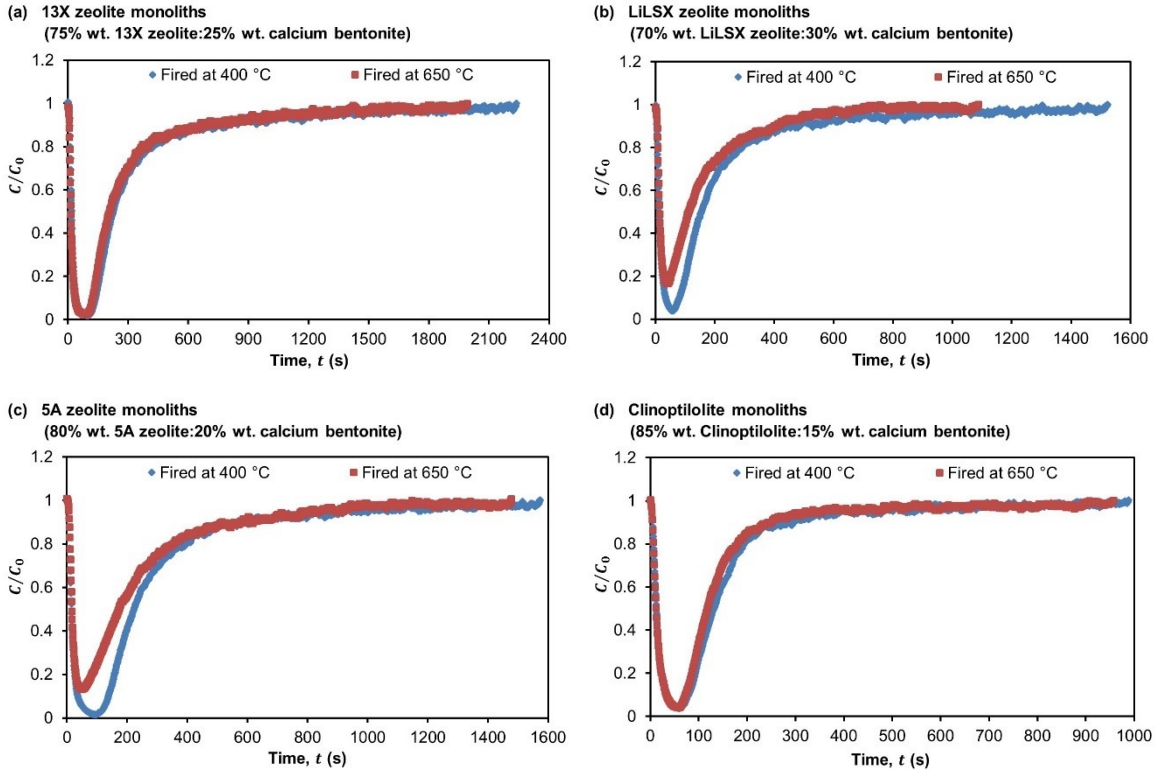


**Figure 6.8** Adsorption of 40% vol. $CO_2$ on (a) 13X zeolite, (b) LiLSX zeolite, (c) 5A zeolite and (d) clinoptilolite monoliths that have been fired at 400 °C or 650 °C.

It was observed that the breakthrough and equilibrium times tend to be shorter when they have higher firing temperature, i.e. 650 °C. This was because the mass transfer front reaches the end of the monolithic bed early and the bed gets saturated with $CO_2$ faster. The reduction in their breakthrough and equilibrium times means that they require more frequent replacement or regeneration than those fired at 400 °C. The study found that the breakthrough and equilibrium adsorption capacities of $CO_2$ (both in terms of mass and volumetric) were slightly reduced when the firing temperature of zeolite monoliths was

increased from 400 °C to 650 °C (see Table 6.5). For example, the adsorption capacities of $CO_2$ (on mass basis) for 13X zeolite monoliths were found to reduce by about 6% at breakthrough and 4% at equilibrium when they were fired at 650 °C instead of 400 °C. This indicates that less adsorption sites were available for $CO_2$ adsorption when zeolite monoliths were fired at 650 °C, which was as a result of reduced structural porosity (as shown in Section 3.4.2.3 of Chapter 3).

It was noticed that the breakthrough curves for LiLSX zeolite and 5A zeolite monoliths in Figures 6.8 (b) and (c) show larger variation at the start of the breakthrough (or larger decrease in breakthrough time) when they were fired at 400 °C and 650 °C compared to 13X zeolite and clinoptilolite monoliths (Figures 6.8 (a) and (d), respectively). This suggests that LiLSX zeolite and 5A zeolite monoliths have much lesser adsorption sites exposed for capturing $CO_2$ when their firing temperature was raised from 400 °C to 650 °C and this might be caused by a large decrease in structural porosity. Due to this reason, the breakthrough and equilibrium adsorption capacities of $CO_2$ for LiLSX zeolite and 5A zeolite monoliths have a larger difference between the two firing temperatures (i.e., 400 °C and 650 °C) compared to 13X zeolite and clinoptilolite monoliths, as indicated in Table 6.5.

**Table 6.5** The adsorption properties of selected zeolite monoliths that have been fired at 400 °C or 650 °C for 40% vol. $CO_2$ adsorption at 2 bar.

| Adsorption properties | | $t_b$ (s) | $t_e$ (s) | $\overline{q}_b$ (mmol g$^{-1}$) & (mmol cm$^{-3}$ in bracket) | $\overline{q}_e$ (mmol g$^{-1}$) & (mmol cm$^{-3}$ in bracket) | $\omega_{bed}$ (%) | $u_{MTZ}$ (cm min$^{-1}$) | $\overline{L}_{MTZ}$ (%) |
|---|---|---|---|---|---|---|---|---|
| **13X zeolite monolith** | **400 °C** | 112 | 2 237 | 0.52 (0.32) | 2.01 (1.23) | 30.2 | 0.30 | 95.0 |
| | **650 °C** | 98 | 1 994 | 0.49 (0.30) | 1.93 (1.19) | 29.3 | 0.34 | 95.1 |
| **LiLSX zeolite monolith** | **400 °C** | 65 | 1 523 | 0.39 (0.20) | 1.83 (0.96) | 26.4 | 0.39 | 95.7 |
| | **650 °C** | 45 | 1 088 | 0.20 (0.11) | 1.15 (0.64) | 25.7 | 0.56 | 95.9 |
| **5A zeolite monolith** | **400 °C** | 110 | 1 573 | 0.54 (0.33) | 1.80 (1.09) | 34.4 | 0.38 | 93.0 |
| | **650 °C** | 58 | 1 478 | 0.21 (0.13) | 1.38 (0.85) | 22.3 | 0.41 | 96.1 |
| **Clinoptilolite monolith** | **400 °C** | 72 | 988 | 0.24 (0.21) | 0.68 (0.60) | 41.4 | 0.62 | 92.7 |
| | **650 °C** | 63 | 958 | 0.21 (0.19) | 0.64 (0.58) | 40.0 | 0.65 | 93.4 |

The results in Table 6.5 indicate that the effectiveness of the monolithic bed utilised for $CO_2$ adsorption was slightly reduced as the firing temperature of zeolite monoliths increased from 400 °C to 650 °C. For example, the utilisation of 13X zeolite monoliths for $CO_2$ adsorption was found to be about 3% less effective when they were fired at 650 °C

compared to those fired at 400 °C. This was because of the reduced structural porosity of the monolithic structure when they were fired at higher temperature (i.e., 650 °C), which limits the accessibility/exposure of adsorption sites to $CO_2$. Moreover, it was discovered that the mass transfer zone velocity and length for the tested zeolite monoliths were about the same for both firing temperatures (see Table 6.5). This confirms that the firing temperature did not has any influence on the mass transfer in zeolite monoliths.

The results from this investigation shows that the most suitable firing temperature for zeolite monoliths was 400 °C. The reasons were because zeolite monoliths that have been fired at this temperature exhibit longer breakthrough and equilibrium times for $CO_2$ adsorption, higher breakthrough and equilibrium adsorption capacities of $CO_2$ and better utilisation of the monolithic bed compared to those fired at 650 °C. Despite having these improvements in $CO_2$ adsorption, it has been demonstrated previously in Chapter 3 (Section 3.4.2.5) that their mechanical compressive strengths were reduced by about 1.4 times for 13X zeolite and clinoptilolite monoliths and 1.8 times for LiLSX zeolite and 5A zeolite monoliths when they were fired at 400 °C instead of 650 °C.

#### 6.3.1.6 Adsorption onto zeolite monoliths of different wall thicknesses

Next, the $CO_2$ adsorption experiments were carried out using 10 cm long zeolite monoliths of different wall thicknesses (i.e., 0.7 mm or 0.9 mm). In this study, 13X zeolite, LiLSX zeolite, 5A zeolite and clinoptilolite monoliths that have been fired at 400 °C were used. Their 40% vol. $CO_2$ adsorption breakthrough curves were compared individually in Figures 6.9 (a) to (d) for each type of zeolite monoliths (of the same zeolite to calcium bentonite ratio). It was seen that the breakthrough curves for zeolite monoliths of 0.7 mm thick walls were slightly sharper than those of 0.9 mm thick walls. This indicates that the mass transfer in zeolite monoliths was more efficient when they have thinner walls.

It was noticed that zeolite monoliths of thinner walls (i.e., 0.7 mm) produced longer breakthrough and equilibrium times compared to those of thicker walls (i.e., 0.9 mm). For example, 13X zeolite monoliths show that their breakthrough time was doubled and their equilibrium time was about 1.5 times longer when their wall thickness was reduced from 0.9 mm to 0.7 mm. This means that zeolite monoliths with 0.7 mm thick walls could be used for $CO_2$ adsorption at a longer time and they have lower frequency of replacement or regeneration than those with 0.9 mm thick walls. The behaviour of zeolite monoliths of different wall thicknesses observed in this study was in agreement with that reported by Lee (1997).

The study found that the breakthrough and equilibrium adsorption capacities of $CO_2$ (both in terms of mass and volumetric) were improved by having thinner monolith walls (see Table 6.6). For example, the $CO_2$ adsorption capacities (on mass basis) for 13X zeolite monoliths were found to improve by about 88% at breakthrough and 67% at equilibrium when their wall thickness was reduced from 0.9 mm to 0.7 mm. This suggests that zeolite monoliths of thinner walls have more adsorption sites exposed for $CO_2$ adsorption compared to those of thicker walls.

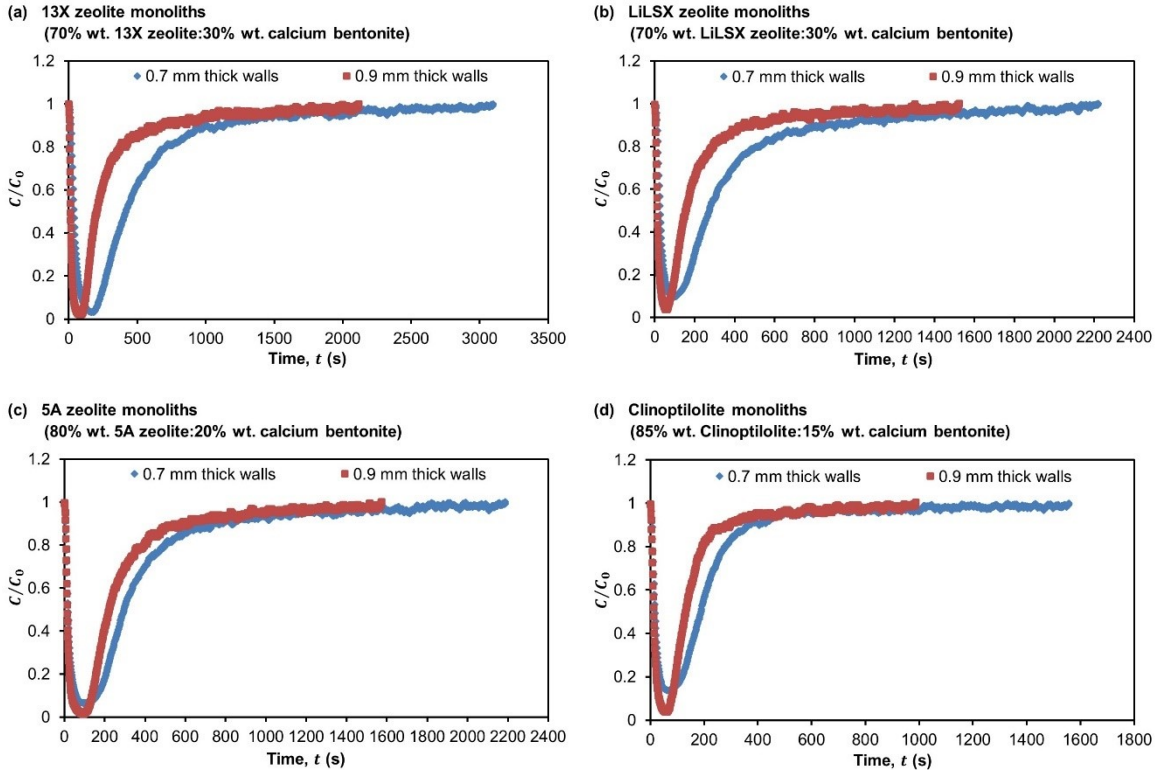


**Figure 6.9** Adsorption of 40% vol. $CO_2$ on (a) 13X zeolite, (b) LiLSX zeolite, (c) 5A zeolite and (d) clinoptilolite monoliths with either 0.7 mm or 0.9 mm thick walls.

It was also found that the reduction in monolith wall thickness improves the effectiveness of the monolithic bed utilised for $CO_2$ adsorption. For example, the use of 13X zeolite monoliths for $CO_2$ adsorption was found to be about 17% more effective when their wall thickness was reduced from 0.9 mm to 0.7 mm, as indicated in Table 6.6. This confirms that the mass transfer in 0.7 mm thick-walled zeolite monoliths was more efficient than that in 0.9 mm thick-walled zeolite monoliths. As a result of efficient mass transfer in thin-walled (i.e., 0.7 mm) zeolite monoliths, it was discovered that they have slower mass transfer velocity and shorter mass transfer zone length than those of thicker walls (refer Table 6.6). For example, it was found that the mass transfer zone velocity of $CO_2$ gas in 13X zeolite monoliths was decreased by about 32% and their mass transfer

zone length was reduced slightly by about 1.8% when their wall thickness was reduced from 0.9 mm to 0.7 mm.

Although this study shows that the $CO_2$ adsorption performance of zeolite monoliths was improved by reducing their wall thickness, it has been demonstrated in Chapter 3 (Section 3.4.2.5) that their mechanical compression strengths were reduced by about 1.4 times for 13X zeolite, 2.6 times for LiLSX zeolite, 1.8 times for 5A zeolite and 1.5 times for clinoptilolite monoliths when their wall thickness was reduced from 0.9 mm to 0.7 mm.

**Table 6.6** The adsorption properties of selected zeolite monoliths with a wall thickness of 0.7 mm or 0.9 mm for 40% vol. $CO_2$ adsorption at 2 bar.

| Adsorption properties | | $t_b$ (s) | $t_e$ (s) | $\overline{q}_b$ (mmol g$^{-1}$) & (mmol cm$^{-3}$ in bracket) | $\overline{q}_e$ (mmol g$^{-1}$) & (mmol cm$^{-3}$ in bracket) | $\omega_{bed}$ (%) | $u_{MTZ}$ (cm min$^{-1}$) | $\overline{L}_{MTZ}$ (%) |
|---|---|---|---|---|---|---|---|---|
| **13X zeolite monolith** | **0.7 mm** | 199 | 3 098 | 0.90 (0.66) | 3.23 (2.36) | 33.9 | 0.21 | 93.6 |
| | **0.9 mm** | 98 | 2 118 | 0.48 (0.30) | 1.93 (1.18) | 29.0 | 0.31 | 95.4 |
| **LiLSX zeolite monolith** | **0.7 mm** | 116 | 2 221 | 0.64 (0.32) | 3.09 (1.55) | 27.6 | 0.27 | 94.8 |
| | **0.9 mm** | 65 | 1 523 | 0.39 (0.20) | 1.83 (0.96) | 26.4 | 0.39 | 95.7 |
| **5A zeolite monolith** | **0.7 mm** | 159 | 2 187 | 0.77 (0.47) | 2.34 (1.44) | 37.8 | 0.27 | 92.7 |
| | **0.9 mm** | 110 | 1 573 | 0.54 (0.33) | 1.80 (1.09) | 34.4 | 0.38 | 93.0 |
| **Clinoptilolite monolith** | **0.7 mm** | 100 | 1 560 | 0.31 (0.27) | 0.91 (0.81) | 41.7 | 0.39 | 93.6 |
| | **0.9 mm** | 72 | 988 | 0.24 (0.21) | 0.68 (0.60) | 41.4 | 0.62 | 92.7 |

#### 6.3.1.7 Adsorption onto zeolite monoliths of different bed lengths

The effect of bed length on the $CO_2$ adsorption properties of zeolite monoliths was also studied. In this investigation, 0.9 mm thick-walled 13X zeolite, LiLSX zeolite, 5A zeolite and clinoptilolite monoliths of 10 cm or 20 cm long were tested for $CO_2$ adsorption. All the tested zeolite monoliths have been fired at 400 °C. Their 40% vol. $CO_2$ adsorption breakthrough curves are shown individually in Figures 6.10 (a) to (d) for each type of zeolite monoliths (of the same zeolite to calcium bentonite ratios). The sharpness of the breakthrough curves was about the same for both 10 cm and 20 cm long beds. This means that the mass transfer in zeolite monoliths was not dependent on the bed length.

It was seen that the breakthrough and equilibrium times were longer for zeolite monoliths of 20 cm long compared to those of 10 cm long. For example, 13X zeolite monoliths shows that their breakthrough time were longer by about 2.3 times and their

equilibrium time were longer by about 1.6 times when their bed length was increased from 10 cm to 20 cm. This shows that the longer the bed length, the longer time they can be used for $CO_2$ adsorption since they have longer breakthrough and equilibrium times and lower frequency of replacement or regeneration than a short bed length. Similar trend was also observed by Wang (2008).

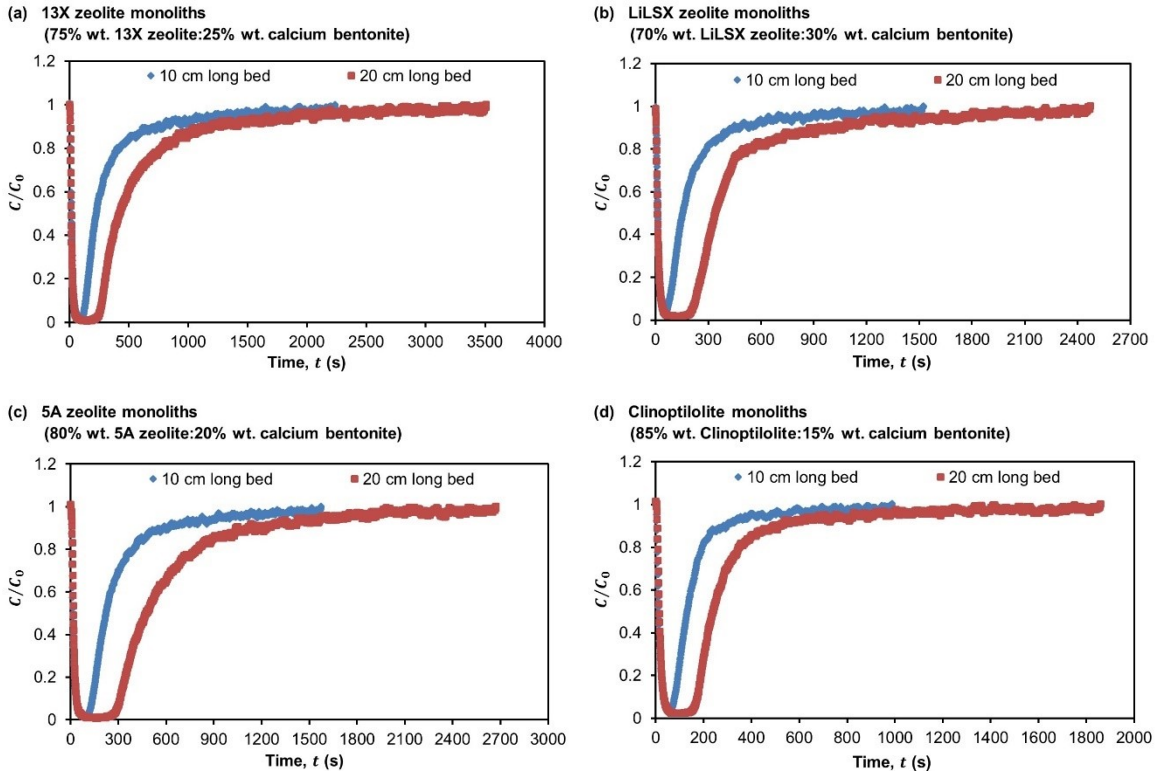


**Figure 6.10** Adsorption of 40% vol. $CO_2$ on (a) 13X zeolite, (b) LiLSX zeolite, (c) 5A zeolite and (d) clinoptilolite monoliths with 10 cm or 20 cm long bed.

The study found that zeolite monoliths of long bed length (i.e., 20 cm) exhibit slightly higher breakthrough and equilibrium adsorption capacities of $CO_2$ (in terms of mass and volumetric, in most cases) compared to those of short bed length (i.e., 10 cm). For example, the results in Table 6.7 indicate that the adsorption capacities of $CO_2$ (on mass basis) for 13X zeolite monoliths were higher by about 44% at breakthrough and 1% at equilibrium when their bed length was increased from 10 cm to 20 cm. The reason was because more adsorption sites were available for $CO_2$ adsorption in a long monolithic bed as there were more zeolite crystals present in the monolithic structure compared to a short monolithic bed.

For this reason, minor improvement in the effectiveness of the monolithic bed utilised for $CO_2$ adsorption was found when the bed length was increased (see Table 6.7). For example, the use of a 20 cm long 13X zeolite monolith for $CO_2$ adsorption was found

to be about 29% more effective than a 10 cm long 13X zeolite monolith. Since the bed length did not have an influence on the mass transfer in zeolite monoliths, the velocity of $CO_2$ gas in the mass transfer zone was about the same for both 10 cm long and 20 cm long zeolite monoliths. The results in Table 6.7 also indicate that the mass transfer zone length was slightly shorter when a longer monolith was used for $CO_2$ adsorption and this was due to the efficient utilisation of the monolithic bed. For example, 13X zeolite monoliths show that their mass transfer zone length was reduced by about 2.2% when their bed length was increased from 10 cm to 20 cm.

**Table 6.7** The adsorption properties of selected zeolite monoliths with 10 cm or 20 cm long bed for 40% vol. $CO_2$ adsorption at 2 bar.

| Adsorption properties | | $t_b$ (s) | $t_e$ (s) | $\bar{q}_b$ (mmol g$^{-1}$) & (mmol cm$^{-3}$ in bracket) | $\bar{q}_e$ (mmol g$^{-1}$) & (mmol cm$^{-3}$ in bracket) | $\omega_{bed}$ (%) | $u_{MTZ}$ (cm min$^{-1}$) | $\bar{L}_{MTZ}$ (%) |
|---|---|---|---|---|---|---|---|---|
| **13X zeolite monolith** | **10 cm** | 112 | 2 237 | 0.52 (0.32) | 2.01 (1.23) | 30.2 | 0.30 | 95.0 |
| | **20 cm** | 252 | 3 510 | 0.75 (0.46) | 2.03 (1.25) | 39.1 | 0.33 | 92.8 |
| **LiLSX zeolite monolith** | **10 cm** | 65 | 1 523 | 0.39 (0.20) | 1.83 (0.96) | 26.4 | 0.39 | 95.7 |
| | **20 cm** | 198 | 2 472 | 0.69 (0.36) | 1.84 (0.97) | 39.5 | 0.49 | 92.0 |
| **5A zeolite monolith** | **10 cm** | 110 | 1 573 | 0.54 (0.33) | 1.80 (1.09) | 34.4 | 0.38 | 93.0 |
| | **20 cm** | 270 | 2 673 | 0.73 (0.43) | 1.81 (1.08) | 42.4 | 0.45 | 89.9 |
| **Clinoptilolite monolith** | **10 cm** | 72 | 988 | 0.24 (0.21) | 0.68 (0.60) | 41.4 | 0.62 | 92.7 |
| | **20 cm** | 152 | 1 859 | 0.29 (0.26) | 0.69 (0.60) | 46.3 | 0.64 | 91.8 |

#### 6.3.1.8 Effect of regeneration temperature on the adsorption properties of zeolite monoliths

Furthermore, 0.9 mm thick-walled 13X zeolite, LiLSX zeolite, 5A zeolite and clinoptilolite monoliths with 4% wt. Licowax C micropowder that have been regenerated at different temperatures (i.e., 150 °C, 200 °C or 250 °C) were tested for $CO_2$ adsorption. This was to find the most suitable regeneration temperature for zeolite monoliths. These different regeneration temperatures were selected such that they are within the temperature range that could be used to regenerate the adsorbed $CO_2$ from zeolites, i.e., from 150 °C to 300 °C (Zeochem, 2008; Yang, 1997) and that they would not degrade/alter the zeolite crystal structure. These selected regeneration temperatures have been considered before in the literature for regeneration sorbents for biogas upgrading applications, for example, Li *et al.* (2013). It should be noted that the regeneration of adsorbent monoliths did not take place in-situ in this study and the reason was because

the selected regeneration temperatures were above the maximum operating temperature of the adsorption column used in the study (i.e., 100 °C).

In this investigation, the tested zeolite monoliths were of 10 cm long and they have been fired at 400 °C. Their 40% vol. $CO_2$ adsorption breakthrough curves are shown individually in Figures 6.11 (a) to (d) for each type of zeolite monoliths (of the same zeolite to calcium bentonite ratios). It was observed that the sharpness of the breakthrough curves was about the same for all the different regeneration temperatures considered in this study. This indicates that the mass transfer in zeolite monoliths was not influence by the regeneration temperature.

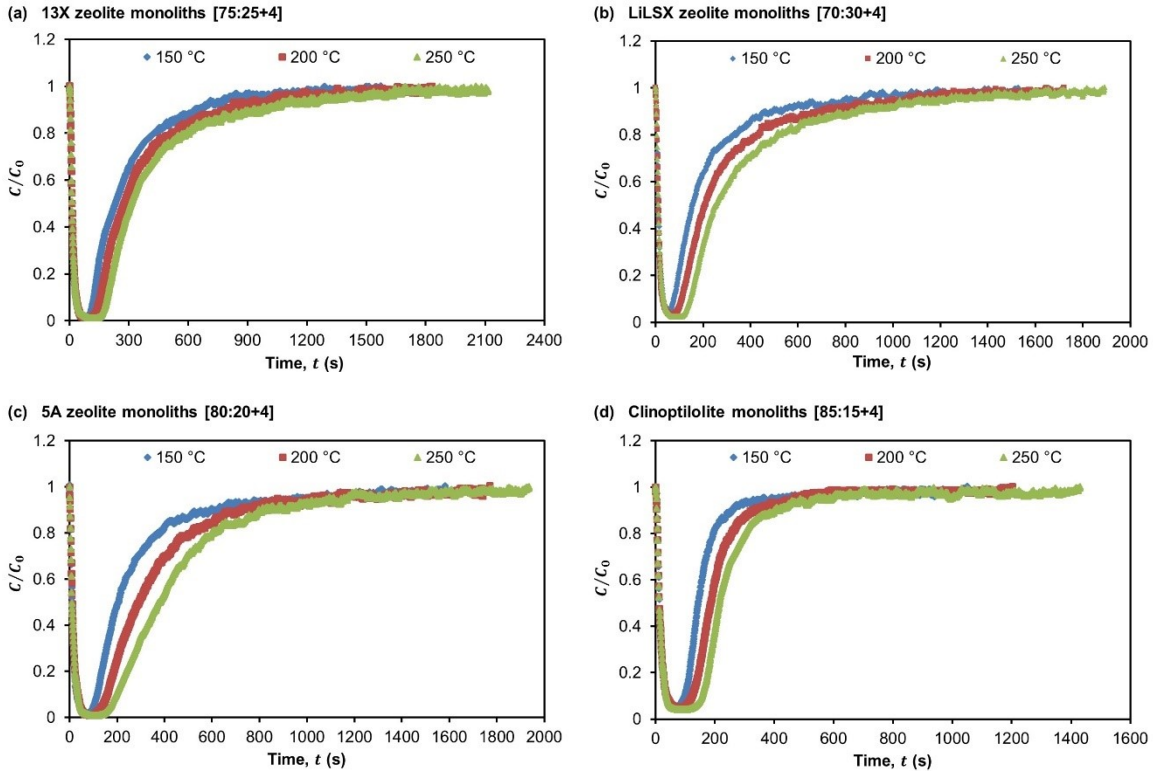


**Figure 6.11** Adsorption of 40% vol. $CO_2$ on (a) 13X zeolite, (b) LiLSX zeolite, (c) 5A zeolite and (d) clinoptilolite monoliths with different regeneration temperatures. Note: Their paste compositions are denoted by [% wt. zeolite:% wt. calcium bentonite+% wt. Licowax C micropowder PM] in the plots.

It was noticed that the breakthrough and equilibrium times increase with increasing regeneration temperature. For example, the increment in the regeneration temperature of 13X zeolite monoliths from 150 °C to 250 °C was found to increase their breakthrough time by about 51% and their equilibrium time by about 31%. This means that zeolite monoliths that have regenerated at higher temperature could be used for a longer time for $CO_2$ adsorption before they need replacement or regeneration. The reason was because

their mass transfer front takes a longer time to reach the end of the monolithic bed and for the bed to get saturated with $CO_2$.

The study found that zeolite monoliths that have been regenerated at higher temperature exhibit higher breakthrough and equilibrium adsorption capacities of $CO_2$ (both in terms of mass and volumetric) compared to those regenerated at lower temperature (see Table 6.8). For example, the adsorption capacities of $CO_2$ (on mass basis) for 13X zeolite monoliths were found to improve by about 74% at breakthrough and 55% at equilibrium when their regeneration temperature was increased from 150 °C to 250 °C. This was because more adsorption sites were available for $CO_2$ adsorption when they were regenerated at higher temperature, which was as a result of efficient desorption and regeneration of zeolite monoliths. The behaviour of zeolite monoliths at increasing regeneration temperatures observed in this study was consistent with that reported Li *et al.* (2013).

**Table 6.8** The adsorption properties of selected zeolite monoliths with different regeneration temperatures for 40% vol. $CO_2$ adsorption at 2 bar.

| Adsorption properties | | $t_b$ (s) | $t_e$ (s) | $\bar{q}_b$ (mmol g$^{-1}$) & (mmol cm$^{-3}$ in bracket) | $\bar{q}_e$ (mmol g$^{-1}$) & (mmol cm$^{-3}$ in bracket) | $\omega_{bed}$ (%) | $u_{MTZ}$ (cm min$^{-1}$) | $\bar{L}_{MTZ}$ (%) |
|---|---|---|---|---|---|---|---|---|
| **13X zeolite monolith** | **150 °C** | 105 | 1 573 | 0.58 (0.34) | 2.01 (1.17) | 32.9 | 0.38 | 93.3 |
| | **200 °C** | 130 | 1 825 | 0.79 (0.45) | 2.62 (1.50) | 33.2 | 0.32 | 92.9 |
| | **250 °C** | 159 | 2 053 | 1.01 (0.57) | 3.12 (1.76) | 35.1 | 0.29 | 92.3 |
| **LiLSX zeolite monolith** | **150 °C** | 67 | 1 527 | 0.40 (0.20) | 1.88 (0.94) | 26.8 | 0.39 | 95.6 |
| | **200 °C** | 80 | 1 721 | 0.58 (0.30) | 2.45 (1.28) | 27.6 | 0.35 | 94.8 |
| | **250 °C** | 119 | 1 891 | 0.81 (0.43) | 2.99 (1.56) | 30.5 | 0.32 | 93.7 |
| **5A zeolite monolith** | **150 °C** | 87 | 1 582 | 0.45 (0.26) | 1.81 (1.03) | 28.5 | 0.39 | 94.5 |
| | **200 °C** | 114 | 1 770 | 0.62 (0.35) | 2.38 (1.36) | 28.9 | 0.35 | 93.6 |
| | **250 °C** | 144 | 1 936 | 0.84 (0.46) | 2.97 (1.64) | 30.6 | 0.32 | 92.6 |
| **Clinoptilolite monolith** | **150 °C** | 80 | 1 051 | 0.30 (0.24) | 0.78 (0.64) | 44.1 | 0.58 | 92.4 |
| | **200 °C** | 102 | 1 203 | 0.41 (0.33) | 1.02 (0.82) | 45.2 | 0.51 | 91.5 |
| | **250 °C** | 126 | 1 430 | 0.53 (0.42) | 1.26 (1.00) | 46.4 | 0.43 | 91.2 |

Due to this reason, the utilisation of zeolite monoliths for $CO_2$ adsorption was slightly improved when they were regenerated at a high temperature. For example, the results in Table 6.8 revealed that the use of 13X zeolite monoliths for $CO_2$ adsorption was about 2%

more effective when their regeneration temperature was increased from 150 °C to 250 °C. The results also indicate that there was no significant change in mass transfer velocity and length when the regeneration temperature of zeolite monoliths was varied (Table 6.8). This validates that the regeneration temperature did not have any impact on the mass transfer in zeolite monoliths. From this investigation, it was found that the most suitable regeneration temperature for zeolite monoliths seems to be 250 °C since they gave better $CO_2$ adsorption performance than those regenerated at 150 °C and 200 °C.

#### 6.3.1.9 Repeatability of experimental results for zeolite monoliths

Lastly, the $CO_2$ adsorption experiments were repeated twice using 0.9 mm thick-walled 13X zeolite, LiLSX zeolite, 5A zeolite and clinoptilolite monoliths with 4% wt. Licowax C micropowder PM to verify their experimental data. The tested zeolite monoliths were of 10 cm long and they have been fired at 400 °C. Their 40% vol. $CO_2$ adsorption breakthrough curves are shown individually in Figures 6.12 (a) to (d) for each type of zeolite monoliths (of the same zeolite to calcium bentonite ratios). The sharpness of the breakthrough curves was identical for both adsorption runs, indicating good reproducibility of experimental data.

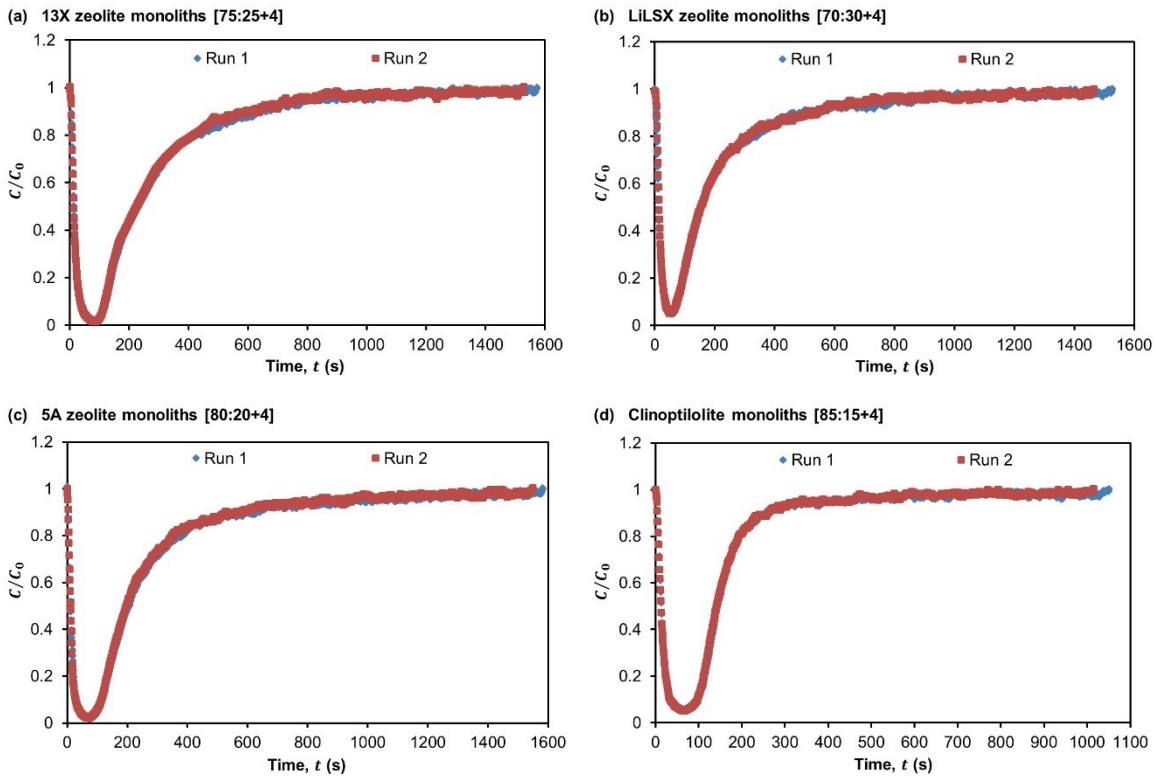


**Figure 6.12** Adsorption of 40% vol. $CO_2$ on (a) 13X zeolite, (b) LiLSX zeolite, (c) 5A zeolite and (d) clinoptilolite monoliths with two repeated adsorption runs. Note: Their paste compositions are denoted by [% wt. zeolite:% wt. calcium bentonite+% wt. Licowax C micropowder PM] in the plots.

It was seen that the breakthrough and equilibrium times were about the same for both adsorption runs. This shows that the experimental data for $CO_2$ adsorption onto zeolite monoliths obtained in this study was quite accurate. The results in Table 6.9 reveal that the breakthrough and equilibrium adsorption capacities of $CO_2$ (both in terms of mass and volumetric) were slightly lower when zeolite monoliths were reused for $CO_2$ adsorption. For example, the adsorption capacities of $CO_2$ (on mass basis) for 13X zeolite monoliths were found to reduce slightly by about 10% at breakthrough and 2% at equilibrium in the second adsorption run compared to the first adsorption run. This suggests that less adsorption sites were available for $CO_2$ adsorption when they were reused again and it could be due to the loss of adsorbent materials during handling or inefficient desorption and regeneration.

Because of these reasons, a minor decrease in the effectiveness of the monolithic bed utilised for $CO_2$ adsorption was found when zeolite monoliths were reused. For example, the results in Table 6.9 show that the use of 13X zeolite monoliths for $CO_2$ adsorption was about 2% less effective when they were reuse for $CO_2$ adsorption for the second time. It was found that the mass transfer zone velocity and length for the tested zeolite monoliths were about the same for both adsorption runs. This demonstrates that the mass transfer in zeolite monoliths was not affected when they were reused for $CO_2$ adsorption.

**Table 6.9** The adsorption properties of selected zeolite monoliths with two repeated adsorption runs for 40% vol. $CO_2$ adsorption at 2 bar.

| Adsorption properties | | $t_b$ (s) | $t_e$ (s) | $\overline{q}_b$ (mmol g$^{-1}$) & (mmol cm$^{-3}$ in bracket) | $\overline{q}_e$ (mmol g$^{-1}$) & (mmol cm$^{-3}$ in bracket) | $\omega_{bed}$ (%) | $u_{MTZ}$ (cm min$^{-1}$) | $\overline{L}_{MTZ}$ (%) |
|---|---|---|---|---|---|---|---|---|
| **13X zeolite monolith** | **Run 1** | 105 | 1 573 | 0.58 (0.34) | 2.01 (1.17) | 32.9 | 0.38 | 93.3 |
| | **Run 2** | 94 | 1 529 | 0.52 (0.29) | 1.96 (1.10) | 30.7 | 0.39 | 93.9 |
| **LiLSX zeolite monolith** | **Run 1** | 67 | 1 527 | 0.40 (0.20) | 1.87 (0.94) | 26.8 | 0.39 | 95.6 |
| | **Run 2** | 58 | 1 466 | 0.33 (0.16) | 1.81 (0.91) | 24.0 | 0.41 | 96.0 |
| **5A zeolite monolith** | **Run 1** | 87 | 1 582 | 0.45 (0.26) | 1.81 (1.03) | 28.5 | 0.39 | 94.5 |
| | **Run 2** | 80 | 1 548 | 0.42 (0.23) | 1.76 (0.98) | 27.6 | 0.40 | 94.8 |
| **Clinoptilolite monolith** | **Run 1** | 80 | 1 051 | 0.30 (0.24) | 0.78 (0.64) | 44.1 | 0.58 | 92.4 |
| | **Run 2** | 72 | 1 015 | 0.26 (0.21) | 0.75 (0.61) | 40.9 | 0.60 | 92.9 |

### 6.3.2 Optimisation of MIL-101(Cr) monoliths

Next, the results and discussion for the optimisation of MIL-101(Cr) monoliths are presented in this section. The parameters considered in the optimisation of MIL-101(Cr) monoliths prepared in the research are: (a) the type of MIL-101(Cr) (either as-synthesized or purified), (b) ratio of MIL-101(Cr) to calcium bentonite, (c) firing temperature, (d) effect of including of a pore forming agent in their paste formulations and (e) regeneration temperature. The results of their $CO_2$ adsorption breakthrough curves analyses are provided and discussed in Sections 6.3.2.1 to 6.3.2.5. Similar to zeolite monoliths, the $CO_2$ adsorption experiments are repeated to check the accuracy of the experimental data for MIL-101(Cr) monoliths and their results are given in Section 6.3.2.6.

#### 6.3.2.1 Adsorption onto as-synthesized and purified MIL-101(Cr) monoliths

Initially, the adsorption of 40% vol. $CO_2$ onto as-synthesized and purified MIL-101(Cr) monoliths was compared to assess their adsorption performances. The tested MIL-101(Cr) monoliths were of the same compositions (i.e., 60% wt. MIL-101(Cr) and 40% wt. calcium bentonite) and they have been fired at 150 °C. Their breakthrough curves are shown in Figure 6.13. Both of them seems to have the same sharpness irrespective of the type of MIL-101(Cr). This indicates that the mass transfer in MIL-101(Cr) monoliths was not affected by the type of MIL-101(Cr).

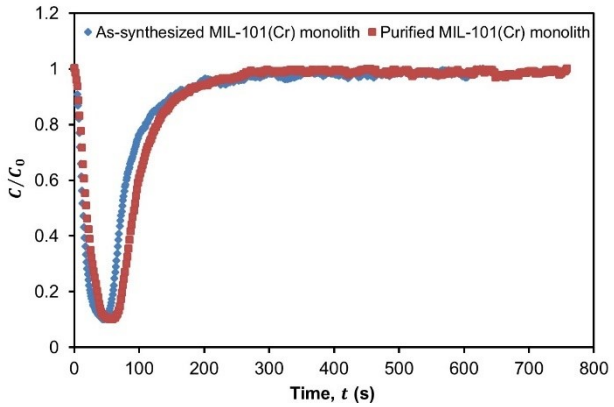


**Figure 6.13** Adsorption of 40% vol. $CO_2$ on as-synthesized and purified MIL-101(Cr) monoliths of the same composition (i.e., 60% wt. MIL-101(Cr):40% wt. calcium bentonite).

It was seen that the purified MIL-101(Cr) monolith took about 13 seconds longer to breakthrough and 129 seconds longer to saturate with $CO_2$ gas compared to the as-synthesized MIL-101(Cr) monolith. The reason was because the mass transfer front takes a longer time to reach the end of the monolithic bed and for the bed to get saturated with $CO_2$. This means that the purified MIL-101(Cr) monolith could be used for a longer time for $CO_2$ adsorption before they need replacement or regeneration.

Table 6.10 indicates that purified MIL-101(Cr) monolith have higher breakthrough and equilibrium adsorption capacities of $CO_2$ (both in terms of mass and volumetric) compared to as-synthesized MIL-101(Cr) monolith. The study found that the adsorption capacities of $CO_2$ (on mass basis) for purified MIL-101(Cr) monolith were slightly higher by about 21% at breakthrough and 8% at equilibrium when compared to the as-synthesized MIL-101(Cr) monolith (refer Table 6.10). This was because more adsorption sites were available for $CO_2$ adsorption when MIL-101(Cr) crystals were purified. Llewellyn ***et al.*** (2008) also observed the same trend as this study. As expected, the $\bar{q}_e$ value for purified MIL-101(Cr) monolith found in this study was lower than the literature value reported for purified MIL-101(Cr) powder, i.e., about 2.7 mmol $g^{-1}$ at 2 bar and 25 °C (Liang ***et al.***, 2013). This indicates that the purified MIL-101(Cr) monolith have less adsorption sites available for $CO_2$ adsorption since some of the pores of MIL-101(Cr) were blocked by calcium bentonite.

**Table 6.10** The adsorption properties of as-synthesized and purified MIL-101(Cr) monoliths for 40% vol. $CO_2$ adsorption at 2 bar.

| Adsorption properties | $t_b$ (s) | $t_e$ (s) | $\bar{q}_b$ (mmol $g^{-1}$) & (mmol $cm^{-3}$ in bracket) | $\bar{q}_e$ (mmol $g^{-1}$) & (mmol $cm^{-3}$ in bracket) | $\omega_{bed}$ (%) | $u_{MTZ}$ (cm $min^{-1}$) | $\bar{L}_{MTZ}$ (%) |
|---|---|---|---|---|---|---|---|
| **As-synthesized MIL-101(Cr) monolith** | 50 | 629 | 0.57 (0.15) | 1.41 (0.37) | 51.4 | 0.83 | 92.1 |
| **Purified MIL-101(Cr) monolith** | 63 | 758 | 0.69 (0.18) | 1.52 (0.39) | 57.0 | 0.69 | 91.6 |

As a result of high $CO_2$ adsorption capacity of purified MIL-101(Cr) monolith, its adsorbent bed utilisation for $CO_2$ adsorption was slightly more effective (i.e., by about 6%) compared to the as-synthesized MIL-101(Cr) monolith. The results in Table 6.10 indicate that the mass transfer zone velocity and length were about the same for both type of MIL-101(Cr) monoliths. This confirms that the type of MIL-101(Cr) did not has any influence on the mass transfer in MIL-101(Cr) monoliths. From this study, it seems that the purified MIL-101(Cr) monolith was the most suitable type of MIL-101(Cr) monoliths for $CO_2$ adsorption since they have better adsorption performance than the as-synthesized MIL-101(Cr) monolith.

### 6.3.2.2 Adsorption onto MIL-101(Cr) monoliths of different MIL-101(Cr) to calcium bentonite ratios

Then, the $CO_2$ adsorption experiments were carried out using purified MIL-101(Cr) monoliths of different MIL-101(Cr) to calcium bentonite ratios (i.e., 60:40 and 75:25). All the tested purified MIL-101(Cr) monoliths have been fired at 150 °C. Their 40% vol. $CO_2$ adsorption breakthrough curves are shown in Figure 6.14. It was seen that the sharpness of the breakthrough curves was the same for both MIL-101(Cr) to calcium bentonite ratios. This implies that the mass transfer in purified MIL-101(Cr) monoliths was not dependent on the MIL-101(Cr) to calcium bentonite ratio.

Similar to zeolite monoliths, the breakthrough and equilibrium times of the purified MIL-101(Cr) monoliths were found to increase with increasing ratio of MIL-101(Cr) to calcium bentonite. This can be explained by the fact that the mass transfer front takes a longer time to reach the end of the monolithic bed and for the bed to get saturated with $CO_2$ when they have high content of MIL-101(Cr). It also means that purified MIL-101(Cr) monoliths of high MIL-101(Cr) to calcium bentonite ratio could be used for $CO_2$ adsorption at a longer time and they would have lower frequency of replacement or regeneration than those of low MIL-101(Cr) to calcium bentonite ratio.

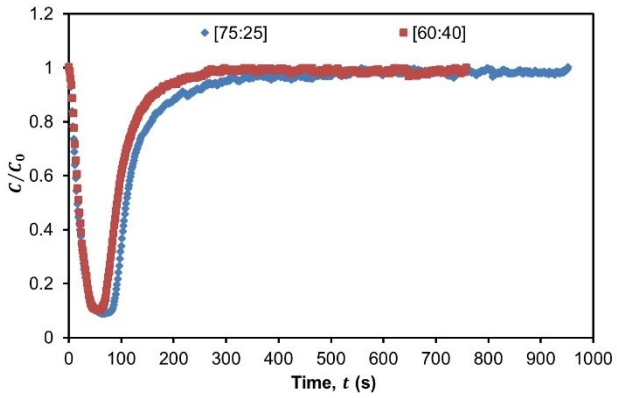


**Figure 6.14** Adsorption of 40% vol. $CO_2$ on purified MIL-101(Cr) monoliths with different MIL-101(Cr) to calcium bentonite ratios, which are denoted by [% wt. MIL-101(Cr):% wt. calcium bentonite] in the plot.

The results in Table 6.11 reveal that the breakthrough and equilibrium adsorption capacities of $CO_2$ (both in terms of mass and volumetric) for purified MIL-101(Cr) monolith increase with increasing weight percentage of MIL-101(Cr). The study found that the adsorption capacities of $CO_2$ (on mass basis) for purified MIL-101(Cr) monoliths were improved slightly by about 17% at breakthrough and 11% at equilibrium when their MIL-101(Cr) content was increased from 60% wt. to 75% wt. MIL-101(Cr). This indicates that more adsorption sites were available for $CO_2$ adsorption when they have high content of

MIL-101(Cr) in the monolithic structure. Similar to that observed previously for zeolite monoliths of different compositions (refer Section 6.3.1.3), the results in Table 6.11 also shows that calcium bentonite did not contribute to the adsorption of $CO_2$ since there was no increase in adsorption capacity of $CO_2$ when the weight percentage of calcium bentonite was increased.

Although a high MIL-101(Cr) to calcium bentonite ratio gave better $CO_2$ adsorption performance than a low MIL-101(Cr) to calcium bentonite ratio, it has been demonstrated in Chapter 4 (Section 4.5.3.5) that a reduction in calcium bentonite content from 40% wt. to 25% wt. reduced the mechanical compressive strengths of purified MIL-101(Cr) monoliths by about 16.5 times.

**Table 6.11** The adsorption properties of purified MIL-101(Cr) monoliths with different MIL-101(Cr) to calcium bentonite ratios (represented by [% wt. purified MIL-101(Cr):% wt. calcium bentonite] in the table) for 40% vol. $CO_2$ adsorption at 2 bar.

| Adsorption properties | $t_b$ (s) | $t_e$ (s) | $\overline{q}_b$ (mmol g$^{-1}$) & (mmol cm$^{-3}$ in bracket) | $\overline{q}_e$ (mmol g$^{-1}$) & (mmol cm$^{-3}$ in bracket) | $\omega_{bed}$ (%) | $u_{MTZ}$ (cm min$^{-1}$) | $\overline{L}_{MTZ}$ (%) |
|---|---|---|---|---|---|---|---|
| **[75:25]** | 83 | 952 | 0.81 (0.27) | 1.68 (0.55) | 57.1 | 0.55 | 91.3 |
| **[60:40]** | 63 | 758 | 0.69 (0.18) | 1.52 (0.39) | 57.0 | 0.69 | 91.6 |

The results in Table 6.11 indicate that the effectiveness of the monolithic bed utilised for $CO_2$ adsorption was the same for both MIL-101(Cr) to calcium bentonite ratios. This validates that the MIL-101(Cr) to calcium bentonite ratio did not have an influence on the mass transfer in purified MIL-101(Cr) monoliths. Due to this reason, no significant change in mass transfer zone velocity and length was found when the MIL-101(Cr) to calcium bentonite ratio was varied (see Table 6.11).

#### 6.3.2.3 Adsorption onto MIL-101(Cr) monoliths that have been fired at different temperatures

Next, the effect of firing temperature on the $CO_2$ adsorption properties of MIL-101(Cr) monoliths was studied to identify a suitable firing temperature for MIL-101(Cr) monoliths. In this study, purified MIL-101(Cr) monoliths that have been fired at 150 °C or 205 °C were tested for $CO_2$ adsorption. Their 40% vol. $CO_2$ adsorption breakthrough curves are illustrated in Figure 6.15 and it was observed that they both have the same sharpness. This indicates that the mass transfer in purified MIL-101(Cr) monoliths was not affected by the firing temperature.

It was also noticed that the breakthrough time was about 12 seconds longer and the equilibrium time was about 70 seconds longer when purified MIL-101(Cr) monoliths were fired at 205 °C instead of 150 °C. The reason was because the mass transfer front takes a longer time to reach the end of the monolithic bed and for the bed to be saturated with $CO_2$. This means that purified MIL-101(Cr) monoliths that have been fired at 205 °C could be used for a longer time for $CO_2$ adsorption before they need replacement or regeneration compared to those fired at 150 °C.

The results in Table 6.12 indicate that there are some improvements in breakthrough and equilibrium adsorption capacities of $CO_2$ (both in terms of mass and volumetric) when the firing temperature of purified MIL-101(Cr) monoliths was increased from 150 °C to 205 °C. The study discovered that their adsorption capacities of $CO_2$ (on mass basis) were slightly improved by about 17% at breakthrough and 4% at equilibrium when their firing temperature was increased from 150 °C to 205 °C (refer Table 6.12). The reason was because more adsorption sites were available for $CO_2$ adsorption when purified MIL-101(Cr) monoliths were fired at 205 °C instead of 150 °C. This was as a result of enhanced structural porosity of purified MIL-101(Cr) monoliths (i.e., by about 11%, as revealed in Section 4.5.3.3 of Chapter 4) after impurities in calcium bentonite were burnt off effectively at 205 °C.

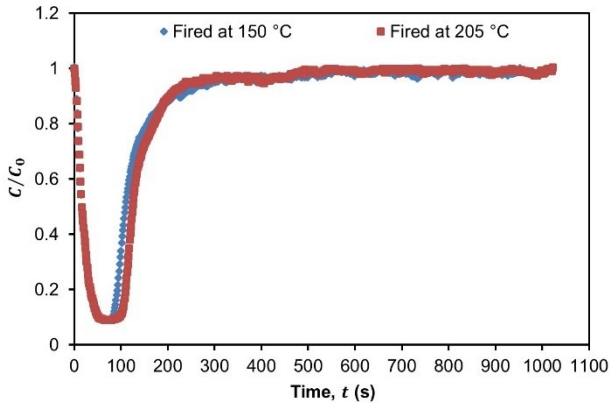


**Figure 6.15** Adsorption of 40% vol. $CO_2$ on 75% wt. purified MIL-101(Cr) monoliths that have been fired at 150 °C or 205 °C.

For this reason, a minor improvement of about 5% in the utilisation of purified MIL-101(Cr) monoliths for $CO_2$ adsorption was found when the firing temperature was increased from 150 °C to 205 °C (see Table 6.12). The results in Table 6.12 also indicate that the mass transfer zone velocity and length for the tested purified MIL-101(Cr) monoliths were about the same for both firing temperatures. This confirms that the firing

temperature did not have any effect on the mass transfer in purified MIL-101(Cr) monoliths. From this study, it seems that 205 °C is a more suitable firing temperature for MIL-101(Cr) monoliths since they gave better $CO_2$ adsorption performance compared to those fired at 150 °C.

**Table 6.12** The adsorption properties of purified MIL-101(Cr) monoliths with a firing temperature of 150 °C or 205 °C for 40% vol. $CO_2$ adsorption at 2 bar.

| Adsorption properties | $t_b$ (s) | $t_e$ (s) | $\overline{q}_b$ (mmol $g^{-1}$) & (mmol $cm^{-3}$ in bracket) | $\overline{q}_e$ (mmol $g^{-1}$) & (mmol $cm^{-3}$ in bracket) | $\omega_{bed}$ (%) | $u_{MTZ}$ (cm $min^{-1}$) | $\overline{L}_{MTZ}$ (%) |
|---|---|---|---|---|---|---|---|
| **150 °C** | 83 | 952 | 0.81 (0.27) | 1.68 (0.55) | 57.1 | 0.55 | 91.3 |
| **205 °C** | 95 | 1 022 | 0.95 (0.32) | 1.75 (0.59) | 61.8 | 0.51 | 90.7 |

### 6.3.2.4 Effect of 4% wt. pore forming agent on the adsorption properties of MIL-101(Cr) monoliths

Additionally, the effect of including 4% wt. pore forming agent (such as Licowax C micropowder PM) in the paste formulations of MIL-101(Cr) monoliths on their $CO_2$ adsorption properties was studied. In this investigation, the $CO_2$ adsorption experiments were carried out using 75% wt. purified MIL-101(Cr) monoliths without and those with 4% wt. Licowax C micropowder PM. The tested purified MIL-101(Cr) monoliths have been fired at 205 °C. Their 40% vol. $CO_2$ adsorption breakthrough curves are compared in Figure 6.16. It was seen that the sharpness of the breakthrough curves was slightly improved by incorporating a pore former in their paste formulations. This indicates that purified MIL-101(Cr) monoliths with a pore former have better mass transfer than those without any pore former, which was as a result of enhanced structural porosity of the monolithic structure after the pore former was burnt off.

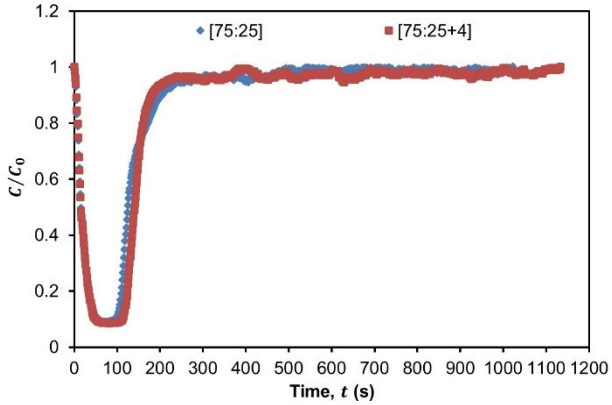


**Figure 6.16** Adsorption of 40% vol. $CO_2$ on 75% wt. purified MIL-101(Cr) monoliths without or with the inclusion of 4% wt. Licowax C micropowder PM as a pore former. Note: Their paste compositions are denoted by [% wt. MIL-101(Cr):% wt. calcium bentonite+% wt. pore former] in the plot.

The study found that purified MIL-101(Cr) monoliths with 4% wt. Licowax C micropowder PM took 16 seconds longer to breakthrough and 111 seconds longer to be completely saturated with $CO_2$ gas compared to those without any pore former. This means that purified MIL-101(Cr) monoliths with a pore former could be for $CO_2$ adsorption at a longer time and they would have lower frequency of replacement or regeneration. It was also found that the adsorption capacities of $CO_2$ (on mass basis) were slightly improved by about 17% at breakthrough and 7% at equilibrium when their paste formulations contained 4% wt. Licowax C micropowder PM, as indicated in Table 6.13. The reason was because more adsorption sites were exposed for $CO_2$ adsorption when the structural porosity of the monolith was enhanced after the pore former was decomposed.

On volumetric basis, the trend was reversed and this behaviour was not observed with zeolite monoliths (refer Section 6.3.1.4). The study found that the breakthrough and equilibrium adsorption capacities of $CO_2$ were slightly higher for purified MIL-101(Cr) monoliths without a pore former compared to those with a pore former. This might be attributed by a small difference in bed diameter of the monolith for adsorption experiments. Since the difference in $\bar{q}_e$ value was small, they were considered to have no difference in volumetric adsorption capacities of $CO_2$ for purified MIL-101(Cr) monoliths without and with a pore former.

**Table 6.13** The adsorption properties of purified MIL-101(Cr) monoliths without or with the inclusion of 4% wt. Licowax C micropowder PM as a pore former for 40% vol. $CO_2$ adsorption at 2 bar. Note that their paste formulations are denoted by [% wt. purified MIL-101(Cr):% wt. calcium bentonite+% wt. pore former] in the table.

| Adsorption properties | $t_b$ (s) | $t_e$ (s) | $\bar{q}_b$ (mmol g$^{-1}$) & (mmol cm$^{-3}$ in bracket) | $\bar{q}_e$ (mmol g$^{-1}$) & (mmol cm$^{-3}$ in bracket) | $\omega_{bed}$ (%) | $u_{MTZ}$ (cm min$^{-1}$) | $\bar{L}_{MTZ}$ (%) |
|---|---|---|---|---|---|---|---|
| **[75:25]** | 95 | 1 022 | 0.95 (0.32) | 1.75 (0.59) | 61.8 | 0.51 | 90.7 |
| **[75:25+4]** | 111 | 1 133 | 1.11 (0.31) | 1.87 (0.52) | 65.7 | 0.50 | 90.2 |

As a result of improved mass transfer in the monolithic structure, it was found that the use of purified MIL-101(Cr) monoliths with 4% wt. Licowax C micropowder PM for $CO_2$ adsorption was about 4% more effective than those without any pore former (Table 6.13). The results in Table 6.13 also indicate that the mass transfer zone velocity and length was about the same for both purified MIL-101(Cr) monoliths without and those with a pore

former. This was because the amount of pore former used in the study was very small, i.e., 4% wt. Licowax C micropowder PM.

#### 6.3.2.5 Effect of regeneration temperature on the adsorption properties of MIL-101(Cr) monoliths

The $CO_2$ adsorption experiments were also carried out using 75% wt. purified MIL-101(Cr) monoliths with 4% wt. Licowax C micropowder PM that have been regenerated at 150 °C, 180 °C or 200 °C. The purpose of this investigation was to determine a suitable regeneration temperature for MIL-101(Cr) monoliths. The tested purified MIL-101(Cr) monoliths have been fired at 205 °C and their 40% vol. $CO_2$ adsorption breakthrough curves are shown in Figure 6.17. It was observed that all the breakthrough curves were of the same sharpness. This gave an indication that the mass transfer in purified MIL-101(Cr) monoliths was not affected by the regeneration temperature.

Similar to zeolite monoliths, this study demonstrates that the breakthrough and equilibrium times for purified MIL-101(Cr) monoliths increase with increasing regeneration temperature. For example, it was found that purified MIL-101(Cr) monoliths took about 34 seconds longer to breakthrough and 294 seconds longer to saturate with $CO_2$ when the regeneration temperature was increased from 150 °C to 200 °C. This implies that purified MIL-101(Cr) monoliths that have been regenerated at a high temperature (i.e., 200 °C) could be used for a longer time for $CO_2$ adsorption before they need replacement or regeneration compared to those regenerated at a low temperature (i.e., 150 °C or 180 °C).

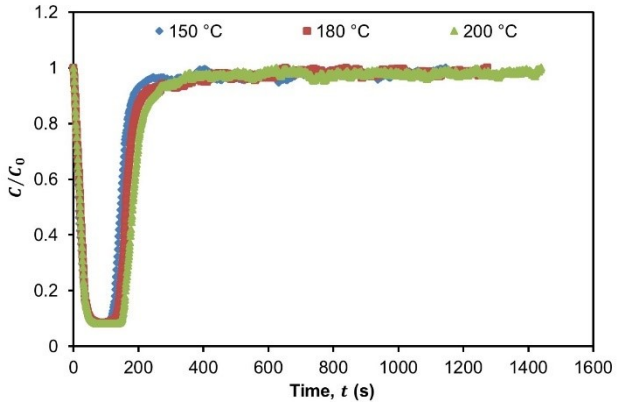


**Figure 6.17** Adsorption of 40% vol. $CO_2$ on 75% wt. purified MIL-101(Cr) monoliths with 4% wt. Licowax C micropowder PM with different regeneration temperatures.

As the regeneration temperature increases, more adsorption sites would be available for $CO_2$ adsorption since the desorption efficiency increases with increasing temperature (Liu *et al.*, 2013). This was demonstrated by the increase in breakthrough

and equilibrium adsorption capacities of $CO_2$ (both in terms of mass and volumetric). The results in Table 6.14 indicate that the adsorption capacities of $CO_2$ (on mass basis) for purified MIL-101(Cr) monoliths were improved by about 31% at breakthrough and 24% at equilibrium when they were regenerated at 200 °C instead of 150 °C. It was found that the use of purified MIL-101(Cr) monoliths for $CO_2$ adsorption was about 3% more effective when their regeneration temperature was elevated from 150 °C to 200 °C (refer Table 6.14). This was due to increasing availability of adsorption sites for $CO_2$ adsorption at higher regeneration temperature.

The results in Table 6.14 also show that their mass transfer zone velocity and length were about the same for all the different regeneration temperature considered in this study. This validates the fact that the regeneration temperature did not have major impact on the mass transfer in purified MIL-101(Cr) monoliths. From this investigation, it was found that the most suitable regeneration temperature for purified MIL-101(Cr) monoliths seems to be 200 °C. The reason was because purified MIL-101(Cr) monoliths that were regenerated at this temperature gave better $CO_2$ adsorption performance than those regenerated at 150 °C and 180 °C.

**Table 6.14** The adsorption properties of purified MIL-101(Cr) monoliths with different regeneration temperatures for 40% vol. $CO_2$ adsorption at 2 bar.

| Adsorption properties | $t_b$ (s) | $t_e$ (s) | $\overline{q}_b$ (mmol $g^{-1}$) & (mmol $cm^{-3}$ in bracket) | $\overline{q}_e$ (mmol $g^{-1}$) & (mmol $cm^{-3}$ in bracket) | $\omega_{bed}$ (%) | $u_{MTZ}$ (cm $min^{-1}$) | $\overline{L}_{MTZ}$ (%) |
|---|---|---|---|---|---|---|---|
| **150 °C** | 115 | 1 145 | 1.16 (0.33) | 1.92 (0.54) | 66.5 | 0.50 | 90.0 |
| **180 °C** | 130 | 1 273 | 1.28 (0.36) | 2.10 (0.59) | 67.0 | 0.45 | 89.8 |
| **200 °C** | 149 | 1 439 | 1.52 (0.43) | 2.38 (0.67) | 69.1 | 0.40 | 89.6 |

### 6.3.2.6 Repeatability of experimental results for MIL-101(Cr) monoliths

To verify the accuracy of the experimental data obtained for MIL-101(Cr) monoliths, the $CO_2$ adsorption experiments were repeated twice using 75% wt. purified MIL-101(Cr) monolith with 4% wt. Licowax C micropowder PM that has been fired at 205 °C. Their 40% vol. $CO_2$ adsorption breakthrough curves are presented in Figure 6.18. It was seen that both breakthrough curves have identical sharpness, indicating good reproducibility of experimental data.

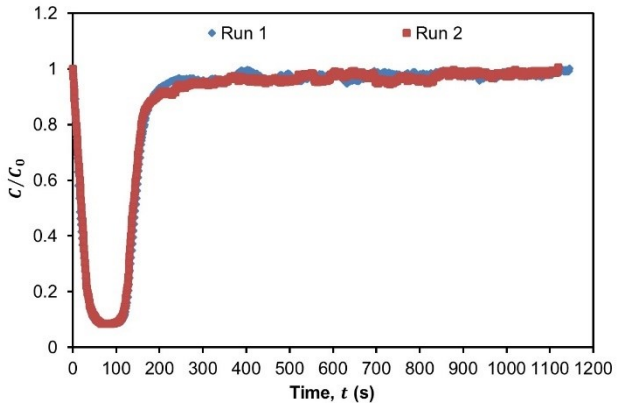


**Figure 6.18** Adsorption of 40% vol. $CO_2$ on 75% wt. purified MIL-101(Cr) monoliths with 4% wt. Licowax C micropowder PM with two repeated adsorption runs.

For both adsorption runs, the breakthrough and equilibrium times were about the same and this demonstrates that the experimental data obtained for the adsorption of $CO_2$ onto purified MIL-101(Cr) monoliths were accurate. The same behaviour was also observed by Zhang *et al.* (2011). It was found that the breakthrough and adsorption capacities of $CO_2$ (both in terms of mass and volumetric) for purified MIL-101(Cr) monoliths were slightly lower when they were reused. In this case, the adsorption capacities of $CO_2$ (on mass basis) were found to reduce by about 9% at breakthrough and 2% at equilibrium when they were reused for $CO_2$ adsorption for the second time (refer Table 6.15). This shows that less adsorption sites were available for $CO_2$ adsorption in the second adsorption run when compared to the first adsorption run. The reasons could be due to the lost adsorbent materials during handling or inefficient desorption and regeneration of purified MIL-101(Cr) monoliths after the first adsorption run.

**Table 6.15** The adsorption properties of purified MIL-101(Cr) monoliths with two repeated adsorption runs for 40% vol. $CO_2$ adsorption at 2 bar.

| Adsorption properties | $t_b$ (s) | $t_e$ (s) | $\overline{q}_b$ (mmol g$^{-1}$) & (mmol cm$^{-3}$ in bracket) | $\overline{q}_e$ (mmol g$^{-1}$) & (mmol cm$^{-3}$ in bracket) | $\omega_{bed}$ (%) | $u_{MTZ}$ (cm min$^{-1}$) | $\overline{L}_{MTZ}$ (%) |
|---|---|---|---|---|---|---|---|
| **Run 1** | 115 | 1 145 | 1.16 (0.33) | 1.92 (0.54) | 66.5 | 0.50 | 90.0 |
| **Run 2** | 110 | 1 119 | 1.06 (0.30) | 1.89 (0.53) | 62.9 | 0.51 | 90.2 |

Because of these reasons, the use of purified MIL-101(Cr) monoliths for $CO_2$ adsorption was about 4% less effective in the second adsorption run (see Table 6.15). The study also found that their mass transfer zone velocity and length were about the same for both adsorption runs, as indicated in Table 6.15. This shows that there was no effect on the mass transfer in purified MIL-101(Cr) monoliths when they were reused again for $CO_2$ adsorption.

### 6.3.3 Optimisation of carbonate-based zeolite foam-monoliths

This section covers that the results and discussion for the optimisation of carbonate-based zeolite foam-monoliths. Some of the parameters that are considered in this optimisation study are: (a) the type of carbonates, (b) effect of 4% wt. pore forming agent, (c) firing temperature, (d) bed length and (e) regeneration temperature. The $CO_2$ sorption breakthrough curves for carbonate-based zeolite foam-monoliths prepared in the research are analysed and discussed in Sections 6.3.3.1 to 6.2.2.5. The $CO_2$ sorption experiments for carbonate-based zeolite foam-monoliths are also repeated to check the accuracy of their experimental data and their results are shown in Section 6.3.3.6.

#### 6.3.3.1 Sorption onto carbonate-based zeolite foam-monoliths of different type of carbonates

First, the $CO_2$ sorption experiments were carried out using 10 cm long carbonate-based zeolite foam-monoliths that contained different type of carbonates (i.e., $K_2CO_3$ or $Na_2CO_3$). This was to identify the most suitable type of carbonate-based zeolite foam-monoliths for $CO_2$ sorption. The tested carbonate-based zeolite foam-monoliths were prepared using 75% wt. 13X zeolite, 25% wt. calcium bentonite and 4% wt. $KHCO_3$ or $NaHCO_3$ and they have been fired at 400 °C. Their 40% vol. $CO_2$ sorption breakthrough curves are shown in Figure 6.19. It was observed that the sharpness of the breakthrough curves was the same for both type of carbonate-based zeolite foam-monoliths. This implies that the mass transfer in carbonate-based zeolite foam-monoliths was not dependent on the type of carbonates.

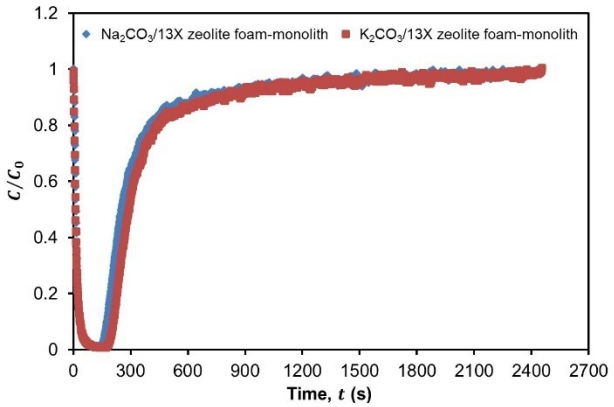


**Figure 6.19** Sorption of 40% vol. $CO_2$ on $Na_2CO_3$/13X zeolite and $K_2CO_3$/13X zeolite foam-monoliths.

It was noticed that the $K_2CO_3$/13X zeolite foam-monolith has slightly longer breakthrough and equilibrium times than the $Na_2CO_3$/13X zeolite foam-monolith. The

results found that the $K_2CO_3$/13X zeolite foam-monolith took about 24 seconds longer to breakthrough and 203 seconds longer to saturate with $CO_2$ than the $Na_2CO_3$/13X zeolite foam-monolith. This means that $K_2CO_3$/13X zeolite foam-monolith could be used for $CO_2$ adsorption at a longer time and it has lower frequency of replacement or regeneration than $Na_2CO_3$/13X zeolite foam-monolith.

The results in Table 6.16 indicate that $K_2CO_3$/13X zeolite foam-monolith has higher breakthrough and equilibrium sorption capacities of $CO_2$ (both in terms of mass and volumetric) than $Na_2CO_3$/13X zeolite foam-monolith. The study found that the sorption capacities of $CO_2$ (on mass basis) for $K_2CO_3$/13X zeolite foam-monolith were higher by about 20% at breakthrough and 16% at equilibrium compared to those for $Na_2CO_3$/13X zeolite foam-monolith, as revealed in Table 6.16. This suggests that more adsorption sites were available for $CO_2$ sorption when $K_2CO_3$ was incorporated onto the foam-monolithic structure instead of $Na_2CO_3$. The reason was because $K_2CO_3$ has higher chemical affinity for $CO_2$ compared to $Na_2CO_3$. Due to this reason, the use of $K_2CO_3$/13X zeolite foam-monolith for $CO_2$ sorption was slightly more effective (i.e., by about 1%) than $Na_2CO_3$/13X zeolite foam-monolith (see Table 6.16).

The results in Table 6.16 indicate that there was no significant change in mass transfer zone velocity and length when the type of carbonates was varied. This confirms that the type of carbonates did not have any effect on the mass transfer in carbonate-based zeolite foam-monoliths. From this investigation, it was found that the most suitable carbonate-based zeolite foam-monoliths for $CO_2$ sorption was $K_2CO_3$/13X zeolite foam-monolith as they exhibit better $CO_2$ sorption performance than $Na_2CO_3$/13X zeolite foam-monolith.

**Table 6.16** The sorption properties of $Na_2CO_3$/13X zeolite and $K_2CO_3$/13X zeolite foam-monoliths for 40% vol. $CO_2$ sorption at 2 bar.

| Sorption properties | $t_b$ (s) | $t_e$ (s) | $\overline{q}_b$ (mmol g$^{-1}$) & (mmol cm$^{-3}$ in bracket) | $\overline{q}_e$ (mmol g$^{-1}$) & (mmol cm$^{-3}$ in bracket) | $\omega_{bed}$ (%) | $u_{MTZ}$ (cm min$^{-1}$) | $\bar{L}_{MTZ}$ (%) |
|---|---|---|---|---|---|---|---|
| **$Na_2CO_3$/13X zeolite foam-monolith** | 156 | 2 251 | 0.81 (0.51) | 2.12 (1.34) | 41.3 | 0.27 | 93.1 |
| **$K_2CO_3$/13X zeolite foam-monolith** | 180 | 2 454 | 0.97 (0.59) | 2.45 (1.49) | 42.1 | 0.23 | 92.7 |

### 6.3.3.2 Effect of 4% wt. pore forming agent on the sorption properties of carbonate-based zeolite foam-monoliths

Then, the effect of including 4% wt. pore forming agent (such as Licowax C micropowder PM) into the paste formulations of carbonate-based zeolite foam-monoliths on their $CO_2$ sorption properties was investigated. In this study, the $CO_2$ sorption experiments were carried out using 10 cm long $Na_2CO_3$/13X zeolite and $K_2CO_3$/13X zeolite foam-monoliths without and those with 4% wt. Licowax C micropowder PM. All the tested carbonate-based zeolite foam-monoliths have been fired at 400 °C. Their 40% vol. $CO_2$ sorption breakthrough curves are shown separately in Figures 6.20 (a) and (b) for each type of carbonate-based zeolite foam-monoliths. It was seen that the breakthrough curves were slightly improved by adding a pore former in their paste formulations, indicating better mass transfer in the foam-monolithic bed. This was due to the enhanced structural porosity of the carbonate-based zeolite foam-monoliths after the pore former was decomposed.

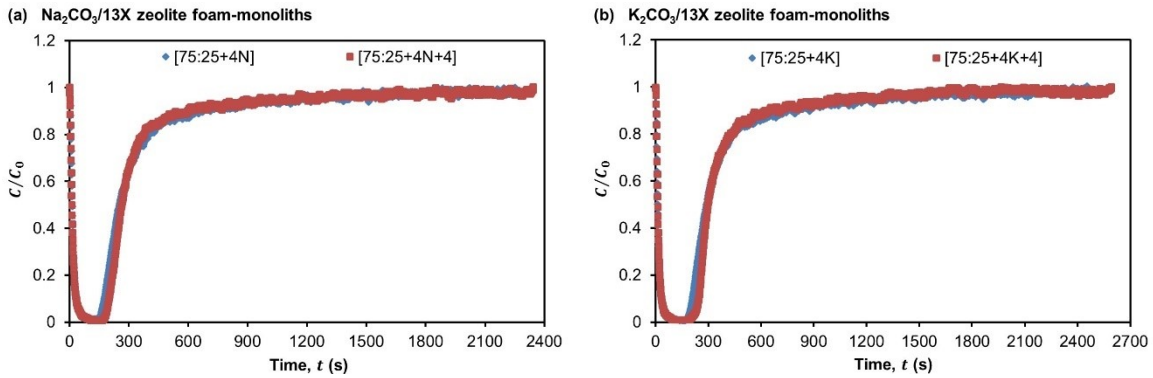


**Figure 6.20** Sorption of 40% vol. $CO_2$ on (a) $Na_2CO_3$/13X zeolite and (b) $K_2CO_3$/13X zeolite foam-monoliths without or with the inclusion of 4% wt. Licowax C micropowder PM as a pore former. Note: Their paste compositions are denoted by [% wt. 13X zeolite:% wt. calcium bentonite+% wt. $NaHCO_3$ (N) or $KHCO_3$ (K)+% wt. pore former] in the plots.

The study shows that the breakthrough and equilibrium times were slightly longer when a pore former was included in the paste formulations of carbonate-based zeolite foam-monoliths. For example, it was found that $K_2CO_3$/13X zeolite foam-monoliths with 4% wt. Licowax C micropowder PM took about 22 seconds longer to breakthrough and 138 seconds longer to saturate with $CO_2$ compared to those without any pore former (refer Table 6.17). This means carbonate-based zeolite foam-monoliths with a pore former could be used for $CO_2$ sorption at a longer time and they would have lower frequency of replacement or regeneration compared to those without any pore former.

The breakthrough and equilibrium sorption capacities of $CO_2$ (in terms of mass and volumetric, in most cases) for carbonate-based zeolite foam-monoliths were also found to

improve by adding a pore former in their paste formulations. For example, the results in Table 6.17 revealed that the $CO_2$ sorption capacities (on mass basis) for $K_2CO_3$/13X zeolite foam-monoliths were improved slightly by about 16% at breakthrough and 2% at equilibrium when their paste formulations contained 4% wt. Licowax C micropowder PM. This was because more adsorption sites were exposed to $CO_2$ when the structural porosity of the foam-monolith was enhanced after the pore former was burnt off.

**Table 6.17** The sorption properties of $Na_2CO_3$/13X zeolite and $K_2CO_3$/13X zeolite foam-monoliths without or with the inclusion of 4% wt. Licowax C micropowder PM as a pore former for 40% vol. $CO_2$ sorption at 2 bar. Note that their paste compositions are denoted by [% wt. 13X zeolite:% wt. calcium bentonite+% wt. $NaHCO_3$ (N) or $KHCO_3$ (K)+% wt. pore former] in the table.

| Sorption properties | | $t_b$ (s) | $t_e$ (s) | $\bar{q}_b$ (mmol g$^{-1}$) & (mmol cm$^{-3}$ in bracket) | $\bar{q}_e$ (mmol g$^{-1}$) & (mmol cm$^{-3}$ in bracket) | $\omega_{bed}$ (%) | $u_{MTZ}$ (cm min$^{-1}$) | $\bar{L}_{MTZ}$ (%) |
|---|---|---|---|---|---|---|---|---|
| **$Na_2CO_3$/13X zeolite foam-monolith** | **[75:25+4N]** | 156 | 2 251 | 0.81 (0.51) | 2.12 (1.34) | 41.3 | 0.27 | 93.1 |
| | **[75:25+4N+4]** | 173 | 2 345 | 0.93 (0.54) | 2.17 (1.26) | 45.4 | 0.26 | 92.6 |
| **$K_2CO_3$/13X zeolite foam-monolith** | **[75:25+4K]** | 180 | 2 454 | 0.97 (0.59) | 2.45 (1.49) | 42.1 | 0.23 | 92.7 |
| | **[75:25+4K+4]** | 202 | 2 592 | 1.13 (0.67) | 2.50 (1.49) | 47.7 | 0.22 | 92.2 |

The study found that the effectiveness of the foam-monolithic bed utilised for $CO_2$ sorption was slightly higher when a pore former was included in their paste formulations. For example, the use of $K_2CO_3$/13X zeolite foam-monoliths for $CO_2$ sorption was found to be about 5% more effective when their paste formulations contained 4% wt. Licowax C micropowder PM compared to those without any pore former (see Table 6.17). Moreover, the incorporation of 4% wt. Licowax C micropowder PM in the paste formulations of carbonate-based zeolite foam-monoliths did not show major change in their mass transfer zone velocity and length, as indicated in Table 6.17. This was because the amount of pore former used in the study was very small. The behaviour of carbonate-based zeolite foam-monoliths with a pore former was similar to those described previously for zeolite and MIL-101(Cr) monoliths (i.e., Sections 6.3.1.4 and 6.3.2.4, respectively) and to the literature, for example, Lee (1997).

#### 6.3.3.3 Sorption onto carbonate-based zeolite foam-monoliths that have been fired at different temperatures

The effect of firing temperature on the $CO_2$ sorption properties of carbonate-based zeolite foam-monoliths was also studied to determine a suitable firing temperature for carbonate-based zeolite foam-monoliths. In this investigation, 10 cm long $Na_2CO_3$/13X zeolite and $K_2CO_3$/13X zeolite foam-monoliths that have been fired at 400 °C or 650 °C

were tested for $CO_2$ sorption. Their 40% vol. $CO_2$ sorption breakthrough curves are shown individually in Figures 6.21 (a) and (b) for each type of carbonate-based zeolite foam-monoliths. It was seen that the sharpness of the breakthrough curves was about the same for both firing temperatures. This implies that the mass transfer in carbonate-based zeolite foam-monoliths was not affected by the firing temperature.

Similar to that exhibit by zeolite and MIL-101(Cr) monoliths, the breakthrough and equilibrium times were shorter when they were fired at higher temperature (i.e., 650 °C). For example, $K_2CO_3$/13X zeolite foam-monoliths show that their breakthrough time was reduced by about 22% and their equilibrium time was reduced by about 7% when their firing temperature was increased from 400 °C to 650 °C. The reason was because their mass transfer front reaches the end of the foam-monolithic bed early and the bed gets saturated with $CO_2$ faster. This means that carbonate-based zeolite foam-monoliths that have been fired at 650 °C could not be used for $CO_2$ adsorption at a longer time and they would require more frequent replacement or regeneration than those fired at 400 °C.

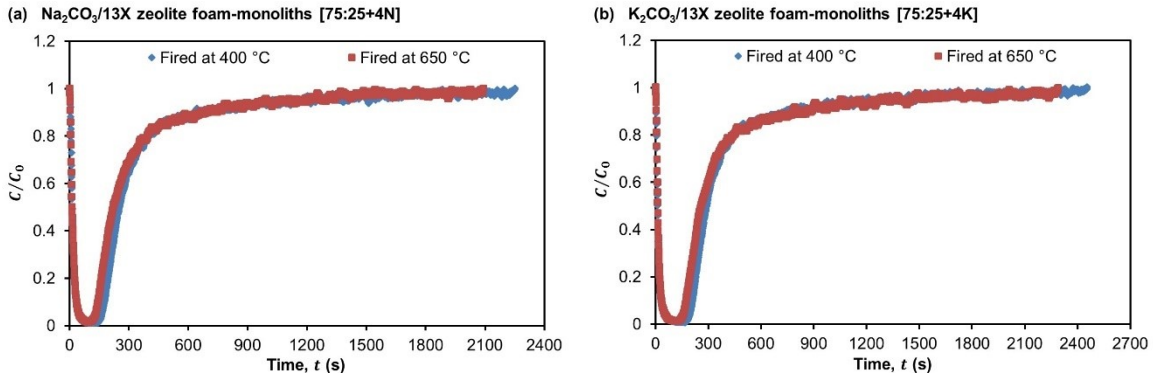


**Figure 6.21** Sorption of 40% vol. $CO_2$ on (a) $Na_2CO_3$/13X zeolite and (b) $K_2CO_3$/13X zeolite foam-monoliths that have been fired at 400 °C or 650 °C. Note: Their paste compositions are denoted by [% wt. 13X zeolite:% wt. calcium bentonite+% wt. $NaHCO_3$ (N) or $KHCO_3$ (K)] in the plots.

The study found that carbonate-based zeolite foam-monoliths exhibit lower breakthrough and equilibrium sorption capacities of $CO_2$ (on mass basis) when they were fired at a higher temperature (i.e., 650 °C). On volumetric basis, the trend was reversed and it might be attributed by a small difference in bed mass of the monolith for adsorption experiments. The sorption capacities of $CO_2$ (on mass basis) for $K_2CO_3$/13X zeolite foam-monoliths were found to reduce slightly by about 25% at breakthrough and 5% at equilibrium as their firing temperature increased from 400 °C to 650 °C, as indicated in Table 6.18. This suggests that less adsorption sites were available for $CO_2$ sorption when they were fired at 650 °C compared to those fired at 400 °C. Because of this reason, the effectiveness of carbonate-based zeolite foam-monoliths utilised for $CO_2$ sorption was

also affected. For example, the results in Table 6.18 reveal that the use of $K_2CO_3$/13X zeolite foam-monoliths for $CO_2$ sorption was about 8% less effective when their firing temperature was increased from 400 °C to 650 °C.

**Table 6.18** The sorption properties of $Na_2CO_3$/13X zeolite and $K_2CO_3$/13X zeolite foam-monoliths that have been fired at 400 °C or 650 °C for 40% vol. $CO_2$ sorption at 2 bar.

| Sorption properties | | $t_b$ (s) | $t_e$ (s) | $\overline{q}_b$ (mmol g$^{-1}$) & (mmol cm$^{-3}$ in bracket) | $\overline{q}_e$ (mmol g$^{-1}$) & (mmol cm$^{-3}$ in bracket) | $\omega_{bed}$ (%) | $u_{MTZ}$ (cm min$^{-1}$) | $\overline{L}_{MTZ}$ (%) |
|---|---|---|---|---|---|---|---|---|
| **$Na_2CO_3$/13X zeolite foam-monolith** | **400 °C** | 156 | 2 251 | 0.81 (0.51) | 2.12 (1.34) | 41.3 | 0.27 | 93.1 |
| | **650 °C** | 119 | 2 091 | 0.61 (0.35) | 1.97 (1.13) | 34.5 | 0.29 | 94.3 |
| **$K_2CO_3$/13X zeolite foam-monolith** | **400 °C** | 180 | 2 454 | 0.97 (0.59) | 2.45 (1.49) | 42.1 | 0.23 | 92.7 |
| | **650 °C** | 141 | 2 290 | 0.73 (0.40) | 2.33 (1.28) | 34.3 | 0.28 | 93.8 |

The results in Table 6.18 also show that the mass transfer zone velocity and length was about the same for both firing temperatures. This confirms that the firing temperature did not have any influence on the mass transfer in carbonate-based zeolite foam-monoliths. From this investigation, it was found that the most suitable firing temperature for carbonate-based zeolite foam-monoliths was 400 °C. The reason was because carbonate-based zeolite foam-monoliths that have been fired at this temperature gave better $CO_2$ sorption performance than those fired at 650 °C.

#### 6.3.3.4 Sorption onto carbonate-based zeolite foam-monoliths of different bed lengths

Next, the $CO_2$ sorption experiments were carried out using carbonate-based zeolite foam-monoliths of different bed lengths (i.e., 10 cm or 20 cm). In this study, $Na_2CO_3$/13X zeolite and $K_2CO_3$/13X zeolite foam-monoliths that have been fired at 400 °C were used. Their 40% vol. $CO_2$ sorption breakthrough curves are shown in Figures 6.22 (a) and (b) for each type of carbonate-based zeolite foam-monoliths. The sharpness of the breakthrough curves was the same for both 10 cm and 20 cm long foam-monolithic beds. This indicates that the bed length did not have any influence on the mass transfer in carbonate-based zeolite foam-monoliths.

It was observed that the breakthrough and equilibrium times increase with increasing bed length. This trend was similar to that observed in previous section for zeolite monoliths (i.e., Section 6.3.1.7) and by Wang (2008). For example, $K_2CO_3$/13X

zeolite foam-monoliths show that their breakthrough time was increased by about 3.3 times and their equilibrium time was increased by about 1.5 times when their bed length was increased from 10 cm to 20 cm. This can be explained by the fact that the mass transfer front takes a longer time to reach the end of the foam-monolithic bed and for the bed to be saturated with $CO_2$. This implies that a long carbonate-based zeolite foam-monoliths could be used for a longer time for $CO_2$ sorption before they need replacement or regeneration.

The results in Table 6.19 indicates that the breakthrough and equilibrium sorption capacities of $CO_2$ (on mass basis) for carbonate-based zeolite foam-monoliths were improved slightly by increasing their bed length. On volumetric basis, the breakthrough sorption capacity of $CO_2$ was increased and the equilibrium sorption capacity of $CO_2$ was decreased slightly. This might be attributed by the difference in bed length of the monolith for adsorption experiments. In this study, the sorption capacities of $CO_2$ (on mass basis) for $K_2CO_3$/13X zeolite foam-monoliths was found to improve by about 53% at breakthrough and 0.8% at equilibrium when their bed length was increased 10 cm to 20 cm (refer Table 6.19). This was because more adsorption sites were available for $CO_2$ sorption since there were more zeolite and carbonate crystals present in the foam-monolithic structure compared to a short foam-monolithic bed.

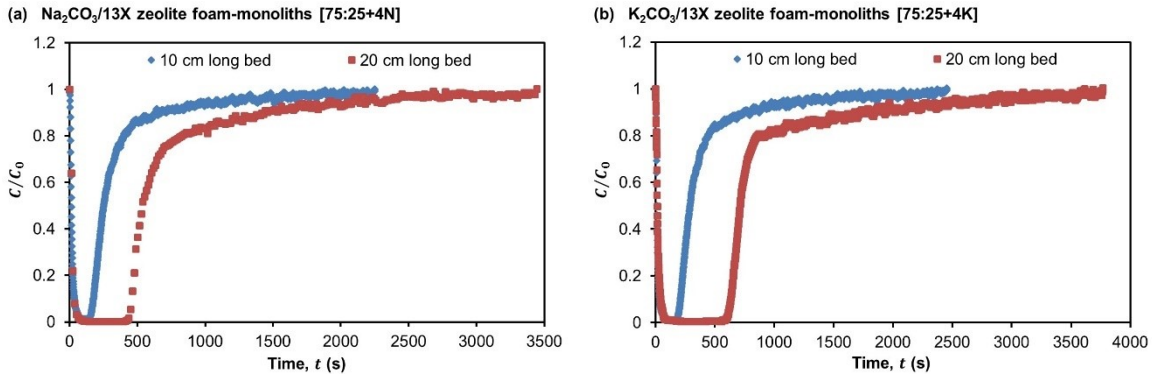


**Figure 6.22** Sorption of 40% vol. $CO_2$ on (a) $Na_2CO_3$/13X zeolite and (b) $K_2CO_3$/13X zeolite foam-monoliths with either 10 cm or 20 cm long bed. Note: Their paste compositions are denoted by [% wt. 13X zeolite:% wt. calcium bentonite+% wt. $NaHCO_3$ (N) or $KHCO_3$ (K)] in the plots.

Due to this reason, the effectiveness of the foam-monolithic bed utilised for $CO_2$ sorption was slightly higher when they have longer bed length. For example, it was found that the use of 20 cm long $K_2CO_3$/13X zeolite foam-monoliths for $CO_2$ sorption was about 19% more effective than 10 cm long $K_2CO_3$/13X zeolite foam-monoliths, as indicated in Table 6.19. Moreover, no significant change in the mass transfer zone velocity was found

when their bed length was varied (see Table 6.19). The reason was because the mass transfer in carbonate-based zeolite foam-monoliths was not dependent on the bed length.

**Table 6.19** The sorption properties of $Na_2CO_3$/13X zeolite and $K_2CO_3$/13X zeolite foam-monoliths with either 10 cm or 20 cm long bed for 40% vol. $CO_2$ sorption at 2 bar.

| Sorption properties | | $t_b$ (s) | $t_e$ (s) | $\overline{q}_b$ (mmol g$^{-1}$) & (mmol cm$^{-3}$ in bracket) | $\overline{q}_e$ (mmol g$^{-1}$) & (mmol cm$^{-3}$ in bracket) | $\omega_{bed}$ (%) | $u_{MTZ}$ (cm min$^{-1}$) | $\overline{L}_{MTZ}$ (%) |
|---|---|---|---|---|---|---|---|---|
| **$Na_2CO_3$/13X zeolite foam-monolith** | **10 cm** | 156 | 2 251 | 0.81 (0.51) | 2.12 (1.34) | 41.3 | 0.27 | 93.1 |
| | **20 cm** | 439 | 3 444 | 1.18 (0.72) | 2.13 (1.30) | 56.4 | 0.35 | 87.3 |
| **$K_2CO_3$/13X zeolite foam-monolith** | **10 cm** | 180 | 2 454 | 0.97 (0.59) | 2.45 (1.49) | 42.1 | 0.23 | 92.7 |
| | **20 cm** | 591 | 3 769 | 1.48 (0.87) | 2.47 (1.46) | 60.7 | 0.32 | 84.3 |

The results in Table 6.19 also indicate that the mass transfer zone length was slightly shorter when a long (i.e., 20 cm) carbonate-based zeolite foam-monolith was used for $CO_2$ sorption. For example, it was found that the mass transfer zone length for $K_2CO_3$/13X zeolite foam-monoliths was reduced by about 8% when their bed length was increased from 10 cm to 20 cm. This was due to the efficient utilisation of foam-monolithic beds for $CO_2$ sorption.

#### 6.3.3.5 Effect of regeneration temperature on the sorption properties of carbonate-based zeolite foam-monoliths

Further $CO_2$ sorption experiments were carried out using $Na_2CO_3$/13X zeolite and $K_2CO_3$/13X zeolite foam-monoliths with 4% wt. Licowax C micropowder PM that have regenerated at different temperatures (i.e., 150 °C, 200 °C or 250 °C). This was to determine a suitable regeneration temperature for carbonate-based zeolite foam-monoliths. The tested carbonate-based zeolite foam-monoliths have been fired at 400 °C and their 40% vol. $CO_2$ sorption breakthrough curves are demonstrated individually in Figures 6.23 (a) and (b) for each type of carbonate-based zeolite foam-monoliths. It was seen that the breakthrough curves were of the same sharpness for all the regeneration temperatures considered in this study. This indicates that the mass transfer in carbonate-based zeolite foam-monoliths was not affected by the regeneration temperature.

Similar to zeolite and MIL-101(Cr) monoliths, the breakthrough and equilibrium times for carbonate-based zeolite foam-monoliths were found to increase with increasing regeneration temperature. For example, $K_2CO_3$/13X zeolite foam-monoliths show that

their breakthrough time was increased by about 57% and their equilibrium time was increased by about 20% when their regeneration temperature was elevated from 150 °C to 250 °C. This means that carbonate-based zeolite foam-monoliths that have been regenerated at higher temperature (i.e., 250 °C) could be used for $CO_2$ sorption at a longer time and they would have lower frequency of replacement or regeneration compared to those regenerated at lower temperature (i.e., 150 °C or 200 °C).

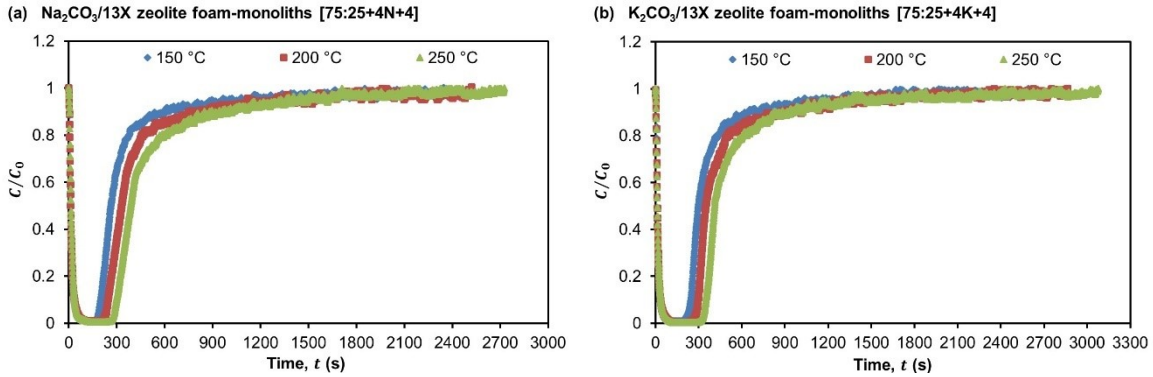


**Figure 6.23** Sorption of 40% vol. $CO_2$ on (a) $Na_2CO_3$/13X zeolite and (b) $K_2CO_3$/13X zeolite foam-monoliths with different regeneration temperatures. Note: Their paste compositions are denoted by [% wt. 13X zeolite:% wt. calcium bentonite+% wt. $NaHCO_3$ (N) or $KHCO_3$ (K)+% wt. pore former] in the plots.

The study found that the breakthrough and equilibrium sorption capacities of $CO_2$ (both in terms of mass and volumetric) were improved when the regeneration temperature of carbonate-based zeolite foam-monoliths was increased. Veselovskaya *et al.* (2015) also observed the same trend. In this case, the sorption capacities of $CO_2$ (on mass basis) for $K_2CO_3$/13X zeolite foam-monoliths were found to increase by about 93% at breakthrough and 62% at equilibrium when they were regenerated at 250 °C instead of 150 °C (refer Table 6.20). This was because more adsorption sites were available for $CO_2$ sorption when they were regenerated at higher temperature (i.e., 250 °C). For this reason, the utilisation of carbonate-based zeolite foam-monolithic beds for $CO_2$ sorption was slightly enhanced, as indicated in Table 6.20. For example, it was found that the use of $K_2CO_3$/13X zeolite foam-monoliths for $CO_2$ sorption was about 7% more effective when they were regenerated at 250 °C compared to those regenerated at 150 °C.

The results in Table 6.20 also show that their mass transfer zone velocity and length were about the same for all regeneration temperatures. This confirms that the mass transfer in carbonate-based zeolite foam-monoliths was not influence by the regeneration temperature. From this investigation, it seems that 250 °C was the most suitable regeneration temperature for carbonate-based zeolite foam-monoliths as they gave better $CO_2$ sorption performance than those regenerated at 150 °C and 200 °C.

**Table 6.20** The sorption properties of $Na_2CO_3$/13X zeolite and $K_2CO_3$/13X zeolite foam-monoliths with different regeneration temperatures for 40% vol. $CO_2$ sorption at 2 bar.

| Sorption properties | | $t_b$ (s) | $t_e$ (s) | $\bar{q}_b$ (mmol g$^{-1}$) & (mmol cm$^{-3}$ in bracket) | $\bar{q}_e$ (mmol g$^{-1}$) & (mmol cm$^{-3}$ in bracket) | $\omega_{bed}$ (%) | $u_{MTZ}$ (cm min$^{-1}$) | $\bar{L}_{MTZ}$ (%) |
|---|---|---|---|---|---|---|---|---|
| **$Na_2CO_3$/13X zeolite foam-monolith** | **150 °C** | 173 | 2 345 | 0.93 (0.54) | 2.17 (1.26) | 45.4 | 0.26 | 92.6 |
| | **200 °C** | 222 | 2 520 | 1.29 (0.71) | 2.86 (1.59) | 47.1 | 0.25 | 91.2 |
| | **250 °C** | 269 | 2 724 | 1.69 (0.88) | 3.50 (1.82) | 50.2 | 0.23 | 90.1 |
| **$K_2CO_3$/13X zeolite foam-monolith** | **150 °C** | 202 | 2 592 | 1.13 (0.67) | 2.50 (1.49) | 47.7 | 0.22 | 92.2 |
| | **200 °C** | 260 | 2 862 | 1.57 (0.91) | 3.21 (1.85) | 50.8 | 0.20 | 90.9 |
| | **250 °C** | 317 | 3 076 | 2.18 (1.13) | 4.06 (2.10) | 55.1 | 0.19 | 89.7 |

### 6.3.3.6 Repeatability of experimental results for carbonate-based zeolite foam-monoliths

The $CO_2$ sorption experiments were repeated twice to check the accuracy of the experimental data obtained for the optimisation of carbonate-based zeolite foam-monoliths. In this study, $Na_2CO_3$/13X zeolite and $K_2CO_3$/13X zeolite foam-monoliths with 4% wt. Licowax C micropowder PM that have been fired at 400 °C were used. Their 40% vol. $CO_2$ sorption breakthrough curves are shown separately in Figures 6.24 (a) and (b) for each type of carbonate-based zeolite foam-monoliths. The sharpness of breakthrough curves was the same for both $CO_2$ sorption runs, indicating good reproducibility of experimental data.

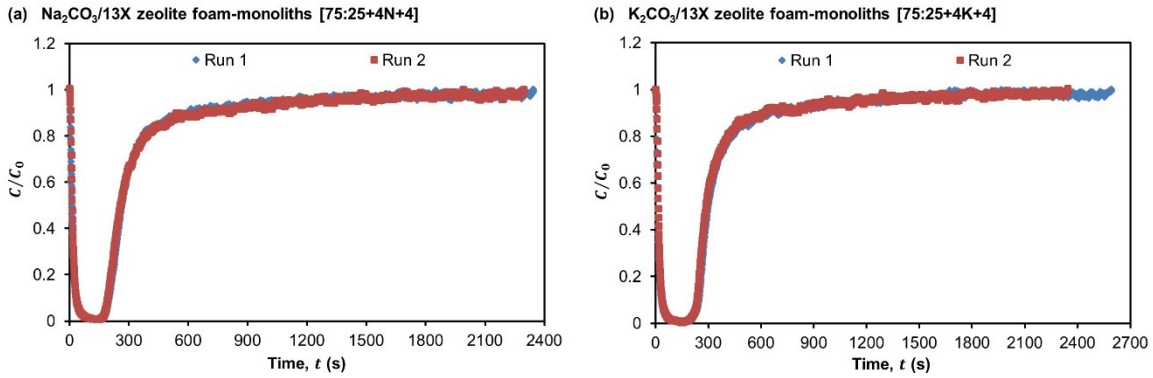


**Figure 6.24** Sorption of 40% vol. $CO_2$ on (a) $Na_2CO_3$/13X zeolite and (b) $K_2CO_3$/13X zeolite foam-monoliths with two repeated sorption runs. Note: Their paste compositions are denoted by [% wt. 13X zeolite:% wt. calcium bentonite+% wt. $NaHCO_3$ (N) or $KHCO_3$ (K)+% wt. pore former] in the plots.

No major difference in breakthrough and equilibrium times were observed when the $CO_2$ sorption experiments were repeated for the second time. This means that the

experimental data for $CO_2$ sorption onto carbonate-based zeolite foam-monoliths obtained in this study was accurate. The study found that the breakthrough and equilibrium sorption capacities of $CO_2$ (in terms of mass and volumetric, in most cases) were slightly reduced when carbonate-based zeolite foam-monoliths were reused. For example, the sorption capacities of $CO_2$ (on mass basis) for $K_2CO_3$/13X zeolite foam-monoliths were found to decrease slightly by about 11% at breakthrough and 2% at equilibrium when they were reused for $CO_2$ sorption for the second time. This indicate that less adsorption sites were available for $CO_2$ sorption in the second sorption run compared to the first sorption run. The reasons may be due to the loss of adsorbent materials during handling or inefficient desorption and regeneration. The same trend was also reported by Jo *et al.* (2016).

As a result of the small reduction in sorption capacity, a minor decrease in the effectiveness of the foam-monolithic bed utilised for $CO_2$ sorption was found. For example, the use of $K_2CO_3$/13X zeolite foam-monoliths for $CO_2$ sorption was found to be about 4% less effective when they were reused for $CO_2$ sorption for the second time (see Table 6.21). The study also found that their mass transfer zone velocity and length were about the same for both $CO_2$ sorption runs, as indicated in Table 6.21. This shows that the mass transfer in carbonate-based zeolite foam-monoliths was not affected when they were reused for $CO_2$ sorption.

**Table 6.21** The sorption properties of $Na_2CO_3$/13X zeolite and $K_2CO_3$/13X zeolite foam-monoliths with two repeated sorption runs for 40% vol. $CO_2$ sorption at 2 bar.

| Sorption properties | | $t_b$ (s) | $t_e$ (s) | $\overline{q}_b$ (mmol g$^{-1}$) & (mmol cm$^{-3}$ in bracket) | $\overline{q}_e$ (mmol g$^{-1}$) & (mmol cm$^{-3}$ in bracket) | $\omega_{bed}$ (%) | $u_{MTZ}$ (cm min$^{-1}$) | $\overline{L}_{MTZ}$ (%) |
|---|---|---|---|---|---|---|---|---|
| **$Na_2CO_3$/13X zeolite foam-monolith** | **Run 1** | 173 | 2 345 | 0.93 (0.54) | 2.17 (1.26) | 45.4 | 0.26 | 92.6 |
| | **Run 2** | 168 | 2 296 | 0.87 (0.51) | 2.14 (1.27) | 43.5 | 0.27 | 92.7 |
| **$K_2CO_3$/13X zeolite foam-monolith** | **Run 1** | 202 | 2 592 | 1.13 (0.67) | 2.50 (1.49) | 47.7 | 0.22 | 92.2 |
| | **Run 2** | 180 | 2 346 | 1.01 (0.58) | 2.46 (1.40) | 44.1 | 0.24 | 92.3 |

### 6.3.4 Comparison of the most suitable adsorbent structures for $CO_2$ adsorption

To identify the most suitable adsorbent structures for $CO_2$ adsorption, the adsorption performances of novel adsorbent structures (such as monoliths and foam-monoliths) prepared in the research and current state-of-the art adsorbent structures such as beads were compared. In this study, 13X zeolite and purified MIL-101(Cr) monoliths, $K_2CO_3$/13X

zeolite foam-monolith and 13X zeolite beads of 1.6 mm to 2.5 mm diameter were used. The tested adsorbent monoliths and foam-monolith have 0.9 mm thick walls and they were of the same composition (i.e., 75% wt. 13X zeolite/MIL-101(Cr), 25% wt. calcium bentonite and 4% wt. Licowax C micropowder PM, with 4% wt. $KHCO_3$ for the foam-monolith).

The breakthrough curves for 40% vol. $CO_2$ adsorption onto 13X zeolite and purified MIL-101(Cr) monoliths, $K_2CO_3$/13X zeolite foam-monolith and a packed bed of 13X zeolite beads are shown in Figure 6.25. It was seen that the breakthrough curves for the prepared adsorbent monoliths and foam-monoliths were slightly sharper than that for the packed bed of adsorbent beads. This indicates that the mass transfer in monoliths and foam-monoliths was slightly better than that in a packed bed of beads. In this case, the sharpest breakthrough curve was produced using purified MIL-101(Cr) monolith. The results from this study was in agreement with Lee (1997), who reported that the curve sharpness of their 90% wt. silicalite monolith was comparable with that of silicalite beads.

It was noticed that the prepared adsorbent monoliths and foam-monoliths exhibit shorter breakthrough and equilibrium times compared to a packed bed of adsorbent beads. This means that the prepared adsorbent monoliths and foam-monoliths could not be used for $CO_2$ adsorption at a longer time and they would require more frequent replacement or regeneration than the commercial adsorbent beads. Among the prepared adsorbent monoliths and foam-monoliths, $K_2CO_3$/13X zeolite foam-monolith has the longest equilibrium time and this indicates that they took a much longer time to saturate with $CO_2$ compared to 13X zeolite and purified MIL-101(Cr) monoliths. In this study, the shortest breakthrough and equilibrium times was found to be exhibited by the purified MIL-101(Cr) monolith.

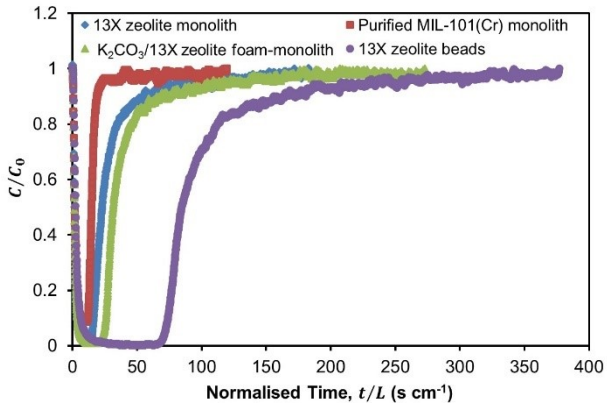


**Figure 6.25** Normalised breakthrough curves for the adsorption of 40% vol. $CO_2$ on 13X zeolite and purified MIL-101(Cr) monoliths, $K_2CO_3$/13X zeolite foam-monolith and 13X zeolite beads.

The results in Table 6.22 indicate that the $\bar{q}_b$ and $\bar{q}_e$ values for the selected adsorbent monoliths and foam-monoliths were lower than the packed bed of 13X zeolite beads on mass basis (in most cases) and on volumetric basis. On average, it was found that the adsorption capacities of $CO_2$ (on mass basis) for the prepared adsorbent monoliths were slightly lower by about 27% at breakthrough and 8% at equilibrium when compared with a packed bed of adsorbent beads (refer Table 6.22). This indicates that the prepared adsorbent monoliths have less adsorption sites available for $CO_2$ adsorption compared to the packed bed of adsorbent beads. For $K_2CO_3$/13X zeolite foam-monolith, their sorption capacities of $CO_2$ (on mass basis) were slightly lower at breakthrough (i.e., by about 14%) but higher at equilibrium (i.e., by about 19%) when compared with a packed bed of adsorbent beads (refer Table 6.22). This shows that the availability of adsorption sites for $CO_2$ sorption was slightly less at breakthrough but more at equilibrium. The reason was because both physical and chemical sorbents are present in the $K_2CO_3$/13X zeolite foam-monolith.

The results in Table 6.22 also indicate that the use of 13X zeolite monolith and $K_2CO_3$/13X zeolite foam-monolith for $CO_2$ adsorption was slightly less effective (i.e., by about 18%, on average) than a packed bed of 13X zeolite beads. This was as a result of less adsorption sites available for $CO_2$ adsorption. The study also found that the use of purified MIL-101(Cr) monolith for $CO_2$ adsorption was about 2% more effective than a packed bed of 13X zeolite beads. The reason was because the mass transfer in purified MIL-101(Cr) monolith was slightly better than that in a packed bed of 13X zeolite beads, as demonstrated by their sharp breakthrough curve.

The mass transfer zone velocity for the prepared adsorbent monoliths and foam-monoliths was found to be about twice as fast as that for the packed bed of adsorbent beads, as indicated in Table 6.22. This shows that the prepared adsorbent monoliths and foam-monoliths has slightly better mass transfer than the packed bed of adsorbent beads. The $\bar{L}_{MTZ}$ values in Table 6.22 indicate that the prepared adsorbent monoliths and foam-monoliths have about the same mass transfer zone length and this implies that they have about the same mass transfer of $CO_2$. When compared to a packed bed of 13X zeolite beads, these adsorbent monoliths and foam-monoliths have longer mass transfer zone length. Similar trend was also observed by Rezaei and Webley (2009).

**Table 6.22** The adsorption properties of 13X zeolite and purified MIL-101(Cr) monoliths, $K_2CO_3$/13X zeolite foam-monolith and 13X zeolite beads for 40% vol. $CO_2$ adsorption at 2 bar.

| Adsorption properties | $t_b$ (s cm$^{-1}$) | $t_e$ (s cm$^{-1}$) | $\overline{q}_b$ (mmol g$^{-1}$) & (mmol cm$^{-3}$ in bracket) | $\overline{q}_e$ (mmol g$^{-1}$) & (mmol cm$^{-3}$ in bracket) | $\omega_{bed}$ (%) | $u_{MTZ}$ (cm min$^{-1}$) | $\overline{L}_{MTZ}$ (%) |
|---|---|---|---|---|---|---|---|
| **13X zeolite monolith** | 14.5 | 182.7 | 0.81 (0.49) | 2.02 (1.21) | 43.9 | 0.33 | 92.1 |
| **Purified MIL-101(Cr) monolith** | 11.6 | 119.3 | 1.11 (0.31) | 1.87 (0.52) | 65.7 | 0.50 | 90.2 |
| **$K_2CO_3$/13X zeolite foam-monolith** | 21.3 | 272.8 | 1.13 (0.67) | 2.50 (1.49) | 47.7 | 0.22 | 92.2 |
| **13X zeolite beads** | 68.5 | 2 337 | 1.32 (1.23) | 2.10 (1.96) | 64.0 | 0.15 | 82.5 |

The results from this study demonstrate that the $CO_2$ adsorption performances of $K_2CO_3$/13X zeolite foam-monolith (in terms of equilibrium adsorption capacity on mass basis) and purified MIL-101(Cr) monolith (in terms of effectiveness of the adsorbent bed utilisation) were comparable to the packed bed of 13X zeolite beads. Due to this reason, they seem to be suitable adsorbent structures for $CO_2$ adsorption.

## 6.4 Conclusions

The work described in this chapter has demonstrated the optimisation of novel adsorbent structures (i.e., monoliths and foam-monoliths) produced in this research with $CO_2$ adsorption. A number of $CO_2$ adsorption experiments have been carried out to obtain the breakthrough curves for the adsorption of 40% vol. $CO_2$ onto the selected adsorbent structures at 2 bar under ambient temperature. These breakthrough curves were analysed to evaluate the $CO_2$ adsorption performance of the tested adsorbent structures.

In this optimisation study, parameters such as the type of adsorbents (i.e., zeolites, MIL-101(Cr) or carbonates), type of bentonites (i.e., calcium bentonite or Wyoming sodium bentonite), ratio of zeolite/MIL-101(Cr) to calcium bentonite, inclusion of a pore forming agent in their paste formulations, firing temperature, monolith wall thickness, adsorbent bed length and regeneration temperature of the adsorbent structures (i.e., monoliths or foam-monoliths) have been investigated. It was found that 13X zeolite and purified MIL-101(Cr) monoliths were the most suitable type of adsorbent monoliths for $CO_2$ adsorption when compared to LiLSX zeolite, 5A zeolite, clinoptilolite and as-synthesized MIL-101(Cr) monoliths. On the other hand, the most suitable type of adsorbent foam-monoliths for $CO_2$ adsorption was found to be $K_2CO_3$/13X zeolite foam-monoliths when compared to $Na_2CO_3$/13X zeolite foam-monoliths.

The study has discovered that calcium bentonite was more suitable for use as a binder since they are less likely to cover the adsorption sites compared to Wyoming sodium bentonite. It was found that adsorbent monoliths of high adsorbent (zeolite/MIL-101(Cr)) to calcium bentonite ratio could be used for $CO_2$ adsorption at a longer time and they have higher breakthrough and equilibrium adsorption capacities of $CO_2$ (both in terms of mass and volumetric) compared to those of low zeolite/MIL-101(Cr) to calcium bentonite ratio. The study has revealed that the inclusion of 4% wt. pore forming agent (such as Licowax C micropowder PM) into the paste formulations of zeolite/MIL-101(Cr) monoliths and carbonate-based zeolite foam-monoliths would improve their $CO_2$ adsorption performance.

The results have shown that the most suitable firing temperature for zeolite monoliths and carbonate-based zeolite foam-monoliths was 400 °C and that for MIL-101(Cr) monoliths was 205 °C. Additionally, it was found that zeolite monoliths of thinner walls (i.e., 0.7 mm) have more efficient mass transfer of $CO_2$ in their monolithic bed and they gave better $CO_2$ adsorption performance than those of thicker walls (i.e., 0.9 mm). The study has demonstrated that a long (i.e., 20 cm) zeolite monolith/carbonate-based zeolite foam-monoliths exhibit longer breakthrough and equilibrium times and higher breakthrough and equilibrium adsorption capacities of $CO_2$ (on mass basis, in most cases) than a short (i.e., 10 cm) zeolite monolith/carbonate-based zeolite foam-monoliths.

It was found that the most suitable regeneration temperature for zeolite monoliths and carbonate based zeolite foam-monoliths was 250 °C and that for MIL-101(Cr) monoliths was 200 °C. The $CO_2$ adsorption experiments have been repeated to check the accuracy of the experimental data obtained in this study. The results showed that the experimental data obtained in the optimisation studies for zeolite and MIL-101(Cr) monoliths and carbonate based zeolite foam-monoliths was reproducible and accurate. The $CO_2$ adsorption performances of 13X zeolite and purified MIL-101(Cr) monoliths and $K_2CO_3$/13X zeolite foam-monolith have also been compared with that of a packed of 13X zeolite beads. The study found that the $CO_2$ adsorption performances of purified MIL-101(Cr) monolith and $K_2CO_3$/13X zeolite foam-monolith were comparable to a packed bed of 13X zeolite beads (in terms of effectiveness of the adsorbent bed utilisation and equilibrium adsorption capacity on mass basis, respectively). This shows they were more suitable for $CO_2$ adsorption than a packed bed of adsorbent beads.

# Chapter 7 Dynamic Adsorption Performances of Adsorbent Monoliths and Foam-Monoliths for Biogas Upgrading

This chapter presents the dynamic adsorption study for the prepared adsorbent monoliths and foam-monoliths using single (such as $CO_2$, $CH_4$ and $H_2S$) and mixed (such as $CO_2/CH_4$ and $CO_2/CH_4/H_2O$ vapour) gases. In this study, 13X zeolite and purified MIL-101(Cr) monoliths and $K_2CO_3$/13X zeolite foam-monoliths are used as model adsorbent monoliths and foam-monoliths. Their dynamic adsorption performances for biogas upgrading will be evaluated by analysing their breakthrough curves. The materials and apparatus used in this study are given in Section 7.1.

The concentration ($C_0$), pressure ($P$) and flow rate ($Q$) of the feed/influent gas will be varied to investigate their effects on the adsorption of selected single or mixed gases onto 13X zeolite and purified MIL-101(Cr) monoliths and $K_2CO_3$/13X zeolite foam-monoliths. The effect of $H_2O$ vapour on the adsorption performance of these adsorbent monoliths and foam-monoliths will also be investigated. The detailed experimental procedures employed in this study are described in Section 7.2. From the breakthrough curve analysis, several adsorption properties of the adsorbent monoliths and foam-monoliths will be determined.

This includes the breakthrough time ($t_b$), equilibrium time ($t_e$), adsorption capacities of $CO_2$ at breakthrough ($\bar{q}_b$) and equilibrium ($\bar{q}_e$), selectivity of $CO_2$ to $CH_4$ ($\alpha_{CO_2/CH_4}$) and purity of $CH_4$ in the effluent gas stream. The breakthrough time, equilibrium time and purity of the upgraded $CH_4$ are obtained directly from the breakthrough curves whereas the breakthrough and equilibrium adsorption capacities of $CO_2$ and selectivity of $CO_2$ to $CH_4$ are calculated using the equations provided in Section 2.2.1 of Chapter 2.

The single and mixed gas adsorption results for 13X zeolite and purified MIL-101(Cr) monoliths and $K_2CO_3$/13X zeolite foam-monolith will be provided and discussed in Section 7.3. Comparison on the adsorption performances of these adsorbent monoliths and foam-monoliths will also be made to assess their suitability for biogas upgrading. Their results are given and discussed in Section 7.3.5. Then, the work described in this chapter will be concluded at the end in Section 7.4.

## 7.1 Materials and Equipment Used in the Dynamic Adsorption Study

As mentioned earlier, 13X zeolite monoliths, purified MIL-101(Cr) monoliths and $K_2CO_3$/13X zeolite foam-monoliths (i.e., Samples 4, M4 and C4, respectively) prepared in the research were used in this study as model adsorbent monoliths and foam-monoliths. They have 0.9 mm thick walls and they have been fired at 400 °C for 13X zeolite monoliths and $K_2CO_3$/13X zeolite foam-monoliths and 150 °C for purified MIL-101(Cr) monoliths. They also have the same composition (i.e., 75% wt. 13X zeolite/MIL-101(Cr), 25% wt. calcium bentonite and 4% wt. Licowax C micropowder PM, with 4% wt. $KHCO_3$ for foam-monoliths).

In this study, 20 cm long 13X zeolite monoliths and $K_2CO_3$/13X zeolite foam-monoliths were used. Due to the limited amount of purified MIL-101(Cr) powder produced in the research, slightly shorter purified MIL-101(Cr) monoliths were used (i.e., 13 cm). It was assumed that the bed length did not have any influence on their adsorption capacities. As shown in Chapter 6, the breakthrough and equilibrium times increase with increasing bed length. So, for better representation of the breakthrough curves, their adsorption time was normalised in terms of their adsorbent mass. This produces a normalised breakthrough curve, which was a plot of $C/C_0$ against normalised time ($\bar{t}$). The 13X zeolite monoliths and $K_2CO_3$/13X zeolite foam-monoliths have a bed mass of about 50.7 g while the purified MIL-101(Cr) monoliths have a bed mass of about 20.6 g.

The model adsorbate gases used in this adsorption study were $CO_2$ (in air or in $CH_4$ mixtures, supplied by BOC Ltd., UK), $CH_4$ (in argon mixture, supplied by BOC Ltd., UK), $H_2S$ (in nitrogen mixture, supplied by BOC Ltd., UK) and $H_2O$ vapour (generated by passing adsorbate gas through a water tank). Their physical properties and concentrations are listed in Table 7.1. Generally, the feed adsorbate gas concentrations were selected according to the typical composition of a biogas. Low concentrations of $CO_2$ (such as 0.4% vol. and 4% vol.) were also used in this study to examine other potential applications, for example, $CO_2$ capture from the flue gas stream. The purging gas used to clean all gas streams in the adsorption system was compressed air.

The equipment used in this adsorption study were the same as those stated in Section 6.1 of Chapter 6. They include: (a) an electric oven (model MOV-112) manufactured by Sanyo Electric Co. Ltd. (Japan) for drying and regenerating the adsorbent monoliths/foam-monoliths, (b) an electric balance (model KERN EG 220-3NM) manufactured by Kern & Sehn GmbH (Germany) for weighing the adsorbent

monoliths/foam-monoliths, (c) a 500 mL glass soap-bubble flowmeter in 100 mL increments purchased from Sigma Aldrich (UK) and a digital stopwatch manufactured by Fisher Scientific (UK) for measuring the gas flow rate, and (d) an adsorption flow-breakthrough apparatus for carrying out the single and mixed gas adsorption experiments.

**Table 7.1** Some of the physical properties and concentration of adsorbate gases used in this study.

| Adsorbate gases | $CO_2$ | $CH_4$ | $H_2S$ | $H_2O$ |
|---|---|---|---|---|
| **Molecular mass (g mol$^{-1}$)** | 44.01 | 16.04 | 34.08 | 18.02 |
| **Molecular diameter (nm)** | 0.28 | 0.40 | 0.36 | 0.32 |
| **Concentration (% vol.)** | 0.4, 4, 40, 50 | 50, 60 | 0.08 | 2.2 (RH ≈ 93%) |

The adsorption flow-breakthrough apparatus used in this study was shown schematically in Figure 7.1. It consists of an influent/feed gas flow system, a 25.5 cm long and 3.1 cm wide internal diameter steel adsorption column (purchased from Agilent Technologies, UK) and an effluent gas analytical system. Depending on the gas components in the feed gas stream, different models of mass flow controller were used to regulate the gas flow rate. For examples, the model of mass flow controller used in $CO_2$, $CO_2$/$CH_4$ and $CO_2$/$CH_4$/$H_2O$ vapour adsorption experiments was 5850S while that in $CH_4$ adsorption experiments was 5850E. As for $H_2S$ adsorption experiments, a mass flow controller model SLA5850 was used. All these mass flow controllers were purchased from Brooks Instruments LLC., USA.

The feed gas flow system of the apparatus also consists of a sealed water tank (model 17530, made by Sartorius AG, Germany). It was used to generate humid $CO_2$/$CH_4$ mixed gas stream for the $CO_2$/$CH_4$/$H_2O$ vapour adsorption experiments by bubbling the mixed $CO_2$/$CH_4$ adsorbate gas under water. The relative humidity and temperature of the feed and effluent mixed gas streams were detected using a relative humidity and temperature transmitter (model HT-748, made by Rense Instruments B.V., Netherlands). An Easidew sampler, which was connected to a dew point transmitter, was used for measuring the $H_2O$ vapour content of the feed and effluent $CO_2$/$CH_4$ mixed gas streams and giving a read-out in °C on a digital dew point hygrometer monitor (purchased from Michell Instruments Ltd., UK).

The gas pressure of all the adsorption experiments, except $H_2S$ adsorption experiments, was detected using a pressure transmitter (model S-10, purchased from WIKA Instruments Ltd., UK) and a digital pressure indicator (model DPI 260, purchased

from Druck Ltd., UK). Because of the highly corrosive nature of the $H_2S$ gas, a low-cost pressure gauge was used in the $H_2S$ adsorption experiments for measuring the $H_2S$ gas pressure. For the same reason, all adsorption experiments except $H_2S$ adsorption experiments comprise of a bidirectional inline flow and pressure controller (model 9041202, manufactured by Metal Work Pneumatics, Italy) for tuning the flow and pressure of the supplied gas.

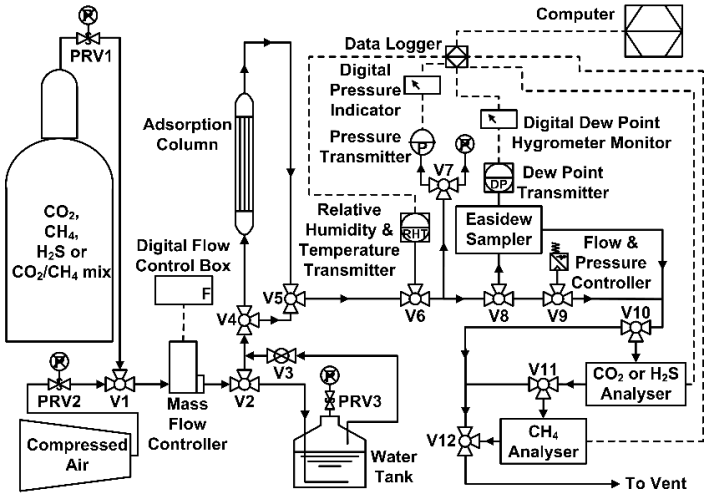


**Figure 7.1** Schematic diagram of an adsorption flow-breakthrough apparatus for the adsorption of single/mixed gases.

Gas analysers for measuring the feed and effluent $CO_2$, $H_2S$ and/or $CH_4$ gas concentrations were connected to the apparatus. In this study, the $CO_2$ gas analyser (model Guardian Plus, purchased from Edinburgh Instruments Ltd., UK) detects the $CO_2$ gas concentration either in ppmv (from 0 ppmv to 4 000 ppmv, which is equal to 0.4% vol.) or % vol. (from 0% vol. to 100% vol.). The digital infrared $CH_4$ gas analyser (model HITOX-IR600, purchased from Hitech Instruments, UK) detects the $CH_4$ gas concentration in % vol. (from 0% vol. to 100% vol.). As for the digital ProCheck TIGER photo-ionization $H_2S$ gas analyser (purchased from Ion Science Ltd., UK), it detects the $H_2S$ gas concentration in ppmv (from 0 ppmv to 20 000 ppmv, which is equal to 2% vol.).

All output signals were sent to a data logger and then to a computer, which records the adsorbate gas concentration and/or $H_2O$ vapour content in time. The $CO_2$ gas concentration was recorded using a LabVIEW programme while the $CH_4$ gas concentration and/or $H_2O$ vapour content was recorded using a PicoLog data acquisition software. On the other hand, the $H_2S$ gas concentration was recorded using a TIGER PC software.

The next section will cover on the experimental procedures employed in this study for the adsorption of single (i.e., $CO_2$, $CH_4$ or $H_2S$) and mixed (i.e., $CO_2/CH_4$ or $CO_2/CH_4/H_2O$ vapour) gases.

## 7.2 Experimental Procedures for Determining the Dynamic Adsorption Performances of Adsorbent Monoliths and Foam-Monoliths

The adsorption experiments carried out in this study follow similar steps as those described in Section 6.2 of Chapter 6. They involve:

a) drying of the adsorbent monoliths/foam-monoliths,

b) packing of the adsorbent monoliths/foam-monoliths in a column,

c) setting the experimental operating conditions and checking the apparatus,

d) running the adsorption experiment,

e) stopping the adsorption experiment and unpacking the adsorbent monoliths/foam-monoliths and

f) regenerating the adsorbent monoliths/foam-monoliths.

The detailed experimental procedures of each of these steps are provided in Sections 7.2.1 to 7.2.6. The handling of the adsorbent monoliths/foam-monoliths and the operation of the adsorption flow-breakthrough apparatus need to be followed in the same sequence as that described in this work. This was to ensure that correct experimental results were obtained from the adsorption experiments.

### 7.2.1 Drying of adsorbent monoliths/foam-monoliths

Prior to any adsorption experiment, the adsorbent monoliths/foam-monoliths were dried in an electric oven for at least 18 hours. This was to remove water molecules from the pores of the adsorbent. In this study, 13X zeolite monoliths and $K_2CO_3$/13X zeolite foam-monoliths were dried at 250 °C while the purified MIL-101(Cr) monoliths were dried at 150 °C. These temperatures were chosen such that they were below their thermal stability temperatures.

### 7.2.2 Packing of adsorbent monoliths/foam-monoliths in a column

Then, each of the adsorbent monoliths/foam-monoliths was weighed on an electric balance and packed in an empty adsorption column. The inlet end of the adsorbent monolith/foam-monolith was first wrapped with a high density PTFE gas sealant tape and then fitted with a 24 mm or 22 mm diameter nitrile O-ring (see Figure 6.3 (a) of Chapter 6). The adsorbent monolith/foam-monolith was packed tightly in the centre of the column so that there was no feed gas flowing between the edge of the adsorbent monolith/foam-monolith and the wall of the column. The packed column was then connected onto the adsorption flow-breakthrough apparatus. The packed column was isolated from the whole system so that there was no adsorbate gas or gases present in the column before the start of the adsorption experiment.

### 7.2.3 Setting the experimental operating conditions and checking the apparatus

Next, the adsorbate (single/mixed) gas was supplied to the adsorption flow-breakthrough apparatus by switching the 3-way valve (V1) such that the purging gas (i.e., compressed air) was isolated from the adsorption system. The desired gas flow rate was set on a digital flow control box and regulated by a mass flow controller. For $CO_2/CH_4/H_2O$ vapour experiments, the $CO_2/CH_4$ mixed gas was bubbled under water in a sealed water tank by opening the 3-way valve (V2) and ball valve (V3) to generate humidified $CO_2/CH_4$ mixed gas stream. After some times, the desired relative humidity (i.e., about 93%) was obtained. No setting/control was required to reach the desired relative humidity value since that was the maximum relative humidity that could be achieved by the sealed water tank.

The relative humidity and temperature of the humidified $CO_2/CH_4$ mixed gas stream was detected using a relative humidity and temperature transmitter by switching the 3-way valve (V6). The $H_2O$ vapour content of the feed and effluent $CO_2/CH_4$ mixed gas streams was measured using an Easidew sampler and a dew point transmitter by switching the 3-way valve (V8). The flow rate of the adsorbate gases such as $CO_2$, $CH_4$ and $H_2O$ vapour were allowed to be fine-tuned with the gas pressure using a flow and pressure controller by switching the 3-way valve (V9) but not for $H_2S$ gas. This was to prevent corrosion on expensive equipment.

Since $H_2S$ gas would cause corrosion on equipment, its pressure was measured using a pressure gauge by switching the 3-way valve (V7) while the gas stream containing

$CO_2$, $CH_4$ and $H_2O$ vapour was detected using a pressure transmitter and gave a read-out on a digital pressure indicator. The gas flow rate of the system was checked using a glass soap-bubble flowmeter and a digital stopwatch.

Adsorbate gas of the desired concentration was connected to the apparatus and supplied to the adsorption system. The ranges of adsorbate gas concentration have been provided previously in Table 7.1. In this study, the adsorption system was set to operate at an absolute pressure ranging from 1 bar to 4 bar with the adsorbate gas flowing at a rate between 250 mL $min^{-1}$ and 1 000 mL $min^{-1}$. All the adsorption experiments were carried out at ambient temperature (i.e., between 19.5 °C and 24.5 °C).

The feed and effluent $CO_2$ (or $H_2S$ gas) concentrations were detected using a $CO_2$ (or $H_2S$ gas analyser) by switching the 3-way valve (V10). As for the feed and effluent $CH_4$ gas concentrations, they were detected using a $CH_4$ gas analyser by switching the 3-way valve (V11). All effluent gas was vented out from the adsorption system by switching the 3-way valve (V12). To ensure accurate measurements were taken, the adsorption flow-breakthrough apparatus was tested for gas leakage before starting any of the adsorption experiments.

### 7.2.4 Running the adsorption experiment

Once the experimental conditions (i.e., adsorbate gas concentration, pressure and flow rate) had stabilised, the adsorption flow-breakthrough apparatus was ready for running the adsorption experiment. The adsorption experiments were started by switching the 3-way valves at the inlet (V4) and outlet (V5) of the adsorption column to enable the adsorbate (single/mixed) gas to flow through the packed adsorption column. All adsorption experiments were allowed to run until a complete breakthrough curve was achieved, i.e. when the effluent adsorbate gas concentration was at least 95% vol. or equal to the feed gas concentration.

### 7.2.5 Stopping the adsorption experiment and unpacking the adsorbent monoliths/foam-monoliths

Once a complete breakthrough curve had attained, the adsorption experiment was stopped by switching the 3-way valves at the inlet (V4) and outlet (V5) of the adsorption column such that the packed adsorption column was isolated from the adsorption system.

The packed column was then disconnected from the apparatus and the adsorbent monolith/foam-monolith was unpacked from the adsorption column.

For the $H_2S$ adsorption experiments, the $H_2S$ gas supplied to the system was first stopped and compressed air was allowed to flow into the system. This was to prevent the leakage of the toxic $H_2S$ gas when the packed column was disconnected from the apparatus. For safety reason, the adsorbent monolith/foam-monolith was unpacked from the adsorption column in a well-ventilated fumed cabinet.

For the $CO_2/CH_4/H_2O$ vapour adsorption experiments, the packed adsorption column was first isolated from the system and then the generation of humid $CO_2/CH_4$ mixed gas was stopped. All gas lines of the adsorption flow-breakthrough apparatus were cleaned by purging compressed air into the adsorption system.

### 7.2.6 Regenerating the adsorbent monoliths/foam-monoliths

After unpacking the saturated adsorbent monolith/foam-monolith from the adsorption column, they were kept in an electric oven for at least 18 hours. This was to desorb the adsorbate gas or gases from the adsorbent pores and to regenerate the adsorbent monolith/foam-monolith for reuse. In this study, the regeneration temperature for 13X zeolite monoliths and $K_2CO_3$/13X zeolite foam-monoliths was 250 °C while that for purified MIL-101(Cr) monoliths was 150 °C.

## 7.3 Results and Discussion of the Dynamic Adsorption Study

The results of the dynamic adsorption study for 13X zeolite and purified MIL-101(Cr) monoliths and $K_2CO_3$/13X zeolite foam-monoliths are presented and discussed in this section. The effects of feed gas concentration, pressure, flow rate and $H_2O$ vapour on the adsorption of single (i.e., $CO_2$, $CH_4$ and $H_2S$) and/or mixed (i.e., $CO_2/CH_4$ and $CO_2/CH_4/H_2O$ vapour) gases onto these adsorbent monoliths and foam-monoliths are investigated and their results are shown in Sections 7.3.1 to 7.3.4. Their adsorption performances are compared in Section 7.3.5 to assess their suitability for biogas upgrading. The error of the data reported in this chapter was estimated to be about 0.01% for breakthrough and equilibrium times ($t_b$ and $t_e$, respectively). The mass and volumetric adsorption capacities at breakthrough and equilibrium ($\bar{q}_b$ and $\bar{q}_e$) were estimated to have

an error of about 2.6% whereas the selectivity of $CO_2$ over $CH_4$ ($\alpha_{CO_2/CH_4}$) was estimated to have an error of about 3.7%.

### 7.3.1 Effect of varying feed gas concentrations

Several experiments were carried out with different $CO_2$ and $CH_4$ concentrations ranging from 0.4% vol. to 50% vol. for $CO_2$ and from 50% vol. to 60% vol. for $CH_4$ with a feed gas flowing at a constant rate of 500 mL $min^{-1}$ at 2 bar. By varying the feed gas concentrations, the gas partial pressure also varies. With a total pressure ($P_T$) of 2 bar, the $CO_2$ feed gas concentrations of 0.4% vol., 4% vol., 40% vol. and 50% vol. correspond to $CO_2$ partial pressures ($P_{CO_2}$) of 0.008 bar, 0.08 bar, 0.8 bar and 1 bar, respectively. The $CH_4$ feed gas concentrations of 50% vol. and 60% vol. correspond to $CH_4$ partial pressures ($P_{CH_4}$) of 1 bar and 1.2 bar, respectively.

The effect of varying $CO_2$ and $CH_4$ feed gas concentrations are shown by the breakthrough curves in Figure 7.2 for 13X zeolite monolith, purified MIL-101(Cr) monolith and $K_2CO_3$/13X zeolite foam-monolith. It was seen in Figures 7.2 (a) to (c) that sharper breakthrough curves were produced when the $CO_2$ feed gas concentration was increased. This indicates efficient mass transfer of $CO_2$ in the adsorbent bed at higher feed gas concentration since they have higher concentration gradient (or $CO_2$ partial pressure) in the adsorbent bed.

At higher $CO_2$ concentration gradient, the mass transfer front reaches the end of the adsorbent bed early and the bed gets saturated with $CO_2$ faster. This was demonstrated by the decrease in breakthrough and equilibrium times as the $CO_2$ feed gas concentration was increased. For example, the study found that the breakthrough time for 13X zeolite monolith was decreased from 8 060 s to 2 635 s and its equilibrium time was decreased from 18 720 s to 7 034 s as the $CO_2$ feed gas concentration increased from 0.4% vol. to 4% vol., as indicated in Table 7.2. Further reduction in breakthrough and equilibrium times was observed at higher $CO_2$ feed gas concentrations. For example, it was found that an increase in feed gas concentration from 4% vol. to 40% vol. $CO_2$ reduced the breakthrough time of 13X zeolite monolith from 2 635 s to 396 s and its equilibrium time from 7 034 s to 2 675 s. These results show that the change in concentration gradient (or gas partial pressure) affects the breakthrough and equilibrium times.

At high feed gas concentration, more $CO_2$ are adsorbed onto the adsorbent bed and this increases their breakthrough and equilibrium adsorption capacities of $CO_2$ (in terms of mass and volumetric, in most cases). For example, on mass basis, the results in Table 7.2 indicate that an increment in feed gas concentration from 0.4% vol. to 40% vol. $CO_2$ increased the adsorption capacities of $CO_2$ of 13X zeolite monolith from 0.27 mmol $g^{-1}$ to 1.34 mmol $g^{-1}$ at breakthrough and from 0.40 mmol $g^{-1}$ to 2.58 mmol $g^{-1}$ at equilibrium. The behaviour of varying the $CO_2$ feed gas concentrations was similar to that reported by Monazam *et al.* (2013).

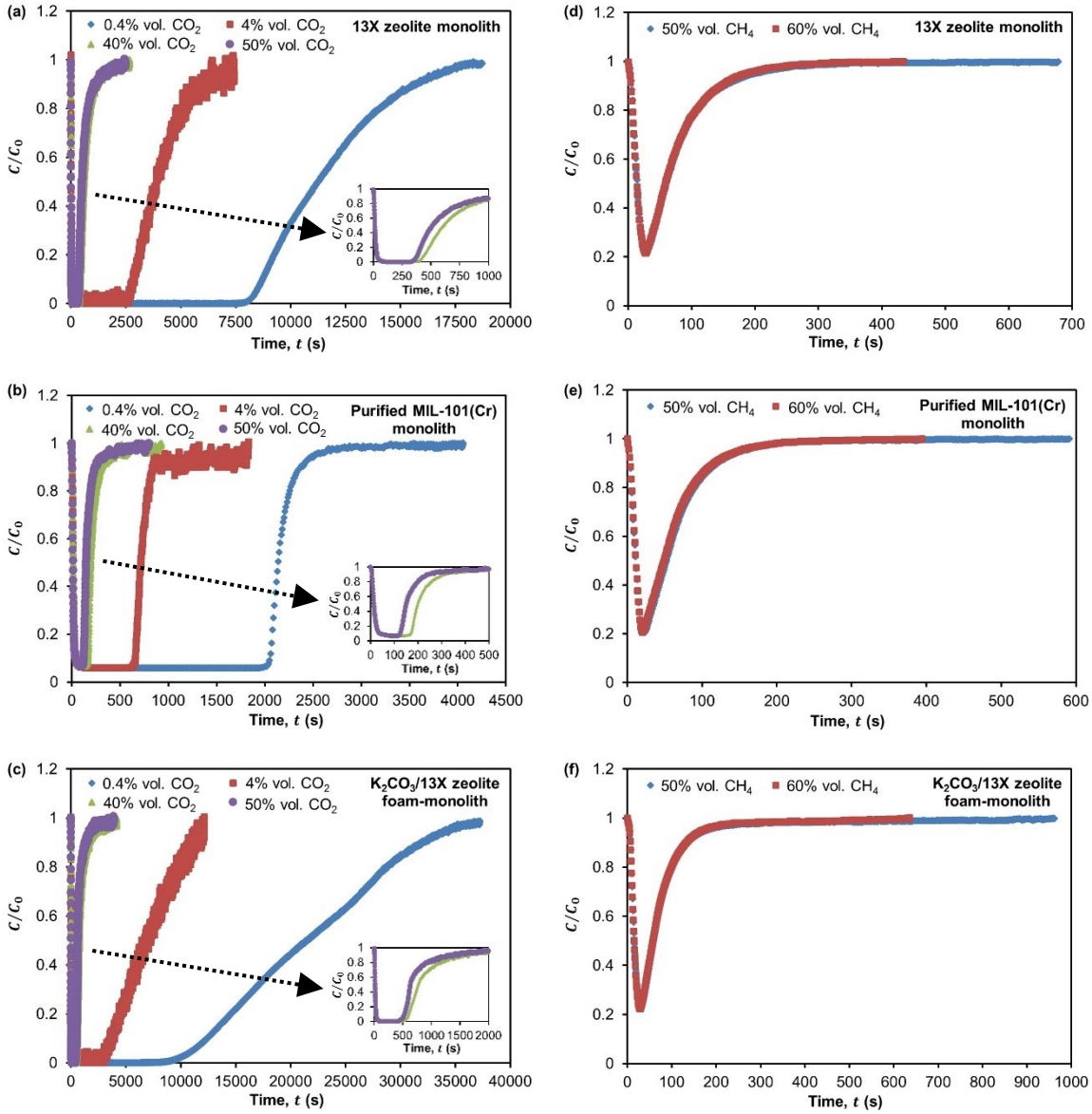


**Figure 7.2** Effect of $CO_2$ (a–c) and $CH_4$ (d–f) feed gas concentrations on breakthrough curves at 2 bar with a gas flows of 500 mL $min^{-1}$ for 13X zeolite monolith, purified MIL-101(Cr) monolith and $K_2CO_3$/13X zeolite foam-monolith.

The breakthrough curves showing the effect of varying $CH_4$ feed gas concentrations from 50% vol. to 60% vol. are presented in Figures 7.2 (d) to (f). No change in the shape

of breakthrough curves was observed since the difference in $CH_4$ feed gas concentrations used in the study was small. To observe a change in the shape of the breakthrough curve, a larger range of $CH_4$ feed gas concentrations should be used in future study. It was seen that 13X zeolite monolith, purified MIL-101(Cr) monolith and $K_2CO_3$/13X zeolite foam-monolith could adsorbed up to about 78% vol. of $CH_4$ from the feed gas stream before they start to breakthrough. $CH_4$ was poorly adsorbed because of the weak interactions (i.e., Van der Waals forces) between $CH_4$ gas molecules and adsorbent surfaces (Li *et al.*, 2013).

**Table 7.2** The adsorption properties of 13X zeolite monolith, purified MIL-101(Cr) monolith and $K_2CO_3$/13X zeolite foam-monolith with different $CO_2$ and $CH_4$ feed gas concentrations that flow at a rate of 500 mL $min^{-1}$ at 2 bar.

| Adsorption properties | $t_b$ (s) | $t_e$ (s) | $\overline{q}_b$ (mmol $g^{-1}$) & (mmol $cm^{-3}$ in bracket) | $\overline{q}_e$ (mmol $g^{-1}$) & (mmol $cm^{-3}$ in bracket) |
|---|---|---|---|---|
| ***0.4% vol. $CO_2$ ($P_T$ = 2 bar; $P_{CO_2}$ = 0.008 bar)*** | | | | |
| **13X zeolite monolith** | 8 060 | 18 720 | 0.27 (0.15) | 0.40 (0.22) |
| **Purified MIL-101(Cr) monolith** | 2 030 | 4 053 | 0.17 (0.05) | 0.18 (0.05) |
| **$K_2CO_3$/13X zeolite foam-monolith** | 9 220 | 37 230 | 0.29 (0.16) | 0.69 (0.37) |
| ***4% vol. $CO_2$ ($P_T$ = 2 bar; $P_{CO_2}$ = 0.08 bar)*** | | | | |
| **13X zeolite monolith** | 2 635 | 7 034 | 0.98 (0.54) | 1.56 (0.86) |
| **Purified MIL-101(Cr) monolith** | 641 | 1 834 | 0.55 (0.16) | 0.70 (0.21) |
| **$K_2CO_3$/13X zeolite foam-monolith** | 3 030 | 12 142 | 1.06 (0.57) | 2.55 (1.36) |
| ***40% vol. $CO_2$ ($P_T$ = 2 bar; $P_{CO_2}$ = 0.8 bar)*** | | | | |
| **13X zeolite monolith** | 396 | 2 675 | 1.34 (0.74) | 2.58 (1.42) |
| **Purified MIL-101(Cr) monolith** | 160 | 929 | 1.26 (0.36) | 1.98 (0.57) |
| **$K_2CO_3$/13X zeolite foam-monolith** | 517 | 4 170 | 1.68 (0.90) | 3.33 (1.79) |
| ***50% vol. $CO_2$ ($P_T$ = 2 bar; $P_{CO_2}$ = 1 bar)*** | | | | |
| **13X zeolite monolith** | 339 | 2 435 | 1.42 (0.80) | 2.86 (1.62) |
| **Purified MIL-101(Cr) monolith** | 120 | 801 | 1.34 (0.33) | 2.22 (0.55) |
| **$K_2CO_3$/13X zeolite foam-monolith** | 441 | 3 802 | 1.82 (0.94) | 3.56 (1.84) |
| ***50% vol. $CH_4$ ($P_T$ = 2 bar; $P_{CH_4}$ = 1 bar)*** | | | | |
| **13X zeolite monolith** | 32 | 678 | 0.06 (0.04) | 0.27 (0.15) |
| **Purified MIL-101(Cr) monolith** | 26 | 591 | 0.13 (0.04) | 0.53 (0.17) |
| **$K_2CO_3$/13X zeolite foam-monolith** | 34 | 965 | 0.07 (0.03) | 0.28 (0.14) |
| ***60% vol. $CH_4$ ($P_T$ = 2 bar; $P_{CH_4}$ = 1.2 bar)*** | | | | |
| **13X zeolite monolith** | 30 | 434 | 0.07 (0.04) | 0.30 (0.17) |
| **Purified MIL-101(Cr) monolith** | 23 | 394 | 0.13 (0.04) | 0.62 (0.19) |
| **$K_2CO_3$/13X zeolite foam-monolith** | 31 | 636 | 0.07 (0.04) | 0.32 (0.15) |

Similar to the effect of varying $CO_2$ feed gas concentrations, the increase of $CH_4$ feed gas concentration leads to shorter breakthrough and equilibrium times. For example, the breakthrough time of 13X zeolite monolith was found to be slightly reduced from 32 s to 30 s and the equilibrium time was found to be reduced from 678 s to 434 s when the

$CH_4$ feed gas concentration was increased from 50% vol. to 60% vol., as indicated in Table 7.2. Due to the small range of $CH_4$ feed gas concentrations used in the study, there was no change in breakthrough adsorption capacity of $CH_4$ (both in terms of mass and volumetric, in most cases). However, a small improvement in equilibrium adsorption capacity of $CH_4$ (both in terms of mass and volumetric) was found. For example, the study found that the equilibrium adsorption capacity of $CH_4$ (on mass basis) of 13X zeolite monolith was improved by about 11% when the $CH_4$ feed gas concentration was increased from 50% vol. to 60% vol., as indicated in Table 7.2. This demonstrates that more $CH_4$ were adsorbed onto the adsorbent bed at higher feed gas concentration.

Tailing of the breakthrough curves was observed in Figure 7.2 as $CO_2$ and $CH_4$ adsorption approaches saturation. This was contributed by the slow intra-crystalline diffusion within the micropores of 13X zeolite and the mesopores of MIL-101(Cr), presence of non-homogeneous particles (i.e., adsorbents and calcium bentonite) and difference in concentration gradients (or gas partial pressures) (Monazam *et al.*, 2013).

### 7.3.2 Effect of varying feed gas pressures

The effect of varying feed gas pressures on 13X zeolite monolith, purified MIL-101(Cr) monolith and $K_2CO_3$/13X zeolite foam-monolith with a constant feed gas flow rate of 500 mL $min^{-1}$ was demonstrated by the breakthrough curves in Figure 7.3 for $CO_2$ (40% vol.) and $CH_4$ (60% vol.) and Figure 7.4 for $H_2S$ (0.08% vol.) and $CO_2/CH_4$ mixture (40:60, % vol.). In this investigation, the feed (total) gas pressure ranges from 1 bar to 4 bar for $CO_2$, $CH_4$ and $CO_2/CH_4$ mixture and from 1 bar to 3 bar for $H_2S$. The corresponding gas partial pressures were stated in Tables 7.3 and 7.4.

No significant change was observed on the steepness of the breakthrough curve when the feed gas pressure was increased (see Figures 7.3 and 7.4). This means the mass transfer of adsorbate gas (or gases) in adsorbent beds was not dependent on the feed gas pressure. Wang (2008) also observed the same trend. At higher feed gas pressure (i.e., higher gas partial pressure), longer breakthrough and equilibrium times were obtained. This was because the mass transfer front to take more time to reach the end of the adsorbent bed and for the bed to be completely saturated (Garcia *et al.*, 2011). For example, an increment in the $CO_2$ feed gas pressure from 1 bar to 4 bar (i.e., $P_{CO_2}$ from 0.4 bar to 1.6 bar) at a constant feed gas flow rate of 500 mL $min^{-1}$ was found to increase the breakthrough time of 13X zeolite monolith from 333 s to 535 s and its equilibrium time from 2 416 s to 3 067 s, as indicated in Table 7.3.

The increase in gas partial pressure at higher feed gas pressure means that more adsorbate gas (or gases) are adsorbed and this leads to the increase in breakthrough and equilibrium adsorption capacities (both in terms of mass and volumetric). For example, the results in Table 7.3 indicate that $CO_2$ adsorption capacities (on mass basis) for 13X zeolite monolith were increased from 1.14 mmol $g^{-1}$ to 1.90 mmol $g^{-1}$ at breakthrough and from 2.26 mmol $g^{-1}$ to 3.38 mmol $g^{-1}$ at equilibrium when the $CO_2$ feed gas pressure was increased from 1 bar to 4 bar. Similar behaviour was also observed for the adsorption of $CH_4$, $H_2S$ and $CO_2/CH_4$ mixture onto 13X zeolite monolith, purified MIL-101(Cr) monolith and $K_2CO_3$/13X zeolite foam-monolith with varying feed gas pressures (see Tables 7.3 and 7.4).

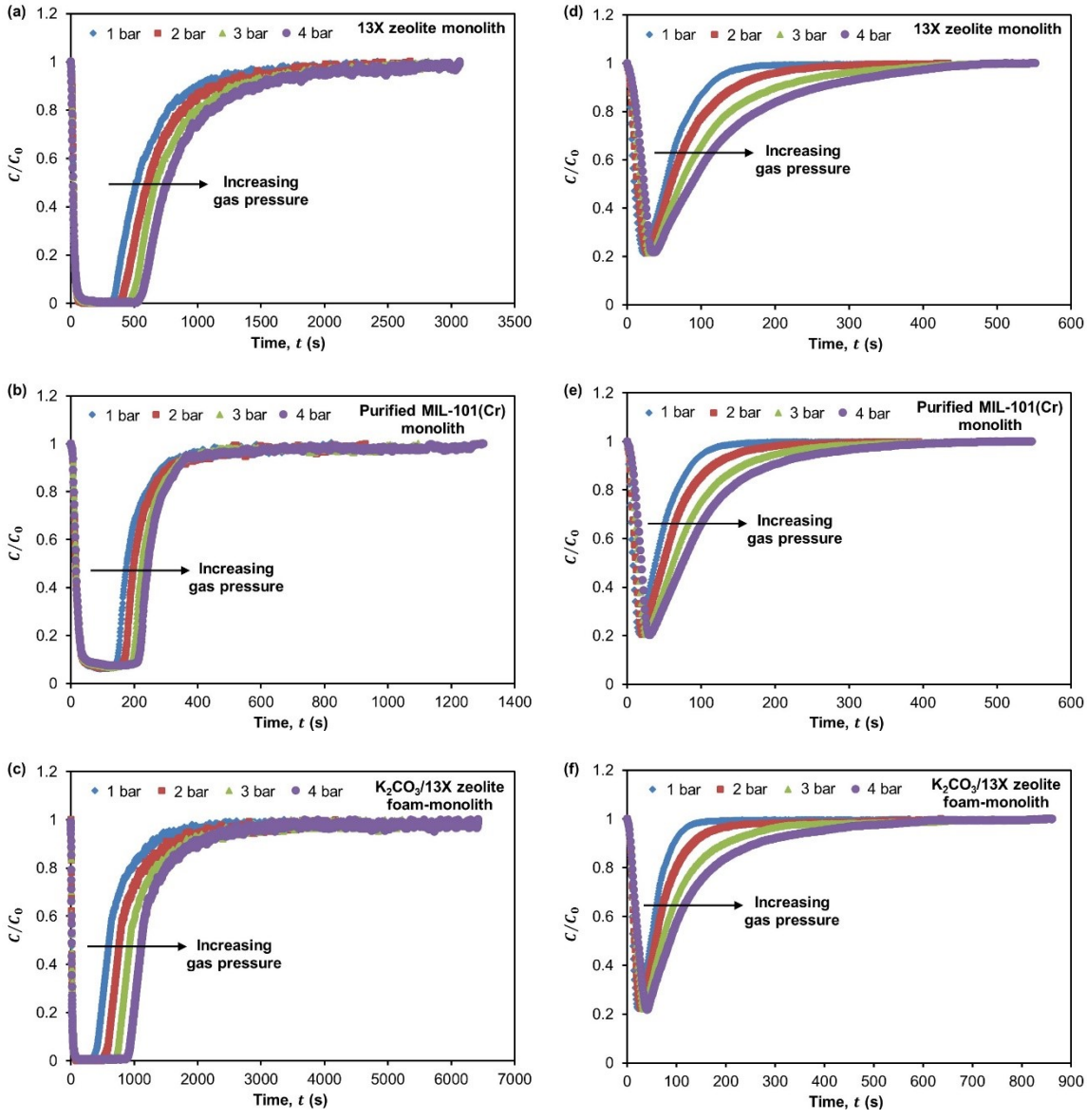


**Figure 7.3** Effect of 40% vol. $CO_2$ (a–c) and 60% vol. $CH_4$ (d–f) feed gas pressures on breakthrough curves with a gas flows of 500 mL $min^{-1}$ for 13X zeolite monolith, purified MIL-101(Cr) monolith and $K_2CO_3$/13X zeolite foam-monolith.

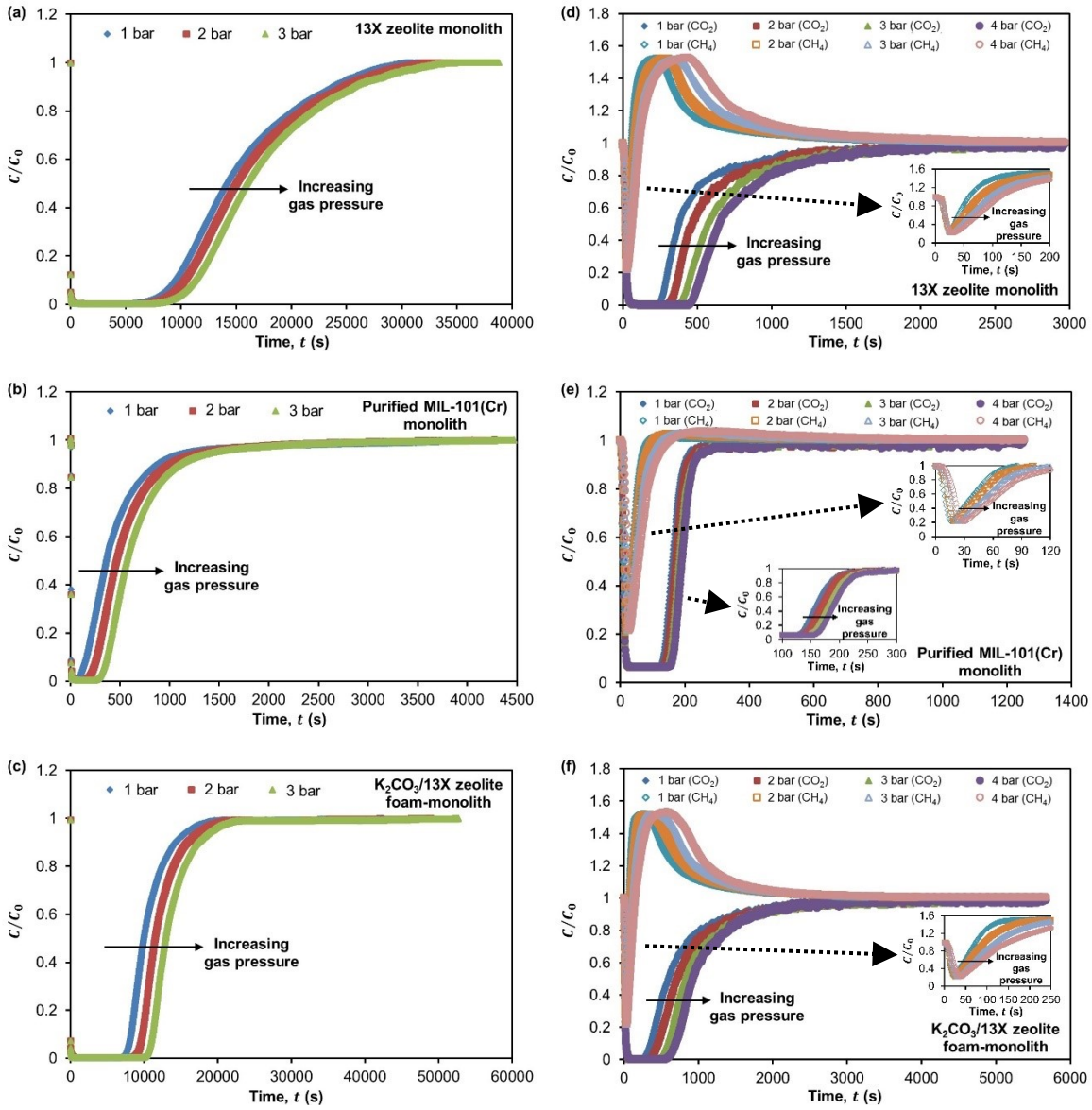


**Figure 7.4** Effect of 0.08% vol. $H_2S$ (a–c) and $CO_2/CH_4$ mixed (40:60, % vol.) (d–f) feed gas pressures on breakthrough curves with a gas flows of 500 mL $min^{-1}$ for 13X zeolite monolith, purified MIL-101(Cr) monolith and $K_2CO_3$/13X zeolite foam-monolith.

For the adsorption of $CO_2/CH_4$ mixture (40:60, % vol.), it was seen in Figures 7.4 (d) to (f) that 13X zeolite monolith and $K_2CO_3$/13X zeolite foam-monolith were excellent for adsorbing $CO_2$ (with $\frac{C}{C_0}$ reaching zero) and purified MIL-101(Cr) monolith could adsorbed up to about 94% vol. of $CO_2$. These adsorbent structures could adsorb up to about 78% vol. of $CH_4$ from the mixed feed gas stream before they start to breakthrough. It was noticed that $CH_4$ always breaks first and its breakthrough curve produces a so-called roll-up or roll-over, in which the molar flow rate of $CH_4$ in the effluent is temporarily higher than that fed to the adsorption bed. This phenomenon can be explained by the fact that $CH_4$ is first adsorbed and thereby concentrated in the adsorbent, but then it is displaced by $CO_2$ whose concentration front moves slower through the column than that of $CH_4$. The

increase of $CH_4$ flow rate above the feed flow rate was attributed by the so-induced desorption of $CH_4$. After some times, the effluent concentrations of $CO_2$ and $CH_4$ reaches the level as the feed concentration, indicating that the adsorbent bed is saturated (Álvarez-Gutiérrez *et al.*, 2016).

Strong roll-up was observed for 13X zeolite monolith and $K_2CO_3$/13X zeolite foam-monolith and this was as a result of the fast displacement of large amount of $CH_4$ by incoming $CO_2$ (Álvarez-Gutiérrez *et al.*, 2016). The study found that a maximum purity of about 98% vol. $CH_4$ was achieved in the effluent using 13X zeolite monolith and $K_2CO_3$/13X zeolite foam-monolith. This means these adsorbent structures could be used to upgrade the biogas to a high quality for use as vehicle fuel and injection into natural gas grid (Persson *et al.*, 2006; Wellinger and Lindberg, 2001). For purified MIL-101(Cr) monolith, the roll-up effect was weaker (see Figure 7.4 (e)) and this was because small amount of $CH_4$ was replaced by incoming $CO_2$ since MIL-101(Cr) intrinsically adsorbs $CH_4$. The maximum $CH_4$ purity in the effluent was found to be about 67% vol. for purified MIL-101(Cr) monolith. This shows that purified MIL-101(Cr) monolith could be used to upgrade the biogas to a moderate quality for used in boilers to produce heat, kitchen stoves for cooking and stationary combined heat and power engines to generate heat and electricity (Persson *et al.*, 2006; Wellinger and Lindberg, 2001).

The results show that 13X zeolite monolith, purified MIL-101(Cr) monolith and $K_2CO_3$/13X zeolite foam-monolith exhibit preferential adsorption for $CO_2$ over $CH_4$. This indicates that $CO_2$ (a polar molecule) was adsorbed more strongly onto these adsorbent structures compare to $CH_4$ (a non-polar molecule) (Rios *et al.*, 2013). The preferential adsorption behaviour for $CO_2$ over $CH_4$ observed in this study was in agreement with those reported by Chen *et al.* (2016) for 13X zeolite, Munusamy *et al.* (2012) for MIL-101(Cr) and Liu *et al.* (2016) for $K_2CO_3$-based sorbents. The study found that the selectivity of $CO_2$ over $CH_4$ decreases with increasing mixed feed gas pressure. Similar trend was also reported by Salmasi *et al.* (2013). In this study, for example, the highest $CO_2/CH_4$ selectivity for 13X zeolite monolith was achieved at 1 bar with a value of 26.4, as indicated in Table 7.4. This implies that more $CO_2$ were adsorbed onto 13X zeolite monolith compared to $CH_4$ at atmospheric pressure. Similar behaviour was also exhibited by purified MIL-101(Cr) monolith and $K_2CO_3$/13X zeolite foam-monolith. The study found that their selectivity of $CO_2$ over $CH_4$ was at the highest at atmospheric pressure (i.e., 1 bar), as indicated in Table 7.4.

**Table 7.3** The adsorption properties of 13X zeolite monolith, purified MIL-101(Cr) monolith and $K_2CO_3$/13X zeolite foam-monolith with different $CO_2$ (40% vol.), $CH_4$ (60% vol.) and $H_2S$ (0.08% vol.) feed gas pressures that flow at a rate of 500 mL $min^{-1}$.

| Adsorption properties | | $t_b$ (s) | $t_e$ (s) | $\overline{q}_b$ (mmol $g^{-1}$) & (mmol $cm^{-3}$ in bracket) | $\overline{q}_e$ (mmol $g^{-1}$) & (mmol $cm^{-3}$ in bracket) |
|---|---|---|---|---|---|
| ***$P_T$ = 1 bar; $P_{CO_2}$ = 0.4 bar; $P_{CH_4}$ = 0.6 bar; $P_{H_2S}$ = 0.0008 bar*** | | | | | |
| **13X zeolite monolith** | **$CO_2$** | 333 | 2 416 | 1.14 (0.63) | 2.26 (1.25) |
| | **$CH_4$** | 25 | 378 | 0.06 (0.04) | 0.23 (0.14) |
| | **$H_2S$** | 6 870 | 34 270 | 0.05 (0.03) | 0.11 (0.07) |
| **Purified MIL-101(Cr) monolith** | **$CO_2$** | 135 | 822 | 1.05 (0.30) | 1.76 (0.51) |
| | **$CH_4$** | 19 | 335 | 0.12 (0.04) | 0.47 (0.14) |
| | **$H_2S$** | 88 | 4 051 | 0.002 (0.0004) | 0.009 (0.003) |
| **$K_2CO_3$/13X zeolite foam-monolith** | **$CO_2$** | 352 | 3 357 | 1.23 (0.63) | 2.79 (1.44) |
| | **$CH_4$** | 25 | 573 | 0.06 (0.03) | 0.24 (0.11) |
| | **$H_2S$** | 7 370 | 42 380 | 0.08 (0.03) | 0.12 (0.04) |
| ***$P_T$ = 2 bar; $P_{CO_2}$ = 0.8 bar; $P_{CH_4}$ = 1.2 bar; $P_{H_2S}$ = 0.0016 bar*** | | | | | |
| **13X zeolite monolith** | **$CO_2$** | 396 | 2 675 | 1.34 (0.74) | 2.58 (1.42) |
| | **$CH_4$** | 30 | 434 | 0.07 (0.04) | 0.30 (0.17) |
| | **$H_2S$** | 7 720 | 36 960 | 0.06 (0.03) | 0.12 (0.07) |
| **Purified MIL-101(Cr) monolith** | **$CO_2$** | 160 | 929 | 1.26 (0.36) | 1.98 (0.57) |
| | **$CH_4$** | 23 | 394 | 0.13 (0.04) | 0.62 (0.19) |
| | **$H_2S$** | 183 | 4 272 | 0.003 (0.001) | 0.010 (0.003) |
| **$K_2CO_3$/13X zeolite foam-monolith** | **$CO_2$** | 517 | 4 170 | 1.68 (0.90) | 3.33 (1.79) |
| | **$CH_4$** | 31 | 636 | 0.07 (0.04) | 0.32 (0.15) |
| | **$H_2S$** | 8 920 | 48 890 | 0.10 (0.04) | 0.13 (0.05) |
| ***$P_T$ = 3 bar; $P_{CO_2}$ = 1.2 bar; $P_{CH_4}$ = 1.8 bar; $P_{H_2S}$ = 0.0024 bar*** | | | | | |
| **13X zeolite monolith** | **$CO_2$** | 460 | 2 818 | 1.63 (0.90) | 2.97 (1.64) |
| | **$CH_4$** | 35 | 493 | 0.08 (0.05) | 0.41 (0.23) |
| | **$H_2S$** | 8 630 | 38 780 | 0.07 (0.04) | 0.13 (0.07) |
| **Purified MIL-101(Cr) monolith** | **$CO_2$** | 176 | 1 095 | 1.39 (0.40) | 2.16 (0.62) |
| | **$CH_4$** | 28 | 465 | 0.15 (0.05) | 0.79 (0.25) |
| | **$H_2S$** | 281 | 4 469 | 0.004 (0.001) | 0.011 (0.004) |
| **$K_2CO_3$/13X zeolite foam-monolith** | **$CO_2$** | 705 | 5 225 | 2.34 (1.25) | 4.01 (2.15) |
| | **$CH_4$** | 37 | 743 | 0.09 (0.04) | 0.43 (0.21) |
| | **$H_2S$** | 10 380 | 52 650 | 0.11 (0.04) | 0.14 (0.06) |
| ***$P_T$ = 4 bar; $P_{CO_2}$ = 1.6 bar; $P_{CH_4}$ = 2.4 bar; $P_{H_2S}$ = 0.0032 bar*** | | | | | |
| **13X zeolite monolith** | **$CO_2$** | 535 | 3 067 | 1.90 (1.04) | 3.38 (1.84) |
| | **$CH_4$** | 41 | 552 | 0.09 (0.05) | 0.52 (0.28) |
| **Purified MIL-101(Cr) monolith** | **$CO_2$** | 203 | 1 301 | 1.63 (0.47) | 2.38 (0.69) |
| | **$CH_4$** | 34 | 547 | 0.17 (0.06) | 0.94 (0.30) |
| **$K_2CO_3$/13X zeolite foam-monolith** | **$CO_2$** | 898 | 6 428 | 3.01 (1.62) | 4.70 (2.52) |
| | **$CH_4$** | 44 | 862 | 0.10 (0.05) | 0.55 (0.27) |

**Table 7.4** The adsorption properties of 13X zeolite monolith, purified MIL-101(Cr) monolith and $K_2CO_3$/13X zeolite foam-monolith with different $CO_2/CH_4$ mixed (40:60, % vol.) feed gas pressures that flow at a rate of 500 mL $min^{-1}$.

| Adsorption properties | | $t_b$ (s) | $t_e$ (s) | $\overline{q}_b$ (mmol $g^{-1}$) & (mmol $cm^{-3}$ in bracket) | $\overline{q}_e$ (mmol $g^{-1}$) & (mmol $cm^{-3}$ in bracket) | $\alpha_{CO_2/CH_4}$ |
|---|---|---|---|---|---|---|
| ***$P_T$ = 1 bar; $P_{CO_2}$ = 0.4 bar; $P_{CH_4}$ = 0.6 bar*** | | | | | | |
| **13X zeolite monolith** | **$CO_2$** | 249 | 2 330 | 0.88 (0.48) | 1.95 (1.07) | 26.4 |
| | **$CH_4$** | 25 | 59 | 0.04 (0.02) | 0.11 (0.06) | |
| **Purified MIL-101(Cr) monolith** | **$CO_2$** | 122 | 804 | 0.87 (0.32) | 1.22 (0.44) | 6.2 |
| | **$CH_4$** | 18 | 87 | 0.08 (0.03) | 0.30 (0.11) | |
| **$K_2CO_3$/13X zeolite foam-monolith** | **$CO_2$** | 273 | 3 268 | 0.90 (0.50) | 2.74 (1.52) | 28.2 |
| | **$CH_4$** | 25 | 74 | 0.05 (0.03) | 0.15 (0.08) | |
| ***$P_T$ = 2 bar; $P_{CO_2}$ = 0.8 bar; $P_{CH_4}$ = 1.2 bar*** | | | | | | |
| **13X zeolite monolith** | **$CO_2$** | 311 | 2 582 | 1.11 (0.62) | 2.29 (1.28) | 22.9 |
| | **$CH_4$** | 28 | 78 | 0.05 (0.03) | 0.15 (0.08) | |
| **Purified MIL-101(Cr) monolith** | **$CO_2$** | 137 | 901 | 1.08 (0.34) | 1.52 (0.48) | 5.9 |
| | **$CH_4$** | 22 | 104 | 0.11 (0.03) | 0.39 (0.12) | |
| **$K_2CO_3$/13X zeolite foam-monolith** | **$CO_2$** | 364 | 3 943 | 1.16 (0.68) | 3.08 (1.79) | 26.4 |
| | **$CH_4$** | 30 | 95 | 0.06 (0.03) | 0.18 (0.10) | |
| ***$P_T$ = 3 bar; $P_{CO_2}$ = 1.2 bar; $P_{CH_4}$ = 1.8 bar*** | | | | | | |
| **13X zeolite monolith** | **$CO_2$** | 379 | 2 723 | 1.38 (0.76) | 2.72 (1.49) | 20.6 |
| | **$CH_4$** | 31 | 95 | 0.06 (0.03) | 0.20 (0.11) | |
| **Purified MIL-101(Cr) monolith** | **$CO_2$** | 147 | 1 056 | 1.26 (0.37) | 1.75 (0.51) | 5.3 |
| | **$CH_4$** | 27 | 128 | 0.14 (0.04) | 0.49 (0.14) | |
| **$K_2CO_3$/13X zeolite foam-monolith** | **$CO_2$** | 480 | 4 771 | 1.60 (0.90) | 3.61 (2.02) | 23.9 |
| | **$CH_4$** | 35 | 117 | 0.07 (0.04) | 0.23 (0.13) | |
| ***$P_T$ = 4 bar; $P_{CO_2}$ = 1.6 bar; $P_{CH_4}$ = 2.4 bar*** | | | | | | |
| **13X zeolite monolith** | **$CO_2$** | 454 | 2 969 | 1.66 (0.91) | 3.04 (1.67) | 18.5 |
| | **$CH_4$** | 35 | 113 | 0.08 (0.04) | 0.25 (0.13) | |
| **Purified MIL-101(Cr) monolith** | **$CO_2$** | 158 | 1 253 | 1.36 (0.39) | 1.89 (0.55) | 4.7 |
| | **$CH_4$** | 32 | 155 | 0.16 (0.05) | 0.60 (0.17) | |
| **$K_2CO_3$/13X zeolite foam-monolith** | **$CO_2$** | 585 | 5 677 | 1.91 (1.09) | 3.85 (2.20) | 21.1 |
| | **$CH_4$** | 42 | 150 | 0.09 (0.05) | 0.27 (0.16) | |

### 7.3.3 Effect of varying feed gas flow rates

The breakthrough curves showing the effect of varying feed gas flow rates (i.e., at 250 mL $min^{-1}$, 500 mL $min^{-1}$ or 1 000 mL $min^{-1}$) with a constant feed gas pressure of 2 bar for 13X zeolite monolith, purified MIL-101(Cr) monolith and $K_2CO_3$/13X zeolite foam-monolith are shown in Figure 7.5 for $CO_2$ (40% vol.) and $CH_4$ (60% vol.) and Figure 7.6 for $H_2S$ (0.08% vol.) and $CO_2/CH_4$ mixture (60:40, % vol.) in the feed stream. It was observed that steeper breakthrough curves were produced at higher feed gas flow rate, indicating that it has efficient mass transfer of adsorbate gas (or gases) in the adsorbent bed. Similar observation was also reported by Wang (2008).

As seen in Figures 7.5 and 7.6, the breakthrough and equilibrium times decrease with increasing feed gas flow rate. This was because the mass transfer front reaches the end of the adsorbent bed early and the bed gets saturated faster since more adsorbate gas (or gases) going through the column at a high feed gas flow rate compared to a low feed gas flow rate (Monazam *et al.*, 2013). For example, it was found that the breakthrough time for 13X zeolite monolith was reduced from 825 s to 161 s and its equilibrium time was reduced from 3 833 s to 1 548 s when the $CO_2$ feed gas flow rate was increased from 250 mL $min^{-1}$ to 1 000 mL $min^{-1}$, as indicated in Table 7.5. At a constant feed gas pressure of 2 bar, the steepest breakthrough curve with the shortest breakthrough and equilibrium times was found to be obtained using a feed gas flow rate of 1 000 mL $min^{-1}$.

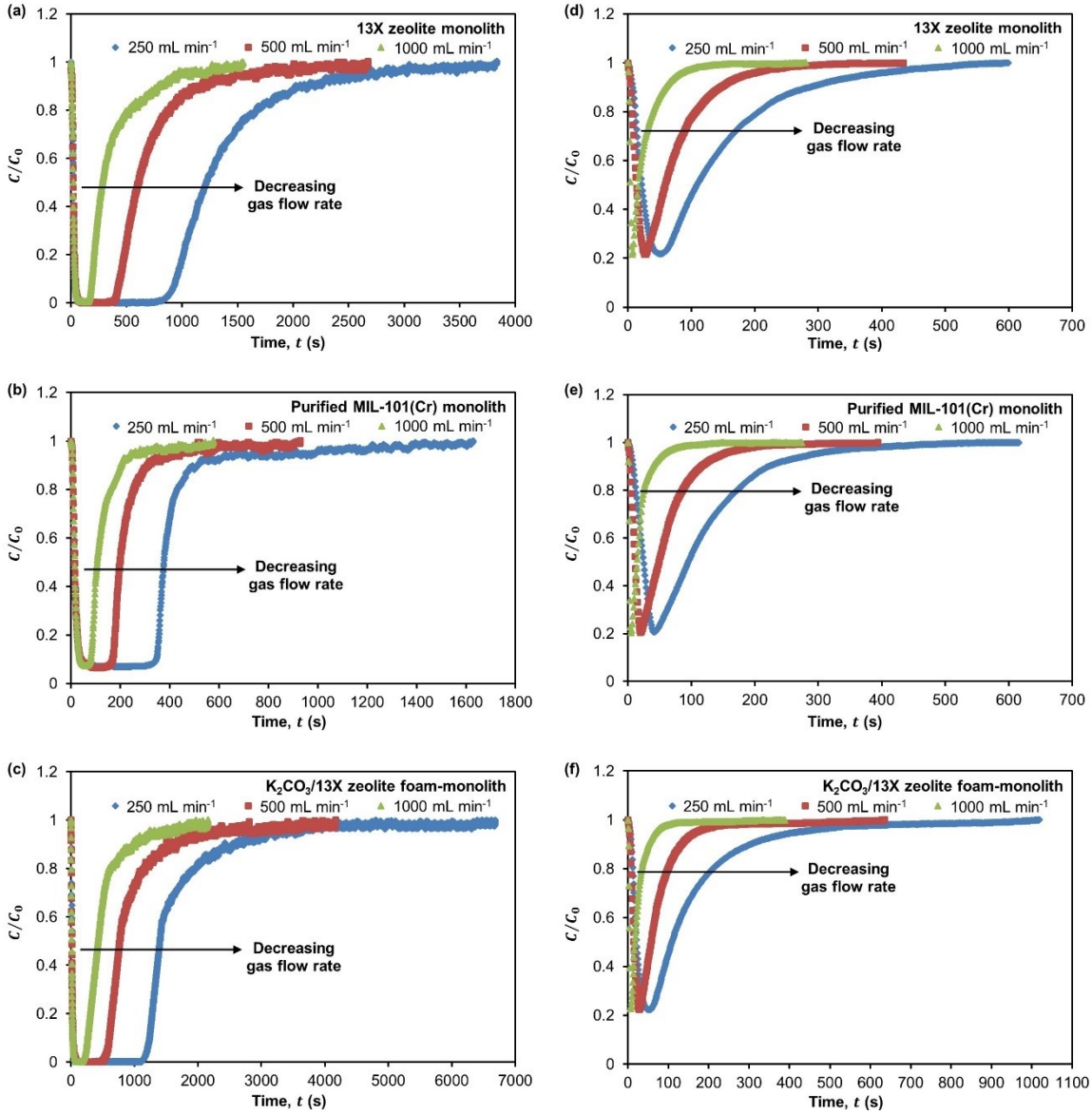


**Figure 7.5** Effect of 40% vol. $CO_2$ (a–c) and 60% vol. $CH_4$ (d–f) feed gas flow rates on breakthrough curves at 2 bar for 13X zeolite monolith, purified MIL-101(Cr) monolith and $K_2CO_3$/13X zeolite foam-monolith.

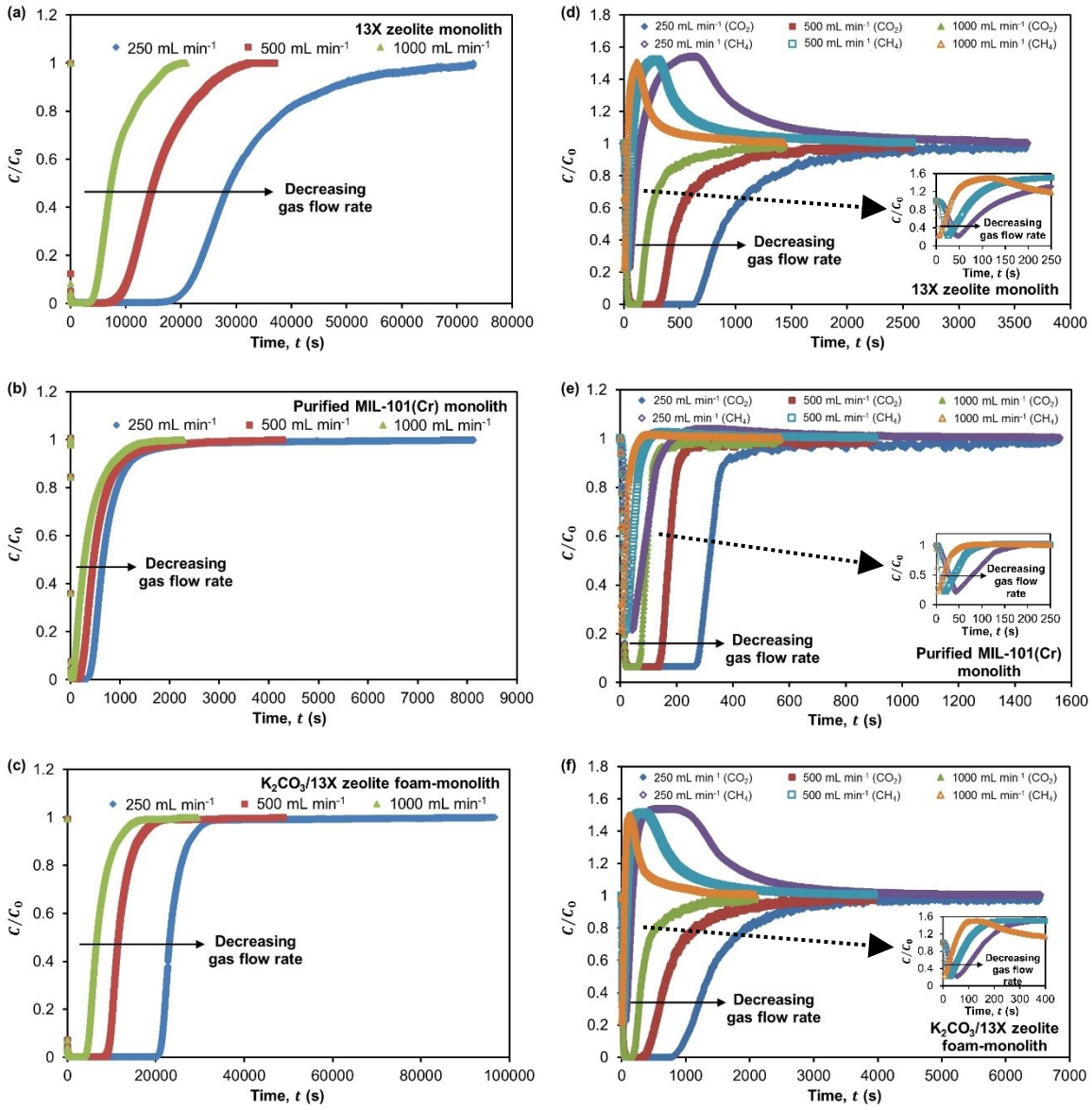


**Figure 7.6** Effect of 0.08% vol. $H_2S$ (a–c) and $CO_2/CH_4$ mixed (40:60, % vol.) (d–f) feed gas flow rates on breakthrough curves at 2 bar for 13X zeolite monolith, purified MIL-101(Cr) monolith and $K_2CO_3$/13X zeolite foam-monolith.

The early breakthrough of the adsorbent bed at high feed gas flow rate leads to lower breakthrough adsorption capacity (in terms of mass and volumetric, in most cases). For example, the breakthrough adsorption capacity of $CO_2$ (on mass basis) for 13X zeolite was found to decrease from 1.42 mmol $g^{-1}$ to 1.00 mmol $g^{-1}$ when the $CO_2$ feed gas flow rate was increased from 250 mL $min^{-1}$ to 1 000 mL $min^{-1}$, as indicated in Table 7.5. Conversely, the equilibrium adsorption capacity was found to increase with increasing feed gas flow rate. This was because more adsorbate gas (or gases) are adsorbed onto the adsorbent bed since more adsorbate gas (or gases) are going through the column at a high feed gas flow rate. For example, the results in Table 7.5 indicate a slight improvement in the equilibrium adsorption capacity of $CO_2$ for 13X zeolite monolith from

2.46 mmol $g^{-1}$ to 2.69 mmol $g^{-1}$ when the feed gas flow rate increased from 250 mL $min^{-1}$ to 1 000 mL $min^{-1}$.

**Table 7.5** The adsorption properties of 13X zeolite monolith, purified MIL-101(Cr) monolith and $K_2CO_3$/13X zeolite foam-monolith with different $CO_2$ (40% vol.), $CH_4$ (60% vol.) and $H_2S$ (0.08% vol.) feed gas flow rates at 2 bar.

| Adsorption properties | | $t_b$ (s) | $t_e$ (s) | $\overline{q}_b$ (mmol $g^{-1}$) & (mmol $cm^{-3}$ in bracket) | $\overline{q}_e$ (mmol $g^{-1}$) & (mmol $cm^{-3}$ in bracket) |
|---|---|---|---|---|---|
| ***250 mL min$^{-1}$*** | | | | | |
| **13X zeolite monolith** | **$CO_2$** | 825 | 3 833 | 1.42 (0.79) | 2.46 (1.36) |
| | **$CH_4$** | 59 | 599 | 0.08 (0.04) | 0.28 (0.17) |
| | **$H_2S$** | 18 270 | 72 980 | 0.07 (0.04) | 0.12 (0.07) |
| **Purified MIL-101(Cr) monolith** | **$CO_2$** | 328 | 1 629 | 1.31 (0.38) | 1.82 (0.53) |
| | **$CH_4$** | 47 | 616 | 0.14 (0.04) | 0.61 (0.18) |
| | **$H_2S$** | 369 | 8 125 | 0.004 (0.001) | 0.009 (0.002) |
| **$K_2CO_3$/13X zeolite foam-monolith** | **$CO_2$** | 1141 | 6 686 | 1.90 (1.01) | 2.90 (1.54) |
| | **$CH_4$** | 61 | 1 018 | 0.08 (0.04) | 0.30 (0.17) |
| | **$H_2S$** | 20 680 | 96 640 | 0.11 (0.04) | 0.13 (0.05) |
| ***500 mL min$^{-1}$*** | | | | | |
| **13X zeolite monolith** | **$CO_2$** | 396 | 2 675 | 1.34 (0.74) | 2.58 (1.42) |
| | **$CH_4$** | 30 | 434 | 0.07 (0.04) | 0.30 (0.17) |
| | **$H_2S$** | 7 720 | 36 960 | 0.06 (0.03) | 0.12 (0.07) |
| **Purified MIL-101(Cr) monolith** | **$CO_2$** | 160 | 929 | 1.26 (0.36) | 1.98 (0.57) |
| | **$CH_4$** | 23 | 394 | 0.13 (0.04) | 0.62 (0.19) |
| | **$H_2S$** | 183 | 4 272 | 0.003 (0.001) | 0.010 (0.003) |
| **$K_2CO_3$/13X zeolite foam-monolith** | **$CO_2$** | 517 | 4 170 | 1.68 (0.90) | 3.33 (1.79) |
| | **$CH_4$** | 31 | 636 | 0.07 (0.04) | 0.32 (0.15) |
| | **$H_2S$** | 8 920 | 48 890 | 0.10 (0.04) | 0.13 (0.05) |
| ***1 000 mL min$^{-1}$*** | | | | | |
| **13X zeolite monolith** | **$CO_2$** | 161 | 1 548 | 1.00 (0.56) | 2.69 (1.49) |
| | **$CH_4$** | 8 | 280 | 0.05 (0.02) | 0.34 (0.13) |
| | **$H_2S$** | 3 570 | 20 910 | 0.05 (0.03) | 0.12 (0.07) |
| **Purified MIL-101(Cr) monolith** | **$CO_2$** | 74 | 577 | 0.98 (0.30) | 2.07 (0.63) |
| | **$CH_4$** | 6 | 274 | 0.11 (0.02) | 0.63 (0.13) |
| | **$H_2S$** | 52 | 2 273 | 0.001 (0.0005) | 0.011 (0.004) |
| **$K_2CO_3$/13X zeolite foam-monolith** | **$CO_2$** | 193 | 2 158 | 1.20 (0.64) | 3.54 (1.90) |
| | **$CH_4$** | 8 | 389 | 0.05 (0.02) | 0.35 (0.11) |
| | **$H_2S$** | 4 030 | 29 380 | 0.07 (0.03) | 0.13 (0.06) |

The behaviour of the adsorption of $CH_4$, $H_2S$ and $CO_2$/$CH_4$ mixture onto 13X zeolite monolith, purified MIL-101(Cr) monolith and $K_2CO_3$/13X zeolite foam-monolith with varying feed gas flow rates were similar to that of $CO_2$ (see Figures 7.5 and 7.6). For the adsorption of $CO_2$/$CH_4$ mixture, a strong roll-up was observed for 13X zeolite monolith and $K_2CO_3$/13X zeolite foam-monolith and a weak roll-up was observed for purified MIL-101(Cr) monolith, as indicated in Figures 7.6 (d) to (f). This behaviour was similar to that

observed previously (refer Figures 7.4 (d) to (f) in Section 7.3.2). The maximum $CH_4$ purity in the effluent was same as that found in previous study (refer Section 7.3.2), i.e., about 98% vol. $CH_4$ for 13X zeolite monolith and $K_2CO_3$/13X zeolite foam-monolith and about 67% vol. $CH_4$ for purified MIL-101(Cr) monolith. The study found that the selectivity of $CO_2$ over $CH_4$ was increased slightly (i.e., by about 3% for 13X zeolite monolith, 5% for purified MIL-101(Cr) monolith and 12% for $K_2CO_3$/13X zeolite foam-monolith) when the mixed feed gas flow rate was increased from 250 mL $min^{-1}$ to 1 000 mL $min^{-1}$, as indicated in Table 7.6.

**Table 7.6** The adsorption properties of 13X zeolite monolith, purified MIL-101(Cr) monolith and $K_2CO_3$/13X zeolite foam-monolith with different $CO_2/CH_4$ mixed (40:60, % vol.) feed gas flow rates at 2 bar.

| Adsorption properties | | $t_b$ (s) | $t_e$ (s) | $\bar{q}_b$ (mmol $g^{-1}$) & (mmol $cm^{-3}$ in bracket) | $\bar{q}_e$ (mmol $g^{-1}$) & (mmol $cm^{-3}$ in bracket) | $\alpha_{CO_2/CH_4}$ |
|---|---|---|---|---|---|---|
| ***250 mL min$^{-1}$*** | | | | | | |
| **13X zeolite monolith** | **$CO_2$** | 638 | 3 614 | 1.19 (0.60) | 2.12 (1.07) | 22.3 |
| | **$CH_4$** | 51 | 142 | 0.06 (0.03) | 0.14 (0.07) | |
| **Purified MIL-101(Cr) monolith** | **$CO_2$** | 271 | 1 558 | 1.09 (0.32) | 1.45 (0.43) | 5.7 |
| | **$CH_4$** | 46 | 190 | 0.12 (0.04) | 0.38 (0.11) | |
| **$K_2CO_3$/13X zeolite foam-monolith** | **$CO_2$** | 820 | 6 539 | 1.30 (0.72) | 2.64 (1.46) | 24.0 |
| | **$CH_4$** | 60 | 162 | 0.07 (0.04) | 0.17 (0.09) | |
| ***500 mL min$^{-1}$*** | | | | | | |
| **13X zeolite monolith** | **$CO_2$** | 311 | 2 582 | 1.11 (0.62) | 2.29 (1.28) | 22.9 |
| | **$CH_4$** | 28 | 78 | 0.05 (0.03) | 0.15 (0.08) | |
| **Purified MIL-101(Cr) monolith** | **$CO_2$** | 137 | 901 | 1.08 (0.34) | 1.52 (0.48) | 5.9 |
| | **$CH_4$** | 22 | 104 | 0.11 (0.03) | 0.39 (0.12) | |
| **$K_2CO_3$/13X zeolite foam-monolith** | **$CO_2$** | 364 | 3 943 | 1.16 (0.68) | 3.08 (1.79) | 26.4 |
| | **$CH_4$** | 30 | 95 | 0.06 (0.03) | 0.18 (0.10) | |
| ***1 000 mL min$^{-1}$*** | | | | | | |
| **13X zeolite monolith** | **$CO_2$** | 129 | 1 436 | 0.92 (0.49) | 2.41 (1.27) | 23.0 |
| | **$CH_4$** | 6 | 33 | 0.03 (0.02) | 0.16 (0.08) | |
| **Purified MIL-101(Cr) monolith** | **$CO_2$** | 63 | 566 | 0.91 (0.30) | 1.61 (0.53) | 6.0 |
| | **$CH_4$** | 5 | 67 | 0.06 (0.02) | 0.40 (0.13) | |
| **$K_2CO_3$/13X zeolite foam-monolith** | **$CO_2$** | 152 | 2 090 | 1.05 (0.53) | 3.29 (1.68) | 26.7 |
| | **$CH_4$** | 7 | 45 | 0.03 (0.02) | 0.19 (0.09) | |

### 7.3.4 Effect of $H_2O$ vapour

In real situations, raw biogas contains some $H_2O$ vapour (generally of about 2% vol. to 7% vol.) in addition to $CO_2$, $CH_4$, $H_2S$ and other contaminants. So, it is important to investigate the effect of $H_2O$ vapour on the adsorption of $CO_2/CH_4$ mixed gases. The $CO_2/CH_4/H_2O$ vapour mixed gas adsorption experiment was carried out using a humidified $CO_2/CH_4$ mixed (40:60, % vol.) feed gas stream with a relative humidity of 93% (i.e., about 2.2% vol. $H_2O$ vapour). The breakthrough curves for $CO_2/CH_4/H_2O$ vapour and $CO_2/CH_4$

mixed gases adsorption onto 13X zeolite monolith, purified MIL-101(Cr) monolith and $K_2CO_3$/13X zeolite foam-monolith at 2 bar with a constant mixed feed gas flow rate of 500 mL $min^{-1}$ are shown in Figure 7.7.

It was seen in Figures 7.7 (a) and (b) that the addition of $H_2O$ vapour in the $CO_2/CH_4$ mixed feed gas stream did not show any change on the steepness of the breakthrough curves for both $CO_2$ and $CH_4$ adsorption on 13X zeolite and purified MIL-101(Cr) monoliths. This implies that the mass transfer of $CO_2$ and $CH_4$ in 13X zeolite and purified MIL-101(Cr) monoliths was not influence by presence of $H_2O$ vapour in the mixed feed gas stream. For $K_2CO_3$/13X zeolite foam-monolith, it was seen in Figure 7.7 (c) that the steepness of its breakthrough curves was improved for $CO_2$ adsorption and there was no change for $CH_4$ adsorption when the mixed feed gas stream was humidified with 93% RH. This shows that the presence of $H_2O$ vapour in the mixed feed gas stream would enhance the mass transfer of $CO_2$ but they have no influence on the mass transfer of $CH_4$ in $K_2CO_3$/13X zeolite foam-monolith.

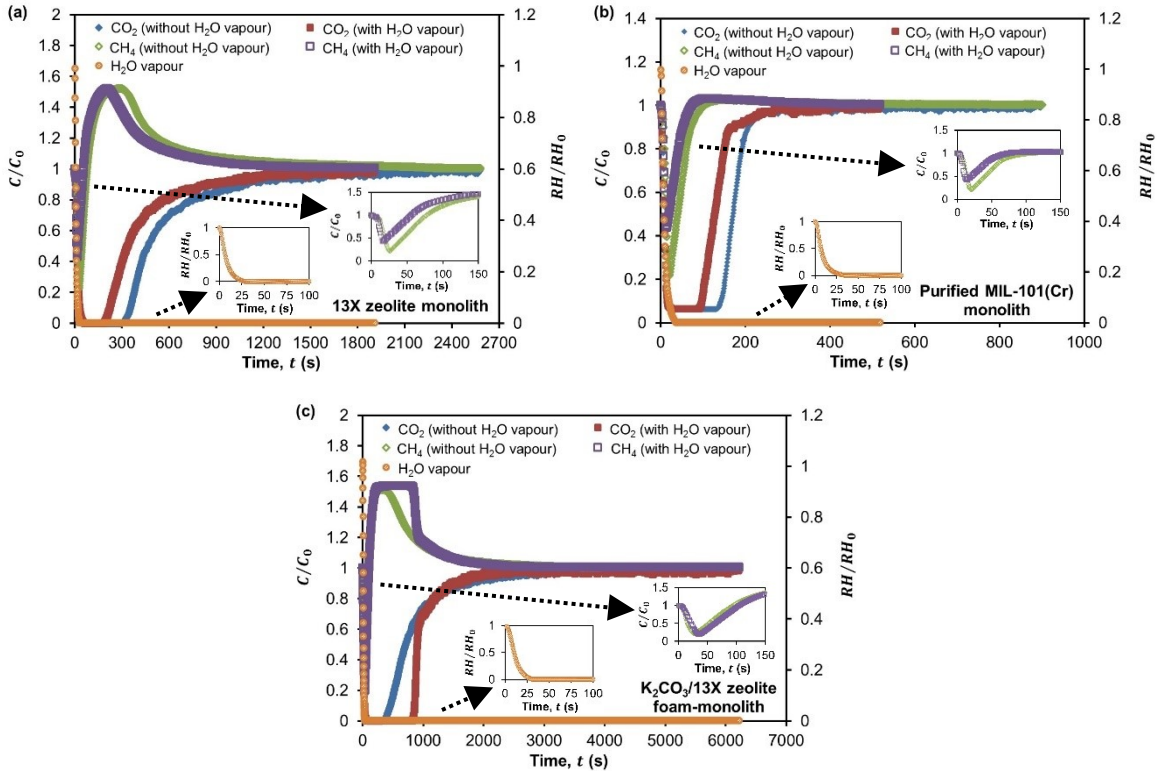


**Figure 7.7** Effect of $H_2O$ vapour (~ 93% RH) on breakthrough curves with $CO_2/CH_4$ mixture (40:60, % vol.) in feed gas at 2 bar and a gas flows of 500 mL $min^{-1}$ for (a) 13X zeolite monolith, (b) purified MIL-101(Cr) monolith and (c) $K_2CO_3$/13X zeolite foam-monolith.

The amplitude of the roll-up was found to slightly lower for 13X zeolite and purified MIL-101(Cr) monoliths when $H_2O$ vapour was present in the mixed feed gas stream. This

gave an indication that the amount of $CH_4$ displaced by incoming $CO_2$ was reduced since the adsorbent bed also adsorbed $H_2O$ vapour. The maximum purity of $CH_4$ achieved by 13X zeolite monoliths was found to reduce from about 98% vol. $CH_4$ to 96% vol. $CH_4$ and that by purified MIL-101(Cr) monoliths was found to reduce from about 66% vol. $CH_4$ to 62% vol. $CH_4$ when the mixed feed gas stream contains $H_2O$ vapour at 93% RH compared to a dry mixed feed gas stream. The study found that the maximum purity of $CH_4$ achieved by $K_2CO_3$/13X zeolite foam-monolith under humid conditions (i.e., at 93% RH) was about the same as that obtained under dry conditions, which was about 99% vol. $CH_4$. This demonstrates that the purity of $CH_4$ in the effluent gas stream was not affected by the presence of $H_2O$ vapour in the mixed feed gas stream for $K_2CO_3$/13X zeolite foam-monolith.

Similar to the adsorption behaviour of $CO_2/CH_4$ mixture seen previously (refer Sections 7.3.2 and 7.3.3), the adsorption of $CO_2/CH_4/H_2O$ vapour mixture also shows that the breakthrough and equilibrium times for $CO_2$ adsorption were longer than those for $CH_4$ adsorption. This shows that 13X zeolite monolith, purified MIL-101(Cr) monolith and $K_2CO_3$/13X zeolite foam-monolith have preferential adsorption for $CO_2$ over $CH_4$ since the adsorbate-adsorbent interaction was stronger between the polar $CO_2$ and adsorbent compared to the non-polar $CH_4$ and adsorbent (Salmasi *et al.*, 2013). It was noticed that 13X zeolite monolith, purified MIL-101(Cr) monolith and $K_2CO_3$/13X zeolite foam-monolith adsorbed $H_2O$ vapour even they were saturated with $CO_2$ and $CH_4$. This indicates that they were excellent for $H_2O$ vapour adsorption compared to $CO_2$ and $CH_4$ adsorption.

When comparing the adsorption behaviour of a dry and humid mixed feed gas stream, the study found that the presence of $H_2O$ vapour in the mixed feed gas stream decreases the breakthrough and equilibrium times for both $CO_2$ and $CH_4$ adsorption on 13X zeolite and purified MIL-101(Cr) monoliths, as indicated in Figures 7.7 (a) and (b). This was due to the high adsorption affinity for $H_2O$ vapour over $CO_2$ and $CH_4$ (Choi *et al.*, 2009). For example, it was found that the breakthrough time for 13X zeolite monolith was reduced from 311 s to 223 s and its equilibrium time was reduced from 2 582 s to 1 908 s for $CO_2$ adsorption when the mixed feed gas stream contains $H_2O$ vapour at 93% RH. As for the $CH_4$ adsorption on 13X zeolite, the presence of 93% RH in the mixed feed gas stream was found to decrease its breakthrough time from 28 s to 18 s and its equilibrium time from 78 s to 57 s.

The early breakthrough and saturation of 13X zeolite and purified MIL-101(Cr) monoliths with humid mixed feed gas stream lead to the reduction in breakthrough and equilibrium adsorption capacities of $CO_2$ and $CH_4$ (both in terms of mass and volumetric). This demonstrates that 13X zeolite and purified MIL-101(Cr) monoliths have preferential adsorption for $H_2O$ vapour over $CO_2$ and $CH_4$. For example, the results in Table 7.7 indicate that the $CO_2$ adsorption capacities (on mass basis) for 13X zeolite monolith were decreased by about 33% at breakthrough and 30% at equilibrium when 93% RH was present in the mixed feed gas stream. The presence of $H_2O$ vapour at 93% RH in the mixed feed gas stream was also found to reduce its $CH_4$ adsorption capacities significantly by about 92% at breakthrough and 95% at equilibrium (see Table 7.7). The effect of $H_2O$ vapour on the adsorption behaviour of 13X zeolite and purified MIL-101(Cr) monoliths was similar to that reported by Li *et al.* (2008).

**Table 7.7** The adsorption properties of 13X zeolite monolith, purified MIL-101(Cr) monolith and $K_2CO_3$/13X zeolite foam-monolith without or with the presence of $H_2O$ vapour (~ 93% RH) in $CO_2/CH_4$ mixed (40:60, % vol.) feed gas stream that flows at a rate of 500 mL $min^{-1}$ at 2 bar.

| Adsorption properties | | $t_b$ (s) | $t_e$ (s) | $\bar{q}_b$ (mmol $g^{-1}$) & (mmol $cm^{-3}$ in bracket) | $\bar{q}_e$ (mmol $g^{-1}$) & (mmol $cm^{-3}$ in bracket) | $\alpha_{CO_2/CH_4}$ |
|---|---|---|---|---|---|---|
| ***$CO_2/CH_4$ (40:60, % vol.)*** | | | | | | |
| **13X zeolite monolith** | **$CO_2$** | 311 | 2 582 | 1.11 (0.62) | 2.29 (1.28) | 22.9 |
| | **$CH_4$** | 28 | 78 | 0.05 (0.03) | 0.15 (0.08) | |
| **Purified MIL-101(Cr) monolith** | **$CO_2$** | 137 | 901 | 1.08 (0.34) | 1.52 (0.48) | 5.9 |
| | **$CH_4$** | 22 | 104 | 0.11 (0.03) | 0.39 (0.12) | |
| **$K_2CO_3$/13X zeolite foam-monolith** | **$CO_2$** | 364 | 3 943 | 1.16 (0.68) | 3.08 (1.79) | 26.4 |
| | **$CH_4$** | 30 | 95 | 0.06 (0.03) | 0.18 (0.10) | |
| ***$CO_2/CH_4/H_2O$ vapour (40:60, % vol. & 93% RH)*** | | | | | | |
| **13X zeolite monolith** | **$CO_2$** | 223 | 1 908 | 0.74 (0.41) | 1.61 (0.89) | 300.5 |
| | **$CH_4$** | 18 | 57 | 0.004 (0.002) | 0.008 (0.004) | |
| **Purified MIL-101(Cr) monolith** | **$CO_2$** | 94 | 518 | 0.73 (0.23) | 1.14 (0.36) | 112.3 |
| | **$CH_4$** | 16 | 74 | 0.005 (0.001) | 0.015 (0.005) | |
| **$K_2CO_3$/13X zeolite foam-monolith** | **$CO_2$** | 831 | 6 217 | 2.68 (1.59) | 3.68 (2.18) | 317.7 |
| | **$CH_4$** | 38 | 106 | 0.007 (0.004) | 0.017 (0.010) | |

Unlike the adsorption behaviour of 13X zeolite and purified MIL-101(Cr) monoliths, the study discovered that $K_2CO_3$/13X zeolite foam-monolith exhibits longer breakthrough and equilibrium times for $CO_2$ and $CH_4$ adsorption when $H_2O$ vapour was present in the mixed feed gas stream (see Figure 7.7 (c) and Table 7.7). This could be due to the formation of hydrated $K_2CO_3 \cdot 1.5H_2O$ (Lee *et al.*, 2006), which caused the mass transfer front to take more time to reach the end of the adsorbent bed and for the bed to be completely saturated. The presence of $H_2O$ vapour in the mixed feed gas stream at 93% RH was found to increase the breakthrough time of $K_2CO_3$/13X zeolite foam-monolith from

364 s to 831 s and its equilibrium time from 3 943 s to 6 217 s for $CO_2$ adsorption, as indicated in Table 7.7. A humid mixed feed gas stream of 93% RH was also found to slightly increase its breakthrough time from 30 s to 38 s and its equilibrium time from 95 s to 106 s for $CH_4$ adsorption (see Table 7.7).

The results in Table 7.7 indicate that the presence of $H_2O$ vapour at 93% RH in the mixed feed gas stream improved the breakthrough and equilibrium adsorption capacities (both in terms of mass and volumetric) for $K_2CO_3$/13X zeolite foam-monolith for $CO_2$ adsorption but not for $CH_4$ adsorption. The improvement in its $CO_2$ adsorption capacities at breakthrough and equilibrium was attributed by the presence of hydrated $K_2CO_3 \cdot 1.5H_2O$ (Lee *et al.*, 2006). The drops in breakthrough and equilibrium adsorption capacities of $CH_4$ suggests that the preferential adsorption for $CO_2$ over $CH_4$ was higher under humid conditions compared to that under dry conditions. The study found that the $CO_2$ adsorption capacities (on mass basis) for $K_2CO_3$/13X zeolite foam-monolith were improved by about 2.3 times at breakthrough and about 1.2 times at equilibrium when the mixed feed gas stream contained $H_2O$ vapour at 93% RH, as indicated in Table 7.7. It was also found that the $CH_4$ adsorption capacities (on mass basis) for $K_2CO_3$/13X zeolite foam-monoliths were reduce by about 8.6 times at breakthrough and about 10.6 times at equilibrium when 93% RH was present in the mixed feed gas stream (see Table 7.7).

The results in Table 7.7 also indicate that the selectivity of $CO_2$ over $CH_4$ for 13X zeolite monolith, purified MIL-101(Cr) monolith and $K_2CO_3$/13X zeolite foam-monolith was improved when the mixed feed gas stream contains $H_2O$ vapour. This shows that the preferential adsorption for $CO_2$ over $CH_4$ of these adsorbent structures was higher under humid conditions than that under dry conditions. It was found that the selectivity of $CO_2$ over $CH_4$ was improved by about 13 times (with a value of 300.5) for 13X zeolite monolith, 19 times (with a value of 112.3) for purified MIL-101(Cr) monolith and 12 times (with a value of 317.7) for $K_2CO_3$/13X zeolite foam-monolith when the mixed feed gas stream was humidified with 93% RH, as indicated in Table 7.7. For both dry and humid conditions, the selectivity of $CO_2$ over $CH_4$ follows the order $K_2CO_3$/13X zeolite foam-monolith > 13X zeolite monolith > purified MIL-101(Cr) monolith.

### 7.3.5 Comparison between 13X zeolite and purified MIL-101(Cr) monoliths and $K_2CO_3$/13X zeolite foam-monoliths for biogas upgrading

To evaluate the suitability of 13X zeolite and purified MIL-101(Cr) monoliths and $K_2CO_3$/13X zeolite foam-monolith for biogas upgrading, their adsorption performances

were compared. Their normalised breakthrough curves for the adsorption of $CO_2/CH_4$ mixture (40:60, % vol.) with a mixed feed gas flowing at a rate of 500 mL $min^{-1}$ at 2 bar are shown in Figure 7.8. It was observed that the steepest normalised $CO_2$ adsorption breakthrough curve was produced using purified MIL-101(Cr) monolith but their normalised $CH_4$ adsorption breakthrough curve was less sharp compared to 13X zeolite monolith and $K_2CO_3$/13X zeolite foam-monolith. This gave an indication that the mass transfer of $CO_2$ was the most efficient in purified MIL-101(Cr) monolith and the mass transfer of $CH_4$ was more efficient in 13X zeolite monolith and $K_2CO_3$/13X zeolite foam-monolith than purified MIL-101(Cr) monolith.

The normalised breakthrough curves in Figure 7.8 demonstrate that both 13X zeolite monolith and $K_2CO_3$/13X zeolite foam-monolith were excellent for adsorbing $CO_2$ (with $\frac{C}{C_0}$ reaching zero) and purified MIL-101(Cr) monolith could adsorb up to about 94% vol. of $CO_2$ from the mixed feed gas stream before they start to breakthrough. For $CH_4$ adsorption, all the tested adsorbent structures showed that they could adsorb up to about 78% vol. of $CH_4$ from the mixed feed gas stream before they start to breakthrough. It was seen that the roll-up effect was stronger for 13X zeolite monolith and $K_2CO_3$/13X zeolite foam-monolith compared to purified MIL-101(Cr) monolith. This was because the amount of $CH_4$ replaced by the incoming $CO_2$ in 13X zeolite monolith and $K_2CO_3$/13X zeolite foam-monolith was more than that in purified MIL-101(Cr) monolith. The study found that both 13X zeolite monolith and $K_2CO_3$/13X zeolite foam-monolith could upgrade the biogas to a high quality with a maximum $CH_4$ purity of about 98% vol. in the effluent gas stream whereas purified MIL-101(Cr) monoliths could upgrade the biogas to a moderate quality with a maximum $CH_4$ purity of about 67% vol. in the effluent gas stream.

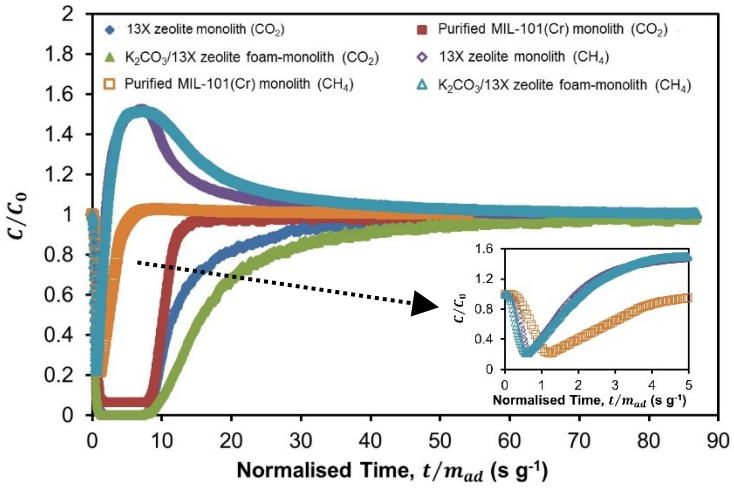


**Figure 7.8** Normalised breakthrough curves for the adsorption of $CO_2/CH_4$ mixed gases (40:60, % vol.) on 13X zeolite and purified MIL-101(Cr) monoliths and $K_2CO_3$/13X zeolite foam-monolith with feed gas flowing at 500 mL $min^{-1}$ at 2 bar.

All the tested adsorbent structures showed that their normalised breakthrough and equilibrium times for $CO_2$ adsorption were longer than those for $CH_4$ adsorption. This implies that they all have stronger adsorption affinity towards $CO_2$ compared with $CH_4$. For $CO_2$ adsorption, the normalised breakthrough time was about the same for all the tested adsorbent structures but the normalised equilibrium time varies with the adsorbent structures. This indicates that the $CO_2$ mass transfer front reaches the end of the adsorbent bed at about the same time but the bed gets saturated with $CO_2$ at different time for different type of adsorbent structures. The longest normalised breakthrough time was obtained using purified MIL-101(Cr) monoliths at about 8.2 s $g^{-1}$ and the longest equilibrium time was obtained using $K_2CO_3$/13X zeolite foam-monoliths at about 86.9 s $g^{-1}$ for $CO_2$ adsorption, as indicated in Table 7.8.

Since purified MIL-101(Cr) monolith have stronger adsorbent affinity for $CH_4$ than 13X zeolite monolith and $K_2CO_3$/13X zeolite foam-monolith, their normalised breakthrough time was longer by about 1.9 times and their normalised equilibrium time was longer by about 3 times compared to 13X zeolite monolith and $K_2CO_3$/13X zeolite foam-monolith for $CH_4$ adsorption (see Table 7.8). The study found that the highest breakthrough and equilibrium adsorption capacities of $CO_2$ (both in terms of mass and volumetric) among the tested adsorbent structures were obtained using $K_2CO_3$/13X zeolite foam-monolith. On mass basis, its sorption capacities of $CO_2$ were about 1.16 mmol $g^{-1}$ at breakthrough and 3.08 mmol $g^{-1}$ at equilibrium (see Table 7.8). This confirms the fact that more $CO_2$ are adsorbed onto $K_2CO_3$/13X zeolite foam-monolith compared to 13X zeolite and purified MIL-101(Cr) monoliths.

**Table 7.8** The $CO_2$ and $CH_4$ adsorption properties of 13X zeolite and purified MIL-101(Cr) monoliths and $K_2CO_3$/13X zeolite foam-monolith with $CO_2/CH_4$ mixed (40:60, % vol.) feed gas flowing at a rate of 500 mL $min^{-1}$ at 2 bar.

| Adsorption properties | | $\bar{t}_b$ (s $g^{-1}$) | $\bar{t}_e$ (s $g^{-1}$) | $\bar{q}_b$ (mmol $g^{-1}$) & (mmol $cm^{-3}$ in bracket) | $\bar{q}_e$ (mmol $g^{-1}$) & (mmol $cm^{-3}$ in bracket) | $\alpha_{CO_2/CH_4}$ |
|---|---|---|---|---|---|---|
| **13X zeolite monolith** | **$CO_2$** | 7.8 | 64.9 | 1.11 (0.62) | 2.29 (1.28) | 22.9 |
| | **$CH_4$** | 0.7 | 2.0 | 0.05 (0.03) | 0.15 (0.08) | |
| **Purified MIL-101(Cr) monolith** | **$CO_2$** | 8.2 | 54.0 | 1.08 (0.34) | 1.52 (0.48) | 5.9 |
| | **$CH_4$** | 1.3 | 6.2 | 0.11 (0.03) | 0.39 (0.12) | |
| **$K_2CO_3$/13X zeolite foam-monolith** | **$CO_2$** | 8.0 | 86.9 | 1.16 (0.68) | 3.08 (1.79) | 26.4 |
| | **$CH_4$** | 0.7 | 2.1 | 0.06 (0.03) | 0.18 (0.10) | |

The results in Table 7.8 also indicate that purified MIL-101(Cr) monolith exhibit the highest adsorption capacities of $CH_4$ at breakthrough (on mass basis) and at equilibrium

(in terms of mass and volumetric) among the tested adsorbent structures. This was due to their high adsorption affinity of $CH_4$, which caused more $CH_4$ to be adsorbed onto purified MIL-101(Cr) monolith. At 2 bar, the adsorption capacities of $CH_4$ (on mass basis) for purified MIL-101(Cr) monolith were found to be about 0.11 mmol $g^{-1}$ at breakthrough and 0.39 mmol $g^{-1}$ at equilibrium, as indicated in Table 7.8. The selectivity of $CO_2$ over $CH_4$ was found to be in the same order as that mentioned previously (refer Section 7.3.4), i.e., $K_2CO_3$/13X zeolite foam-monolith > 13X zeolite monolith > purified MIL-101(Cr) monolith. This shows that $K_2CO_3$/13X zeolite foam-monolith was more selective for adsorbing $CO_2$ over $CH_4$ since its sorption affinity of $CO_2$ was higher than 13X zeolite and purified MIL-101(Cr) monolith. From the results presented in this study, it seems that 13X zeolite and purified MIL-101(Cr) monoliths and $K_2CO_3$/13X zeolite foam-monolith prepared in the research are suitable for biogas upgrading application since they could upgrade the biogas either to a high or moderate quality.

## 7.4 Conclusions

The adsorption of single ($CO_2$, $CH_4$ and $H_2S$) and mixed ($CO_2$/$CH_4$) gases onto 13X zeolite and purified MIL-101(Cr) monoliths and $K_2CO_3$/13X zeolite foam-monolith have been investigated either at different feed gas concentrations, pressures or flow rates. The adsorption behaviours of these adsorbent monoliths and foam-monoliths were evaluated by analysing their adsorption breakthrough curves. The study showed that their breakthrough curves were affected by feed gas concentration and flow rate but not pressure. Generally, steeper breakthrough curves and shorter breakthrough and equilibrium times were obtained at high feed gas concentration and flow rate.

The breakthrough and equilibrium times were found to be longer at high feed gas pressure. For the adsorption of $CO_2$/$CH_4$ mixture, a strong roll-up was observed for 13X zeolite monolith and $K_2CO_3$/13X zeolite foam-monolith and a weak roll-up was observed for purified MIL-101(Cr) monolith. All the tested adsorbent structures showed that their breakthrough adsorption capacity (in terms of mass and volumetric, in most cases) increase with increasing feed gas concentrations and pressures but decrease with increasing flow rates, which was due to the early breakthrough of adsorbent beds. The tested adsorbent structures also showed that their equilibrium adsorption capacity (in terms of mass and volumetric, in most cases) increase with increasing feed gas concentrations, pressures and flow rates. The study discovered that the selectivity of $CO_2$ over $CH_4$ increases with decreasing mixed feed gas pressures and with increasing mixed feed gas flow rate.

The effect of $H_2O$ vapour (at 93% RH) on the adsorption of $CO_2/CH_4$ mixed gases (40:60, % vol.) has also been investigated. Both 13X zeolite and purified MIL-101(Cr) monoliths showed that their breakthrough and equilibrium times were shorter and their breakthrough and equilibrium adsorption capacities of $CO_2$ and $CH_4$ (both in terms of mass and volumetric) were lower when the mixed feed gas stream was humid. Conversely, $K_2CO_3$/13X zeolite foam-monolith showed longer breakthrough and equilibrium times (for $CO_2$ and $CH_4$ adsorption) and improvements in breakthrough and equilibrium adsorption capacities of $CO_2$ (both in terms of mass and volumetric) when $H_2O$ vapour was present in the mixed feed gas stream. This could be attributed by the presence of hydrated $K_2CO_3 \cdot 1.5H_2O$ on the adsorbent bed.

In summary, the dynamic adsorption study presented in this chapter has demonstrated that 13X zeolite monolith and $K_2CO_3$/13X zeolite foam-monolith were excellent for $CO_2$, $H_2S$ and $H_2O$ vapour adsorption and they could upgrade the biogas to a high quality by achieving a maximum $CH_4$ purity of about 98% vol. in the effluent gas stream. For purified MIL-101(Cr) monolith, it was found to be relatively good for $CO_2$, $H_2S$, $CH_4$ and $H_2O$ vapour adsorption and they could upgrade the biogas to a moderate quality by achieving a maximum $CH_4$ purity of about 67% vol. in the effluent gas stream. Among the tested adsorbent structures, $K_2CO_3$/13X zeolite foam-monolith exhibit the highest selectivity of $CO_2$ over $CH_4$ with a value of 26.4 under dry conditions and a value of 317.7 under humid conditions. It was concluded that 13X zeolite and purified MIL-101(Cr) monoliths and $K_2CO_3$/13X zeolite foam-monolith prepared in the research are suitable for biogas upgrading.

# Chapter 8 Kinetic Adsorption and Gas Flow Dynamic Performances of Adsorbent Monoliths and Packed Beds of Adsorbent Beads

In addition to dynamic adsorption study, kinetic adsorption and gas flow dynamic studies are also carried out and they are described in this chapter for adsorbent monoliths and packed beds of adsorbent beads. The kinetic adsorption performance of adsorbent monoliths is similar to adsorbent foam-monoliths. This has been shown in Chapter 7 (see Figure 7.8 in Section 7.3.5) that the $CO_2$ and $CH_4$ adsorption breakthrough curves for adsorbent monoliths and foam-monoliths are of the same steepness, which indicate that they have same mass transfer of $CO_2$ and $CH_4$ in the adsorbent beds. Since the adsorbent monoliths and foam-monoliths prepared in the research are of similar geometrical configurations (i.e., cell density, channel diameter and wall thickness), their gas flow dynamic performances are assumed to be equal.

So, in this work, adsorbent monoliths are chosen as an example of novel adsorbent structures. Their kinetic adsorption and gas flow dynamic performances for biogas upgrading are compared with packed beds of conventional adsorbent structures such as beads. The studies will use LiLSX zeolite monoliths and beads of different geometries as illustrations despite their low $CO_2$ adsorption capacities. For comparative purposes, LiLSX zeolite monoliths and beads of almost the same sizes (i.e., channel diameters of 0.9 mm and 1.0 mm and bead diameters of 0.6 mm and 1.5 mm) will be used.

In the kinetic adsorption study, mass transfer and diffusional resistances in LiLSX zeolite monoliths and beads will be evaluated assuming that the adsorption process is only governed by the mass transfer. In the gas flow dynamic study, axial dispersions and pressure drops in LiLSX zeolite monoliths and packed beds of LiLSX zeolite beads will be determined. To model the biogas upgrading system, the flowing gas is assumed to contain 40% vol. $CO_2$ and 60% vol. $CH_4$ mixture. The materials, calculation parameters and equipment used in the kinetic adsorption and gas flow dynamic studies are provided in Section 8.1.

The kinetic adsorption and gas flow dynamic performances of LiLSX zeolite monoliths and packed beds of LiLSX zeolite beads will be assessed experimentally and theoretically. Adsorption and pressure drop experiments will be carried out using these

adsorbent structures. The mass transfer, gas diffusion and axial dispersion coefficients and pressure drops in LiLSX zeolite monoliths and packed beds of LiLSX zeolite beads will be estimated theoretically using experimental correlations reported in the literature. The effects of superficial gas velocity and geometry of LiLSX zeolite monoliths and beads on the kinetic adsorption and gas flow dynamic performances of LiLSX zeolite monoliths and packed beds of LiLSX zeolite beads will also be investigated.

The experimental procedures and theoretical calculations used in this work are described in Section 8.2. Then, the results of the kinetic adsorption and gas flow dynamic studies for LiLSX zeolite monoliths and packed beds of LiLSX zeolite beads will be compared and discussed in Section 8.3. Also included in this section is the comparison between the experimental and theoretical pressure drops in LiLSX zeolite monoliths and packed beds of LiLSX zeolite beads. Lastly, the work described in this chapter will be concluded in Section 8.4.

## 8.1 Materials, Calculation Parameters and Equipment Used in the Kinetic Adsorption and Gas Flow Dynamic Studies

In the kinetic adsorption and gas flow dynamic studies, LiLSX zeolite monoliths (i.e., Sample 10) and beads were used as model adsorbent structures. The LiLSX zeolite monoliths were prepared using the unique extrusion techniques described in Chapter 3 of this thesis and they have an adsorbent content of 70% wt. LiLSX zeolite. On the other hand, the LiLSX zeolite beads were purchased from Zeochem AG (Switzerland) and their adsorbent content was assumed to be 90% wt. LiLSX zeolite since no data was provided by the supplier. These LiLSX monoliths and beads were of different geometrical sizes and their structural properties are provided in Tables 8.1 and 8.2, respectively.

**Table 8.1** Structural properties of LiLSX zeolite monoliths.

| Square-channelled LiLSX zeolite monoliths | Monolith 1 | Monolith 2 |
|---|---|---|
| Cell density, $\rho_{cell}$ (cells cm$^{-2}$) | 30 | 34 |
| Channel diameter, $d_c$ (mm) | 0.9 | 1.0 |
| Wall thickness, $t_w$ (mm) | 0.9 | 0.7 |
| Bed porosity, $\varepsilon$ (-) | 0.25 | 0.35 |
| External specific surface area, $A_s$ (m$^2$ m$^{-3}$) | 1 111.1 | 1 384.1 |

**Table 8.2** Structural properties of packed beds of LiLSX zeolite beads.

| Spherical LiLSX zeolite beads | Beads 1 | Beads 2 |
|---|---|---|
| Particle diameter, $d_p$ (mm) | 0.6 | 1.5 |
| Particle density, $\rho_p$ (kg m$^{-3}$) | 884.2 | 1018.6 |
| Bulk density, $\rho_b$ (kg m$^{-3}$) | 746.6 | 746.6 |
| Bed porosity, $\varepsilon$ (-) | 0.16 | 0.27 |
| External specific surface area, $A_s$ (m$^2$ m$^{-3}$) | 8 443.7 | 2 931.8 |

For the kinetic adsorption study, LiLSX zeolite monoliths and packed beds of LiLSX zeolite beads of similar masses (i.e., about 52.6 g) were used. The bed length of LiLSX zeolite monoliths was 20 cm long and the packed beds of LiLSX zeolite beads was 10 cm long. In the adsorption experiments, 40% vol. $CO_2$ in air mixture (purchased from BOC Ltd., UK) was used as an adsorbate feed gas and compressed air was used as a purging gas.

For the gas flow dynamic study, the bed length of LiLSX zeolite monoliths and packed beds of LiLSX zeolite beads were kept constant, i.e., 20 cm long. The LiLSX zeolite monoliths have a mass of about 52.6 g and a bed diameter of about 21.6 mm. The packed beds of LiLSX zeolite beads have a mass of about 112.7 g and a bed diameter of 3.1 cm. The flowing gas used in the pressure drop experiments was compressed air, assuming that the type of flowing gas has no influence on the gas dynamic in the adsorbent structures.

To model the kinetic adsorption and gas flow dynamic for a biogas upgrading system, the physical properties of $CO_2$ and $CH_4$ mixture at 20 °C and 1 bar were used in the mass transfer, gas diffusion, axial dispersion and pressure drop calculations. At 20 °C and 1 bar, the gas mixture of $CO_2$ and $CH_4$ has a density of 1.17 kg m$^{-3}$ and a dynamic viscosity of 1.31 × 10$^{-5}$ N s m$^{-2}$. The density and dynamic viscosity calculations for $CO_2$ and $CH_4$ mixture are given in Appendix 3. It was assumed that the flowing gas was a mixture of 40% vol. $CO_2$ and 60% vol. $CH_4$ and the adsorbent beds (monoliths and packed beds of beads) were of the same length, i.e., 20 cm long. The masses and bed diameters of the monoliths and packed beds used in all the calculations were similar to those used in the gas flow dynamic study.

The equipment used in the kinetic adsorption and pressure drop studies were the same as those described in Section 6.1 of Chapter 6. The adsorption flow-breakthrough apparatus used for carrying out the pressure drop experiments was slightly different to that used for carrying out the $CO_2$ adsorption experiments. As illustrated in Figure 8.1, the apparatus used in the pressure drop study involves a pressure drop measurement system in addition to the influent gas flow system, a 25.5 cm long and 3.1 cm wide internal diameter steel adsorption column (purchased from Agilent Technologies, UK) and an effluent gas analytical system.

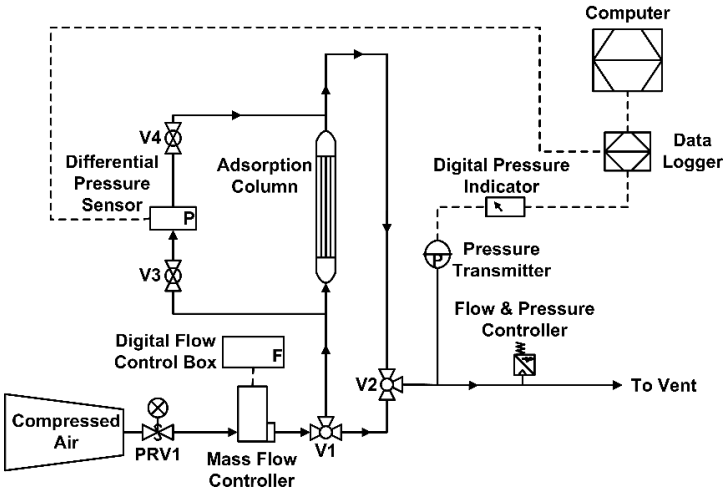


**Figure 8.1** Schematic diagram of an adsorption flow-breakthrough apparatus for pressure drop experiments.

The influent gas flow system comprises of a compressed air supply and a mass flow controller (model 5850S, purchased from Brooks Instruments LLC., USA), which was connected to a digital flow control box (purchased from Brooks Instruments LLC., USA) for regulating the air flow rate. The pressure drop measurement system was mainly made up of a differential pressure sensor (model BBDXD0FHS870BEP, manufactured by Ashdown Process Control Ltd., UK) that was used for measuring the pressure difference at the inlet and outlet of the column.

The effluent gas analytical system consists of (a) a bidirectional inline flow and pressure controller for fine-tuning the air flow and pressure, (b) a pressure transmitter for detecting the air pressure that was connected to a digital pressure indicator for giving a read-out of the pressure in bar (gauge), (c) a data logger for receiving the output signals from the differential pressure sensor and digital pressure indicator and (d) a computer for recording the differential pressure using a LabVIEW programme.

## 8.2 Methods of Determining the Kinetic Adsorption and Gas Flow Dynamic Performances of LiLSX Zeolite Monoliths and Packed Beds of LiLSX Zeolite Beads

In this work, the kinetic adsorption and gas flow dynamic performances of LiLSX zeolite monoliths and packed beds of LiLSX zeolite beads were evaluated experimentally (i.e., by carrying out adsorption and pressure drop experiments) and theoretically (i.e., using experimental correlations obtained from the literature). The experimental procedures used in the kinetic adsorption and pressure drop studies are described in Section 8.2.1. Then, the theoretical calculations used in the kinetic adsorption and gas flow dynamic studies are given in Section 8.2.2.

### 8.2.1 Experimental procedures for evaluating the kinetic adsorption and pressure drop in LiLSX zeolite monoliths and packed beds of LiLSX zeolite beads

Both $CO_2$ adsorption and pressure drop experiments were carried out similar to the steps mentioned in Section 6.2 of Chapter 6, which were:

a) drying of the LiLSX zeolite monoliths and beads,

b) packing of the LiLSX zeolite monoliths and beads in an adsorption column,

c) setting the experimental operating conditions and checking the apparatus,

d) running the adsorption/pressure drop experiment,

e) stopping the adsorption/pressure drop experiment and unpacking the LiLSX zeolite monoliths and beads and

f) regenerating the LiLSX zeolite monoliths and beads.

The detailed experimental procedures of each of these steps for $CO_2$ adsorption experiments were not covered in this section since they were exactly the same as those described in Section 6.2 of Chapter 6. For pressure drop experiments, the experimental procedures of the first three steps and the last step were the same as the $CO_2$ adsorption experiments. The fourth and fifth steps for pressure drop experiments involve additional procedures since the pressure difference at the inlet and outlet of the adsorption column needs to be measured at a range of operating conditions. The pressure drop experiments

were carried out with air pressure ranging from 1 bar to 4 bar and air flow rate ranging from 250 mL $min^{-1}$ to 1 000 mL $min^{-1}$ under ambient temperature of about 20 °C.

The pressure drop experiments were run by passing a steady flow of air with the desired air pressure and flow rate through the packed column by switching the 3-way valves at the inlet (V1) and outlet (V2) of the column. Then, the pressure difference between the inlet and outlet of the column was measured using a differential pressure sensor by opening the ball valves (V3 and V4). It was assumed that the saturation of LiLSX zeolite monoliths/beads occurs very fast, i.e. in a few seconds. The pressure drop readings were recorded on a computer.

When all the pressure drop measurements have been taken, the pressure drop experiments were stop by closing the ball valves (V3 and V4) and the 3-way valves at the inlet (V1) and outlet (V2) of the column. The packed column was then disassembled from the apparatus to unpack the saturated LiLSX zeolite monoliths/beads from the column. The saturated adsorbent monoliths/beads were desorbed and regenerated by keeping them in an electric oven at 150 °C for at least 18 hours.

### 8.2.2 Theoretical calculations for estimating the kinetic adsorption and gas flow dynamic performances of LiLSX zeolite monoliths and packed beds of LiLSX zeolite beads

As mentioned earlier, the kinetic adsorption and gas flow dynamic performances of LiLSX zeolite monoliths and packed beds of LiLSX zeolite beads for biogas upgrading were evaluated using experimental correlations reported in the literature, which has been described in Sections 2.2.2 to 2.2.3 of Chapter 2. This includes the mass transfer, diffusion and axial dispersion coefficients and pressure drops in square-channelled monoliths and packed bed of spherical beads. Their sample calculations are shown below. The kinetic adsorption and gas flow dynamic analysis described in this study was limited for gas flow of $Re$ < 10 000.

First, the Maxwellian diffusion coefficient of the flowing gas (i.e., a mixture of 40% vol. $CO_2$ and 60% vol. $CH_4$) was calculated using the following equation (i.e., equation 2.24, refer Section 2.2.2.2 of Chapter 2). Given that $CO_2$ and $CH_4$ have molecular masses of 44.01 g $mol^{-1}$ and 16.04 g $mol^{-1}$, respectively, and the $CO_2$ and $CH_4$ mixture has an average collision diameter of 0.39 nm and a collision integral of 1.17. The calculations of

the average collision diameter and collision integral for $CO_2$ and $CH_4$ mixture are given in Appendix 3.

$$D_M = \frac{(1.8583\times10^{-9})T^{\frac{3}{2}}\left[\left(\frac{1}{M_{w,CO_2}}\right)+\left(\frac{1}{M_{w,CH_4}}\right)\right]^{\frac{1}{2}}}{P\vartheta^2{}_{CO_2,CH_4}\Omega_{CO_2,CH_4}}$$

Then, $D_M = \frac{(1.8583\times10^{-9})(293.15\ \mathrm{K})^{\frac{3}{2}}\left[\left(\frac{1}{44.01\ \mathrm{g\ mol^{-1}}}\right)+\left(\frac{1}{16.04\ \mathrm{g\ mol^{-1}}}\right)\right]^{\frac{1}{2}}}{(1\ \mathrm{bar})(0.39\ \mathrm{nm})^2(1.17)}$ = 1.50 × $10^{-5}$ $m^2$ $s^{-1}$

The Knudsen diffusion coefficient was calculated using the equation below. Given that the universal gas constant was 8.314 × $10^{-5}$ $m^3$ bar $mol^{-1}$ $K^{-1}$ and the pore diameter was 104.1 nm for LiLSX zeolite monoliths and 56.2 nm for LiLSX zeolite beads. Note that the pore diameter of LiLSX zeolite monoliths and beads were determined using MIP.

$$D_K = \frac{\left(d_{pore}\times10^4\right)}{3}\left(\frac{8R_gT}{\pi M_{CH_4}}\right)^{\frac{1}{2}} = 48.5d_{pore}\left(\frac{T}{M_{CH_4}}\right)^{\frac{1}{2}}$$

Then, $D_K = 48.5(1.041\times10^{-7}\ \mathrm{m})\left(\frac{293.15\ \mathrm{K}}{16.04\ \mathrm{g\ mol^{-1}}}\right)^{\frac{1}{2}}$ = 2.16 × $10^{-6}$ $m^2$ $s^{-1}$ for LiLSX zeolite monoliths and $D_K = 48.5(5.62\times10^{-8}\ \mathrm{m})\left(\frac{293.15\ \mathrm{K}}{16.04\ \mathrm{g\ mol^{-1}}}\right)^{\frac{1}{2}}$ = 1.17 × $10^{-6}$ $m^2$ $s^{-1}$ for LiLSX zeolite beads.

Knowing the values of Maxwellian and Knudsen diffusion coefficients, the overall diffusion coefficient could be calculated using the equation below assuming that the adsorbate gas travels in a straight cylindrical pore.

$$\frac{1}{D_o} = \frac{1}{D_M} + \frac{1}{D_K}$$

For LiLSX zeolite monoliths, $D_o = \frac{1}{\frac{1}{1.50\times10^{-5}\ \mathrm{m^2\ s^{-1}}}+\frac{1}{2.16\times10^{-6}\ \mathrm{m^2\ s^{-1}}}}$ = 1.89 × $10^{-6}$ $m^2$ $s^{-1}$

For LiLSX zeolite beads, $D_o = \frac{1}{\frac{1}{1.50\times10^{-5}\ \mathrm{m^2\ s^{-1}}}+\frac{1}{1.17\times10^{-6}\ \mathrm{m^2\ s^{-1}}}}$ = 1.08 × $10^{-6}$ $m^2$ $s^{-1}$

The effective diffusivity was then calculated using the relation below, provided that the bed porosity was 0.250 for LiLSX zeolite monoliths and 0.156 for packed bed of LiLSX zeolite beads. This was to account for the diffusion of adsorbate gas molecules in the internal surface of the adsorbent material as they travel tortuously along the pore network and hindered by inaccessible adsorbent particles.

$$D_e = \varepsilon^2 D_o$$

For LiLSX zeolite monoliths, $D_e = (0.250)^2(1.89 \times 10^{-6}\ \mathrm{m^2\ s^{-1}})$ = $1.18 \times 10^{-7}$ m$^2$ s$^{-1}$

For LiLSX zeolite beads, $D_e = (0.156)^2(1.08 \times 10^{-6}\ \mathrm{m^2\ s^{-1}})$ = $2.62 \times 10^{-8}$ m$^2$ s$^{-1}$

With known values of effective diffusivity, the pore mass transfer coefficient could be evaluated using:

$k_p = \frac{2D_e d_c}{d_c t_w + t_w^2}$ for a monolith and $k_p = \frac{10D_e}{d_p}$ for a packed bed of beads

For LiLSX zeolite monoliths of equal channel diameter and wall thickness of 0.9 mm,

$k_p = \frac{2(1.18 \times 10^{-7}\ \mathrm{m^2\ s^{-1}})(0.0009\ \mathrm{m})}{(0.0009\ \mathrm{m} \times 0.0009\ \mathrm{m}) + (0.0009\ \mathrm{m})^2}$ = $1.31 \times 10^{-4}$ m s$^{-1}$

For a packed bed of 0.6 mm diameter LiLSX zeolite beads,

$k_p = \frac{10(2.62 \times 10^{-8}\ \mathrm{m^2\ s^{-1}})}{0.0006\ \mathrm{m}}$ = $4.36 \times 10^{-4}$ m s$^{-1}$

Then, the external gas film mass transfer coefficient was calculated using the correlations below. With known density, viscosity and Maxwellian diffusion coefficient of the flowing gas, the Schmidt number was calculated to be 0.75. It was assumed that the LiLSX zeolite monolith and a packed bed of LiLSX zeolite beads were 20 cm long. For a superficial gas velocity of 0.02 m s$^{-1}$, the Reynolds number was 1.83 for LiLSX zeolite monolith and 1.22 for a packed bed of LiLSX zeolite beads.

$Sh = \frac{k_f d_c}{D_M} = 2.98\left[1 + 0.095\ Re\ Sc\ \left(\frac{d_c}{L}\right)\right]^{0.45}$ for a monolith

And, $Sh = \frac{k_f d_p}{D_M} = 2.0 + 1.1\ Sc^{0.33}\ Re^{0.6}$ for a packed bed of beads

Then, $k_f = \frac{(1.50 \times 10^{-5}\ \mathrm{m^2\ s^{-1}})2.98}{0.0009\ \mathrm{m}}\left[1 + 0.095(1.83)(0.75)\left(\frac{0.0009\ \mathrm{m}}{0.2\ \mathrm{m}}\right)\right]^{0.45}$ = 0.05 m s$^{-1}$ for a LiLSX zeolite monolith.

And, $k_f = \frac{(1.50 \times 10^{-5}\ \mathrm{m^2\ s^{-1}})}{0.0006\ \mathrm{m}}[2.0 + 1.1\ (0.75)^{0.33}\ (1.22)^{0.6}]$ = 0.08 m s$^{-1}$ for a packed bed of LiLSX zeolite beads.

The overall mass transfer coefficient for a LiLSX zeolite monolith and a packed bed of LiLSX zeolite beads could then be calculated using:

$$k = \frac{k_f k_p}{(k_f + k_p)}$$

For a monolith, $k = \frac{0.05\ \text{m s}^{-1} \times (1.31\times10^{-4}\ \text{m s}^{-1})}{[0.05\ \text{m s}^{-1} + (1.31\times10^{-4}\ \text{m s}^{-1})]}$ = 1.31 × $10^{-4}$ m $s^{-1}$

For a packed bed of beads, $k = \frac{0.08\ \text{m s}^{-1} \times (4.36\times10^{-4}\ \text{m s}^{-1})}{[0.08\ \text{m s}^{-1} + (4.36\times10^{-4}\ \text{m s}^{-1})]}$ = 4.34 × $10^{-4}$ m $s^{-1}$

Next, the axial dispersion coefficients in a LiLSX zeolite monolith and a packed bed of LiLSX zeolite beads were estimated using:

$D_{ax} = D_M + \frac{u_s^2 d_c^2}{192\varepsilon^2 D_M}$ for a monolith and $D_{ax} = \frac{D_M}{\varepsilon}(20 + 0.5\ Re\ Sc)$ for a packed bed

Then, $D_{ax} = (1.50 \times 10^{-5}\ \text{m}^2\ \text{s}^{-1}) + \frac{(0.02\ \text{m s}^{-1})^2 (0.0009\ \text{m})^2}{192(0.25)^2(1.50 \times 10^{-5}\ \text{m}^2\ \text{s}^{-1})}$ = 1.73 × $10^{-5}$ $m^2$ $s^{-1}$ for a LiLSX zeolite monolith.

And, $D_{ax} = \frac{(1.50 \times 10^{-5}\ \text{m}^2\ \text{s}^{-1})}{0.156}[20 + 0.5(1.22)(0.75)]$ = 1.97 × $10^{-3}$ $m^2$ $s^{-1}$ for a packed bed of LiLSX zeolite beads.

Knowing the values of axial dispersion coefficients, the Vessel Dispersion number could be determined using the relation:

$$VD = \frac{\varepsilon D_{ax}}{u_s L}$$

For a LiLSX zeolite monolith, $VD = \frac{0.25(1.50 \times 10^{-5}\ \text{m}^2\ \text{s}^{-1})}{0.02\ \text{m s}^{-1} \times 0.2\ \text{m}}$ = 9.54 × $10^{-4}$

And, for a packed bed of LiLSX zeolite beads, $VD = \frac{0.156(1.50 \times 10^{-5}\ \text{m}^2\ \text{s}^{-1})}{0.02\ \text{m s}^{-1} \times 0.2\ \text{m}}$ = 0.07

Lastly, the pressure drops in a LiLSX zeolite monolith and a packed bed of LiLSX zeolite beads were calculated using the correlations below.

$\frac{\Delta P}{L} = \frac{28.4 \mu u_S}{\varepsilon d_c^2}$ for a monolith and $\frac{\Delta P}{L} = \frac{150(1-\varepsilon)^2 \mu u_S}{\varepsilon^3 d_p^2} + \frac{1.75(1-\varepsilon)\rho u_S^2}{\varepsilon^3 d_p}$ for a packed bed

Then, $\frac{\Delta P}{L} = \frac{28.4(1.31\times10^{-5}\ \text{N s m}^{-2})(0.02\ \text{m s}^{-1})}{0.25(0.0009\ \text{m})^2}$ = 41.60 Pa $m^{-1}$ for a LiLSX zeolite monolith.

And, $\frac{\Delta P}{L} = \frac{150(1-0.156)^2(1.31\times10^{-5}\ \text{N s m}^{-2})(0.02\ \text{m s}^{-1})}{(0.156)^3(0.0006\ \text{m})^2} + \frac{1.75(1-0.156)(1.17\ \text{kg m}^3)(0.02\ \text{m s}^{-1})^2}{(0.156)^3(0.0006\ \text{m})}$

= 23 765.32 Pa $m^{-1}$ for a packed bed of LiLSX zeolite beads.

## 8.3 Results and Discussion of the Kinetic Adsorption and Gas Flow Dynamic Studies

This section presents the results and discussion of the kinetic adsorption and gas flow dynamic studies for LiLSX zeolite monoliths and packed beds of LiLSX zeolite beads. The results of kinetic adsorption study are provided and discussed in Section 8.3.1. It covers: (a) the interpretation of $CO_2$ adsorption breakthrough curves in relation to mass transfer and diffusional resistances and (b) the theoretical evaluations of mass transfer and gas diffusional coefficients for LiLSX zeolite monoliths and packed beds of LiLSX zeolite beads under various superficial gas velocities.

Then, the results of gas flow dynamic study for LiLSX zeolite monoliths and packed beds of LiLSX zeolite beads are provided and discussed in two parts, i.e., Section 8.3.2 for axial dispersions and Section 8.3.3 for pressure drops. Comparison between experimental and theoretical pressure drops in these adsorbent structures are also included.

### 8.3.1 Mass transfer and gas diffusion in LiLSX zeolite monoliths and packed beds of LiLSX zeolite beads

The kinetic adsorption performances of LiLSX zeolite monoliths and packed beds of LiLSX zeolite beads were evaluated in this section. First, the shape of the breakthrough curves was interpreted in terms of mass transfer and diffusional resistances. The breakthrough curves for the adsorption of 40% vol. $CO_2$ onto LiLSX zeolite monoliths and packed beds of LiLSX zeolite beads of different geometries with a constant gas flow of 500 mL $min^{-1}$ at 2 bar are shown in Figure 8.2. It was seen that LiLSX zeolite monoliths produce broader breakthrough curves than packed beds of LiLSX zeolite beads. This indicates that the overall mass transfer resistance in LiLSX zeolite monoliths was higher than that in packed beds of LiLSX zeolite beads.

With a laminar gas flow, the overall mass transfer resistance in an adsorbent bed is mainly contributed by the external gas film mass transfer resistance as well as the macropore and micropore resistances. It was observed that the breakthrough curves for LiLSX zeolite monoliths near to the breakthrough point were broader than those for packed beds of LiLSX zeolite beads. This implies that LiLSX zeolite monoliths have lower external gas film mass transfer coefficient compared to packed beds of LiLSX zeolite beads. The breakthrough curves for LiLSX zeolite monoliths near to the saturation point

seems to be broader than those for packed beds of LiLSX zeolite beads. This gave an indication that the internal (i.e., macropore and micropore) resistances were higher in monoliths than those in packed beds of beads. Lee (1997) also observed the same trend when comparing its silicalite monolith with a packed bed of silicalite beads.

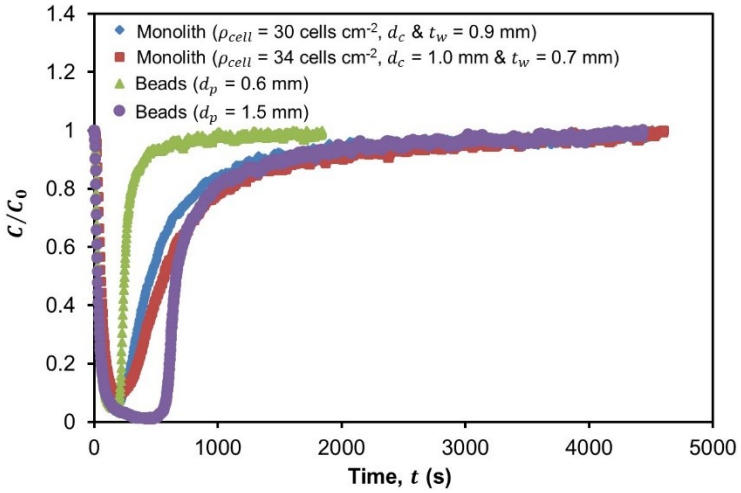


**Figure 8.2** Adsorption of 40% vol. $CO_2$ on LiLSX zeolite monoliths and beads of different geometries with a feed gas flowing at a rate of 500 mL min$^{-1}$ at 2 bar.

Figure 8.2 also demonstrates that the steepness of the breakthrough curves was slightly affected when the monolith channel diameter was increased and the wall thickness was reduced. Similar pattern was also observed when the bead diameter was increased. This suggests that the overall mass transfer resistance in monoliths and packed beds of beads increases with increasing channel/bead diameters and decreasing monolith wall thickness. For both LiLSX zeolite monoliths and packed beds of LiLSX zeolite beads, their breakthrough curves near to the breakthrough and saturation points were slightly distended as their channel/bead diameters were increased and their monolith wall thicknesses were reduced. This shows that the external gas film mass transfer and internal resistances were higher in monoliths of larger channel diameters and thinner monolith walls and in beads of larger bead diameters compared to those of smaller channel/bead diameters and thicker monolith walls.

The mass transfer and gas diffusion coefficients for LiLSX zeolite monoliths and packed beds of LiLSX zeolite beads were also evaluated for a biogas upgrading system. As shown by the sample calculations in Section 8.2.2, the LiLSX zeolite monolith with equal channel diameter and wall thickness of 0.9 mm has an overall mass transfer coefficient of $1.31 \times 10^{-4}$ m s$^{-1}$ and the packed bed of 0.6 mm diameter LiLSX zeolite beads has an overall mass transfer coefficient of $4.34 \times 10^{-4}$ m s$^{-1}$. This validates that

LiLSX zeolite monoliths have higher overall mass transfer resistance than packed beds of LiLSX zeolite beads. Since the overall mass transfer resistance in an adsorbent bed is contributed by external gas film mass transfer, macropore and micropore resistances, a high overall mass transfer resistance means that the adsorbent bed has high external gas film mass transfer and internal resistances.

With a Maxwellian diffusion coefficient of $1.50 \times 10^{-5}$ $m^2$ $s^{-1}$ and a superficial gas velocity of 0.02 m $s^{-1}$, it was found that the external gas film mass transfer coefficient for a LiLSX zeolite monolith of 0.9 mm wide channel diameter was 0.05 m $s^{-1}$ and that for a packed bed of 0.6 mm diameter was 0.08 m $s^{-1}$. The low external gas film mass transfer coefficient in LiLSX zeolite monoliths means that they have higher external gas film mass transfer resistance than packed beds of LiLSX zeolite monoliths. It was calculated that a LiLSX zeolite monolith with a pore diameter of 104.1 nm have a Knudsen diffusion coefficient of $2.16 \times 10^{-6}$ $m^2$ $s^{-1}$ and a LiLSX zeolite beads with a pore diameter of 56.2 nm have a Knudsen diffusion coefficient of $1.17 \times 10^{-6}$ $m^2$ $s^{-1}$. With known values of Maxwellian and Knudsen diffusion coefficients, the overall diffusion coefficient was found to be about $1.89 \times 10^{-6}$ $m^2$ $s^{-1}$ for LiLSX zeolite monoliths and $1.08 \times 10^{-6}$ $m^2$ $s^{-1}$ for packed beds of LiLSX zeolite beads.

Then, the effective diffusivity was estimated to be about $1.18 \times 10^{-7}$ $m^2$ $s^{-1}$ for a LiLSX zeolite monolith with a bed porosity of 0.25 and $2.62 \times 10^{-8}$ $m^2$ $s^{-1}$ for a packed bed of LiLSX zeolite beads with a bed porosity of 0.156. This gives a pore mass transfer coefficient of $1.31 \times 10^{-4}$ m $s^{-1}$ for a LiLSX zeolite monolith with equal channel diameter and wall thickness of 0.9 mm and $4.36 \times 10^{-4}$ m $s^{-1}$ for a packed bed of 0.6 mm diameter LiLSX zeolite beads. The low pore mass transfer coefficient of the monoliths confirms that they have higher internal resistance compared to packed beds. It was noted that the external gas film mass transfer coefficient was higher than the pore mass transfer coefficient for both LiLSX zeolite monoliths and packed beds of LiLSX zeolite beads. This indicates that the mass transfer in these adsorbent structures mainly occurs between the bulk gas phase and the external surface of the adsorbent. Rezaei and Webley (2009) also reported the same results and their study reveals that monoliths have lower pore mass transfer coefficient than packed beds of pellets and that the external gas film mass transfer coefficient was higher than the pore mass transfer coefficient for both monoliths and packed beds of pellets.

The variation of external gas film mass transfer coefficient with superficial velocity and geometry of LiLSX zeolite monoliths and packed beds of LiLSX zeolite beads were evaluated and they are illustrated in Figure 8.3 (a). It was seen that the external gas film mass transfer coefficient for LiLSX zeolite monoliths was not affected by the superficial gas velocity but it was slightly increased by about 11% when the channel diameter was reduced from 1.0 mm to 0.9 mm and the wall thickness was increased from 0.7 mm to 0.9 mm. For packed beds of LiLSX zeolite beads, their external gas film mass transfer coefficient was found to increase with increasing superficial gas velocity and decreasing bead diameter.

As seen in Figure 8.3 (a), the external gas film mass transfer coefficient for a packed bed of 1.5 mm diameter LiLSX zeolite beads was equal to that for a LiLSX zeolite monolith with a channel diameter of 1.0 mm and a wall thickness of 0.7 mm at a superficial gas velocity of about 0.032 m $s^{-1}$. As the superficial gas velocity increases to about 0.045 m $s^{-1}$, the external gas film mass transfer coefficient for a packed bed of 1.5 mm diameter LiLSX zeolite beads appears to be the same as that for a LiLSX zeolite monolith with equal channel diameter and wall thickness of 0.9 mm. Further increase in superficial gas velocity results in higher external gas film mass transfer coefficient for the packed bed of 1.5 mm diameter LiLSX zeolite beads when compared with LiLSX zeolite monoliths. The results in Figure 8.3 (a) show similar behaviour as that reported by Lee (1997), who study the variation of external gas film mass transfer coefficient for various geometric sizes of silicalite monoliths and packed beds of silicalite beads.

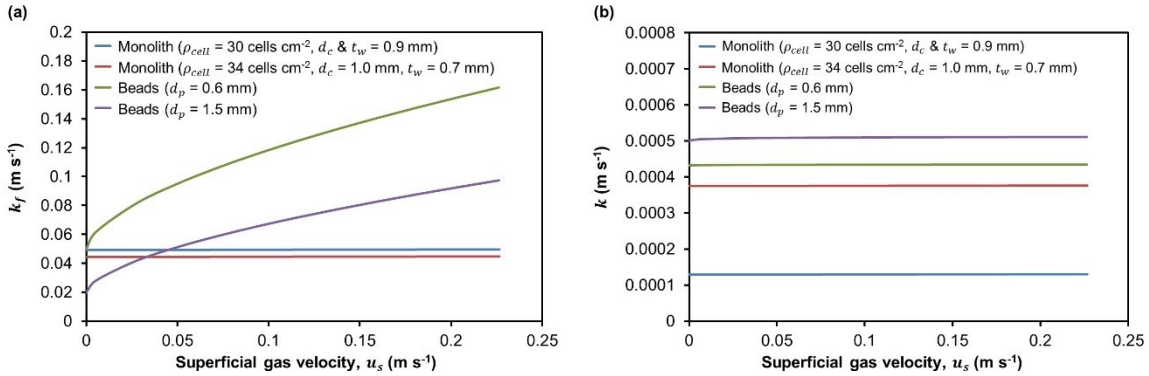


**Figure 8.3** Effects of superficial gas velocity and geometry of LiLSX zeolite monoliths and packed beds of LiLSX beads on (a) external gas film mass transfer coefficient and (b) overall mass transfer coefficient.

The effects of superficial gas velocity and geometry of LiLSX zeolite monoliths and packed beds of LiLSX zeolite beads on overall mass transfer coefficient were also evaluated and they are presented in Figure 8.3 (b). It was observed that the overall mass

transfer coefficient was influenced by the geometry of adsorbent structures and not by the superficial gas velocity. For both monoliths and packed beds, the overall mass transfer coefficient was increased by increasing the channel/bead diameter and reducing the monolith wall thickness. It was also noticed that the overall mass transfer coefficient was higher for packed beds of LiLSX zeolite beads compared to LiLSX zeolite monoliths. This verified that LiLSX zeolite monoliths used in this study have higher overall mass transfer resistance than packed beds of LiLSX zeolite beads.

### 8.3.2 Axial dispersion in LiLSX zeolite monoliths and packed beds of LiLSX zeolite beads

Next, the axial dispersion in LiLSX zeolite monoliths and packed beds of LiLSX zeolite beads was evaluated for a biogas upgrading system. The sample calculations shown in Section 8.2.2 indicate that the axial dispersion coefficient for a LiLSX zeolite monolith with equal channel diameter and wall thickness of 0.9 mm was about $1.73 \times 10^{-5}$ $m^2$ $s^{-1}$ and that for a packed bed of 0.6 mm diameter LiLSX zeolite beads was about $1.97 \times 10^{-3}$ $m^2$ $s^{-1}$ under a constant superficial gas velocity of 0.02 m $s^{-1}$. This implies that LiLSX zeolite monoliths have less axial dispersion of gases in adsorbent beds when compared with packed beds of LiLSX zeolite beads.

Assuming that LiLSX zeolite monoliths and packed beds of LiLSX zeolite beads were of 20 cm long, the Vessel Dispersion number for the LiLSX zeolite monolith with a bed porosity of 0.25 was estimated to be about $9.54 \times 10^{-4}$ and that for the packed bed of LiLSX zeolite beads with a bed porosity of 0.156 was estimated to be about 0.07. This means the effect of axial dispersion on mass transfer can be neglected for the LiLSX zeolite monolith but not for the packed bed of LiLSX zeolite beads since its Vessel Dispersion number was greater than 0.01, according to Levenspiel (1999).

The variation of axial dispersion coefficient with superficial gas velocity and geometry of LiLSX zeolite monoliths and packed beds of LiLSX zeolite beads was studied and they are demonstrated in Figure 8.4 (a). It was seen that the axial dispersion coefficient increases with increasing superficial gas velocity. According to this model, the axial dispersion coefficient was reduced by having monoliths of larger channel diameter and thinner walls and beads of larger diameter. Figure 8.4 (a) also shows that LiLSX zeolite monoliths have much lower axial dispersion coefficient compared to packed beds of LiLSX zeolite beads. This validates that monolithic adsorbent beds have lesser axial

dispersion of gases compared to packed beds of adsorbent beads. The results shown in Figure 8.4 (a) is consistent with the results reported by Lee (1997).

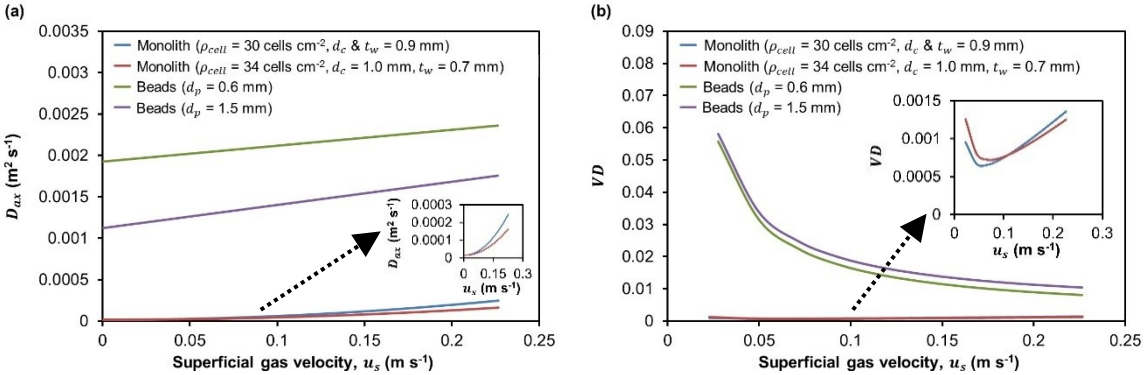


**Figure 8.4** Effects of superficial gas velocity and geometries of LiLSX zeolite monoliths and packed beds of LiLSX beads on (a) axial dispersion coefficient and (b) Vessel Dispersion number.

The effects of superficial gas velocity and geometry of LiLSX zeolite monoliths and packed beds of LiLSX zeolite beads on Vessel Dispersion number were also evaluated and they are shown in Figure 8.4 (b). It was observed that the Vessel Dispersion number for packed beds of LiLSX zeolite beads decreases with increasing superficial gas velocity and decreasing bead diameter. On the contrary, at very low superficial gas velocity (i.e., up to about 0.07 m s$^{-1}$, on average), the Vessel Dispersion number for LiLSX zeolite monoliths decreases with increasing superficial gas velocity and then it starts to increase gradually as the superficial gas velocity increases further.

In the region of very low superficial gas velocity, the Vessel Dispersion number for LiLSX zeolite monolith was lower when their they have smaller channel diameter and thicker walls. When the superficial gas velocity was higher than 0.11 m s$^{-1}$, the Vessel Dispersion number for LiLSX zeolite monolith increases with decreasing channel diameter and increasing wall thickness. It was also noticed in Figure 8.4 (b) that LiLSX zeolite monoliths have very low Vessel Dispersion number compared to packed beds of LiLSX zeolite beads. This clearly confirms that the axial dispersion of gases did not contribute to the mass transfer in monolithic adsorbent beds but it contributes to the mass transfer in packed beds of adsorbent beads.

### 8.3.3 Pressure drop in LiLSX zeolite monoliths and packed beds of LiLSX zeolite beads

In addition to axial dispersion, the pressure drops in LiLSX zeolite monoliths and packed beds of LiLSX zeolite beads were also evaluated for a biogas upgrading system. The sample calculations demonstrated in Section 8.2.2 indicate that the LiLSX zeolite monolith of 0.9 mm wide channels with a bed porosity of 0.25 has a pressure drop of about 41.60 Pa $m^{-1}$ while the packed bed of 0.6 mm diameter LiLSX zeolite beads with a bed porosity of 0.156 has a pressure drop of about 23 765.32 Pa $m^{-1}$ at a constant superficial gas velocity of 0.02 m $s^{-1}$. This shows that the pressure drop in LiLSX zeolite monoliths was much lower (i.e., by about 571 times) compared to packed beds of LiLSX zeolite beads. The low pressure drop characteristics of adsorbent monoliths means that the adsorption process would be more energy efficient and economic than using packed beds of adsorbent beads for biogas upgrading.

The variation of pressure drop with superficial gas velocity and geometry of LiLSX zeolite monoliths and packed beds of LiLSX zeolite beads was evaluated and they are presented in Figure 8.5. It was seen that the pressure drop increases with increasing superficial gas velocity for both LiLSX zeolite monoliths and packed beds of LiLSX zeolite beads. According to the pressure drop model, the pressure drop in monoliths could be reduced by increasing the channel diameter and decreasing the wall thickness. For packed beds of beads, their pressure drop could be reduced by increasing the bead diameter. Figure 8.5 also demonstrates that LiLSX zeolite monoliths have lower pressure drop than packed beds of LiLSX zeolite beads. The results in Figure 8.5 show the same trend as that reported Lee (1997).

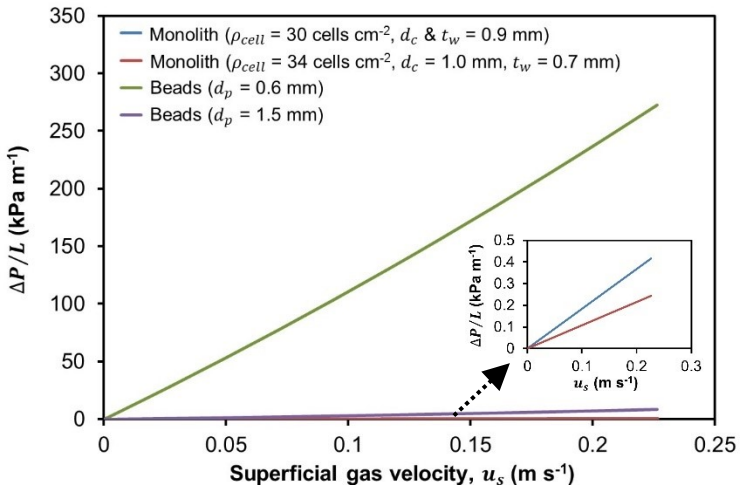


**Figure 8.5** Pressure drops in LiLSX zeolite monoliths and packed beds of LiLSX beads of different geometries at various superficial gas velocities.

The pressure drop values calculated using empirical correlations reported from the literature and those obtained from the pressure drop experiments for a LiLSX zeolite monolith with 1.0 mm wide channel and 0.7 mm thick walls and a packed bed of 1.5 mm diameter LiLSX zeolite beads under various superficial gas velocities are compared in Figure 8.6. It shows that the experimental data fits around the theoretical data. Both theoretical model and experiments demonstrate that the pressure drop increases with increasing superficial gas velocity. They also verify that the pressure drop in a LiLSX zeolite monolith was much lower than that in a packed bed of LiLSX zeolite beads. As seen in Figure 8.6, the difference in pressure drops between the monolith and the packed bed increases with increasing superficial gas velocity. This pressure drop behaviour between a monolith and a packed bed of beads at increasing superficial gas velocity was also observed by Li (1998).

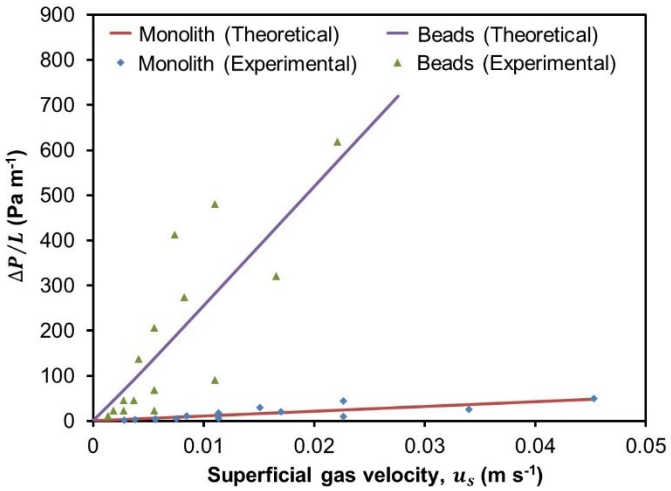


**Figure 8.6** Theoretical and experimental pressure drops in a LiLSX zeolite monolith and a packed bed of LiLSX zeolite beads with different superficial gas velocities.

## 8.4 Conclusions

Kinetic adsorption and gas flow dynamic studies have been carried out using LiLSX zeolite monoliths and packed beds of LiLSX zeolite beads. Mass transfer, gas diffusion and axial dispersion coefficients and pressure drops in these adsorbent structures were evaluated for biogas upgrading system. The effects of superficial gas velocity and geometry of LiLSX zeolite monoliths and beads on the kinetic adsorption and gas flow dynamic performances were also investigated.

The kinetic adsorption study showed that LiLSX zeolite monoliths have slightly higher overall mass transfer resistance compared to packed beds of LiLSX zeolite beads. This was because the external gas film mass transfer and internal (macropore and micropore) resistances in LiLSX zeolite monoliths were higher than those in packed beds of LiLSX zeolite beads. It was demonstrated experimentally and theoretically that the overall mass transfer resistance (which also includes the external gas film mass transfer and internal resistances) in these adsorbent structures was lower for monoliths of smaller channel diameter and thicker walls and beads of smaller diameter.

The study found that the external gas film mass transfer coefficient for packed beds of LiLSX zeolite beads increases with increasing superficial gas velocity. But, for LiLSX zeolite monoliths, their external gas film mass transfer coefficient showed no impact when the superficial gas velocity was varied. The study also demonstrated that the superficial gas velocity has no influence on the overall mass transfer coefficient for both monoliths and packed beds of beads. Axial dispersion coefficient and Vessel Dispersion number for LiLSX zeolite monoliths and packed beds of LiLSX zeolite beads were evaluated. The results showed that the axial dispersion of gases did not contribute to the mass transfer in monoliths but they contribute to the mass transfer in packed beds of beads.

For both monoliths and packed beds, the axial dispersion coefficient was found to increase with increasing superficial gas velocity. Lower axial dispersion coefficient was obtained using monoliths of wider channels and thinner walls and larger bead diameter. The pressure drops in LiLSX zeolite monoliths and packed beds of LiLSX zeolite beads were also evaluated. Both experimental and theoretical data showed that LiLSX zeolite monoliths have lower pressure drop compared to packed beds of LiLSX zeolite beads. The study demonstrated that pressure drop increases with increasing superficial gas velocity. It was found that pressure drop was lower for monoliths of wider channels and thinner walls and beads of larger diameter.

# Chapter 9 Conclusions and Future Developments

This chapter covers the overall conclusions and future developments of the works described in this thesis. The former will be described in Section 9.1 and the latter will be described in Section 9.2.

## 9.1 Overall Conclusions of the Work Described in this Thesis

The development and optimisation of regenerative novel adsorbent structures such as monoliths and foam-monoliths for removing $CO_2$ and other contaminants such as $H_2S$ and $H_2O$ vapour from the biogas stream has been presented for the first time in this thesis. The adsorbent monoliths and foam-monoliths have been fabricated successfully using the unique paste extrusion technique described in this thesis that is different to those reported in the literature, for examples, Lee (1997) and Li (1998). Various types of adsorbent monoliths have been prepared based on novel formulations, which were 13X zeolite, LiLSX zeolite, 5A zeolite, clinoptilolite and MIL-101(Cr) monoliths. Additionally, carbonate based zeolite foam-monoliths such as $K_2CO_3$/13X zeolite and $Na_2CO_3$/13X zeolite foam-monoliths have also been manufactured successfully according to the special formulations described in this thesis.

The study has demonstrated that the incorporation a decomposable pore former such as Licowax C micropowder PM into the paste formulations of these adsorbent monoliths and foam-monoliths enhances their structural porosity. This was confirmed by the formation of additional pores within the monolithic/foam-monolithic structures after the pore former was decomposed. By enhancing the structural porosity of the adsorbent structures, more adsorption sites would be exposed for capturing contaminants such as $CO_2$, $H_2O$ vapour and $H_2S$ from the biogas stream. This would, in turn, improves the mass transfer in the adsorbent monoliths and foam-monoliths. It has been shown that the addition 4% wt. pore former in the paste formulations of these adsorbent monoliths and foam-monoliths improves their $CO_2$ adsorption performance.

The characterisation study showed that the selected zeolites (i.e., 13X zeolite, LiLSX zeolite, 5A zeolite and clinoptilolite) and bentonites (i.e., calcium bentonite and Wyoming sodium bentonite) have high thermal stabilities and their crystal structures were maintained even when they were heated at a high temperature such as 400 °C or 650 °C. For MIL-101(Cr), their powders that are prepared in the research showed that they have

relatively high thermal stabilities, i.e., up to about 375 °C, on average. The thermal analyses on sodium and potassium bicarbonates showed that they start to decompose at 80 °C for the former and at 100 °C for the latter to form sodium/potassium carbonates. It was demonstrated that all zeolite monoliths prepared in the research were mechanically stronger than the commercial zeolite beads/granules. The prepared zeolite and MIL-101(Cr) monoliths and carbonate-based zeolite foam-monoliths were shown to be strong enough for use in the experiments described in this thesis.

The optimisation study found that the most suitable binder for use in this research was calcium bentonite as they were less likely to cover the adsorption sites compared to Wyoming sodium bentonite. It was discovered that the ideal firing temperature for zeolite monoliths and carbonate-based zeolite monoliths was 400 °C while that for MIL-101(Cr) monoliths was 205 °C. The suitable regeneration temperature for zeolite monoliths and carbonate-based zeolite monoliths was found to be 250 °C and that for MIL-101(Cr) monoliths was found to be 200 °C. The study discovered that the most suitable adsorbent monoliths and foam-monoliths for $CO_2$ adsorption were 13X zeolite and purified MIL-101(Cr) monoliths and $K_2CO_3$/13X zeolite foam-monoliths. The reasons were because they have relatively high structural porosity, good adsorption performance and good thermal stability.

The dynamic adsorption study has demonstrated that high breakthrough adsorption capacities (in terms of mass and volumetric, in most cases) for 13X zeolite and purified MIL-101(Cr) monoliths and $K_2CO_3$/13X zeolite foam-monoliths were obtained at high feed gas concentrations and pressures and at low gas flow rates. The equilibrium adsorption capacities (in terms of mass and volumetric, in most cases) for these adsorbent structures were found to increase with increasing feed gas concentrations, pressures and flow rates. The roll-up effect was observed for the adsorption of $CO_2$/$CH_4$ mixture. Both 13X zeolite monolith and $K_2CO_3$/13X zeolite foam-monolith showed a strong roll-up and purified MIL-101(Cr) monolith showed a weak roll-up. It was discovered that their selectivity of $CO_2$ over $CH_4$ was higher at low mixed feed gas pressure and at high mixed feed gas flow rate. The study also demonstrated that the adsorption performances of 13X zeolite and purified MIL-101(Cr) monoliths were affected when the mixed feed gas stream contained $H_2O$ vapour. But, for $K_2CO_3$/13X zeolite foam-monoliths, the presence of $H_2O$ vapour in the mixed feed gas stream was found to improve their $CO_2$ adsorption performance.

Under humid conditions, the selectivities of $CO_2$ over $CH_4$ for 13X zeolite and purified MIL-101(Cr) monoliths and $K_2CO_3$/13X zeolite foam-monoliths were found to be

higher compared to those under dry conditions as a result of higher preferential adsorption for $CO_2$ over $CH_4$. The study revealed that 13X zeolite monoliths and $K_2CO_3$/13X zeolite foam-monoliths were excellent for $CO_2$, $H_2S$ and $H_2O$ vapour adsorption and they could upgrade the biogas to a high quality by achieving a maximum $CH_4$ purity of about 98% vol. in the effluent gas stream. For purified MIL-101(Cr) monoliths, it was discovered that they were relatively good for $CO_2$, $H_2S$, $CH_4$ and $H_2O$ vapour adsorption and they could upgrade the biogas to a moderate quality by achieving a maximum $CH_4$ purity of about 67% vol. in the effluent gas stream. The highest selectivity of $CO_2$ over $CH_4$ was exhibited by $K_2CO_3$/13X zeolite foam-monoliths under both humid and dry conditions.

The kinetic adsorption study has demonstrated that LiLSX zeolite monoliths prepared in the research have slightly higher overall mass transfer resistance than packed beds of LiLSX beads. This was due to the high external gas film mass transfer and internal resistances in monoliths. The mass transfer model has shown that the overall mass transfer resistance in monoliths was lower when the monoliths have smaller channel diameter and thicker walls. Additionally, it was found that the axial dispersion of gases did not contribute to the mass transfer in monoliths but it contributes to the mass transfer in packed beds. The pressure drop study has confirmed that LiLSX zeolite monoliths have lower pressure drop compared to packed beds of LiLSX zeolite beads. It was shown that lower pressure drop was obtained by decreasing the superficial gas velocity, increasing the monolith channel/bead diameter and reducing the monolith wall thickness.

It can be concluded that 13X zeolite and purified MIL-101(Cr) monoliths and $K_2CO_3$/13X zeolite foam-monoliths were suitable for use in biogas upgrading. The reason was because they exhibit better adsorption performance and more energy efficient (i.e., by having lower pressure drop) compared to packed beds of adsorbent beads. This implies that this research can enable the creation of a new generation of energy efficient adsorbent monolith/foam-monolith systems for removing contaminants.

## 9.2 Future Developments of the Research

The results presented in this thesis have showed that 13X zeolite and purified MIL-101(Cr) monoliths and $K_2CO_3$/13X zeolite foam-monoliths are potential adsorbent structures for biogas upgrading application. The configuration of these adsorbent structures need to be modified to reduce their mass transfer resistances. It can be anticipated that further work will be carried out on the modifications of these adsorbent structures, which could include the following:

a) To improve the mass transfer properties of adsorbent monoliths and foam-monoliths. One way of achieving this would be to reduce its channel diameter and/or increase its wall thickness. However, by doing this, it would increase the pressure drop of these adsorbent structures. So, studies should be made to determine a suitable configuration of monoliths/foam-monoliths that would give reasonably good mass transfer properties and low pressure drop.

b) To estimate the lifespan of 13X zeolite and purified MIL-101(Cr) monoliths and $K_2CO_3$/13X zeolite foam-monoliths for biogas upgrading. This can be studied by carrying out a number of repeated adsorption experiments using $CO_2/CH_4$ mixture (40:60, % vol.). However, it should be noted that the adsorption capacity of these adsorbent structures would be reduced after consecutive adsorption-desorption cycles (Crittenden and Thomas, 1998).

c) To perform further adsorption experiments using 13X zeolite and purified MIL-101(Cr) monoliths and $K_2CO_3$/13X zeolite foam-monoliths. As mentioned in Section 7.3.1 (Chapter 7), a wider range of $CH_4$ feed gas concentrations should be used in future study to observe if there is any change on breakthrough curves and adsorption properties by varying $CH_4$ feed gas concentrations. Generally, steeper breakthrough curves with shorter breakthrough and equilibrium times are produced at higher feed gas concentration, as seen in Figure 7.2 of Section 7.3.1 (Chapter 7) for $CO_2$ adsorption. For further investigation on the effect of $H_2O$ vapour on the adsorption of $CO_2/CH_4$ mixture, a range of relative humidities should be used. Yi *et al.* (2007) has reported that $CO_2$ removal by potassium carbonate-based sorbents increases with increasing $H_2O$ vapour content.

d) The use of factorial/statistical design of experiments. This approach could be an efficient alternative to the one-factor-at-a-time approach that was used in this research since it gives the possibility of analysing the effects and interaction of variables with reduced number of experiments (Nieto-Sanchez *et al.*, 2013). It can be used to optimise the adsorption performances of adsorbent monoliths and foam-monoliths and studying the effects and interaction of variables such as feed gas concentrations, pressures and flow rates. Examples on the use of factorial/statistical design of experiments can be found in Garcia *et al.* (2011) and Mulgundmath *et al.* (2010).

# References


Akhtar, F. and Bergström, L., 2011. Colloidal processing and thermal treatment of binderless hierarchically porous zeolite 13X monoliths for $CO_2$ capture. *Journal of the American Ceramic Society*, 94(1), pp.92-98.

Akhtar, F., Andersson, L., Ogunwumi, S., Hedin, N. and Bergström, L., 2014. Structuring adsorbents and catalysts by processing of porous powders. *Journal of the European Ceramic Society*, 34(7), pp.1643-1666.

All Reactions, 2015a. *Sodium carbonate $Na_2CO_3$* [online]. Available from: http://www.allreactions.com/index.php/group-1a/natrium/sodium-carbonate [Accessed on 17 September 2015].

All Reactions, 2015b. *Potassium carbonate $K_2CO_3$* [online]. Available from: http://www.allreactions.com/index.php/group-1a/potassium-k/potassium-carbonate-k2co3 [Accessed on 17 September 2015].

Allegue, L.B. and Hinge, J., 2012. *Biogas and bio-syngas upgrading* [online]. Aarhus, Denmark: Danish Technological Institute. Available from: http://www.teknologisk.dk/_root/media/52679_Report-Biogas and syngas upgrading.pdf [Accessed on 1 January 2017].

Alonso-Vicario, A., Ochoa-Gómez, J.R., Gil-Río, S., Gómez-Jiménez-Aberasturi, O., Ramírez-López, C.A., Torrecilla-Soria, J. and Domínguez, A., 2010. Purification and upgrading of biogas by pressure swing adsorption on synthetic and natural zeolites. *Microporus and Mesoporous Materials*, 134, pp.100-107.

Álvarez-Gutiérrez, N., García, S., Gil, M.V., Rubiera, F. and Pevida, C., 2016. Dynamic performance of biomass-based carbons for $CO_2/CH_4$ separation. Approximation to a pressure swing adsorption process for biogas upgrading. *Energy & Fuels*, 30(6), pp.5005-5015.

Barrer, R.M., 1978. *Zeolites and clay minerals as sorbents and molecular sieves*. London: Academic Press.

Bart, H.J. and Gemmingen, U.V., 2012. Adsorption. *In*: *Ullmann's Encyclopedia of Industrial Chemistry* [online]. Weinheim: Wiley-VCH Verlag GmbH & Co. KGaA. Available from: http://onlinelibrary.wiley.com/doi/10.1002/14356007.b03_09.pub2/pdf [Accessed 12 January 2012].

Bauer, F., Persson, T., Hulteberg, C. and Tamm, D., 2013. Biogas upgrading – technology overview, comparison and perspectives for the future. *BioFuels, Bioproducts and Biorefining*, 7(5), pp.499-511.

Beil, M., 2009. *Overview on bogas upgrading technologies* [online]. European Biomethane Fuel Conference, Goteborg, Sweden, Biogasmax. Available from: http://www. biogasmax.eu/media/3t3_overview_on_upgrading_iset__062510600_0654_3009-2009.pdf [Accessed on 3 January 2017].

Benbow, J.J., Oxley, E.W. and Bridgwater, J., 1987. The extrusion mechanics of pastes-the influence of paste formulation on extrusion parameters. *Chemical Engineering Science*, 42(9), pp.2151-2162.

Biernat, K. and Samson-Bręk, I., 2011. Review of technology for cleaning biogas to natural gas quality. *CHEMIK*, 65(5), pp.435-444.

Bird, R.B., Stewart, W.E. and Lightfoot, E.N., 2002. *Transport phenomena*. 2nd ed. New York; Chichester: Wiley.

Bogdanov, B., Georgiev, D., Angelova, K. and Yaneva, K., 2009. *Natural zeolites: Clinoptilolite*. International Science Conference, Stara Zagora, Bulgaria. Available from: http://s3.amazonaws.com/academia.edu.documents/31265067/1.pdf?AWSAccessKeyId=AKIAIWO

WYYGZ2Y53UL3A&Expires=1486889549&Signature=sxvlOoU5Zi4VVs8yFoiW%2Bl6tTrc%3D&response-content-disposition=inline%3B%20filename%3DZEOLITES.pdf [Accessed on 15 April 2012].

Bromberg, L., Diao, Y., Wu, H., Speakman, S.A. and Hatton, T.A., 2012. Chromium(III) terephthalate metal organic framework (MIL-101): HF-free synthesis, structure, polyoxometalate composites, and catalytic properties. *Chemistry of Materials*, 24(9), pp.1664-1675.

Buhl, J.C., Gerstmann, M., Lutz, W. and Ritzmann, A., 2004. Hydrothermal stability of the novel zeolite type LSX in comparison to the traditional 13X modification. *Zeitschrift für anorganische und allgemeine Chemie*, 630(4), pp.604-608.

Cavenati, S., Grande, C.A. and Rodrigues, A.E., 2004. Adsorption equilibrium of methane, carbon dioxide, and nitrogen on zeolite 13X at high pressures. *Journal of Chemical & Engineering Data*, 49(4), pp.1095-1101.

CETCO, 2013. *Sodium bentonite: Its structure and properties* [online]. CETCO. Available from: http://www.cetco.com/DesktopModules/Bring2mind/DMX/Download.aspx?Command=Core_Download&PortalId=0&EntryId=538 [Accessed on 17 September 2015].

Chaiwang, P., Chalermsinsuwan, B. and Piumsomboon, P., 2016. Thermogravimetric analysis and chemical kinetics for regeneration of sodium and potassium carbonate solid sorbents. *Chemical Engineering Communications*, 203(5), pp.581-588.

Chapman, S. and Cowling, T.G., 1951. *The mathematical theory of non-uniform gases*. New York: Cambridge University Press.

Chen, C., Park, D.W. and Ahn, W.S., 2014. $CO_2$ capture using zeolite 13X repared from bentonite. *Applied Surface Science*, 292, pp.63-67.

Chen, S.J., Fu, Y., Huang, Y.X., Tao, Z.C. and Zhu, M., 2016. Experimental investigation of $CO_2$ separation by adsorption methods in natural gas purification. *Applied Energy*, 179, pp.329-337.

Choi, S., Drese, J.H. and Jones, C.W., 2009. Adsorbent materials for carbon dioxide capture from large anthropogenic point sources. *ChemSusChem*, 2(9), pp.796-854.

Chowdhury, P., Bikkina, C. and Gumma, S., 2009. Gas adsorption properties of the chromium-based metal organic framework MIL-101. *The Journal of Physical Chemistry C*, 113(16), pp.6616-6621.

Collins, J.J., 1967. The LUB/equilibrium section concept for fixed-bed adsorption. *Chemical Engineering Progress Symposium*, 63(74), pp.31-35.

Crittenden, B., Patton, A., Jouin, C., Perera, S., Tennison, S. and Echevarria, J., 2005. Carbon monoliths: A comparison with granular materials. *Adsorption*, 11(1), pp.537-541.

Crittenden, B.D. and Thomas, W.J., 1998. *Adsorption technology and design*. Oxford: Butterworth-Heinemann.

Cruciani, G., 2006. Zeolites upon heating: Factors governing their thermal stability and structural changes. *Journal of Physics and Chemistry of Solids*, 67(9–10), pp.1973-1994.

Deluca, J.P. and Campbell, L.L., 1977. Monolithic catalyst supports. *In*: Burton, J.J. and Garten, R.L., eds. *Advanced materials in catalysis*. New York; London: Academic Press.

Deublein, D. and Steinhauser, A. eds., 2008. *Biogas from waste and renewable resources: An introduction*. Weinheim: Wiley-VCH Verlag GmBH & Co. KGaA.

Dirkse, E.H.M., 2009. *Biogas upgrading using the DMT Carborex® PWS Technology* [online]. DMT Environmental Technology. Available from: www.dirkse-milieutechniek.com/dmt/do/download/_/true/210370/Biogas_upgrading_using_the_DMT_Carborex_PWS__Technology.__2009.pdf [Accessed on 8 March 2013].

Electrigaz Technologies Inc., 2008. *Feasibility study – Biogas upgrading and grid injection in the Fraser Valley, British Columbia* [online]. Swedish Biogas Centre. Available from: http://www.catalystpower.ca/pdf/fvf.pdf [Accessed on 1 January 2017].

EPRI, 2006. *Assessment of fuel gas cleanup systems for waste gas fueled power generation – 1012763* [online]. Palo Alto, California, United States of America: Electric Power Research Institute, Inc. (EPRI). Available from: http://www.epri.com/abstracts/Pages/ProductAbstract.aspx?ProductId=000000000001012763 [Accessed on 1 January 2017].

Ergun, S., 1952. Fluid flow through packed columns. *Chemical Engineering Progress*, 48(2), pp.89-94.

Esmaili, J. and Ehsani, M.R., 2014. Development of new potassium carbonate sorbent for $CO_2$ capture under real flue gas conditions. *Iranian Journal of Oil & Gas Science and Technology*, 3(3), pp.39-46.

Férey, G., Mellot-Draznieks, C., Serre, C., Millange, F., Dutour, J., Surblé, S. and Margiolaki, I., 2005. A chromium terephthalate-based solid with unusually large pore volumes and surface area. *Science*, 309(5743), pp.2040-2042.

Field, J.H., Johnson, G.E., Benson, H.E. and Tosh, J.S., 1960. *Removing hydrogen sulfide by hot potassium carbonate absorption*. United States Department of the Interior, Bureau of Mines.

Forzatti, P., Ballardini, D. and Sighicelli, L., 1998. Preparation and characterization of ceramic catalysts. *Catalysis Today*, 41(1-3), pp.87-94.

Froment, G.F., Bischoff, K.B. and Wilde, J.D., 2010. *Chemical reactor analysis and design*. 3rd ed. United States of America: John Wiley & Sons, Inc.

Garcia, S., Gil, M.V., Martin, C.F., Pis, J.J., Rubiera, F. and Pevida, C., 2011. Breakthrough adsorption study of a commercial activated carbon for pre-combustion $CO_2$ capture. *Chemical Engineering Journal*, 171(2), pp.549-556.

Gatehouse, B.M. and Lloyd, D.J., 1973. Crystal structure of anhydrous potassium carbonate. *Journal of the Chemical Society, Dalton Transactions*, pp.70-72.

Goetz, V., Pupier, O. and Guillot, A., 2006. Carbon dioxide-methane mixture adsorption on activated carbon. *Adsorption*, 12(1), pp.55-63.

Grande, C.A., 2011. Biogas upgrading by pressure swing adsorption. *In: Bernardes, M.A.D.S., ed. Biofuel's Engineering Process Technology*, Rijeka: InTech, pp.65-84.

Håkansson, A., 2006. *Preventing microbial growth on pall rings when upgrading biogas using absorption with water wash* [online]. Swedish Biogas Centre. Available from: http://www.sgc.se/ckfinder/userfiles/files/SGC166.pdf [Accessed on 1 January 2017].

Hamon, L., Serre, C., Devic, T., Loiseau, T., Millange, F., Férey, G.R. and Weireld, G.D., 2009. Comparative study of hydrogen sulfide adsorption in the MIL-53(Al, Cr, Fe), MIL-47(V), MIL-100(Cr), and MIL-101(Cr) metal−organic frameworks at room temperature. *Journal of the American Chemical Society*, 131(25), pp.8775-8777.

Hawthorn, R.D., 1974. Afterburner catalysts - effects of heat and mass transfer between gas and catalyst surface. *AIChE Symposium Series*, 70(137), pp.428-438.

Hofmann, D.J., Butler, J.H. and Tans, P.P., 2009. A new look at atmospheric carbon dioxide. *Atmospheric Environment*, 43(12), pp.2084-2086.

Hong, W.Y., Perera, S.P. and Burrows, A.D., 2015. Manufacturing of metal-organic framework monoliths and their application in $CO_2$ adsorption. *Microporous and Mesoporous Materials*, 214, pp.149-155.

Huang, C.Y., Song, M., Gu, Z.Y., Wang, H.F. and Yan, X.P., 2011. Probing the adsorption characteristic of metal–organic framework MIL-101 for volatile organic compounds by quartz crystal microbalance. *Environmental Science & Technology*, 45(10), pp.4490-4496.

IEA, 2015. *Upgrading plant lists – Dec 2015* [online]. International Energy Agency (IEA). Available from: http://www.iea-biogas.net/plant-list.html [Accessed on 1 January 2017].

Inglethorpe, S.D.J., Morgan, D.J., Highley, D.E. and Bloodworth, A.J., 1993. *Industrial Minerals Laboratory Manual: Bentonite*. BGS Technical Report WG/93/20 [online]. United Kingdom: British Geological Survey. Available from: http://www.bgs.ac.uk/research/international/dfid-kar/WG93020_col.pdf [Accessed on 11 June 2012].

IZA-SC, 2008. *Database of zeolite structures: Framework type HEU* [online]. Structure Commission of the International Zeolite Association. Available from: http://izasc.ethz.ch/fmi/xsl/IZA-SC/ftc_fw.xsl?-db=Atlas_main&-lay=fw&-max=25&STC=HEU&-find [Accessed on 7 September 2015].

Jiang, H., Zhao, B.Y. and Xie, Y.C., 2002. Influence of water on adsorption properties of lithium exchangedlow silica X zeolite. *ACTA PHYSICO-CHIMICA SINICA*, 18(7), pp.577-580.

Jo, S.B., Lee, S.C., Chae, H.J., Cho, M.S., Lee, J.B., Baek, J.I. and Kim, J.C., 2016. Regenerable potassium-based alumina sorbents prepared by $CO_2$ thermal treatment for post-combustion carbon dioxide capture. *Korean Journal of Chemical Engineering*, 33(11), pp.3207-3215.

Keller-II, G.E., Anderson, R.A. and Yon, C.M., 1987. Adsorption. In: Rousseau, R.W., ed. *Handbook of separation process technology*. New York; Chichester: Wiley, pp.644-696.

Khan, N.A., Kang, I.J., Seok, H.Y. and Jhung, S.H., 2011. Facile synthesis of nano-sized metal-organic frameworks, chromium-benzenedicarboxylate, MIL-101. *Chemical Engineering Journal*, 166(3), pp.1152-1157.

Khelifa, A., Hasnaoui, A., Derriche, Z. and Bengueddach, A., 2001. Adsorption of carbon dioxide by X zeolites exchanged with bivalent cations. *Annales de Chimie Science des Matériaux*, 26(2), pp.55-66.

Kim, J.B., 2003. $Li^+$- and $H^+$-exchanged low silica X zeolite as selective nitrogen adsorbent for air separation. *Bulletin of the Korean Chemical Society*, 24(12), pp.1814-1818.

Kovach, J.L., 1988. Gas-phase adsorption. *In*: Schweitzer, P.A., ed. *Handbook of separation techniques for chemical engineers*. 2nd ed. New York; London: McGraw-Hill.

Küsgens, P., Rose, M., Senkovska, I., Fröde, H., Henschel, A., Siegle S. and Kaskel, S., 2009. Characterisation of metal-organic frameworks by water adsorption. *Microporous and Mesoporous Materials*, 120, pp.325-330.

Lee, J.B., Ryu, C.K., Baek, J.I., Lee, J.H., Eom, T.H. and Kim, S.H., 2008. Sodium-based dry regenerable sorbent for carbon dioxide capture from power plant flue gas. *Industrial & Engineering Chemistry Research*, 47(13), pp.4465-4472.

Lee, L.Y., 1997. *Control of volatile organic chemical emissions by adsorption onto hydrophobic and organophilic adsorbents*. Thesis (PhD), University of Bath, Bath, United Kingdom.

Lee, S.C., Choi, B.Y., Ryu, C.K., Ahn, Y.S., Lee, T.J. and Kim, J.C., 2006. The effect of water on the activation and the $CO_2$ capture capacities of alkali metal-based sorbents. *Korean Journal of Chemical Engineering*, 23(3), pp.374-379.

Levenspiel, O., 1999. *Chemical reaction engineering*. 3rd ed. New York: John Wiley & Sons, Inc.

Li, C.Y. and Rees, L.V.C., 1986. The thermal stability of faujasites with different Si/Al ratios. *ZEOLITES*, 6(1), pp.60-65.

Li, G., Singh, R., Li, D., Zhao, C., Liu, L. and Webley, P.A., 2009. Synthesis of biomorphic zeolite honeycomb monoliths with 16 000 cells per square inch. *Journal of Materials Chemistry*, 19(44), pp.8372-8377.

Li, G., Xiao, P., Webley, P., Zhang, J., Singh, R. and Marshall, M., 2008. Capture of $CO_2$ from high humidity flue gas by vacuum swing adsorption with zeolite 13X. *Adsorption*, 14(2-3), pp.415-422.

Li, Y., Yi, H., Tang, X., Li, F. and Yuan, Q., 2013. Adsorption separation of $CO_2/CH_4$ gas mixture on the commercial zeolites at atmospheric pressure. *Chemical Engineering Journal*, 229, pp.50-56.

Li, Y.Y., 1998. *Air separation with monolithic adsorbents*. Thesis (PhD), University of Bath, Bath, United Kingdom.

Liabastre, A.A. and Orr, C., 1978. An evaluation of pore structure by mercury penetration. *Journal of Colloid and Interface Science*, 64(1), pp.1-18.

Liang, Y., Harrison, D.P., Gupta, R.P., Green, D.A. and McMichael, W.J., 2004. Carbon dioxide capture using sodium-based sorbents. *Energy & Fuels*, 18(2), pp.569-575.

Liang, Z., Marshall, M., Ng, C.H. and Chaffee, A.L., 2013. Comparison of conventional and HF-free-synthesized MIL-101 for $CO_2$ adsorption separation and their water stabilities. *Energy & Fuels*, 27(12), pp.7612-7618.

Liu, D., Yi, H., Tang, X., Zhao, S., Wang, Z., Gao, F., Li, Q. and Zhao, B., 2016. Adsorption separation of $CO_2/CH_4$ gas mixture on carbon molecular sieves modified by potassium carbonate. *Journal of Chemical & Engineering Data*, 61(7), pp.2197-2201.

Liu, Q., Ning, L., Zheng, S., Tao, M., Shi, Y. and He, Y., 2013. Adsorption of carbon dioxide by MIL-101(Cr): Regeneration conditions and influence of flue gas contaminants. *Scientific Reports 3*, 2916, pp.1-6.

Llewellyn, P.L., Bourrelly, S., Serre, C., Vimont, A., Daturi, M., Hamon, L., Weireld, G.D., Chang, J.S., Hong, D.Y., Hwang, Y.K., Jhung, S.H. and Férey, G., 2008. High uptakes of $CO_2$ and $CH_4$ in mesoporous metal-organic frameworks MIL-100 and MIL-101. *Langmuir*, 24(14), pp.7245-7250.

Makaruk, A., Miltner, M. and Harasek, M., 2010. Membrane upgrading processes for the production of natural gas substitute. *Separation and Purification Technology*, 74(1), pp.83-92.

Mansouri, N., Rikhtegar, N., Panahi, H.A., Atabi, F. and Shahraki, B.K., 2013. Porosity, characterization and structural properties of natural zeolite – clinoptilolite – as a sorbent. *Environmental Protection Engineering*, 39(1), pp.139-152.

McCabe, W.L., Smith, J.C. and Harriott, P., 2005. Adsorption and fixed-bed separation. *In*: *Unit operations of chemical engineering*. 7th ed. Boston; London: McGraw-Hill, pp.836-863.

Melo, D.M.A., de Souza, J.R., Melo, M.A.F., Martinelli, A.E., Cachima, G.H.B. and Cunha, J.D., 2006. Evaluation of the zinox and zeolite materials as adsorbents to remove $H_2S$ from natural gas. *Colloids and Surfaces A: Physicochemical and Engineering Aspects*, 272(1–2), pp.32-36.

Millward, A.R. and Yaghi, O.M., 2005. Metal−organic frameworks with exceptionally high capacity for storage of carbon dioxide at room temperature. *Journal of the American Chemical Society*, 127(51), pp.17998-17999.

Mishra, D., 2004. IR X-ray and thermal studies zeolite-13X zeolite and its Mn(II) and Zn(II) exchange and adsorbed derivatives. *Studies in Surface Science and Catalysis*, 154, pp.1693-1699.

Mishra, D., 2007. Exploration studies on Na-13X zeolite and its derivatives for environmental protection. *Journal of Environmental Research and Development*, 1(4), pp.365-368.

Mofarahi, M. and Gholipour, F., 2014. Gas adsorption separation of $CO_2/CH_4$ system using zeolite 5A. *Microporous and Mesoporous Materials*, 200, pp.1-10.

Monazam, E.R., Spenik, J. and Shadle, L.J., 2013. Fluid bed adsorption of carbon dioxide on immobilized polyethylenimine (PEI): Kinetic analysis and breakthrough behaviour. *Chemical Engineering Journal*, 223, pp.795-805.

Mulgundmath, V. and Tezel, F.H., 2010. Optimisation of carbon dioxide recovery from flue gas in a TPSA system. *Adsorption*, 16(6), pp.587-598.

Mulgundmath, V.P., Tezel, F.H., Saatcioglu, T. and Golden, T.C., 2012. Adsorption and separation of $CO_2/N_2$ and $CO_2/CH_4$ by 13X zeolite. *The Canadian Journal of Chemical Engineering*, 90(3), pp.730-738.

Munusamy, K., Sethia, G., Patil, D.V., Rallapalli, P.B.S., Somani, R.S. and Bajaj, H.C., 2012. Sorption of carbon dioxide, methane, nitrogen and carbon monoxide on MIL-101(Cr): Volumetric measurements and dynamic adsorption studies. *Chemical Engineering Journal*, 195–196, pp.359-368.

Murray, H.H., 2012. Clays. *In*: *Ullmann's Encyclopedia of Industrial Chemistry* [online]. Weinheim: Wiley-VCH Verlag GmbH & Co. KGaA. Available from: http://onlinelibrary.wiley.com/doi/10.1002/14356007.a07_109.pub2/pdf [Accessed on 12 January 2012].

Navigant Research, 2016. *Navigant Research release key findings on global biogas* [online]. Navigant Research. Available from: http://www.renewableenergyfocus.com/view/44173/navigant-research-release-key-findings-on-global-biogas-market/ [Accessed on 28 June 2016].

Newcamp, J., 2002. *Bluff body aerodynamics and flow separation* [online]. United States of America: California State University, Los Angeles. Available from: http://instructional1.calstatela.edu/cwu/me413/examplereport.pdf [Accessed on 6 December 2015].

Pakseresht, S., Kazemeini, M. and Akbarnejad, M.M., 2002. Equilibrium isotherms for CO, $CO_2$, $CH_4$ and $C_2H_4$ on the 5A molecular sieve by a simple volumetric apparatus. *Separation and Purification Technology*, 28(1), pp.53-60.

Panezai, H., Fan, M., Sun, J., Bai, S. and Wu, X., 2016. Influence of $Ca^{2+}$ or $Na^{+}$ extraframework cations on the thermal dehydration and related kinetic performance of LSX zeolite. *Journal of Physics and Chemistry of Solids*, 99, pp.1-10.

Park, S.W., Sung, D.H., Choi, B.S., Oh, K.J. and Moon, K.H., 2006. Sorption of carbon dioxide onto sodium carbonate. *Separation Science and Technology*, 41(12), pp.2665-2684.

Patterson, T., Esteves, S., Dinsdale, R. and Guwy, A., 2011. An evaluation of the policy and techno-economic factors affecting the potential for biogas upgrading for transport fuel use in the UK. *Energy Policy*, 39(3), pp.1806-1816.

Patton, A., Crittenden, B.D. and Perera, S.P., 2004. Use of the linear driving force approximation to guide the design of monolithic adsorbents. *Chemical Engineering Research and Design*, 82(8), pp.999-1009.

Persson, M., Jönsson, O. and Wellinger, A., 2006. Biogas upgrading to vehicle fuel standards and grid injection. *Task 37: Energy from biogas and landfill gas* [online]. IEA Bioenergy. Available from: http://www.iea-biogas.net/_download/publi-task37/upgrading_report_final.pdf [Accessed on 16 June 2012].

Petersson, A. and Wellinger, A., 2009. Biogas upgrading technologies – developments and innovations. *Task 37: Energy from biogas and landfill gas* [online]. IEA Bioenergy. Available from: http://www.iea-biogas.net/_download/publi-task37/upgrading_rz_low_final.pdf [Accessed on 16 June 2012].

Poling, B.E., Thomson, G.H., Friend, D.G., Rowley, R.L. and Wilding, W.V., 2008. Physical and chemical data. *In*: Green, D.W. and Perry, R.H., eds. *Perry's chemical engineers' handbook*. 8th ed. New York: McGraw-Hill, pp.2-1–2-517.

Pollard, W.G. and Present, R.D., 1948. On gaseous self-diffusion in long capillary tubes. *Physical Review*, 73(7), pp.762-774.

PubChem, 2015a. *Potassium bicarbonate* [online]. National Center for Biotechnology Information. PubChem Compund Database; CID = 516893. Available from: http://pubchem.ncbi.nlm.nih.gov/compound/Potassium_bicarbonate#section=Top [Accessed on 17 September 2015].

PubChem, 2015b. *Sodium bicarbonate* [online]. National Center for Biotechnology Information. PubChem Compund Database; CID = 516892. Available from: http://pubchem.ncbi.nlm.nih.gov/compound/sodium_bicarbonate#section=Top [Accessed on 17 September 2015].

Reynolds, J.P., Jeris, J.S. and Theodore, L., 2002. Adsorption. *In: Handbook of chemical and environmental engineering calculations.* New York: John Wiley & Sons, pp.414-437.

Rezaei, F. and Webley, P., 2009. Optimum structured adsorbents for gas separation processes. *Chemical Engineering Science*, 64(24), pp.5182-5191.

Rezaei, F. and Webley, P., 2010. Structured adsorbents in gas separation processes. *Separation and Purification Technology*, 70(3), pp.243-256.

Richardson, J.F., Harker, J.H. and Backhurst, J.R., 2002. *Coulson and Richardson's chemical engineering. Volume 2, particle technology and separation processes*. 5th ed. Oxford: Butterworth-Heinemann.

Rios, R.B., Stragliotto, F.M., Peixoto, H.R., Torres, A.E.B., Bastos-Neto, M., Azevedo, D.C.S. and Cavalcante Jr., C.L., 2013. Studies on the adsorption behaviour of $CO_2$-$CH_4$ mixtures using activated carbon. *Brazilian Journal of Chemical Engineering*, 30(4), pp.939-951.

Roland, E. and Kleinschmit, P., 2012. Zeolites. *In*: *Ullmann's Encyclopedia of Industrial Chemistry* [online]. Weinheim: Wiley-VCH Verlag GmbH & Co. KGaA. Available from: http://onlinelibrary.wiley.com/doi/10.1002/14356007.a28_475/pdf [Accessed on 12 January 2012].

Rootare, H.M. and Prenzlow, C.F., 1967. Surface areas from mercury porosimeter measurements. *The Journal of Physical Chemistry*, 71(8), pp.2733-2736.

Rouquerol, F., Rouquerol, J. and Sing, K.S.W., 1999. *Adsorption by powders and porous solids: Principles, methodology, and applications*. San Diego: Academic Press.

Ruthven, D.M., 1984. *Principles of adsorption and adsorption processes*. New York: John-Wiley & Sons, Inc.

Ruthven, D.M., 2005. Adsorption. *In*: *Kirk-Othmer Encyclopedia of Chemical Technology* [online]. John Wiley & Sons, Inc. Available from: http://onlinelibrary.wiley.com/doi/10.1002/0471238961.0104191518212008.a01.pub2/pdf [Accessed 11 January 2012].

Ryan, W., 1978. *Properties of ceramic raw materials*. 2nd ed. London: Pergamon Press Ltd.

Ryckebosch, E., Drouillon, M. and Vervaeren, H., 2011. Techniques for transformation of biogas to biomethane. *Biomass and Bioenergy*, 35(5), pp.1633-1645.

Salmasi, M., Fatemi, S., Rad, M.D. and Jadidi, F., 2013. Study of carbon dioxide and methane equilibrium adsorption on silicoaluminophosphate-34 zeotype and T-type zeolite as adsorbent. *International Jounral of Environmental Science and Technology*, 10(5), pp.1067-1074.

Samanta, A., Zhao, A., Shimizu, G.K.H., Sarkar, P. and Gupta, R., 2011. Post-combustion $CO_2$ capture using solid sorbents: A review. *Industrial & Engineering Chemistry Research*, 51(4), pp.1438-1463.

Sanabria, N.R., Ávila, P., Yates, M., Rasmussen, S.B., Molina, R. and Moreno, S., 2010. Mechanical and textural properties of extruded materials manufactured with AlFe and AlCeFe pillared bentonites. *Applied Clay Science*, 37(3), pp.283-289.

Sarikaya, Y., Önal, M., Baran, B. and Alemdaroğlu, T., 2000. The effect of thermal treatment on some of the physicochemical properties of a bentonite. *Clays and Clay Minerals*, 48(5), pp.557-562.

Sawin, J.L., Seyboth, K., Sverrisson, F., Appawou, F., Brown, A., Epp, B., Leidreiter, A., Lins, C., Murdock, H.E., Musolino, E., Petrichenko, K., Farrell, T.C., Krader, T.T., Tsakiris, A., Skeen, J. and Savacool, B., 2016. *Renewables 2016 Global Status Report – Key Findings* [online]. France: REN21. Available from: http://www.ren21.net/wp-content/uploads/2016/06/GSR_2016_KeyFindings1.pdf [Accessed on 28 June 2016].

Sayari, A., Belmabkhout, Y. and Serna-Guerrero, R., 2011. Flue gas treatment via $CO_2$ adsorption. *Chemical Engineering Journal*, 171(3), pp.760-774.

Seader, J.D. and Henley, E.J., 1998. *Separation process principles*. New York; Chichester: John Wiley.

SEAI, 2012. *Upgrading biogas to biomethane* [online]. Ireland: Sustainable Energy Authority of Ireland (SEAI). Available from: http://www.seai.ie/Publications/Renewables_Publications/Upgrading_Biogas_to_Biomethane.pdf [Accessed on 6 April 2012].

Sircar, S., Golden, T.C. and Rao, M.B., 1996. Activated carbon for gas separation and storage. *Carbon*, 34(1), pp.1-12.

Sircar, S. and Myers, A.L., 2003. Gas separation by zeolite. *In*: Auerbach, S.M., Carrado, K.A. and Dutta, P.K., eds. *Handbook of zeolite science and technology*. New York: Marcel Dekker, pp.1063-1104.

Siriwardane, R.V., Shen, M.S., Fisher, E.P. and Poston, J.A., 2001. Adsorption of $CO_2$ on molecular sieves and activated carbon. *Energy & Fuels*, 15(2), pp.279-284.

Siriwardane, R.V., Shen, M.S. and Fisher, E.P., 2003. Adsorption of $CO_2$, $N_2$, and $O_2$ on natural zeolites. *Energy & Fuels*, 17(3), pp.571-576.

Sokolova, N.A. and Kazanskii, V.B., 2005. Diffusion of ethane-hydrogen mixtures in LiLSX and CaA zeolites studied by diffuse reflectance IR spectroscopy. *Kinetics and Catalysis*, 46(6), pp.879-883.

Stuckert, N.R. and Yang, R.T., 2011. $CO_2$ capture from the atmosphere and simultaneous concentration using zeolites and amine-grafted SBA-15. *Environmental Science & Technology*, 45(23), pp.10257-10264.

Sun, Q., Li, H., Yan, J., Liu, L., Yu, Z. and Yu, X., 2015. Selection of appropriate biogas upgrading technology-a review of biogas cleaning, upgrading and utilisation. *Renewable and Sustainable Energy Reviews*, 51, pp.521-532.

Tobi, 2009. *Biogas use in developing countries and the UK* [online]. Centre for Alternative Technology. Available from: http://www.transitioncitylancester.org/groups/largescaleenergy/biogas/Biogas.pdf [Accessed on 16 June 2012].

Todd, R.S., 2003. *A theoretical and experimental study of a rapid pressure swing adsorption system for air separation*. Thesis (PhD), Monash University, Melbourne, Australia.

Veselovskaya, J., Derevschikov, V.S., Kardash, T.Y. and Okunev, A.G., 2015. Direct $CO_2$ capture from ambient air by $K_2CO_3$/alumina composite sorbent for synthesis of renewable methane. *Renewable Bioresources*, 3(1), pp.1-7.

Verboekend, D., Keller, T.C., Milina, M., Hauert, R. and Pérez-Ramírez, T., 2013. Hierarchy brings function: Mesoporous clinoptilolite and L zeolite catalysts synthesized by tandem acid-base treatments. *Chemistry of Materials*, 25(9), pp.1947-1959.

Wakao, N. and Funazkri, T., 1978. Effect of fluid dispersion coefficients on particle-to-fluid mass transfer coefficients in packed beds: Correlation of sherwood numbers. *Chemical Engineering Science*, 33(10), pp.1375-1384.

Wakao, N. and Smith, J.M., 1962. Diffusion in catalyst pellets. *Chemical Engineering Science*, 17(11), pp.825-834.

Wang, D.M., 2008. *Breakthrough behaviour of $H_2S$ removal with an iron oxide based CG-4 adsorbent in a fixed-bed reactor*. Thesis (MSc), University of Saskatchewan, Saskatoon, Canada.

Ward, R.L. and McKague, H.L., 1994. Clinoptilolite and heulandite structural differences as revealed by multinuclear nuclear magnetic resonance spectroscopy. *The Journal of Physical Chemistry*, 98(4), pp.1232-1237.

Washburn, E.W., 1921. The dynamics of capillary flow. *Physical Review*, 17(3), pp.273-283.

Weber, H., Grave, I.D. and Röhrl, E., 2012. Foamed plastic. *In*: *Ullmann's Encyclopedia of Industrial Chemistry* [online]. Weinheim: Wiley-VCH Verlag GmbH & Co. KGaA. Available from: http://onlinelibrary.wiley.com/doi/10.1002/14356007.a11_435/pdf [Accessed 12 January 2012].

Wellinger, A. and Lindberg, A., 2001. Biogas upgrading and utilisation. *Task 24: Energy from biological conversion of organic waste* [online]. IEA Bioenergy. Available from: http://www.iea-biogas.net/_download/publi-task37/Biogas%20upgrading.pdf [Accessed on 28 September 2011].

Welty, J., Wicks, C.E., Rorrer, G.L. and Wilson, R.E., 2007. *Fundamentals of momentum, heat and mass transfer*. London: Wiley-VCH.

Yang, R.T., 1997. *Gas separation by adsorption processes*. London: Imperial College Press.

Yaşyerli, S., Ar, İ., Doğu, G. and Doğu, T., 2002. Removal of hydrogen sulfide by clinoptilolite in a fixed bed adsorber. *Chemical Engineering and Processing: Process Intensification*, 41(9), pp.785-792.

Yates, M., Martin-Luengo, M.A., Vega Argomaniz, L. and Nogales Velasco, S., 2012. Design of activated carbon-clay composites for effluent decontamination. *Microporous and Mesoporous Materials*, 154, pp.87-92.

Yi, C.K., Jo, S.H., Seo, Y., Lee, J.B. and Ryu, C.K., 2007. Continuous operation of the potassium-based dry sorbent $CO_2$ capture process with two fluidized-bed reactors. *International Journal of Greenhouse Gas Control*, 1(1), pp.31-36.

Yon, C.M. and Sherman, J.D., 2003. Adsorption, Gas separation. *In*: *Kirk-Othmer Encyclopedia of Chemical Technology* [online]. John Wiley & Sons, Inc. Available from: http://onlinelibrary.wiley.com/doi/10.1002/0471238961.0104191519080518.a01.pub2/pdf [Accessed 11 January 2012].

Zeochem, 2008. *Molecular sieve Z01-02 for air prepurification* [online]. Switzerland: Zeochem AG. Available from: http://www.zeochem.ch/information/pdfs/Purification%20of%20hydrocarbon%20streams%20with%20Z10-03.pdf [Accessed on 29 February 2012].

Zhang, Y., Su, W., Sun, Y., Liu, J., Liu, X. and Wang, X., 2015. Adsorption equilibrium of $N_2$, $CH_4$, and $CO_2$ on MIL-101. *Journal of Chemical & Engineering Data*, 60(10), pp.2951-2957.

Zhang, Z., Huang, S., Xian, S., Xi, H. and Li, Z., 2011. Adsorption equilibrium and kinetics of $CO_2$ on chromium terephthalate MIL-101. *Energy & Fuels*, 25(2), pp.835-842.

# Appendices

## Appendix 1: Results from Blank Tests

The blank test for the simultaneous TGA and DSC analysis was carried out using an empty alumina crucible under heated air from 20 °C to 900 °C at a rate of 10 °C $min^{-1}$. All the TGA and DSC curves provided in the thesis have been corrected with this blank test data. Figure A.1 below shows the TG and DSC curves for an empty alumina crucible.

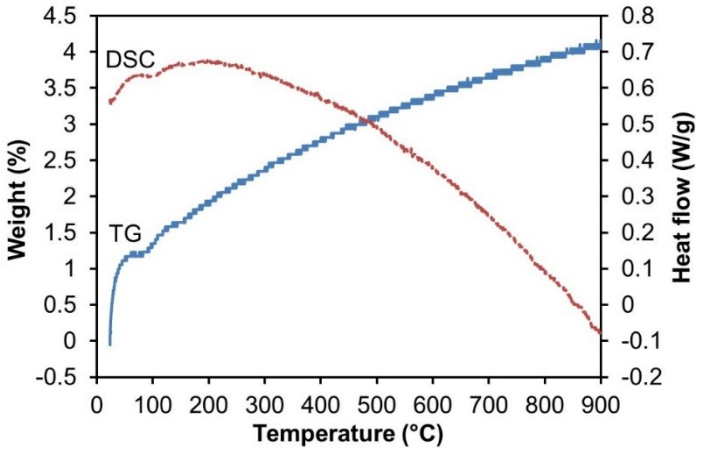


**Figure A.1** The TG and DSC curves for an empty alumina crucible.

For the MIP analysis, all the MIP results provided in the thesis have been corrected with the blank data (i.e. using an empty penetrometer) automatically by the MIP machine. Figure A.2 below shows the pore size distribution of an empty penetrometer used in the MIP tests.

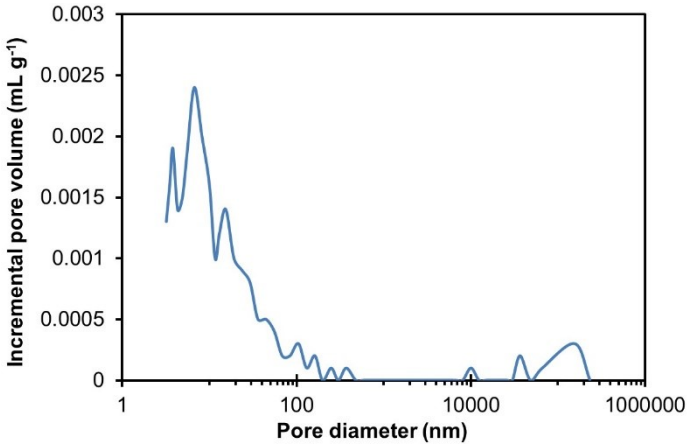


**Figure A.2** The pore size distribution of an empty penetrometer.

# Appendix 2: Calculations of Adsorption Properties for Single and Mixed Gases

The calculations employed in this study for single gas ($CO_2$, $CH_4$ or $H_2S$) adsorption and mixed gases ($CO_2/CH_4$ or $CO_2/CH_4/H_2O$ vapour) adsorption are shown by the following example calculations.

**Example 1:** Consider that a 75% wt. 13X zeolite monolith (Sample 2) was challenged with 40% vol. $CO_2$ that flows at a rate of 500 mL min$^{-1}$ at 2 bar and 20 °C. The bed length, $L$, was 10 cm and the bed diameter, $D$, was 21.47 mm. It has a bed mass of about 31.5 g. A portion of its experimental data was provided in Table A.1 and the sample's adsorption breakthrough curve was presented in Figure A.3. The molecular mass, $M_w$, of $CO_2$ is 44.01 g mol$^{-1}$.

**Calculations for Example 1:**

The adsorbent mass, $m_{ad}$, of the sample is: 31.5 g × 0.75 = 23.6 g

The bed volume, $V_{bed}$, was: $\frac{\pi D^2 L}{4} = \frac{\pi(2.147\text{ cm})^2(10\text{ cm})}{4}$ = 36.2 cm$^3$

According to the ideal gas law, $PV = nR_gT$ where $P$ is pressure (bar), $V$ is volume (m$^3$), $n$ is number of moles (mol), $R_g$ is Universal gas constant (≈ 8.314 × 10$^{-5}$ m$^3$ bar mol$^{-1}$ K$^{-1}$) and $T$ is temperature (K). Re-arranging the ideal gas law equation gives: $C_0 = \frac{n}{V} = \frac{P}{R_gT}$

In this case, $P$ = 2 bar and $T$ = 20 °C + 273.15 = 293.15 K.

Then, the influent gas concentration, $C_0$, in g m$^{-3}$ was:

$$C_0 = \frac{0.4\times44.01\text{ g mol}^{-1}\times 2\text{ bar}}{8.314\times10^{-5}\text{ m}^3\text{ bar mol}^{-1}\text{ K}^{-1}\times293.15\text{ K}} = 1\,444.58\text{ g m}^{-3}$$

Since the gas pressure in the adsorption column was 2 bar and the outlet gas pressure was 1 bar. The actual gas flow rate, $Q$, was:

$$\frac{\text{Flow rate}\times P_{out}}{P_{column}} = \frac{500\text{ mL min}^{-1}\times1\text{ bar}}{2\text{ bar}}\left|\frac{1\text{ m}^3}{10^6\text{ mL}}\right|\left|\frac{1\text{ min}}{60\text{ s}}\right| = 4.17\times10^{-6}\text{ m}^3\text{ s}^{-1}$$

Then, the molar gas flow rate, $\hat{Q}$, was:

$$\hat{Q} = \frac{QC_0}{M_w} = \frac{4.17\times10^{-6}\text{ m}^3\text{ s}^{-1}\times1\,444.58\text{ g m}^{-3}}{44.01\text{ g mol}^{-1}\left|\frac{1\text{ mol}}{1\,000\text{ mmol}}\right|} = 0.137\text{ mmol s}^{-1}$$

From its breakthrough curve (Figure A.3), the breakthrough time, $t_b$, was 112 s and the equilibrium time, $t_e$, was 2 237 s.

As mentioned previously (refer Section 2.2.1.1 of Chapter 2), the breakthrough adsorption capacity, $\bar{q}_b$, is represented by the area above the breakthrough curve from $t = 0$ to $t = t_b$ (i.e., Area $A$) and the equilibrium adsorption capacity, $\bar{q}_e$, is represented by the area above the breakthrough curve from $t = 0$ to $t = t_e$ (i.e., Areas $A$ and $B$). Both areas under the curve were estimated using the trapezoidal rule and its example calculation are shown in

Table A.1. It was estimated that the total area under the curve at breakthrough was about 22 s and the total area under the curve at equilibrium was about 1 891 s.

This means the area under the curve between breakthrough and equilibrium was about: 1 891 s – 22 s = 1 869 s.

**Table A.1** A portion of the sample data.

| Time | Effluent gas concentration | | Area under the curve between $t_n$ and $t_{n-1}$ |
|---|---|---|---|
| $t$ (s) | $C$ (% vol.) | $\frac{C}{C_0}$ | $A_{(t_n \, to \, t_{n-1})}$ (s) |
| $t_1$ | $C_1$ | $\frac{C_1}{C_0}$ | 0 |
| $t_2$ | $C_2$ | $\frac{C_2}{C_0}$ | $0.5(t_2 - t_1)\left[\left(\frac{C}{C_0}\right)_1 + \left(\frac{C}{C_0}\right)_2\right]$ |
| $t_n$ | $C_n$ | $\frac{C_n}{C_0}$ | $0.5(t_n - t_{n-1})\left[\left(\frac{C}{C_0}\right)_{n-1} + \left(\frac{C}{C_0}\right)_n\right]$ |
| 5 | 39.40 | 0.985 | 0.988 |
| 6 | 39.04 | 0.976 | 0.981 |

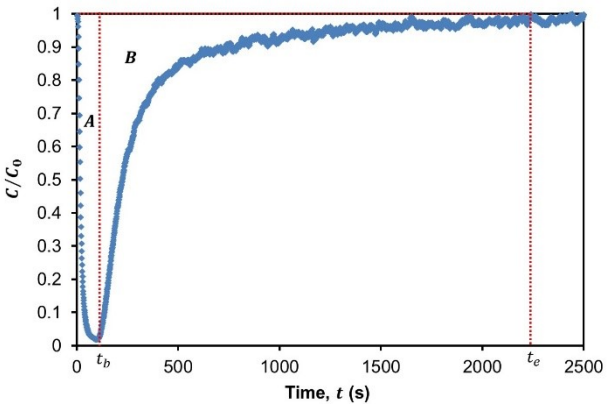


**Figure A.3** Adsorption of 40% vol. $CO_2$ on a 75% wt. 13X zeolite monolith at 2 bar with a feed gas flowing at 500 mL $min^{-1}$.

Equation 2.4 was used to calculate the breakthrough adsorption capacity, $\bar{q}_b$:

$$\bar{q}_b = \frac{\hat{Q}}{m_{ad}}\left(t_b - \sum_{t=0}^{t=t_b}\frac{C}{C_0}dt\right) \tag{2.4}$$

The term $\left(\sum_{t=0}^{t=t_b}\frac{C}{C_0}dt\right)$ on the right side of the equation represents the total area under the curve at breakthrough. The volumetric breakthrough adsorption capacity can be calculated by replacing $m_{ad}$ with $V_{bed}$ in equation 2.4. In this example,

$$\bar{q}_b = \frac{0.137 \text{ mmol s}^{-1}}{23.6 \text{ g}}(112 \text{ s} - 22 \text{ s}) = 0.52 \text{ mmol g}^{-1}$$

or, in volumetric capacities, $\bar{q}_b = \frac{0.137 \text{ mmol s}^{-1}}{36.2 \text{ cm}^3}(112 \text{ s} - 22 \text{ s}) = 0.34 \text{ mmol cm}^{-3}$

The equilibrium adsorption capacity, $\bar{q}_e$, was calculated using equation 2.5:

$$\bar{q}_e = \frac{\hat{Q}}{m_{ad}}\left(t_e - \sum_{t=0}^{t=t_e}\frac{C}{C_0}dt\right) \tag{2.5}$$

The term ($\sum_{t=0}^{t=t_e} \frac{C}{C_0} dt$) on the right side of the equation represents the total area under the curve at equilibrium. Similarly, the volumetric equilibrium adsorption capacity can be calculated by replacing $m_{ad}$ with $V_{bed}$ in equation 2.5. In this example,

$$\bar{q}_e = \frac{0.137 \text{ mmol s}^{-1}}{23.6 \text{ g}} (2\,237 \text{ s} - 1\,891 \text{ s}) = 2.01 \text{ mmol g}^{-1}$$

or, in volumetric capacities, $\bar{q}_b = \frac{0.137 \text{ mmol s}^{-1}}{36.2 \text{ cm}^3} (2\,237 \text{ s} - 1\,891 \text{ s}) = 1.31 \text{ mmol cm}^{-3}$

The stoichiometric time, $t_s$, was estimated by subtracting $t_e$ with the area under the curve between breakthrough and equilibrium: $t_s = 2\,237 \text{ s} - 1\,869 \text{ s} = 368 \text{ s}$

Knowing the values of $L$, $t_b$ and $t_s$, the length of unused bed, $LUB$, can be calculated using equation 2.8 (refer Section 2.2.1.3 of Chapter 2).

$$LUB = L\left(\frac{t_s - t_b}{t_s}\right) \quad (2.8)$$

$$LUB = 10 \text{ cm}\left(\frac{368 \text{ s} - 112 \text{ s}}{368 \text{ s}}\right) = 7 \text{ cm}$$

The length of equilibrium section, $LES$, can be determined using equation 2.7 by assuming that the adsorbent bed consists of equilibrium section and unused bed.

$$LES = L - LUB \quad (2.7)$$

$$LES = 10 \text{ cm} - 7 \text{ cm} = 3 \text{ cm}$$

Then, the effectiveness of adsorbent bed utilisation, $\varpi_{bed}$, can be estimated using equation 2.9:

$$\varpi_{bed} = \frac{LES}{L} \times 100\% \quad (2.9)$$

$$\varpi_{bed} = \frac{3 \text{ cm}}{10 \text{ cm}} \times 100\% = 30\%$$

Next, the mass transfer zone length, $L_{MTZ}$, was determined using equation 2.10 (refer Section 2.2.1.4 of Chapter 2).

$$L_{MTZ} = L\left(\frac{t_e - t_b}{t_e}\right) \quad (2.10)$$

$$L_{MTZ} = 10 \text{ cm}\left(\frac{2\,237 \text{ s} - 112 \text{ s}}{2\,237 \text{ s}}\right) = 9.5 \text{ cm}$$

Knowing the value of $L_{MTZ}$, the mass transfer zone velocity, $u_{MTZ}$, can be calculated using equation 2.11:

$$u_{MTZ} = \frac{L_{MTZ}}{(t_e - t_b)} \quad (2.11)$$

$$u_{MTZ} = \frac{9.5 \text{ cm}}{(2\,237 \text{ s} - 112 \text{ s})\left|\frac{1 \text{ min}}{60 \text{ s}}\right|} = 0.27 \text{ cm min}^{-1}$$

And, the percentage length of mass transfer zone in the adsorbent bed, $\bar{L}_{MTZ}$, was calculated using equation 2.12:

$$\bar{L}_{MTZ} = \frac{L_{MTZ}}{L} \times 100\% \quad (2.12)$$

$$\bar{L}_{MTZ} = \frac{9.5\text{ cm}}{10\text{ cm}} \times 100\% = 95\%$$

Note: The calculations used for $CH_4$ and $H_2S$ adsorption were the same as that shown in Example 1. The $M_w$ value need to change to the respective molecular mass of the adsorbate gas considered in the calculations. The molecular masses of $CH_4$ and $H_2S$ were 16.04 g mol$^{-1}$ and 34.08 g mol$^{-1}$, respectively.

**Example 2:** Consider that a 75% wt. 13X zeolite monolith (Sample 2) was challenged with 40% vol. $CO_2$ and 60% vol. $CH_4$ mixed gases that flows at a rate of 500 mL min$^{-1}$ at 2 bar and 20 °C. The bed length, $L$, was 20 cm and the bed diameter, $D$, was 21.47 mm. It has a bed mass of about 50.7 g.

**Calculations for Example 2:**

The experimental data for $CO_2$ and $CH_4$ adsorption on a 13X zeolite monolith was evaluated separately using the same calculations as that shown in Example 1 to determine their $\bar{q}_b$ and $\bar{q}_e$. In this case, it was found that $\bar{q}_{b,\mathrm{CO_2}}$ was 1.11 mmol g$^{-1}$, $\bar{q}_{e,\mathrm{CO_2}}$ was 2.29 mmol g$^{-1}$, $\bar{q}_{b,\mathrm{CH_4}}$ was 0.05 mmol g$^{-1}$ and $\bar{q}_{e,\mathrm{CH_4}}$ was 0.15 mmol g$^{-1}$.

Their $t_b$ and $t_e$ were determined directly from their breakthrough curves. It was found that $t_b$ and $t_e$ for $CO_2$ adsorption were 311 s and 2 582 s, respectively, and those for $CH_4$ adsorption were 28 s and 78 s, respectively.

The selectivity of $CO_2$ over $CH_4$, $\alpha_{CO_2/CH_4}$, was calculated using equation 2.6 (refer Section 2.2.1.2 of Chapter 2). Given that the mole fractions of $CO_2$ and $CH_4$ in the gas phase, $y_{CO_2}$ and $y_{CH_4}$, were 0.4 and 0.6, respectively.

$$\alpha_{CO_2/CH_4} = \frac{\left(\bar{q}_{e,\mathrm{CO_2}}/y_{CO_2}\right)}{\left(\bar{q}_{e,\mathrm{CH_4}}/y_{CH_4}\right)} \qquad (2.6)$$

$$\alpha_{CO_2/CH_4} = \frac{\left(2.29\text{ mmol g}^{-1}/0.4\right)}{\left(0.15\text{ mmol g}^{-1}/0.6\right)} = 22.9$$

Note: The calculations used for $CO_2/CH_4/H_2O$ vapour mixed gas adsorption were the same as that shown in Example 2.

# Appendix 3: Calculations of Physical Properties for $CO_2$ and $CH_4$ Mixture

The calculations of physical properties for 40% vol. $CO_2$ and 60% vol. $CH_4$ mixture are shown below. Given that $CO_2$ has a density of 1.93 kg $m^{-3}$ and a dynamic viscosity of 1.46 × $10^{-5}$ N s $m^{-2}$ while $CH_4$ has a density of 0.67 kg $m^{-3}$ and a dynamic viscosity of 1.10 × $10^{-5}$ N s $m^{-2}$ at 20 °C and 1 bar. The critical temperature of $CO_2$ is 304.21 K and that of $CH_4$ is 190.56 K. The critical pressure of $CO_2$ is 72.86 atm and that of $CH_4$ is 45.39 atm.

Then, the density and dynamic viscosity of $CO_2$ and $CH_4$ mixture at 20 °C and 1 bar are:

$$\rho_{CO_2/CH_4\,mix} = y_{CO_2}\rho_{CO_2} + y_{CH_4}\rho_{CH_4} = (0.4{\times}1.93\ \mathrm{kg\,m^{-3}}) + (0.6{\times}0.67\ \mathrm{kg\,m^{-3}})$$

= **1.17 kg $m^{-3}$**

And,
$$\mu_{CO_2/CH_4\,mix} = \frac{y_{CO_2}\mu_{CO_2}\sqrt{M_{w,CO_2}T_{c,CO_2}} + y_{CH_4}\mu_{CH_4}\sqrt{M_{w,CH_4}T_{c,CH_4}}}{y_{CO_2}\sqrt{M_{w,CO_2}T_{c,CO_2}} + y_{CH_4}\sqrt{M_{w,CH_4}T_{c,CH_4}}}$$

$$= \frac{0.4\left(1.46{\times}10^{-5}\ \mathrm{N\,s\,m^{-2}}\right)\sqrt{(44.01\ \mathrm{g\,mol^{-1}})(304.21\ \mathrm{K})} + 0.6\left(1.10{\times}10^{-5}\ \mathrm{N\,s\,m^{-2}}\right)\sqrt{(16.04\ \mathrm{g\,mol^{-1}})(190.56\ \mathrm{K})}}{0.4\sqrt{(44.01\ \mathrm{g\,mol^{-1}})(304.21\ \mathrm{K})} + 0.6\sqrt{(16.04\ \mathrm{g\,mol^{-1}})(190.56\ \mathrm{K})}}$$

= **1.31 × $10^{-5}$ N s $m^{-2}$**

The collision diameters of pure $CO_2$ and $CH_4$ are:

$$\vartheta_{CO_2} = 2.44\left(\frac{T_{c,CO_2}}{P_{c,CO_2}}\right)^{\frac{1}{3}} = 2.44\left(\frac{304.21\ \mathrm{K}}{72.86\ \mathrm{atm}}\right)^{\frac{1}{3}} = 0.3929\ \mathrm{nm}$$

And,
$$\vartheta_{CH_4} = 2.44\left(\frac{T_{c,CH_4}}{P_{c,CH_4}}\right)^{\frac{1}{3}} = 2.44\left(\frac{190.56\ \mathrm{K}}{45.39\ \mathrm{atm}}\right)^{\frac{1}{3}} = 0.3936\ \mathrm{nm}$$

Then, the average collision diameter of $CO_2$/$CH_4$ mixture is:

$$\vartheta_{CO_2/CH_4\,mix} = \frac{\vartheta_{CO_2} + \vartheta_{CH_4}}{2} = \frac{0.3929\ \mathrm{nm} + 0.3936\ \mathrm{nm}}{2} = \mathbf{0.3933\ nm}$$

The characteristic energies of pure $CO_2$ and $CH_4$ are:

$$\xi_{CO_2}/k_B = 0.77T_{c,CO_2} = 0.77{\times}304.21\ \mathrm{K} = 234.24\ \mathrm{K}$$

And,
$$\xi_{CH_4}/k_B = 0.77T_{c,CH_4} = 0.77{\times}190.56\ \mathrm{K} = 146.73\ \mathrm{K}$$

Then, the characteristic energy of $CO_2$/$CH_4$ mixture is:

$$\xi_{CO_2/CH_4\,mix}/k_B = \sqrt{\xi_{CO_2}\xi_{CH_4}} = \sqrt{234.24\ \mathrm{K}{\times}146.73\ \mathrm{K}} = 185.39\ \mathrm{K}$$

With $T$ = 293.15 K, the collision integral of $CO_2$/$CH_4$ mixture is:

$$\Omega_{CO_2/CH_4\,mix} = \frac{1.06036}{\left(\frac{k_BT}{\xi_{CO_2/CH_4\,mix}}\right)^{0.1561}} + \frac{0.193}{e^{\left(\frac{0.47635k_BT}{\xi_{CO_2/CH_4\,mix}}\right)}} + \frac{1.03587}{e^{\left(\frac{1.52996k_BT}{\xi_{CO_2/CH_4\,mix}}\right)}} + \frac{1.76474}{e^{\left(\frac{3.89411k_BT}{\xi_{CO_2/CH_4\,mix}}\right)}}$$

$$= \frac{1.06036}{\left(\frac{293.15\ \mathrm{K}}{185.39\ \mathrm{K}}\right)^{0.1561}} + \frac{0.193}{e^{\left(\frac{0.47635{\times}293.15\ \mathrm{K}}{185.39\ \mathrm{K}}\right)}} + \frac{1.03587}{e^{\left(\frac{1.52996{\times}293.15\ \mathrm{K}}{185.39\ \mathrm{K}}\right)}} + \frac{1.76474}{e^{\left(\frac{3.89411{\times}293.15\mathrm{K}}{185.39\ \mathrm{K}}\right)}}$$

= **1.17**

# Appendix 4: Publications

Some of the studies and findings of this research have been published as peer-reviewed journal paper and presented either in the forms of posters or oral presentations at a number of national and international conferences and seminars. The lists of publications are provided below.

**Journal**

- Hong, W.Y., Perera, S.P. and Burrows, A.D., 2015. Manufacturing of metal-organic framework monoliths and their application in $CO_2$ adsorption. *Microporous and Mesoporous Materials*, 214, pp. 149-155.

**Conferences/Seminars**

- Hong, W.Y., Perera, S.P. and Burrows, A.D., 2014. Enhanced $CO_2$ adsorption by MIL-101(Cr) MOF monolith: A porous and regenerative structured adsorbent for $CO_2$ capture. *In*: *IChemE Fluid Separations Interest Group Symposium – Emerging Separation Technologies (Oral Presentation), IChemE*, 10 October 2014, London, UK.

- Hong, W.Y., Perera, S.P. and Burrows, A.D., 2014. Manufacturing and characterisation of carbonate-based zeolite monoliths. *In*: *6th International Federation of European Zeolite Associations (FEZA) Conference – Porous Systems: From Novel Materials to Sustainable Solutions (Poster Presentation), University of Leipzig*, 8-11 September 2014, Leipzig, Germany.

- Hong, W.Y., 2014. $CO_2$ capture using novel zeolite monoliths. *In*: *Department of Chemical Engineering Seminar (Oral Presentation), University of Bath*, 18 February 2014, Bath, UK.

- Hong, W.Y., Perera, S.P. and Burrows, A.D., 2013. Development of energy efficient novel adsorbent monolith for $CO_2$ removal. *In*: *IChemE Fluid Separations Interest Group Symposium – Separation Technologies for $CO_2$ Capture (Oral Presentation), University of Edinburgh*, 19 April 2013, Edinburgh, UK.

- Hong, W.Y., Perera, S.P. and Burrows, A.D., 2013. Characterisation of adsorbent monolith. *In*: *Microscopy and Analysis Conference (Poster Presentation), University of Bath*, 9 January 2013, Bath, UK.

- Hong, W.Y., 2012. Development of monolithic adsorbent for the removal of carbon dioxide. *In*: *Department of Chemical Engineering Seminar (Oral Presentation), University of Bath*, 11 December 2012, Bath, UK.